A STUDY OF CP-VIOLATION THROUGH

A PRECISION MEASUREMENT OF

η_{00}/η_{+-}

BY

ROBERT H. BERNSTEIN

DECEMBER, 1984

THE UNIVERSITY OF CHICAGO

A STUDY OF CP-VIOLATION THROUGH A PRECISION MEASUREMENT OF η_{00}/η_{+-}

A DISSERTATION SUBMITTED TO

THE FACULTY OF THE DIVISION OF PHYSICAL SCIENCES

IN CANDIDACY FOR THE DEGREE OF

DOCTOR OF PHILOSOPHY

DEPARTMENT OF PHYSICS

BY

ROBERT H. BERNSTEIN

CHICAGO, ILLINOIS

DECEMBER, 1984

ACKNOWLEDGMENTS

I first thank Bruce Winstein, my thesis sponsor, for the direction and support he has given me over the last six years. His dedication and passion for detail have shaped the experiment and provided a high standard to follow.

I also thank my other collaborators: from Chicago, James Cronin, Gregory Bock, Duncan Carlsmith, David Coupal, George Gollin, Koichiro Nishikawa, and Wen Ke-Ling; from Saclay, René Turlay, Bernard Peyaud, and Armand Zylberstejn. Our engineering staff turned our blurred visions into working reality: Thomas Shea, Adrian Alexander, Richard Armstrong, Sollie Lucero, Richard Northrop, and Harold Sanders and the Electronic Development Group. The staff at Fermilab, especially of the Meson Lab and Computation Center, were friendly and helpful despite little acknowledgment and less (overt) gratitude.

Finally, research in physics requires considerable time and patience. Those of us with families know that more patience is required of them than of us: I would like to thank my wife, Denice, and son, Seth, for their sacrifice and support throughout this work.

Table of Contents

ACKNOWLEDGMENTS ii

LIST OF ILLUSTRATIONS vi

LIST OF TABLES xiv

ABSTRACT xv

Chapter

I. INTRODUCTION, MOTIVATION, AND EXPECTATIONS 1
- A. Introduction
- B. CP-Violation and the Phenomenology of K_L decays
- C. Experimental Knowledge of ϵ and ϵ'
- D. Current Predictions for ϵ'

II. PRINCIPLES OF THE MEASUREMENT 13
- A. Systematic Errors in a Measurement of η_{00}/η_{+-}
- B. Momentum Bin Analysis
- C. Backgrounds
- D. Detector Requirements
- E. The Regenerator and its Optimization; Beam Momentum

III. THE BEAM LINE, APPARATUS, AND TRIGGER 22
- A. Beam Line
- B. Apparatus
  - 1. Regenerator Region
  - 2. The Decay Region and Conversion Hodoscope
  - 3. The Separation Pipe and its Window
  - 4. The Charged Particle Spectrometer
  - 5. $3\pi^0$ Anticounters
- C. Charged Mode Trigger
- D. Neutral Mode Trigger

TABLE OF CONTENTS--(continued)

Chapter page

IV. THE LEAD GLASS 55

A. The Lead Glass and Its Properties
B. Light Coupling and Optical Filters; Photostatistics
C. The Photomultipliers and the Bases
D. Assembly and Construction
E. The ADC System
F. The Monitoring System
G. Calibration

V. CHARGED MODE RECONSTRUCTION AND BACKGROUND SUBTRACTIONS 109

A. Event Reconstruction
1. Drift Chamber Alignment
2. Track Fitting and Kinematic Analysis
B. Cuts Used in the Analysis
C. Isolation and Measurment of the Backgrounds
D. Isolation of the Signal; Background Subtractions
E. Incoherent K_S Background Subtractions

VI. NEUTRAL MODE RECONSTRUCTION AND BACKGROUND SUBTRACTIONS 160

A. Track Reconstruction
B. Cluster Finding; Energy and Position Determinations
1. Cluster Finding; Energy of a Cluster
2. Position Measurement and Track Correlation
C. Definition of Photons and the Analysis of Bremstrahlung
D. Event Reconstruction
E. Cuts Used in the Analysis
1. Track Requirements
2. Cluster Finding and Cluster Reconstruction Cuts
3. Kinematic Reconstruction Cuts
F. Background Subtractions

VII. EXTRACTION OF ϵ'/ϵ 263

A. Determination of ϵ'/ϵ
B. Checks of the Answer
C. Estimates of Systematic Errors

VIII. COMPARISONS AND CONCLUSIONS 288

A. Comparisons with Previous Measurements
B. Comparisons with Theoretical Predictions

TABLE OF CONTENTS--(continued)

Appendices page

A. REGENERATION 297

B. THE MONTE CARLO 301

REFERENCES 333

LIST OF ILLUSTRATIONS

Figure page

1. The mixing term and 'Penguin' diagram of the Kobayashi-Maskawa model. 11

2. A schematic of the beam line. 25

3. The double beam profile at the Regenerator, derived from reconstructed $K_S \rightarrow \pi^+\pi^-$. 27

4. A schematic of the apparatus. 29

5. A schematic of the Regenerator region. 33

6. A schematic of the conversion hodoscope. 37

7. The cell structure of the drift chambers. 41

8. The principle behind the use of mean timers. 47

9. The arrangement of the lead glass. 51

10. The initial gain distribution of the array. 61

11. A schematic of a calorimeter cell. 63

12. The effect of the five-count threshold on the ADC readout. 69

13. The lead glass response as a function of timing. 71

14. A schematic of the monitoring system. 73

15. The shift in gain from beam-on to beam-off conditions. 77

16. The variation of the gain with time within the spill, for randomly selected channels. 79

17. The standard deviation of the pedestals for a typical run. 81

18. A typical distribution of the lead glass response to a muon. 83

19. The average nonlinearity in the more nonlinear of the two neutral mode data sets. 85

20. The fraction of energy deposited in a block as a function of the impact point of the electromagnetic shower. 91

21. The energy in the glass divided by the momentum in the chambers. 93

22. The FWHM of E/p vs. $1/\sqrt{E}$ for electrons. 95

23. Two Showers, one at 20 Gev and one at 4 Gev of energy. 99

24. The π^o mass peak, after calibration. 101

25. The π^o mass as a function of π^o energy for the more nonlinear of the two neutral mode data sets. 103

26. The effect of systematic errors on the drift chamber residuals. 115

27. The distance of closest approach for charged tracks. 117

28. The z-vertex distribution for the $K_L \rightarrow \pi^+\pi^-$ sample. 119

29. The z-vertex distribution for the $K_S \rightarrow \pi^+\pi^-$ sample. 121

30. An inelastically produced K_S crossing between the beams before decaying. 123

31. The calculation of q^2 in the charged mode. 125

32. E/p for electrons after calibration in the charged mode. 129

33. The $m_{P\pi}$ distribution, showing a clear Λ^o peak. 131

34. The vacuum $K\pi 2$ sample for 30 GeV/c $< p_K <$ 40 GeV/c. 133

35. The distribution shown in Figure 34 for 50 $< p_K <$ 60 GeV/c. 135

36. The $m_{\pi\pi}$ vs. q^2 distribution for the identified $K\mu 3$ sample. 139

37. The $m_{\pi\pi}$ vs. q^2 distribution for the identified $Ke3$ sample. 141

38. The $m_{\pi\pi}$ vs. q^2 distribution for the vacuum $K\pi 2$ sample. 143

39. The mass distribution for the identified $K\mu 3$ sample for $q^2 < 300$ (MeV/c) ^{2}. 147

40. The distribution of Figure 39 for the identified $Ke3$ sample. 149

41. The mass distribution for the vacuum $K\pi 2$ sample summed over momentum. 151

42. The $m_{\pi\pi}$ vs. q^2 distribution for the regenerated $K\pi 2$ sample. 153

43. The q^2 distribution of the regenerated $K\pi 2$ sample in each bin of momentum. 157

44. The mass distribution of the regenerated $K\pi 2$ sample in each bin of momentum. 159

45. Two close tracks passing through the spectrometer. 163

46. Energy mismeasurement in 'fused' clusters. 167

47. The position resolution of the lead glass. 171

48. Photon pairings and the calculation of the z-vertex in the neutral mode. 175

49. The χ^2 distribution for the $K_S \rightarrow \pi^o \pi^o$ sample. 179

50. The $K_L \rightarrow 3\pi^o$ mass peak. 181

51. The z-vertex distribution for the $K_L \rightarrow \pi^o \pi^o$ sample. 183

52. The distribution of Figure 51 for the $K_S \rightarrow \pi^o \pi^o$ sample. 185

53. The use of the converted pair in determining the vertex. 189

54. The transverse vertex distribution for the coherent $K_S \rightarrow \pi^o \pi^o$ sample. 191

55. The xy deviation of tracks at the conversion hodoscope. 195

56. A typical $SEP2$ distribution. 197

57. The $m_{\pi\pi}$ vs. q^2 distribution for the

$K_L \rightarrow \pi^0\pi^o$ sample. 201

58. The $m_{\pi\pi}$ vs. q^2 distribution for the

$K_S \rightarrow \pi^o\pi^o$ sample. 203

59. The mass distribution of the $K_S \rightarrow \pi^o\pi^o$

sample for 50 $< p_K <$ 60 GeV/c. 207

60. The distribution of Figure 59 for 60 $< p_K <$ 70 GeV/c. 209

61. The distribution of Figure 59 for 70 $< p_K <$ 80 GeV/c. 211

62. The distribution of Figure 59 for 80 $< p_K <$ 90 GeV/c. 213

63. The distribution of Figure 59 for 90 $< p_K <$ 100 GeV/c. 215

64. The distribution of Figure 59 for 100 $< p_K <$ 110 GeV/c. 217

65. The distribution of Figure 59 for 110 $< p_K <$ 120 GeV/c. 219

66. The distribution of Figure 59 for 120 $< p_K <$ 130 GeV/c. 221

67. The distribution of Figure 59 for 130 $< p_K <$ 140 GeV/c. 223

68. The mass distribution of the $K_L \rightarrow \pi^o\pi^o$

sample for 70$< p_K <$ 80 GeV/c

and 10000 $< q^2 <$ 50000 (MeV/c) ^{2}. 225

69. The dependence of the shape of the neutron background

upon momentum. 227

70. The dependence of the shape of the $3\pi^o$ background

upon momentum. 229

71. The mass distribution of the $K_L \rightarrow \pi^o \pi^o$ sample for $50 < p_K < 60$ GeV/c. 233

72. The distribution of Figure 71 for $60 < p_K < 70$ GeV/c. 235

73. The distribution of Figure 71 for $70 < p_K < 80$ GeV/c. 237

74. The distribution of Figure 71 for $80 < p_K < 90$ GeV/c. 239

75. The distribution of Figure 71 for $90 < p_K < 100$ GeV/c. 241

76. The distribution of Figure 71 for $100 < p_K < 110$ GeV/c. 243

77. The distribution of Figure 71 for $110 < p_K < 120$ GeV/c. 245

78. The distribution of Figure 71 for $120 < p_K < 130$ GeV/c. 247

79. The distribution of Figure 72 for $130 < p_K < 140$ GeV/c. 249

80. The global $K_L \rightarrow \pi^o \pi^o$ distribution with the $3\pi^o$ and neutron backgrounds indicated separately. 251

81. The distribution of Figure 80 with the two sources of backgrounds summed. 253

82. The distribution of Figure 80, rebinned, with the Monte Carlo superimposed. 255

83. The q^2 dependence of the $K_S \rightarrow \pi^o \pi^o$ sample in each bin of kaon momentum. 257

84. The q^2 dependence of the $K_L \rightarrow \pi^o \pi^o$ sample for $70 < p_K < 90$ GeV/c. 259

85. $|(f - \bar{f})/k|$ for Carbon as measured by E82. 269

98. The converted photon energy spectrum for coherent K_S, data and Monte Carlo, in the neutral mode. 321

99. The unconverted photon energy spectrum for coherent K_S, data and Monte Carlo, in the neutral mode. 323

100. The distance between photons for coherent K_S, data and Monte Carlo. 325

101. The χ^2 distribution of coherent K_S, data and Monte Carlo, in the neutral mode. 327

102. The coherent K_S and K_L z-vertex distribution, $60 < p_K < 70$ GeV/c and $90 < p_K < 100$ GeV/c, data and Monte Carlo, in the charged mode. 329

103. The coherent K_S energy spectrum, data and Monte Carlo, in the charged mode. 331

86. $|(f-\bar{f})/k|$ for Carbon as measured by the present experiment, in the charged mode. 271

87. $|(f-\bar{f})/k|$ for Carbon as measured by the present experiment, in the neutral mode. 273

88. η_{oo}/η_{+-} as a function of kaon momentum. 283

89. A comparison of the value of ϵ'/ϵ with previous measurements. 293

90. A recent theoretical prediction for ϵ'/ϵ in the Kobayashi-Maskawa model. 295

91. The $K_L \rightarrow 3\pi^o$ z-vertex distribution, $60 < p_K < 70$ GeV/c, data and Monte Carlo. 307

92. The distribution of Figure 90, $70 < p_K < 80$ GeV/c. 309

93. The distribution of Figure 90, $80 < p_K < 90$ GeV/c. 311

94. The distribution of Figure 90, $90 < p_K < 100$ GeV/c. 313

95. The coherent K_S and K_L z-vertex distribution for $60 < p_K < 70$ GeV/c and $90 < p_K < 100$ GeV/c, data and Monte Carlo, in the neutral mode. 315

96. The z-vertex distribution of all coherent K_S, data and Monte Carlo, in the neutral mode. 317

97. The coherent K_S energy spectrum, data and Monte Carlo, in the neutral mode. 319

LIST OF TABLES

Table page

1. Positions and Properties of the Elements of the Spectrometer 31

2. Parameters of Drift Chamber Performance 39

3. Data Sets used in the Analysis 108

4. Number of $K_L \rightarrow \pi^+\pi^-$ decays 145

5. Number of $K_S \rightarrow \pi^+\pi^-$ decays 155

6. Number of $K_L \rightarrow \pi^o\pi^o$ decays 261

7. Number of $K_S \rightarrow \pi^o\pi^o$ decays 262

8. Constants Used in the Fits 266

9. $|(f - \bar{f})/k|$ in the charged and neutral modes 267

10. Number of $K_L \rightarrow \pi^o\pi^o$ cut at z_{RA} 278

11. Number of Events in the (p,z) bins 279

12. $|\eta_{oo}/\eta_{+-}|^2$ vs. kaon momentum 281

13. Systematic Errors 287

14. Acceptances for K_L , $K_S \rightarrow \pi^o\pi^o$ 305

15. Acceptances for K_L , $K_S \rightarrow \pi^+\pi^-$ 332

ABSTRACT

We have measured the ratio of the CP-nonconservation parameters $|\eta_{oo}|$ and $|\eta_{+-}|$ and thereby determined the value of $|\epsilon' / \epsilon|$, which reflects the contribution of 'direct' CP-violation compared to the CP-violation arising from the 'mixing' of K^o and $\overline{K}^o$. The measurement was performed using regeneration of K_S in an initially pure K_L beam in a double beam arrangement: two nearly parallel, side-by-side beams, one containing K_L and the other a regenerator to produce K_S. By using the double beam technique systematic errors arising from flux monitoring and dead-time corrections were minimized. The charged and neutral decays were measured in the same beam line with minimal changes to the apparatus; the same regenerator was used for both charged and neutral decays and hence there is no systematic error arising from uncertainty in the regeneration amplitude. We have collected 3150 $K_L \rightarrow \pi^o \pi^o$ decays, roughly ten times the previous world sample.

Our improved statistical power and reduced systematic error have reduced the errors a factor of four over any previous measurement. We find $|\epsilon' / \epsilon| = -0.0046 \pm 0.0053(stat.) \pm 0.0024(syst.)$ This value is in disagreement with predictions for $|\epsilon' / \epsilon|$ from the Kobayashi-Maskawa model but is consistent with zero and the superweak hypothesis of CP-violation.

CHAPTER I

INTRODUCTION, MOTIVATION, AND EXPECTATIONS

A. Introduction

Symmetries and conservation laws are central to our understanding of the physical world. The macroscopic symmetries of space and time translation imply the conservation of momentum and of energy; both of these svmmetries and their conservation laws have guided physics for centuries.

In our time the discovery of quantum phenomena has revealed a range of microscopic symmetries. Three of these are parity (P), charge conjugation (C) and time reflection(T). Invariance under P means that the mirror image of an experiment yields the same result as the original. Charge conjugation (C) changes particles into their antiparticles, and C-symmetry means that experiments performed in a world made mostly of antimatter gives the same results as those performed in our own, mostly matter, world. Time reflection exchanges t for $-t$; momenta and angular momenta are reversed.

The CPT theorem of Luders and Pauli[1] connects these transformations: under weak assumptions in a local field theory fundamental processes are invariant under the combined operation CPT. It was first assumed that C, P, and T were con-

served separately. The discovery of P-violation in nucleon decay[2] and of C-violation in π and μ decay[3] refuted this simple picture. The combined product CP was taken to replace the separate conservation of C and P.

The discovery of CP-violation in 1964[4] shattered this hope as well. The assumptions required for the validity of the CPT theorem are so general that T-violation had to be accepted. The violation of T-symmetry may have profound consequences. Although the tiny CP- violating effect has never been seen outside the K^o system, recent work[5] implies it may also explain the excess of matter over antimatter in the universe.

Since the discovery of CP-violation we have attempted to understand its source. Is there a new, fifth force in nature responsible for the effect? Can we incorporate CP-violation into the 'standard model' of quarks and leptons, and if so, how?

The work described in this thesis is an experimental study of CP- violation in two pion decays of the K_L. In this chapter we review some of the phenomenology of CP-violation, defining the quantity we have measured and explaining its importance. Next we summarize our knowledge about CP-violation. Finally we discuss models of CP- violation and their predictions.

B. CP-Violation and the Phenomenology of K_L Dècays

The strong eigenstates of the neutral K^o meson system are the $|K^o>$ and the $|\overline{K}^o>$, which have strangeness +1 and -1 respectively. The weak interactions do not conserve strangeness and can mix the states through second-order weak transitions. Hence $|K^o>$ and $|\overline{K}^o>$ are not eigenstates of the weak interaction Hamiltonian. If CP were conserved (we assume CPT invariance) the eigenstates would be:

$$|K_1> = \frac{|K^o> + |\overline{K}^o>}{\sqrt{2}} \qquad CP = +1 \tag{1.1a}$$

$$|K_2> = \frac{|K^o> - |\overline{K}^o>}{\sqrt{2}} \qquad CP = -1 \tag{1.1b}$$

as originally pointed out by Gell-Mann and Pais (who assumed C-invariance).[6] Now both $<\pi^+\pi^-|\mathrm{CP}|\pi^+\pi^->$ and $<2\pi^o|\mathrm{CP}|2\pi^o> = +1$ for pions in a state of angular momentum zero. Hence the K_1 can decay into two pions but the K_2 cannot. The two-pion decay is preferred over three body-decays because of phase space; hence this closed channel causes the K_2 to be longer-lived than the K_1. The discovery of CP-violation was the observation of the longer-lived component, the supposedly pure CP-odd state, decaying into the CP-even two-pion state. Including CP-violation, we write the decay eigenstates as:

$$|K_L> = \frac{|K_2> + \epsilon|K_1>}{\sqrt{2(1+|\epsilon^2|)}} \qquad (\textit{mostly CP odd}) \tag{1.2a}$$

$$|K_S> = \frac{|K_1> + \epsilon|K_2>}{\sqrt{2(1+|\epsilon^2|)}} \qquad (\textit{mostly CP even}) \tag{1.2b}$$

Thus ϵ measures the CP-impurity in the decay eigenstates. The parameter ϵ can be defined in terms of the mass (M) and decay (Γ) matrices which control the

time evolution of the K^o and $\overline{K}^o$ system:[7]

$$\epsilon = \frac{-\mathrm{Im}M_{12} + i\,\mathrm{Im}\Gamma_{12}\,/\,2}{i(m_S - m_L) + (\Gamma_S - \Gamma_L)/2} \tag{1.3}$$

Γ_S and Γ_L are the K_L and K_S decay rates and m_S and m_L their masses, respectively. Limits on $\mathrm{Im}\Gamma_{12}$ can be determined from the observed decay rates of K_S and K_L to the various decay modes. $\mathrm{Im}\Gamma_{12}$ is known[8] to be $\leq .3\times10^{-3}$, which we shall see is small compared to ϵ. Also $\Gamma_L << \Gamma_S$ and we shall ignore it henceforth.

Is CP-violation completely measured by ϵ? CP-violation in $K_L \rightarrow 2\pi$ can occur in two ways: either the K_2 directly decays into two pions or it does not. If it does not, CP-violation occurs only in the formation of the K_L , as measured by ϵ, and not in its decay. The ϵ contribution to CP-violation is the part that has been measured. There is no evidence for the direct CP-violating decay of the K_2; our experiment attempted to determine whether the direct decay occurs.

How can we separate K_1 from K_2 decays within the K_L? Let us assume that the K_2 does not decay into two pions; we note that for a two-pion state:

$$\begin{aligned}\frac{amp(K_L \rightarrow 2\pi)}{amp(K_S \rightarrow 2\pi)} &= \frac{<2\pi|H_W|K_L>}{<2\pi|H_W|K_S>} \\ &= \frac{\epsilon\ <2\pi|H_W|K_1>}{<2\pi|H_W|K_1>} = \epsilon\end{aligned} \tag{1.4}$$

regardless of whether the two-pion state is $\pi^o\pi^o$ or $\pi^+\pi^-$. If we now define

$$\eta_{oo} = \frac{amp(K_L \rightarrow 2\pi^o)}{amp(K_S \rightarrow 2\pi^o)} = |\eta_{oo}|\ e^{i\Phi_{oo}} \tag{1.5a}$$

$$\eta_{+-} = \frac{amp(K_L \rightarrow \pi^+\pi^-)}{amp(K_S \rightarrow \pi^+\pi^-)} = |\eta_{+-}|\ e^{i\Phi_{+-}} \tag{1.5b}$$

then

$$\frac{\eta_{oo}}{\eta_{+-}} = 1 \tag{1.6}$$

This is the 'superweak' prediction, which confines CP-violation to the impurity in the decay eigenstates. This experiment measures $|\eta_{oo}/\eta_{+-}|$. We will now see that if the K_2 directly decays into two pions, η_{oo}/η_{+-} need not be equal to one.

It is clear from equation (1.4) that if $<2\pi|H|K_2>$ is not zero, η_{oo}/η_{+-} can deviate from unity. We now define a parameter ϵ' which expresses this difference. We first decompose the $\pi\pi$ final states into isospin states; the allowed states for two pions with zero angular momentum are I = 0 and I = 2. In the notation of Wu and Yang[9] we find

$$\eta_{oo} = \epsilon - 2\frac{\epsilon'}{1-\sqrt{2}\omega} \tag{1.7}$$

$$\eta_{+-} = \epsilon + \frac{\epsilon'}{1+\omega/\sqrt{2}} \tag{1.8}$$

where

$$\epsilon' = \frac{1}{\sqrt{2}}\mathrm{Im}\frac{A_2}{A_0} \quad e^{i(\frac{\pi}{2}+\delta_2-\delta_0)} \tag{1.9}$$

$$A_2 = amp(K^o \rightarrow 2\pi) \quad (I=2) \tag{1.10a}$$

$$A_0 = amp(K^o \rightarrow 2\pi) \quad (I=0) \tag{1.10b}$$

$$\omega = \frac{1}{\sqrt{2}}\mathrm{Re}\frac{A_2}{A_0} \quad e^{i(\delta_2-\delta_0)} \tag{1.10c}$$

and δ_2 and δ_0 are the strong interaction $\pi\pi$ phase shifts for the I = 2 and I = 0 final states respectively. The parameter ω measures the ΔI = 3/2 amplitude; it is of order 5% and can be neglected in calculating η_{oo}/η_{+-}.[10] If there is a phase difference between the ΔI = 1/2 and ΔI = 3/2 parts of the K $\rightarrow 2\pi$ amplitude,

direct CP violation will occur with the signature:

$$\frac{\eta_{oo}}{\eta_{+-}} = \frac{\epsilon - 2\epsilon'}{\epsilon + \epsilon'} \tag{1.11}$$

C. Experimental Knowledge of ϵ and ϵ'

The Particle Data Book values for η_{+-} and η_{oo} are:

$$\eta_{+-} = (2.27 \pm .02) \times 10^{-3} \quad e^{i(44.6^o \pm 1.2^o)} \tag{1.11a}$$

$$\eta_{oo} = (2.33 \pm .08) \times 10^{-3} \quad e^{i(54^o \pm 5^o)} \tag{1.11b}$$

which are reasonably consistent with $\eta_{oo} = \eta_{+-} = \epsilon$. We can see from equation (1.3) that $\mathrm{Im}\Gamma_{12} << \eta_{+-}$. Hence the 'natural' phase of ϵ is

$$\Phi_N = arg\ \epsilon = \tan^{-1} \frac{-2\Delta M}{\Gamma_S} \tag{1.13}$$

where

$$\Delta \mathrm{m} = m_L - m_S$$

The quantities Δm and Γ_S have been accurately measured in a series of experiments:[11] $\Delta m = (0.5349 \pm 0.0022) \times 10^{10}\ h\ \mathrm{sec}^{-1}$ and $\Gamma_S = (1.121 \pm .003) \times 10^{11} \mathrm{sec}^{-1}$. The phase Φ_N then has the value $43.7^o \pm 0.2^o$, which is consistent with the Φ_{+-} measurements. The value of Φ_{oo} is principally due to Christenson[12] and is in slight disagreement with Φ_N.

Another determination of ϵ is obtained from measuring the charge asymmetry

$$\Delta_L = \frac{\Gamma(K_L \to \pi^- l^+ \nu_l) - \Gamma(K_L \to \pi^+ l^- \bar{\nu}_l)}{\Gamma(K_L \to \pi^- l^+ \nu_l) + \Gamma(K_L \to \pi^+ l^- \bar{\nu}_l)} \tag{1.14}$$

The $\Delta Q = \Delta S$ rule requires a K^o to decay into a π^- rather than a π^+; expanding K_L and K_S in terms of K^o and $\overline{K}^o$ yields:

$$\Delta_L = 2\mathrm{Re}\ \epsilon \tag{1.15}$$

where we have assumed the $\Delta Q = -\Delta S$ amplitude is negligible compared to the $\Delta Q = \Delta S$ amplitude.[13]

The experimental value for $\Delta_L = (3.30 \pm .12) \times 10^{-3}$ and the phase Φ_{+-} give a value for ϵ of $(2.3 \pm 0.1) \times 10^{-3}$, consistent with the η_{oo} and η_{+-} determinations of ϵ.

The determinations of ϵ provide no evidence for direct CP-violation. The value of ϵ determined from the charge asymmetry is consistent with the values of η_{oo} and η_{+-}, and with an ϵ' of zero. We saw in equation (1.9) that the phase of ϵ' is governed by the $\pi\pi$ phase shifts. δ_2 and δ_0 have been accurately measured:[14] $\delta_2 = -7.2 \pm 1.3^o$ and $\delta_o = 46^o \pm 5^o$. Therefore the phase of ϵ' is $37^o \pm 5^o$, close to the phase of ϵ, so that the value of Φ_{+-} and Φ_{oo} are not sensitive to a non-zero ϵ'.

How then can we extract ϵ' ? We know $\eta_{oo} \approx \eta_{+-}$ in both phase and magnitude; therefore ϵ' is small. If we now use this information in equation (1.11), we find

$$|\eta_{oo}/\eta_{+-}|^2 \approx 1\text{–}6\ \frac{\epsilon'}{\epsilon}$$

and a measurement of $|\eta_{oo}/\eta_{+-}|$ is a direct measurement of $|\epsilon'/\epsilon|$!

Three previous experiments have measured $|\eta_{oo}/\eta_{+-}|$: Banner *et.al.*[15], obtained 1.03 ± 0.07; Holder, *et.al.*[16], 1.00 ± 0.06; and Christenson, *et.al.*[17] ,1.00 ± 0.09.

These results are again consistent with $\epsilon' = 0$. The first two experiments directly measured $|\eta_{oo}/\eta_{+-}|$ by observing the decays of K_L and K_S into two pions.

These two experiments were based on approximately 150 $K_L \rightarrow 2\pi^o$ events each, severely limiting their power. The third experiment observed K_L and K_S simultaneously; it examined the proper-time distribution of a coherent mixture of K_L and K_S and relied on their interference to measure η_{oo} and η_{+-} separately. We will discuss these experiments more thoroughly in the final chapter.

D. Current Predictions for ϵ'

The simplest explanation of CP-violation is the superweak model. Wolfenstein [18] hypothesized a direct $\Delta S = 2$ CP-violating interaction. This new force interferes with the second-order weak interaction to provide the CP-violating $\Delta S = 2$ amplitude. The strength of the superweak interaction is of order 10^{-7} of the weak interaction. The only parameter in the model is this strength, reflected by ϵ. Unfortunately the model is purely phenomenological ; ϵ itself is a parameter measured from the data without any relation to quantities outside the K^o system. It would be more satisfying to understand CP-violation as part of the standard model of the interactions of quarks and leptons.

In 1973 Kobayashi and Maskawa[19] proposed a natural method of incorporating the source of both ϵ and ϵ' into the framework of weak currents among quarks. They pointed out that if there were three quark doublets, in addition to two new Cabbibo-like angles there would also be a free phase in the couplings which could give rise to CP-violation and account for both ϵ and ϵ' effects.

The generalized current is given by (c_i and s_i are the cosine and sine of the ith

The generalized current is given by (c_i and s_i are the cosine and sine of the ith Cabbibo-angle):

$$(\ u\ \ c\ \ t\ )\begin{pmatrix} c_1 & -s_1c_3 & -s_1s_3 \\ s_1c_2 & c_1c_2c_3-s_2s_3e^{i\delta} & c_1c_2s_3+s_2c_3e^{i\delta} \\ s_1s_2 & c_1s_2c_3+c_2s_3e^{i\delta} & c_1s_2s_3-c_2c_3e^{i\delta} \end{pmatrix}\begin{pmatrix} d \\ s \\ b \end{pmatrix}$$

The phase $e^{i\delta}$ is responsible for both the CP-violating part of the mixing of K^o and $\overline{K}^o$ (ϵ) and for the direct decays (ϵ'). Much work[20] has been devoted to the so-called 'Penguin diagram' as a possible source for a non-zero ϵ' and as the origin of the $\Delta I = 1/2$ rule. Figure 1 shows the possible mixing term and the Penguin diagram.

Numerous authors[21] have estimated the size of $|\eta_{oo}/\eta_{+-}|$ in the Kobayashi-Maskawa model. The calculations are particularly difficult because they involve translating the weak interactions of quarks into the weak interactions of hadrons and uncertain because they require experimental input which is not well determined.

The size of both ϵ and ϵ' is proportional to $s_2c_2s_3\sin\delta$. The magnitude of ϵ'/ϵ depends upon the bottom lifetime (through its constraints on the Cabbibo angles), the top quark mass, and various strong interaction corrections. The sign of ϵ'/ϵ is constrained to be positive. The argument is principally based on the bound[22] B(b $\rightarrow$ u)/B(b $\rightarrow$ c) $<$ .09, which requires $s_2c_2s_3\sin\delta$ to be positive, and the fact that ΔI = 1/2 transitions are enhanced rather than suppressed. Conservative estimates[23] suggest that $\epsilon'/\epsilon > .005$.

Figure 1. The mixing term and Penguin diagram of the Kobayashi-Maskawa model. The mixing term is thought to be responsible for K^o $\bar{K}^o$ mixing (ϵ effects) and the Penguin diagram is a possible source of 'direct' CP-violation (ϵ' effects).

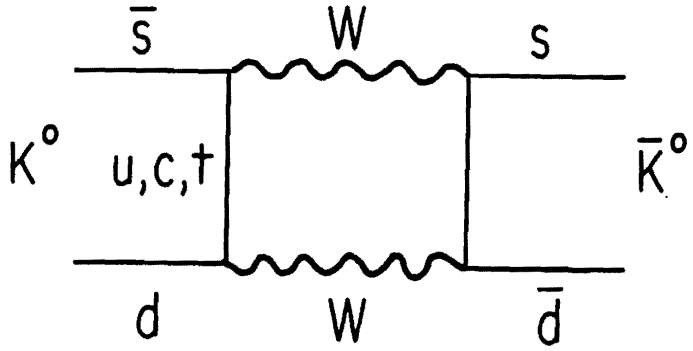

Mixing Term

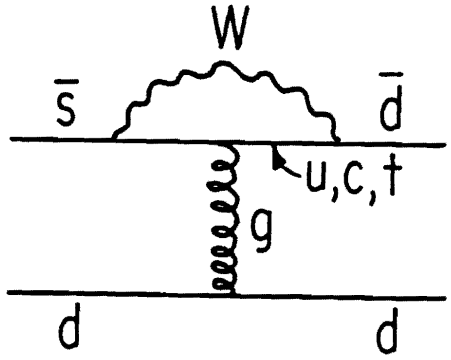

Penguin Diagram

There are at least two other models which predict a non-zero ϵ'. Left-right symmetric models have a group structure $SU(2)_L \times SU(2)_R \times U(1)$. These models predict a wide range for $|\epsilon'/\epsilon|$[24] Another model, due to Weinberg[25], places CP-violation in the Higgs sector. It predicts a value of $|\epsilon'/\epsilon| \leq$ -.02, and is thus almost ruled out already. The model also predicts a neutron electric dipole moment of roughly 10^{-25} e-cm. The current experimental upper limit quoted in the Particle Data Book for the neutron electric dipole moment is 6×10^{-25} at 90% confidence. The electric dipole moment in the Kobayashi-Maskawa model is about 10^{-30} e-cm, far beyond any foreseeable experimental sensitivity.

In summary, a measurement of a non-zero ϵ' would greatly increase our knowledge of CP-violation. A measurement of $|\eta_{oo}/\eta_{+-}|$ to an accuracy of a percent would place severe constraints on all theoretical predictions. A clear deviation of η_{oo}/η_{+-} from unity would prove CP-violation is not due to a new, 'superweak' force. Disagreement with the Kobayashi-Maskawa model could signal a range of new phenomena.

CHAPTER II

PRINCIPLES OF THE MEASUREMENT

In this experiment we measure $|\eta_{oo}/\eta_{+-}|$; we have chosen to perform separate measurements of η_{oo} and η_{+-} in the same beam line with only slight modifications to the apparatus. In the η_{+-} measurement (which we will refer to as the charged mode) we detect the decays of K_L and K_S into charged pions and reconstruct the event. In the η_{oo} measurement (which we will refer to as the neutral mode) we detect all four photons from the decay $K_L \rightarrow \pi^o \pi^o$, where the π^o decays into two photons. We place the apparatus far from the K source to provide a pure K_L beam and then use a regenerator to produce K_S (A discussion of regeneration is given in Appendix I).

In this chapter, we first explain the systematic problems associated with a measurement of $|\eta_{oo}/\eta_{+-}|$; we then show how our experimental method makes us insensitive to some of these problems, leading us to a preview of the analysis. We then discuss the sources of background. The method and the need to reduce the backgrounds place definite requirements on the detector; we list these requirements and the apparatus used to meet them, reserving a full treatment for Chapters III and IV.

A. Systematic Errors in a Measurement of η_{oo}/η_{+-}

We begin this section by writing down expressions for the observed number of K_L decays in a pure K_L beam (a 'vacuum' beam) , and a similar expression for the observed number of K_S decays following a regenerator. These expressions will help us understand the systematic errors in a measurement of $|\eta_{oo}/\eta_{+-}|$ and guide us to an experimental method for minimizing them.

Denote by $N^L{}_V(p)$ the number of K_L of momentum p incident on a detector. Then the distribution of detected $K_L \rightarrow 2\pi^o$ decays, $I^{oo}{}_V$,('V' stands for vacuum) decaying with momentum p at vertex z (z is along the direction of motion of the beam) is proportional to:

$$I^{oo}{}_V = N^L{}_V\, |\eta_{oo}|^2\, \epsilon_{oo}{}^V(p,z)\, L_V \tag{2.1}$$

where $\epsilon_{oo}{}^V(p,z)$ is the acceptance as a function of p and z and L_V is the livetime. Now consider $N^L{}_R(p)$ K_L incident on a regenerator. The distribution of observed K_S decays is (we ignore the contribution of K_L):

$$I^{oo}{}_R = N^L{}_R\, |\rho|^2\, \epsilon_{oo}{}^R(p,z) L_R\, e^{-X}\, e^{-z/\Lambda_S} \tag{2.2}$$

where R stands for regenerator. The factor e^{-X} measures the absorption of K_L in the regenerator and e^{-z/Λ_S} reflects the K_S lifetime. The parameter ρ is the regeneration amplitude; we have suppressed its momentum dependence.

The ratio of observed K_L to observed K_S in any bin of momentum and z-vertex is

$$R^{oo} = \frac{N^L{}_V(p)}{N^L{}_R(p)}\ \frac{\epsilon^{oo}{}_V(p,z)}{\epsilon^{oo}{}_R(p,z)}\ \frac{e^X e^{z/\Lambda_S}}{|\rho|^2}\frac{L_V}{L_R}\ |\eta_{oo}|^2 \tag{2.3}$$

A similar expression holds in the charged mode. We can determine η_{oo}/η_{+-} by taking the ratio R^{oo}/R^{+-}.

The sources of systematic error can be seen directly: we must know the ratio of fluxes, the ratio of acceptances, the regeneration amplitude, and the ratio of lifetimes.

How can we eliminate these sources of error? We have used a 'double beam': two parallel, side-by-side beams, in one of which we place a regenerator. The decays $K_L \rightarrow 2\pi^o$ and $K_S \rightarrow 2\pi^o$ are measured simultaneously. Small changes are then made to the detector and $K_L \rightarrow \pi^+\pi^-$ and $K_S \rightarrow \pi^+\pi^-$ are measured together.

The double beam arrangement causes all but one of the systematic errors to cancel in forming R^{oo}/R^{+-}. We insure that the flux ratio between the two beams, $N^L{}_V/N^L{}_R$ cancels by frequently alternating the regenerator between the two beams. We insure L_V/L_R cancels by performing the K_L and K_S experiments simultaneously. These two factors cancel in taking the K_L to K_S ratio for the charged mode and neutral mode separately. Since we use the identical regenerator in both the $\pi^o\pi^o$ and $\pi^+\pi^-$ measurements, the regeneration amplitude and absorption cancel between the charged and neutral modes in forming $|\eta_{oo}/\eta_{+-}|$.

We are left with the ratio of acceptances. The K_L lifetime is hundreds of meters long at our energies; the K_S lifetime is approximately five meters. The K_L and K_S decays therefore have a different spatial distribution and so K_L and K_S decays have different acceptances. If we bin the data in small bins of momentum

and z-vertex, the ratio of acceptances will cancel within each bin. Smearing across the bins will distort the K_S distribution more than the K_L distribution, again because of the different lifetimes. The bin size must be chosen carefully and the resolution must be small compared to the bin size for the cancellation to be effective. The e^{z/Λ_S} term will cancel in each bin of p and z from the charged to neutral modes. We then find:

$$\frac{R^{oo}}{R^{+-}} = |\frac{\eta_{oo}}{\eta_{+-}}|^2 \tag{2.4}$$

in each bin of momentum and z-vertex.

This discussion ignored the contribution of K_L decays in the regenerated beam. We quoted the distribution for K_S decays; the observed distribution of 2π decays contains the contribution from the remaining K_L and an interference term between K_S and K_L; the precise form is given in Appendix I. The significance of these terms will be described in the next section. If we bin the data as described here the correction is small and calculable.

B. Momentum Bin Analysis

We have chosen to bin the data in momentum but not in z-vertex. This method then will require a Monte Carlo to calculate the ratio of acceptances between K_L and K_S decays. The method has two advantages. First we are far less dependent on an understanding of the resolution smearing than if we analyzed the experiment in bins of momentum and z-vertex. The second advantage is statistical; we shall be able to increase the number of K_L decays by more than 1/3.

In Appendix I we quote the form for the proper time distribution of coherent 2π decays following a regenerator. Here we integrate that distribution over a decay region from z_1 to z_2; assuming a fixed kaon momentum, the integral over z becomes an integral over proper time τ, from 0 to $\tau_{\max}$:

$$R^R(p) = |\rho|^2 \left(1-e^{-\Gamma_S \tau_{\max}}\right) + |\eta|^2 \left(1-e^{-\Gamma_L \tau_{\max}}\right) + \left| \frac{2\mathrm{Re}(\rho\eta^*)}{1/2 - i\Delta m/\Gamma_S} \left(1-e^{-\Gamma_S(1/2-i\Delta m/\Gamma_S)\tau_{\max}}\right) \right|^2 \tag{2.5}$$

and for the K_L (the vacuum beam)

$$R^V(p) = |\eta|^2 \left(1-e^{-\Gamma_L \tau_{\max}}\right) \tag{2.6}$$

Here η denotes either η_{oo} or η_{+-}, depending on whether the charged or neutral decays are observed. We have assumed the phase of η is the same as the phase of ϵ. The ratio $R_R(p)/R_V(p)$ is a function of the parameters Δm, Γ_S and Γ_L, and the phases of the regeneration amplitude and of ϵ. It is not a function of ρ and η separately, but only of the ratio ρ/η.

We wish to relate the ratio $R_R(p)/R_V(p)$ to the observed numbers of decays in the two beams. $R_R(p)/R_V(p)$ is the ratio of the true number of vacuum beam decays to the true number of regenerated beam decays. To obtain this ratio from the data we divide the observed number of regenerated beam decays by the observed number of vacuum beam decays and then correct for the ratio of acceptances. Denote the acceptance-corrected yield by Y; then

$$\frac{Y^{oo}{}_R(p)}{Y^{oo}{}_V(p)} = \frac{R^{oo}{}_R(p)}{R^{oo}{}_V(p)} \tag{2.7}$$

$$\frac{Y^{+-}{}_R(p)}{Y^{+-}{}_V(p)} = \frac{R^{+-}{}_R(p)}{R^{+-}{}_V(p)} \tag{2.8}$$

The left side of these expressions is a function of the observed numbers of events and the acceptances. The right side is a function of ρ/η. We can assume $\eta_{oo} = \eta_{+-} = \epsilon$ and fit for ρ in the charged mode and ρ in the neutral mode separately. Since we use the same regenerator in each mode, and $R_R(p)/R_V(p)$ only contains ρ/η, we can measure a shift in ρ from the charged mode to the neutral mode and interpret the change as due to a non-zero ϵ'. We will refine this analysis in Chapter VIII.

There is a statistical advantage to binning in momentum over binning in momentum and vertex. Since the K_S distribution drops rapidly with z-vertex, in an experiment with finite statistics there will be many empty (p,z) bins in the K_S beam which are well populated in the K_L beam. These K_L decays cannot be used in the (p,z) bin technique. There are also many K_L decays upstream of the regenerator in the K_L beam; we cannot use these since there are no K_S decays upstream of the regenerator. Both of these regions can be used if we know the acceptance and bin in momentum. The statistical increase referred to above was obtained by using these two regions of K_L decays.

C. Backgrounds

Backgrounds do not cancel in calculating η_{oo}, η_{+-}, or their ratio. This section summarizes the principal backgrounds in the vacuum beam first for the charged

and then for the neutral mode. The purpose is to establish how the backgrounds shape the design of the experiment.

The charged mode backgrounds come primarily from semileptonic decays of the K_L, $K\mu 3$ and $Ke3$ decays. The branching ratios of $K_L \rightarrow \pi e \nu$ and $K_L \rightarrow \pi \mu \nu$ relative to $K_L \rightarrow \pi^+ \pi^-$ are approximately 60 and 130; we must reject these decays to achieve a reasonable trigger rate. These decays also provide a background which must be subtracted.

The most severe background in the neutral mode is the decay $K_L \rightarrow 3\pi^o$. This decay has a branching ratio of about 230 relative to the two-pion decay and presents considerable triggering difficulties. It can also 'fake' $2\pi^o$ decays. The three neutral pions decay into six photons. If two photons miss the detector, only four photons are observed, just as in a $K \rightarrow 2\pi^o$ decay. Photons can 'fuse'; they may be indistinguishable because of the finite spatial resolution of the detector, and we may again see fewer than six photons. This second requirement demands a fine-grained photon detector.

D. Detector Requirements

This section will set forth the 'ingredients' for the detector. It lists the requirements established in the earlier section and indicates the corresponding apparatus.

In the neutral mode, we detect photons from $K \rightarrow 2\pi^o$ decays. In order to reconstruct the event, we need the energy and position of the photons. We have

chosen lead glass for our electromagnetic calorimeter.

We need to know in which of our two beams the decay occurred, in order to distinguish K_L from K_S. For this reason we have chosen to convert one of the four photons in a thin converter and use a drift chamber system to track the pair back to a transverse vertex. Multiple scattering in the detector forced us to have a fine-grained hodoscope at the conversion plane to improve our transverse resolution.

The formidable $3\pi^0$ background must be rejected. In order to reject decays at the trigger level, we have placed anticounters at various locations in the detector. We have also taken signals from the lead glass and calculated the total energy along with the first and second moment of the energy distribution and used this information in the trigger.

In the charged mode, we detect charged pions. We need to reconstruct the tracks and obtain the vector momenta of the two pions. We have used the drift chamber system referred to above and a dipole magnet to measure the momenta of the tracks.

The backgrounds in the charged mode require the rejection of electrons and muons. To reject electrons at the trigger level, we used lead to start an electromagnetic shower and scintillator to detect the energy deposit. The majority of pions did not interact and were not rejected. Muons were rejected using a steel pile which stopped all but minimum-ionizing particles; the pile was followed by a scintillation hodoscope.

E. The Regenerator and its Optimization; Beam Momentum

Two factors were considered in the choice of the regenerator: the material and its length. $|\rho|$ is proportional to $\approx A^{-0.08}$ for a regenerator of a fixed number of interaction lengths (see Appendix I). Furthermore, the typical q^2 of inelastic production falls as the square of the nuclear radius; increasing the atomic weight increases the number of inelastically produced K_S near $q^2 = 0$. These inelastic K_S are a background to the coherent K_S, which are produced at $q^2 = 0$ and have a finite q^2 due to resolution. For both these reasons we would like to choose a regenerator of small atomic weight and have chosen Carbon as the regeneration material.

As is demonstrated in Appendix I, the coherent production rate is maximized if the length of the regenerator is twice the interaction length: we used this length of Carbon.

Finally, we have chosen to perform the experiment at the highest possible energy. The regeneration amplitude drops with momentum, but the resolution improves and so the backgrounds are smaller. Reducing the K_L background was far more important than increasing the K_S statistics; we chose to perform the experiment at FNAL.

CHAPTER III

THE BEAM LINE, APPARATUS, AND TRIGGER

This chapter describes how the dual beams were produced, gives the details of the apparatus used to detect K_L and K_S decays, and explains the trigger. The lead glass calorimeter will be discussed in Chapter IV; here we only explain its role in the trigger.

A. Beam Line

A schematic of the beam line appears in Figure 2. A beryllium target was struck by a beam of 400 GeV/c protons. The targeting angle was nominally 0 mr. in the charged mode and 4 mr. in the neutral mode; the targeting angle was in the horizontal plane. The resultant spray of particles was then collimated into a single beam. At 105 meters from the target, the beam struck an absorber used to reduce the flux to manageable levels while enhancing the ratio of kaons to neutrons. The charged mode data normally had 44.8 cm of Beryllium and 25.4 cm. of Carbon; the neutral mode typically used 61. cm. of Beryllium and 12.7 cm. of Carbon. After the absorber the neutron to kaon ratio was about 5 in the charged mode and 3 in the neutral mode. Following the absorber was a 7.6 cm. lead piece which converted photons in the beam.

The two beams were then formed by passing the single beam through a two-hole collimator 107 meters from the target. The two holes were horizontally separated, in the

The two beams were then formed by passing the single beam through a two-hole collimator 107 meters from the target. The two holes were horizontally separated, in the same plane as the targeting angle; the difference in targeting angle between the two beams was then .26 mr.

The beams were further defined and collimated in both the horizontal and vertical directions at 200 m. and 310 m. Charged particles were eliminated by sweeping magnets following the two hole collimator and the two downstream stations. Both of these collimations were performed in vacuum.

The beginning of the apparatus was located 406 meters from the target; this is 75 K_S lifetimes at 100 GeV, so there is a negligible K_S component to the beams. The double beam profile at the regenerator, derived from reconstructed $K_S \rightarrow \pi^+\pi^-$ is shown in Figure 3; the beams are cleanly separated. The two beams were 12.7 cm. high by 10.2 cm. wide with a 5.1 cm. separation at 480 meters. The momentum spectrum of K_L incident on the regenerator was obtained from a parameterization given by Atherton[26]. We used this spectrum as an input to the Monte Carlo and obtained good agreement with the observed K_L spectrum; the comparison is shown in Appendix II.

B. Apparatus

We have now seen how the beams were formed and their approximate composition when they reach the detection apparatus. We now describe the apparatus used in the measurement. The organization essentially follows the layout of the spectrometer. A overall schematic of the apparatus appears in Figure 4.

Figure 2. A schematic of the Beam Line. The Figure is not to scale; the positions of the beam line elements are given in meters from the production target.

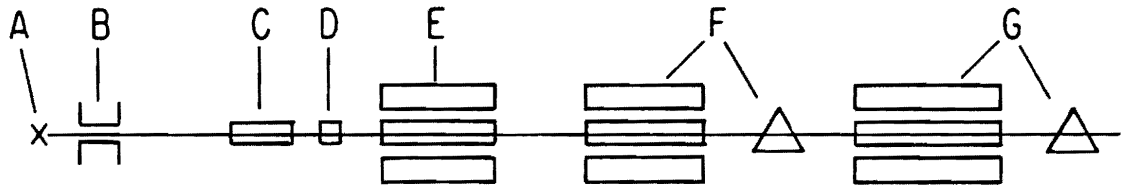

element		location
A	Production Target	0 m
B	Collimation and Sweeping	
C	Be Moderator	105
D	Pb Photon Converter	106
E	Two-Hole Collimator (defines double beam)	107
F	Collimation + Sweeping (Vertical, Horizontal, & Septum)	200
G	Same as F	310

Figure 3. The double beam profile at the regenerator, derived from reconstructed $K_S \rightarrow \pi^+\pi^-$. The profile is in the x-direction and shows the separation between the beams. The regenerator was in the west beam for the left-hand plot and the east beam for the right-hand plot.

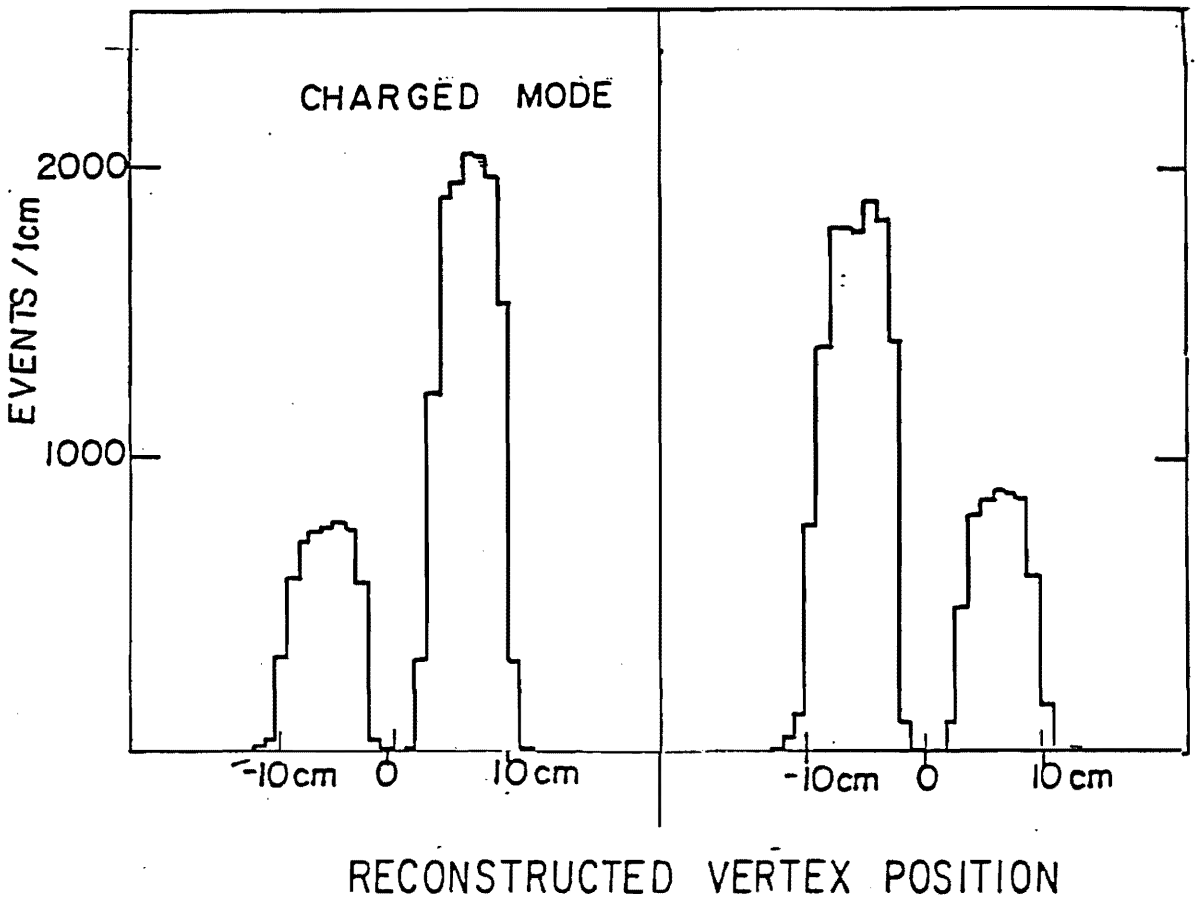
CHARGED MODE
2000
1000
EVENTS / 1cm
-10cm
0
10cm
-10cm
0
10cm
RECONSTRUCTED VERTEX POSITION

Figure 4. A schematic of the apparatus, showing the main elements and their relative layout.

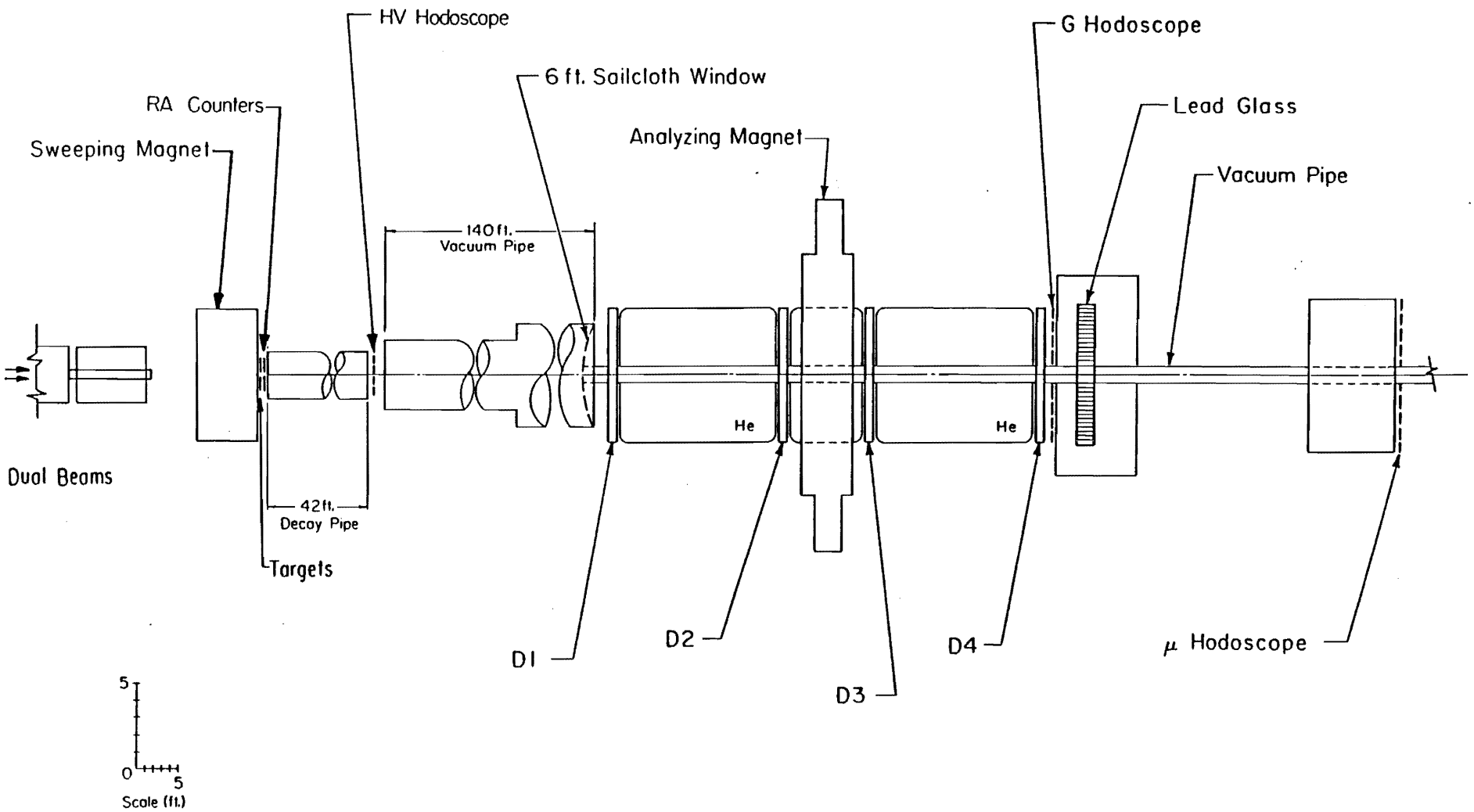
HV Hodoscope
G Hodoscope
6 ft. Sailcloth Window
RA Counters
Lead Glass
Sweeping Magnet
Analyzing Magnet
Vacuum Pipe
140 ft.
Vacuum Pipe
He
He
Dual Beams
42 ft.
Decay Pipe
Targets
D1
D2
D3
D4
μ Hodoscope
5
0
5
Scale (ft.)

1. Regenerator Region

Recall the important considerations for the regenerator: it must alternate from beam to beam and we must be able to veto inelastically produced K_S. A schematic of the region appears in Figure 5. Table 1 contains the positions and relevant properties of the components in this region.

The regenerator itself was a 101.6 cm. Carbon block wide enough to completely cover one of the beams. The regenerator sat in a tray within a sweeping magnet (BM109) used to eliminate charged particles produced in the regenerator; the magnet had a p_T kick of approximately 1 GeV/c. The tray moved from beam to beam between pulses. Far upstream of the regenerator, downstream of the two-hole collimator, was a 66 cm. Carbon absorber. This absorber was used to moderate the neutron flux on the regenerator; it moved back and forth with the regenerator each pulse. Neither the absorber nor the regenerator was changed during the experiment; hence the absorption and regeneration canceled between the charged and neutral mode. We controlled and recorded the positions of both the regenerator and absorber with limit switches.

The maximum rate of K_S decays in the decay region would be obtained by placing the regenerator as close to the decay region as possible; however, the neutrons hitting the regenerator produced a large charged particle flux which had to be swept away: hence we had to move the regenerator back far enough within the sweeping magnet for the sweeping to be effective. The regenerator was moved as far downstream as the rates would allow; once positioned, it was not moved during the data-taking.

TABLE 1

POSITIONS AND PROPERTIES OF THE ELEMENTS OF THE SPECTROMETER

Element	z (center)	width (cm.)	height (cm.)	length	radiation lengths
Regenerator	404.167	13.01	10.31	101.6	4.12
Regenerator Anticounters	406.114	12.06	10.16	.016	.00606
Decay Pipe (including windows)	412.83	40.6 (radius)	--	1211.4	.0048
A-counter	420.091	55.88	27.94	1.2	.0069
Lead Converter	420.095	55.88	27.94	0.16	0.053
V-bank	420.098	55.88	27.94	016	.0035
H-bank	420.101	55.88	27.94	0.16	.0069
Housing for Conversion Hodoscope	--	--	--	.0060	
Expansion Pipe(including windows)	443.	180. (radius)	--	43.	.0050
Air before Chamber A	464.0	--	--	25.	.0020
Chamber A(includes He bags)	464.609	200.	100.	23.	.011
Chamber B	469.505	200.	100.	23.	.011
Chamber C	473.118	200.	100.	23.	.011
Chamber D	478.105	200.	100.	23.	.011
G-bank	479.21	205.0	101.2	0.635	.009
Lead Glass	480.274	226.59	122.01	60.	19.9
μ-filter	490.142	>200 cm.	>100 cm.	300 cm.	

Figure 5. A schematic of the regenerator region, showing the relative arrangement of the regenerator, regenerator anticounters, and lead plug.

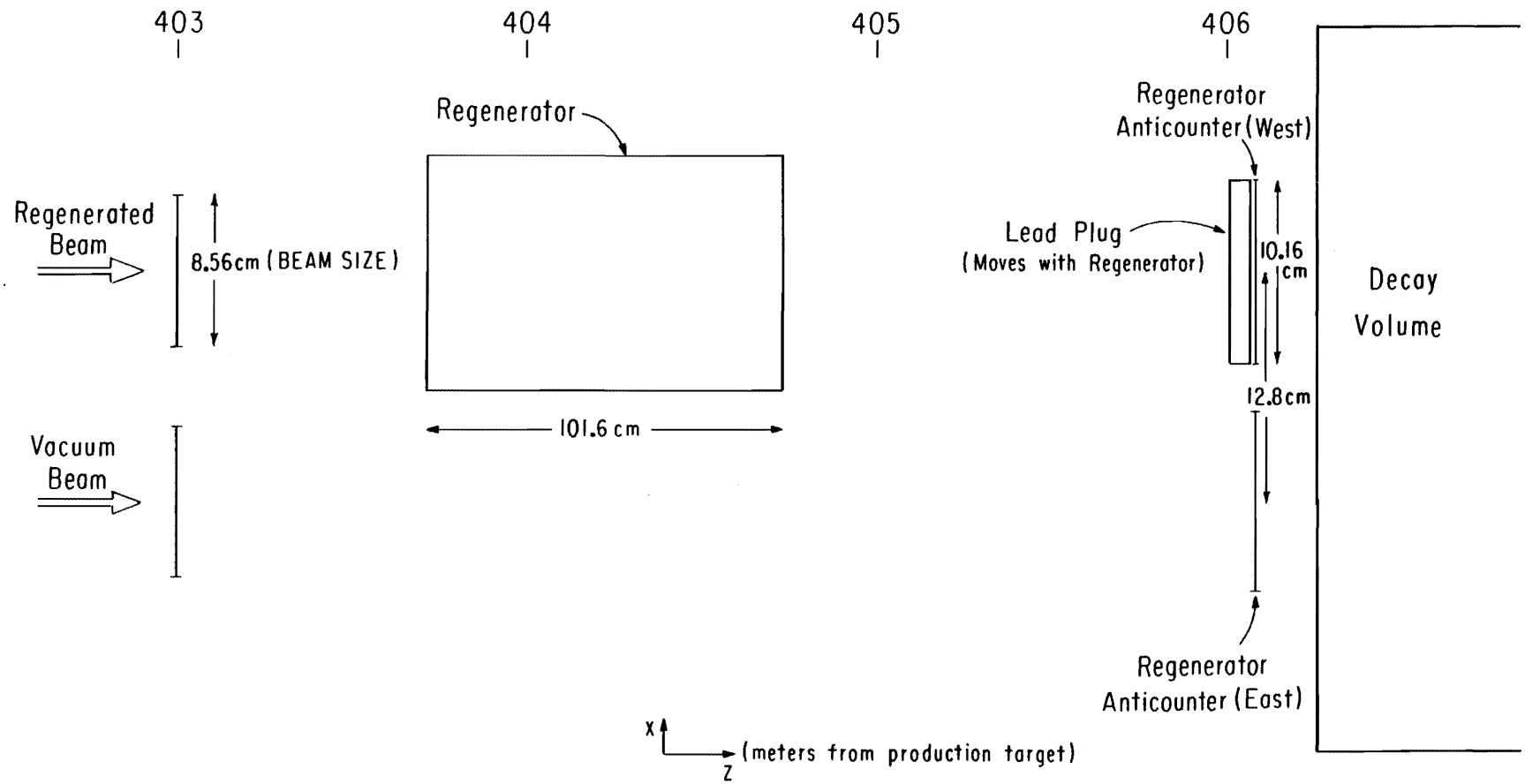
403
404
405
406
Regenerator
Regenerated Beam
8.56cm (BEAM SIZE)
Vacuum Beam
101.6 cm
Regenerator Anticounter (West)
Lead Plug
(Moves with Regenerator)
10.16 cm
12.8cm
Decay Volume
Regenerator Anticounter (East)
X
Z
(meters from production target)

We used two anticounters to define the entrance to the decay region. In the regenerated beam we place a 1.27 cm. thick lead plug, which converted photons from K_S decays and neutron interactions upstream of this point; an anticounter immediately followed. In the vacuum beam there was only an anticounter. These two regenerator anticounters (RA) were 12.06 cm. high by 10.16 cm. wide with 12.05 cm. between their centers. They were made of polystyrene scintillator and were thin (.16 cm.) to lessen both neutron interactions and regeneration. Each was viewed by a single RCA 8575 photomultiplier[27]; we used a transistorized base used to withstand high rates, which had been used for an identical purpose in a previous experiment.[28]

2. The Decay Region and Conversion Hodoscope

The decay region itself was an evacuated pipe 1.22 m. in diamter and 13.6m long, kept at a pressure under 20μ Hg. The pipe was terminated with a thin Aluminum window on the upstream end and sailcloth on the downstream end. Downstream of the pipe, in air, was the conversion hodoscope. Figure 6 shows the arrangement of the hodoscope in the neutral mode. The precise locations and properties of the apparatus described in this section appear in Table 1.

The hodoscope began with an anticounter (A) 55.88 cm. wide by 27.94 cm. high. It was viewed by four photomultipliers whose outputs were summed and discriminated. This counter, in the neutral mode, was used to veto charged particles leaving the decay region. This anticounter was followed by a .053 cm. (nearly .1 radiation length) lead

sheet of the same transverse dimensions as the A counter. This sheet converted exactly one photon out of four from a $K_L \rightarrow 2\pi^o$ decay 24% of the time. Following the lead were two scintillation banks used to detect the converted pair. The first bank (H) consisted of 22 horizontal staves 1.27 cm. across and 55.88 cm. long. The second bank (V) consisted of 44 vertical staves 1.27 cm. across and 27.94 cm. long. The A anticounter, the lead sheet, and the V and H banks then covered the same transverse area. The individual staves in the V and H banks were placed as close as possible to each other to lessen the uncovered area; the gap between a counter and its neighbor was roughly .05 mm. The entire assembly of the A anticounter, lead sheet, and V and H banks was placed in a light-tight box.

For charged mode data-taking we removed the A anticounter and the lead sheet. This was the only change made to this region to change from charged to neutral data-taking.

3. The Separation Pipe and Its Window

Following the conversion hodoscope was a 43 m. long, 1.8 m. diameter vacuum pipe in which the decay products could separate. The pipe was terminated at the downstream end with a rectangular Mylar/ sailcloth window. It was critical that the window be as thin as possible; multiple scattering in the window degraded the transverse position resolution, and hence our ability to distinguish between the beams, at the decay vertex some 60 m. upstream. In contrast to the resolution requirement we had to con-

Figure 6. A schematic of the Conversion Hodoscope as arranged in the Neutral Mode data-taking. The conversion of a photon is depicted; the distance between the electron and positron is greatly exaggerated.

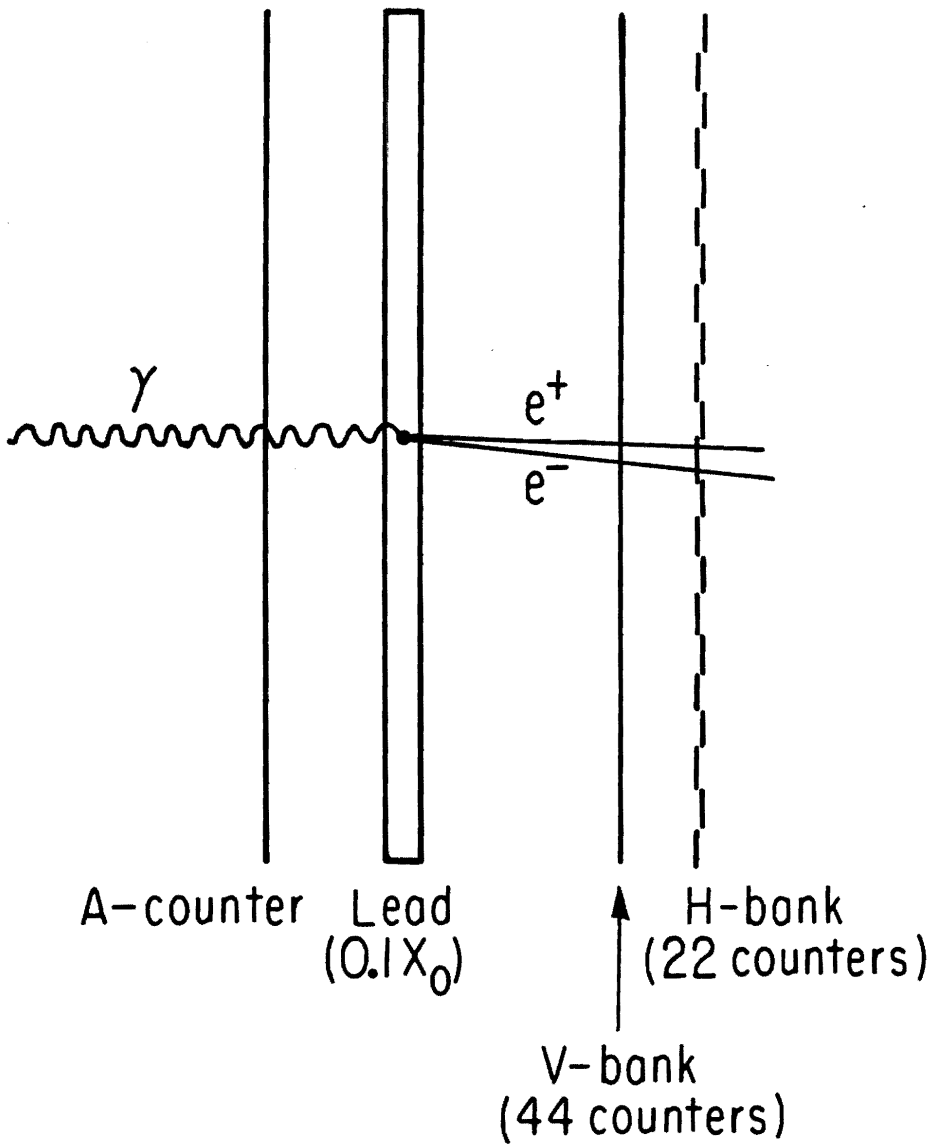
γ
e+
e−
A-counter
Lead
(0.1 X0)
H-bank
(22 counters)
V-bank
(44 counters)

sider the megajoule of stored energy from the vacuum; a failure of the window would have been disastrous. The window therefore had to be especially thin yet strong. A further complication arose because the window marked the beginning of the spectrometer; from this point a rectangular vacuum pipe ran through the apparatus to transport the neutron beam. The window had to be coupled to the pipe and so have a hole in its center! The window and pipe were coupled by a specially designed slip joint; the window could deform freely while the pipe was being evacuated.

4. The Charged Particle Spectrometer

The charged particle spectrometer followed the window. It consisted of four drift chambers, a dipole magnet, and scintillation counters, and performed muon and electron identification. The overall layout was shown in Figure 4; the dimensions and properties are given in Table 1. Table 2 contains information relevant to the precision and performance of the drift chambers.

The chambers were 2 m. wide by 1 m. high with a central hole for the passage of the beam pipe. Each chamber performed both x (left/right) and y (up/down) determinations using two measuring planes in each view; the two planes in a view were offset by half a cell to remove the twofold ambiguity. The cell structure is shown in Figure 7. The most downstream chamber was split in the y-determining view; we knew whether a track at a given height was on the left side or the right side of the spectrometer.

The electron and positron tracks in the neutral mode will in general be close; the

TABLE 2

PARAMETERS OF THE DRIFT CHAMBERS

Property	Value or Comment
Number of Chambers	4 (2 x and 2 y-measuring planes/chamber)
Size	2 m. in x by 1 m. in y (approximate)
Number of Sense Wires	680
Gas	Argon/Ethane 50/50 at Atmospheric Pressure
Drift Velocity	50 μ/nsec. (nominal)
Resolution	160 μ/chamber, 220 μ/plane
Dead Time	100 nsec./ wire
Readout	Binned in 6.3 nsec. bins

Figure 7. The cell structure of the drift chambers. A typical track is indicated. The dimensions are in inches.

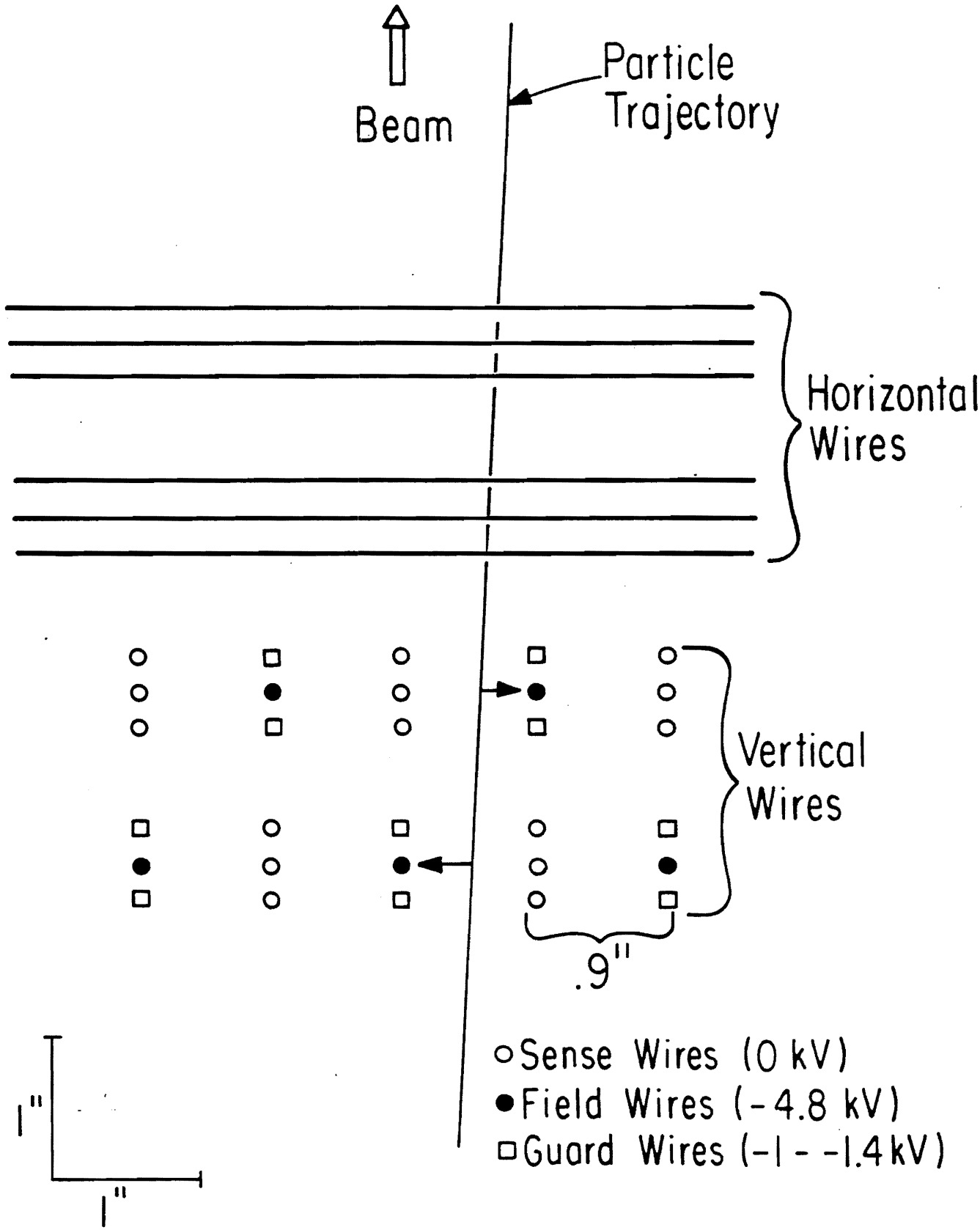
Beam
Particle Trajectory
Horizontal Wires
Vertical Wires
.9"
1"
1"
Sense Wires (0 kV)
Field Wires (-4.8 kV)
Guard Wires (-1 - -1.4 kV)

pair is separated only by multiple scattering before being bent apart by the analysis magnet. We therefore need to know the limitations on resolving nearby tracks. The first limitation is the dead time of a wire, about 100 nsec; with our drift velocity of 50 μ/nsec., this resulted in a minimum resolving distance of about 5 mm. Arrival times of hits on the wires were binned in 6.3 nsec bins by our readout system. This corresponds to about .3 mm. The details of the readout system have been covered elsewhere[29] and we will not discuss them here.

The analyzing magnet was a conventional dipole 254 cm. wide by 101.6 cm. high. It provided a p_T kick of 212 MeV/c in the charged mode and 107.6 MeV/c in the neutral mode. The field map had been accurately measured when the magnet was constructed and had been checked in a previous experiment in the same beam line.[30]

Multiple scattering throughout the spectrometer was minimized; helium- filled bags were placed in the spaces between the chambers.

Following the last drift chamber was a scintillator plane (G) consisting of 40 staves, each 10.16 cm. high by 60.96 cm. tall and 0.635 cm. thick. The staves ran vertically; 20 were above the pipe center and 20 below; the staves immediately above or below the beam pipe were offset to permit its passage. Immediately upstream of this bank was a 'lead curtain' which could be moved in and out of the spectrometer. The curtain consisted of five radiation lengths of lead; its purpose was to initiate electromagnetic showers of electrons from $Ke3$ decays so that the shower could be detected in the G counters. Recall that $Ke3$ decays are a background to the $K\pi 2$ signal.

The lead glass followed the G bank; it is the most intricate portion of the apparatus and we shall reserve further discussion of it for Chapter IV.

Downstream of the glass was an eight foot thick steel pile. Hadrons and electrons stopped in this filter; behind it was a plane of scintillation counters, allowing us to identify muons.

5. $3\pi^o$ Anticounters

$3\pi^o$ decays were dangerous both for reasons of trigger rate and background. Hence the neutral mode anticounter system was designed to detect photons which otherwise would have escaped the apparatus. All counters had three radiation lengths of lead before the scintillator to convert photons; the probability of rejection is greater than 95%. We discuss these anticounters in turn from the most upstream to the most downstream.

The first anticounter was located 380 m. from the target, roughly 25 meters upstream of the decay region. It surrounded the vacuum pipe and rejected $3\pi^o$ decays upstream of this point. Immediately following the conversion hodoscope was another set of anticounters (decay region anti, or DRA), which surrounded the conversion hodoscope in the xy plane. The next set of counters was located above and below the aperture of the analyzing magnet (hence magnet anti, or MA). Just before the G-bank was the 'collar anti'; four counters surrounded the vacuum pipe and overlapped the inner ring of the array (the fourteen blocks closest to the center). Photons or electrons striking the collar

anti would also strike the inner ring of the glass; these showers would be difficult to reconstruct because much of the shower would be inside the beam pipe, and it was therefore useful to reject these showers in hardware. The drift chambers also became inefficient around their edge; it was therefore useful to veto particles passing near this edge as well. Finally, at 535.2 meters was the 'back anti'. This counter was designed to pick up photons which had traveled down the vacuum pipe and emerged after the muon filter. Many $3\pi^o$ decays sent a photon down the pipe, so it was useful to detect as many of these as possible.

C. Charged Mode Trigger

The charged mode trigger was designed to search for two charged tracks, originating in the decay region, with one in the upper half and one in the lower half of the spectrometer. For part of the charged mode data-taking the trigger rejected both electrons, using the lead curtain, and muons, using the steel filter.

The trigger first required that the regenerator anticounter in the regenerated beam be off ($\overline{RA}_{alt}$). Neutron interactions and inelastically produced K_S were vetoed, as well as coherently produced K_S which decayed upstream of the RA; charged particles were vetoed directly and photons striking the lead plug would convert and veto the event. The counter in the vacuum beam was not in veto but was tagged and recorded.

The RA requirement insured that no charged track entered the decay region; the trigger from the conversion hodoscope required that two charged tracks leave the decay region. The trigger demanded that at least one H counter and at least one V counter

($\geq 1H \cdot \geq 1V$) but fewer than three H counters ($\overline{3H}$) had fired. We suppressed neutron interactions in the hodoscope by requiring that no H counter have more than ten times the minimum-ionizing pulse height ($\overline{H_{10}}$). The lead sheet and the A-counter were removed for the charged mode data-taking.

The scintillator requirement at the G-bank looked for one upward-moving and one downward-moving track, as required by momentum balance. Recall that the G-counters were split up/down; hence this requirement is simple to implement ($G_{up} \cdot G_{down}$).

The charged mode data-taking was of two sorts, distinguished by lepton rejection in the trigger. In the so-called 'biased' running, electrons and muons were eliminated in the trigger. Muons were eliminated by placing the muon bank in veto. Electrons were rejected using the lead curtain(which was removed when not in use). Electrons showering in the lead would deposit more energy than minimum-ionizing particles; the trigger checked for five times the minimum-ionizing pulse height in any G counter ($\overline{G_5}$). The 'unbiased' runs rejected neither muons nor electrons in the trigger.

Finally, the magnet anticounter, decay region anticounter, and collar anticounter were in veto as well ($\overline{MA} \cdot \overline{DRA} \cdot \overline{CA}$).

We have discussed the scintillation portion of the trigger. The trigger also used the drift chambers by measuring the time at which a particle passed through them. The trigger then compared this time to the time of the scintillation trigger to reduce false coincidences. To explain how these 'mean timers' worked, we refer to Figure 8 which shows a track passing through the two offset planes in one of the views of a chamber. Let the particle pass through the chamber at time t (we assume that the particle passes

Figure 8. The principle behind the use of 'mean timers'. A track is shown passing through the two offset planes of a single view of a chamber. The distance from the track to the sense wires of the ith plane is indicated by d_i, and the drift velocity is v.

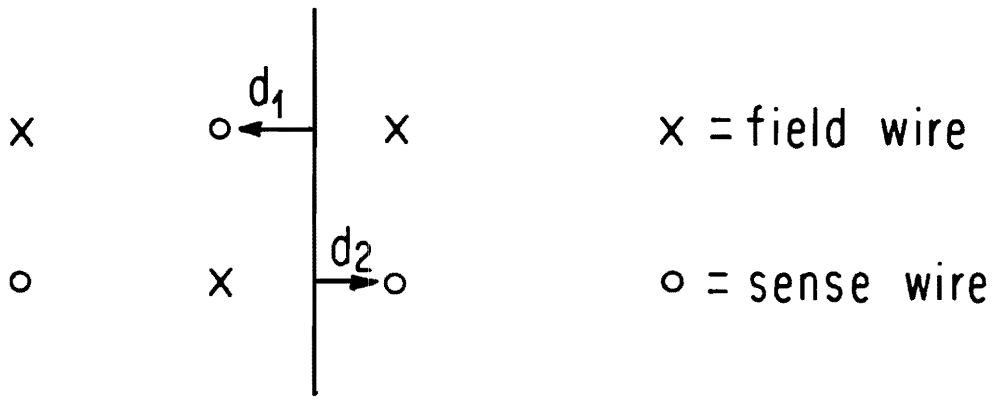

$$t_1 = t + d_1/v_0$$
$$t_2 = t + d_2/v_0$$

through the chamber instantaneously). Then

$$t_1 = t + \frac{d_1}{v_o} \tag{3.1}$$
$$t_2 = t + \frac{d_2}{v_o}$$

where t_i is the time that a signal arrives at the wire, v_o the drift velocity, and d_i the appropriate drift distance. Hence the average of the arrival times is

$$\frac{t_1 + t_2}{2} = t + \frac{d_1 + d_2}{2v_o} = t + \frac{d}{2v_o} \tag{3.2}$$

This relation is true independent of the point of passage of the track through the cell for tracks traveling perpendicular to the chamber (The correction for the small angles of real tracks as well as nonuniformities in the drift velocities are negligible for this discussion). A measurement of the mean time thus measures the time of passage of the particle through the chamber! The calculation of this mean time was ingeniously performed in hardware.[31] By using all the hits in a chamber, we can search for two tracks, which appear as two pairs of hits with the proper mean time. We required one of the first or third chambers to have two tracks in the x-view ($MTA2 + MTC2$).

The machine pulse delivering the beam actually consisted of discrete 'buckets' 18.9 nsec. apart, spaced evenly over the entire 850 msec. spill. A radiofrequency signal (53.1 MHz) with this period is sent to all experiments. We placed a crest of this waveform in coincidence with the scintillation portion of the trigger; since the spill is bunched we can improve the time resolution of the trigger by requiring it to occur within one of the buckets. If this preliminary trigger was satisfied a coincidence signal was formed and delayed approximately 500 nsec. until the information from the mean timers had arrived.

A final coincidence checked that the data acquisition computer was ready to accept another event.

The full charged mode trigger was then:

$$\overline{RA_{alt}} \cdot \geq 1H \cdot \geq 1V \cdot \overline{3H} \cdot \overline{H_{10}} \cdot$$
$$G_{up} \cdot G_{down} \cdot \overline{MA} \cdot \overline{DRA} \cdot \overline{CA} \cdot MTA2 + MTC2 \cdot RF$$

and in the biased mode we added $\overline{G_5} \cdot \overline{\mu}$.

D. Neutral Mode Trigger

The neutral mode trigger was designed to search for electron-positron pairs originating at the conversion hodoscope. It also made requirements on the amount and distribution of energy in the lead glass calorimeter.

The trigger demanded that there be no charged tracks before the lead converter. Both of the regenerator anticounters were in veto ($\overline{RA}$), marking the entrance to the decay region. The requirements at the conversion hodoscope then searched for a converted pair. The A counter vetoed ($\overline{A}$) charged particles leaving the decay region. The lead sheet was next; if a single photon was converted, the pair had no chance to move apart before it struck the H bank. Hence the trigger searched for one charged track, requiring $\geq 1H \cdot \geq 1V \cdot \overline{2H}$. Neutron interactions in the lead could fake electron-positron pairs; there would be no hit in the regenerator anticounters or the A counter, and possibly a single hit in each of the H and V banks. To suppress neutron interactions we required no H counter have more than ten times the minimum-ionizing pulse height ($\overline{H_{10}}$).

Figure 9. The arrangement of the Lead Glass. A typical group of nine is indicated by the cross-hatched region in the upper left-hand corner.

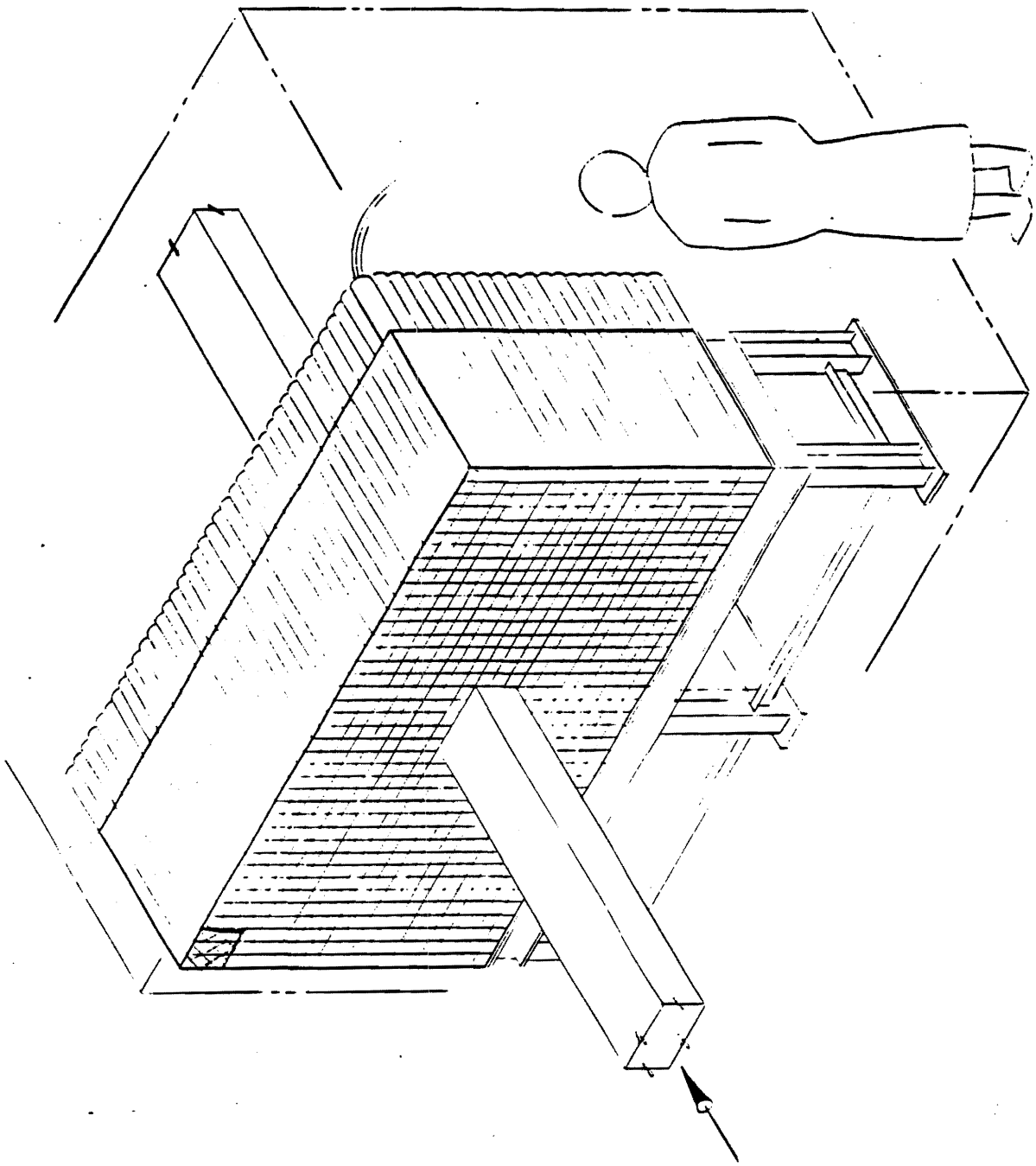

The trigger also used the G-bank. The magnet separated the tracks in the x-view (left/right) but not the y-view (up/down). Aside from multiple scattering, the electron and positron followed the y-view trajectory of the parent photon. The tracks therefore rose or fell together; as in the charged mode trigger, the up/down arrangement of the G-bank made the requirement simple to implement. We demanded either two upper-half G counters or two lower-half G counters have fired. A veto on three G counters completed the requirements $(2G_{up} + 2G_{down}) \cdot \overline{3G}$.

The lead glass was actively used in the trigger through the 'mass box'. The calorimeter consisted of 804 lead glass blocks in a 'fly's eye' arrangement, as shown in Figure 9. The outputs of each photomultiplier were sent to ADC's. The outputs were 'picked off' and added together in groups of nine blocks; a typical group of nine is shown as the cross-hatched region in the Figure.

The calculations of the mass box presumed all channels of the calorimeter had identical gains. In adding outputs to form groups of nine, and in the calculations which follow, the outputs from the different groups of nine were added together without correcting for differences in gain among the channels. We attempted to make the gains as equal as possible before the experiment started, as we will discuss in Chapter V.

The mass box calculated the total energy in the glass by summing the groups of nine. A cut of 40 GeV was applied to

$$E_T = \sum_i E_i \tag{3.3}$$

The first moment was then obtained:

$$E_X = \sum_i E_i x_i \tag{3.4}$$

The x_i correspond to the center of the ith group of nine. In performing the sum, the E_i were attenuated according to the distance of the particular group of nine from the center. The size of the attenuation represents the value of x_i; groups near the center were attenuated the most. The quantity E_X / E_T is then a measure of the center of energy of the event in the glass. Good events must fall within the beam pipe, at about $\pm$ 15 cm.; we cut at $\pm$ 40 cm.

Finally, the second moment was calculated:

$$E_2 = \sum_i E_i r_i^2 \tag{3.5}$$

where r_i is the radial distance of the group of nine from the center. It is easy to show that for a particle traveling along the z axis and decaying into photons at vertex Z meters from the lead glass, the invariant mass is given by:

$$m^2 = \frac{E_T E_2}{Z^2} \tag{3.6}$$

We chose to cut at a mass of 250 MeV/c ^{2} for a particle decaying at the entrance to the decay region. This becomes a progressively higher mass cut as the decay vertex moves toward the glass.

The magnet anticounter and decay region anticounter were in veto; the other anticounters were tagged and recorded offline. The scintillator trigger was delayed and placed in coincidence with the decision from the mass box, which took roughly 175 nsec. The trigger was placed in coincidence with the Fermilab RF just as in the charged mode.

In summary, the neutral mode trigger was:

$$\overline{A} \cdot \geq 1H \cdot \geq 1V \cdot \overline{2H} \cdot \overline{H_{10}} \cdot \overline{RA} \cdot (2G_{up} + 2G_{down}) \cdot \overline{3G} \cdot$$
$$\overline{MA} \cdot \overline{DRA} \cdot E_T \cdot E_X \cdot (E_T E_2) \cdot RF$$

CHAPTER IV

THE LEAD GLASS

The lead glass calorimeter was the most important and most demanding portion of the apparatus. We relied on its performance at every step of the analysis of the neutral mode data. The response of each cell of the calorimeter had to be understood at all times. The experiment required linearity over a wide dynamic range: the energy of an individual photon was often as high as 75 GeV; the energy deposit of an interesting shower in an individual block was often as low as 100 MeV. Nonlinearities in the response of any of the photomultiplier tubes, their bases, or the ADCs could wreck our reconstruction.

The calorimeter and its monitoring system were therefore designed to extract as precise information as was possible. In this chapter we first describe the materials and construction of the calorimeter, with necessary brief asides into optics and the physics of electromagnetic showers. We then turn to a discussion of the ADC system. The monitoring system and its uses and limitations are explained. Finally, we describe the calibration of the calorimeter and indicate the problems and our successes.

A. The Lead Glass and its Properties

The lead glass used in the calorimeter was Schott Optical Glass Type F2.[32] As noted in Chapter III, the glass was placed in a 'fly's eye' arrangement in a stack 39 blocks across by 21 blocks high with a 5 block by 3 block gap in the center to permit the passage of the beam. The dimensions of an individual block were 5.81 cm. in x by 5.81 cm. in y by 60.96 cm. in z. The radiation length of Schott F2 glass is 3.06 cm.; hence one block was just under two radiation lengths square and twenty radiation lengths deep. These parameters are important: the longitudinal depth of the glass determines how much of the shower is contained in the array as a whole, and the transverse components determine how much of the shower is contained in an individual block and how much is shared with its neighbors. The sharing of energy allows us to determine the impact point of a photon or electron by comparing the energy deposited among the different blocks.

The longitudinal containment of an electromagnetic shower is logarithmically dependent upon the shower energy; for showers in our energy range of 1-100 GeV we contained between 95% and 98% of the energy. The radial dependence of the energy distribution in lead glass is again only weakly dependent on the energy; roughly 90% of the shower is contained in a cylinder centered on the shower axis and one radiation length in radius.[33]

B. Light Coupling and Optical Filters; Photostatistics

The development of electromagnetic showers fluctuates from shower to shower. In a photon-induced shower, the location of the first conversion determines where the shower begins. In a lead glass block of finite dimensions and attenuation length these fluctuations cause variations in the amount of collected light. Lead glass has an attenuation length which is strongly dependent on wavelength, varying from one meter in the blue to tens of meters in the red. A one radiation length (3.06 cm.) shift in the location of the first conversion causes a 3% variation in the amount of blue light collected, where our photomultipliers are the most sensitive.

To decrease this contribution to the resolution we have followed Morrison *et.al.* [34] by placing an optical filter between the lead glass block and the photomultiplier. The filter, Wratten 2A[35], cut off transmission of light with wavelengths shorter than 4400 Å . The filter cut the light level by 1/3, as measured in beam tests.

In order to hold the filter in place and to optically couple the block to the photomultiplier we used a Sylgard Optical Gel. [36] The filter was embedded in the gel, which made optical contact with the photomultiplier on one side and with the block on the other. The gel was stable; it did not yellow as glue often does. It also had an index of refraction (n=1.45) well suited to transmit light between the lead glass (n=1.6) and the photomultiplier (n=1.4).

A 1 Gev shower provided approximately 800 photoelectrons. This was calculated in a Monte Carlo which included the average shower development, the photocathode quantum efficiency, and the optical filter. A minimum- ionizing particle passing through the

block, according to the same program, should leave the equivalent of 2/3 GeV in a block. Both of these figures were verified in the data. We can then calculate the expected resolution of the glass. In a linear calorimeter, the observed number of photoelectrons is proportional to the energy and is Gaussian-distributed. The statistical error will then be the error from the number of photoelectrons combined with the statistical error of the amplification process. The RCA photomultiplier manual[37] derives the statistical error; we need to know the average gain, which is 60000 for our ten-stage tube. Equation (47) of that manual then applies with the result that:

$$\frac{\sigma}{E} = \sqrt{\frac{\lambda}{N}}\sqrt{\frac{1}{E}} \approx \sqrt{\frac{3}{800}}\sqrt{\frac{1}{E}} \approx \frac{6\%}{\sqrt{E}}$$

where N is the number of photoelectrons per GeV of shower energy, and λ is the average gain per stage of amplification.

C. The Photomultipliers and the Bases

We chose an Amperex 2202 10-stage photomultiplier with a bi-alkali photocathode.[38] The photomultiplier ran at approximately -1200 V. The base was of our own design. It was designed to handle up to 100,000 photoelectrons without nonlinearity. We included a tunable potentiometer in the base design; hence we could adjust its gain if necessary.

We discovered in our initial tests that the gain of the photomultipliers varied with the light level to which they were exposed; this shift was often of order 10% for the few μA of current expected in the experiment. We therefore measured for each photomultiplier the gain shift at different light levels and graded them accordingly. Tubes with less

than a 1% shift at ten times the expected light level were assigned to blocks near the center of the array where the rates were highest; those with progressively worse dependence went further out.

We wished to make the array response as uniform as possible; recall that our 'mass box' made no differentiation among the gains of the channels. We therefore measured the gain of each photomultiplier and of each base and matched them in order to minimize the initial gain spread. Photomultipliers were tested using a standard radioactive source shining on a scintillator and a single base; the voltage required to give a preselected response was recorded. The bases were sorted according to their response using a standard photomultiplier and an LED (the potentiometer of the base had been adjusted to give the highest possible gain).

The photomultipliers and the bases were then paired; a high-gain photomultiplier would be paired with a low-gain base. The combination was assigned to one of twenty-six high voltage distribution panels. The typical voltage change from one panel to the next was 10 V; the typical gain change of the photomultiplier/base pair was 0.1% per volt. The initial gain distribution of the array, as measured by minimum-ionizing particles, is shown in Figure 10.

C. Assembly and Construction

We have discussed the individual elements of the array: the blocks, the photomultipliers, and the bases. This section will describe how these elements were assembled into a cell of the calorimeter and how the calorimeter was constructed. Figure 11 shows the

Figure 10. The initial gain distribution of the array, as measured by minimum-ionizing muons. The histogram shows the mean number of counts above pedestal registered for a muon for each channel of the array. The average response is about forty counts.

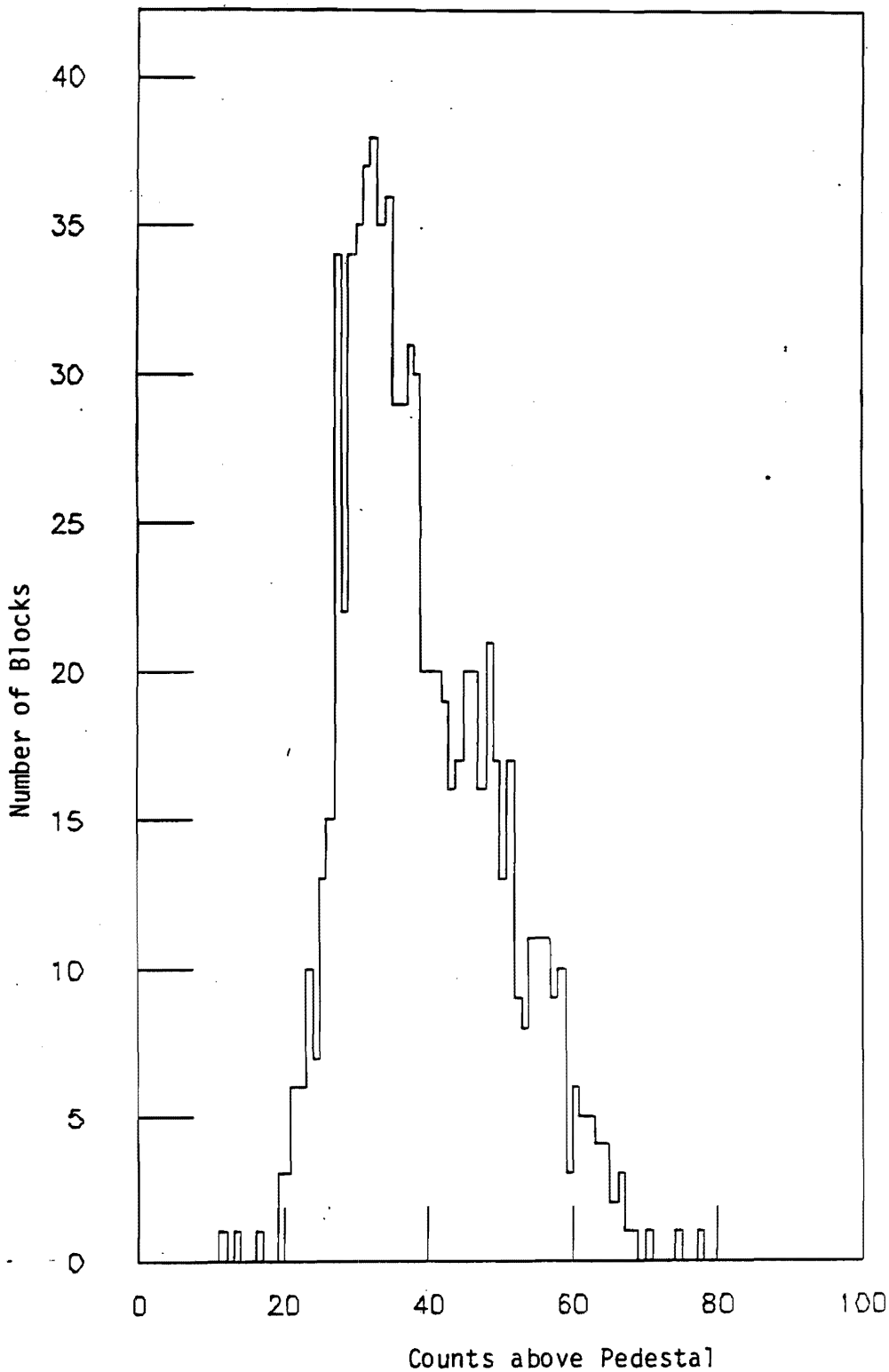
40
35
30
25
20
15
10
5
0
Number of Blocks
0
20
40
60
80
100
Counts above Pedestal

Figure 11. A schematic of a calorimeter cell (not to scale). The top, cutaway picture shows the phototube within the layers of mylar and conetic shielding; the phototube and these layers are contained within a magnetic shield can epoxied to the lead glass. The expansion ring, used to push the optical gel against the block and provide good optical contact, is indicated. The bottom diagram shows the arrangement of the optical gel and filter. The size of the gel is exaggerated.

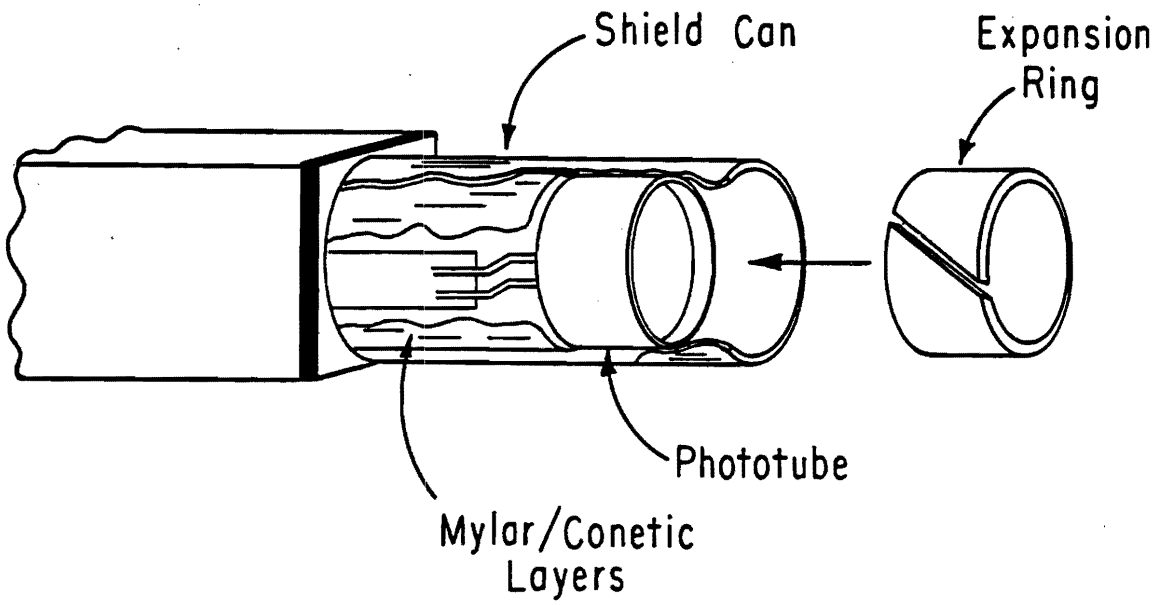
Shield Can
Expansion Ring
Phototube
Mylar/Conetic Layers

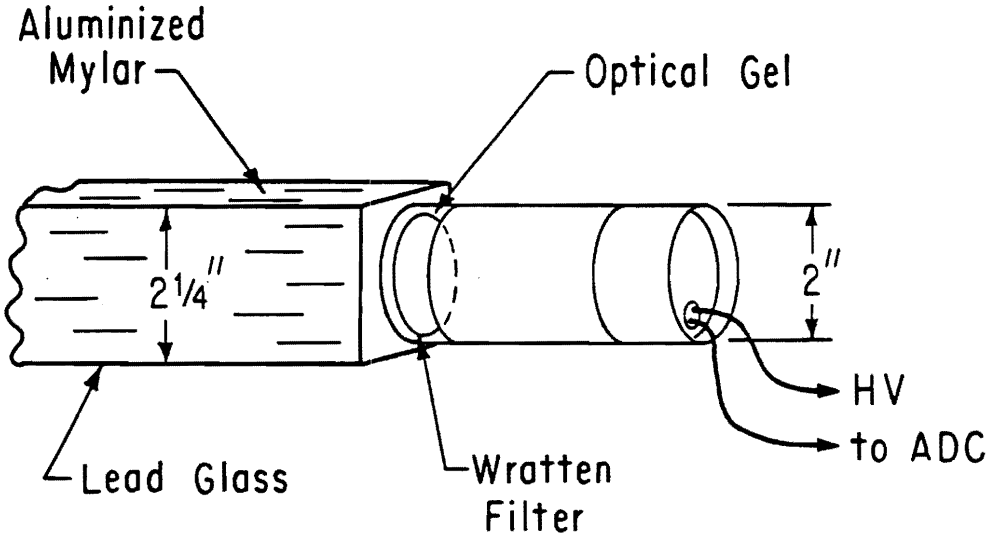
Aluminized Mylar
Optical Gel
2 1/4"
2"
HV
to ADC
Lead Glass
Wratten Filter

final arrangement of the individual elements within a cell.

The photomultiplier/base pair was soldered together. A phenolic can was placed around the base flush with the photomultiplier. A potting compound protected and insulated the base. The potentiometer in the base was adjusted with a screw which extended past the potting compound.

After the potting compound had hardened, the optical gel was poured into a dam on top of the photocathode and the filter inserted; the gel hardened around the filter. Two pairs of Mylar and conetic foil[39] were then wrapped around the photomultiplier, for electrostatic and magnetic shielding respectively.

The assembly of the photomultiplier and the base were supported by a magnetic shield can. The can was glued to the lead glass block; then a dam was made and epoxy poured around the outside of the can. After the epoxy had hardened, the photomultiplier and base were slipped inside the can. The epoxy supported the weight of the can and of the photomultiplier and base. An expansion ring was placed behind the base and inside the shield can; when opened, it pressed against the phenolic can around the base, ultimately pressing the optical gel firmly against the face of the block.

(We encountered problems with using epoxy on the glass. Because of failures in the heating and air-conditioning systems, our storage room for the lead glass construction phase had severe temperature fluctuations. A 40° F swing in 24 hours occurred several times. The different expansion rates of the glass and of the epoxy caused over 1/3 of the blocks to crack at the corners. The glass cracked in a repairable way; a piece cracked off, still attached to the epoxy, rather than the glass having shattered and formed

shards. We could then cleanly repair the damage with epoxy, gluing the glass and epoxy back on to the glass with no detectable loss in strength of the support or the quality of the response).

Finally, the block was wrapped in 0.5 mil Aluminized Mylar to optically isolate it from other blocks. The unit was then ready for stacking in the array.

We attempted to stack all the blocks along an ideal grid. However, the blocks varied in size and were not perfectly rectangular; the largest deviation was under 1 mm. A random arrangement of blocks would cause an uneven array with mechanical stresses on the glass and worsened position resolution in the reconstruction. To avoid these problems we measured the blocks at three places along their length and used a computer program to find an acceptable configuration.

No attempt was made to make the individual blocks light-tight. Instead, the entire array was placed in a light-tight, temperature controlled house which allowed the temperature to vary by no more than 1°F. Red safety lights were used to illuminate the house if necessary; since the photocathode efficiency is low in the red, we did not need to turn off the high voltages to make the half-dozen repairs and adjustments required during the data-taking.

D. ADC System

We used a LeCroy 2285 12-bit ADC[40] to read out the glass, with a gain of 0.1 pC/count. The system had two special features. First, each channel had a preset pedestal which could be subtracted; this pedestal could be updated at will. This first feature

made possible the second: the system had 'sparse readout'; only channels satisfying a preselected criterion were read out. The ADC processor searched for channels which had more than 5 counts (roughly 80 MeV) after the automatic pedestal subtraction. If a channel satisfied this test, that channel and the channels before and after were read out. In our arrangement, this resulted in a block and the blocks to the left and to the right being read out; the blocks above and below were queried independently. The arrangement is illustrated in Figure 12.

The gate width was 175 nsec. We set the peak of the signal about 40 nsec. into the gate, contrary to LeCroy's instructions that the signal be a minimum of 50 nsec. into the gate. Figure 13 is a plot of glass response as a function of this timing determined from electrons. We see a clear dependence of about .4%/nsec. The timing drifted with small changes in the magnitude and phase of the Fermilab-supplied RF (the received signal changed; we do not mean to imply that the RF structure of the machine varied).

The ADC's were DC-coupled so that 60 Hz noise had to be carefully minimized ; the average pedestal jitter was under a channel. This is important for two reasons: (1) 60 Hz noise is a slow variation compared to the 175 nsec gate, and (2) the noise tends to be coherent over all channels; at any time, all the channels of the ADC see the same sign and magnitude of the noise. Therefore when we sum over different channels to obtain an energy, the error will grow linearly in the number of blocks read out. Since a typical event might have 100 blocks read out, a one channel systematic error in the pedestals

would produce an 1.66 GeV mismeasurement of the total energy.

E. Monitoring System

The monitoring system had two design goals. The first was to monitor the performance of the calorimeter throughout the data-taking, detecting dead or saturated channels, high levels of noise or similar problems. The second was to study long-term drifts as an aid to the calibration. Nonlinearities and other problems proved so severe that the system was not useful for the second goal; for on-line monitoring and trouble shooting, the system behaved admirably.

A schematic of the monitoring system appears in Figure 14. The light source was a Xenon corporation nanopulser[41]; the device is a spark gap which produces light. It produced a spectrum and pulse shape comparable to Cerenkov signals in the glass. Light levels large enough to saturate every block in the array were easily obtained. We normally ran at a light level equivalent to a 20 GeV shower. The nanopulser had two problems. First, it produced a great deal of RF noise; considerable care went into shielding the system. Second, the spark gap degraded with use; the point of the gap wore away, gradually increasing the light level. Eventually the gap would require an adjustment. The pulser completely broke down twice and had to be replaced.

A fiber optics system[42] was used to distribute the light. A common end containing over 40000 fibers was exposed to the light source. The individual fibers in this common end were fanned out to one of 44 legs. This randomization eliminated spatial variations in the light level over the common face. Since both the intensity and the spatial distri-

Figure 12. The effect of the five-count threshold on the ADC readout. Each square indicates a lead glass block, or channel of the array; the number within the square is the number of counts above pedestal, which is ideally proportional to the energy deposited in the block. The top row has no blocks above the five-count threshold and hence none of the blocks are read out; the bottom row has one block above threshold and hence three blocks are read out.

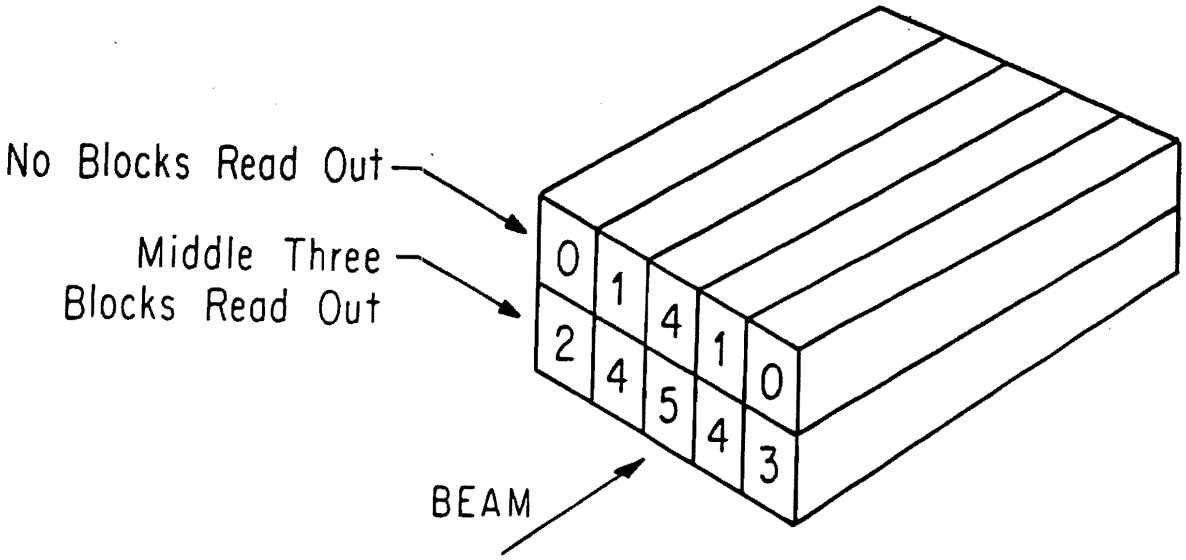
No Blocks Read Out
Middle Three
Blocks Read Out
BEAM
0
1
4
1
0
2
4
5
4
3

Figure 13. The lead glass response as a function of timing. The plot shows energy E measured in the glass divided by the momentum p measured in the chambers as a function of the relative arrival time of the signal with respect to the beginning of the ADC gate. The mean of E/p increases as the signal moves further away from the beginning of the gate, indicating a threshold effect in the ADC system.

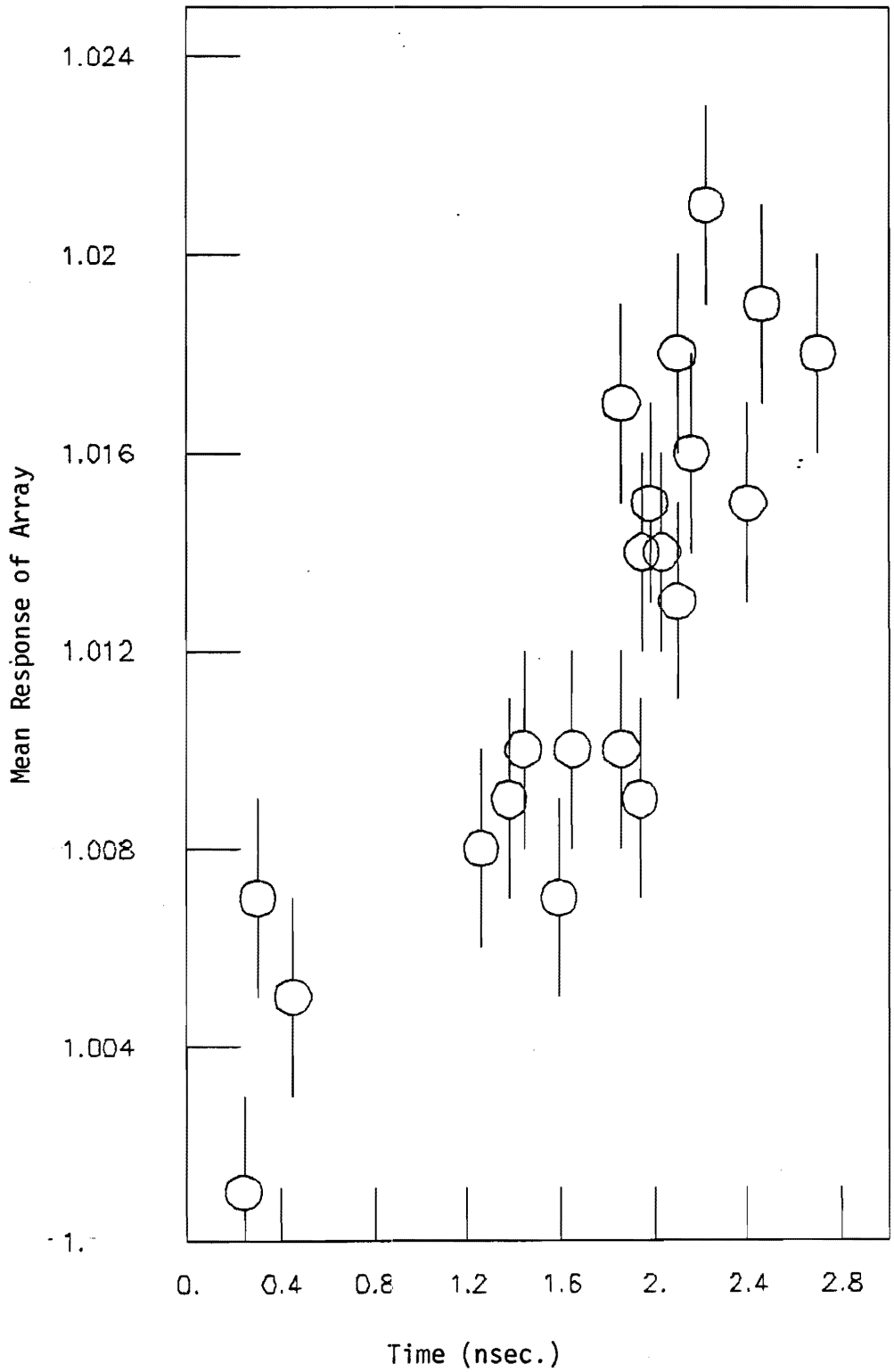
1.024
1.02
1.016
1.012
1.008
1.004
1.
Mean Response of Array
0.
0.4
0.8
1.2
1.6
2.
2.4
2.8
Time (nsec.)

Figure 14. A schematic of the monitoring system for the Lead Glass. The light from a spark gap illuminates a fiber optics system which in turn illuminates each block of the array. Two reference phototubes are used to monitor the light level of the spark gap for normalization; their gains are monitored by using an ^{241}Am source.

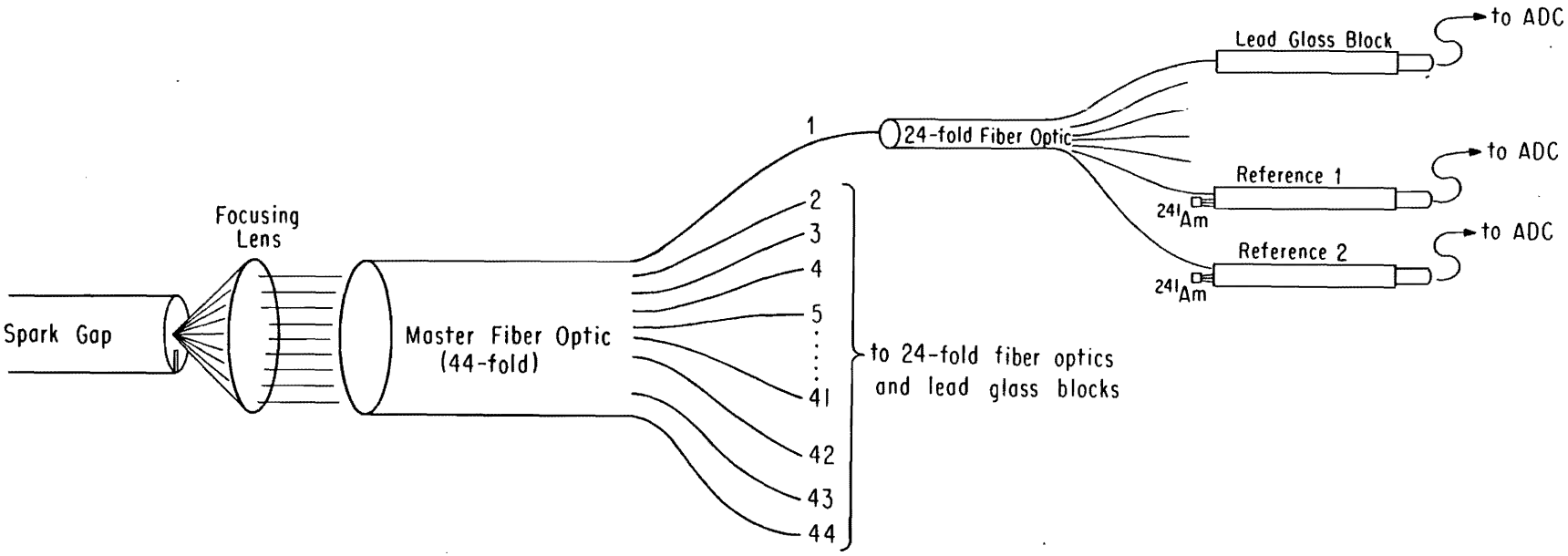
Spark Gap
Focusing Lens
Master Fiber Optic (44-fold)
1
2
3
4
5
41
42
43
44
to 24-fold fiber optics and lead glass blocks
24-fold Fiber Optic
Lead Glass Block
Reference 1
Reference 2
241Am
241Am
to ADC
to ADC
to ADC

bution of light from the spark gap varied from flash to flash, without the randomization it would have been impossible to know how much light went into any given photomultiplier, making any monitoring impossible. Thirty-nine of the forty-four legs were in turn used to illuminate similar 24-leg systems. Twenty-one of these twenty-four legs are fanned out to individual blocks. The legs were mechanically held in place just next to and pointing directly at the face of the block opposite the photocathode, through a small gap in the Mylar wrapping.

The light level was monitored by two reference photomultipliers which were coupled to lead glass blocks identically to the rest of the array. The only difference was that an ^{241}Am-doped NaI crystal illuminated these blocks as well. We could monitor the gains of the reference channels by following their response to the sources. The gain of a reference channel at time t is given by

$$g_{ref}(t) = g_{ref}(t_o) \; \frac{NaI(t)}{NaI(t_o)} \tag{4.1}$$

where $NaI(t)$ is the response to the source at time t. The monitoring then went as follows: the spark gap produced a flash of light; the response was recorded by the ADC's. Now if the response (number of channels above pedestal) of the ith channel is denoted by $R_i(t)$, and its gain by g_i, then

$$\frac{g_i(t)}{g_{ref}(t_o)} = \frac{R_i(t)}{R_{ref}(t_o)} \tag{4.2}$$

and then

$$g_i(t) = \frac{R_i(t)}{R_{ref}(t) \; / \; g_{ref}(t)} \tag{4.3}$$

The response of the reference tubes is corrected by their source-measured gains;

variations in the overall light level of the flash are taken out by normalizing to the response of the reference channels. Hence by calculating $g_i(t)$ we can monitor the gain of any channel. We measured the gain four times during the spill and once between spills. The *NaI* response was measured once between spills. In addition, before and after each spill we measured a pedestal for each channel.

F. Calibration

The gain of each channel must be accurately known in order to determine the energy of photons and electrons. In an ideal calorimeter, which is linear in response and unchanging in time, we only need to determine one number for each channel: the gain, which converts counts in the ADC to energy deposit in the block. A real calorimeter is more complicated. First, the gain may change as a function of time. Second, there may be no single 'gain' at all: if the calorimeter is nonlinear, each channel has a time-dependent function to be determined rather than a single constant. Nonlinearities can occur in the photomultiplier, or the base, or the ADC, or the physics of the shower!

We found a further complication in our attempts to calibrate the array. Recall that we attempted to compensate for gain changes with exposure to light by placing the most unstable photomultipliers at the outside of the array. Despite these attempts, there were substantial gain shifts with the presence of beam. Figure 15 shows the shift in gain, as measured by our monitoring system, from beam-on to beam-off conditions. We also found significant variations within the spill itself! Figure 16 shows the time variation of the gain within the spill for randomly chosen channels; we see up to 10%

Figure 15. The shift in gain from beam-on to beam-off conditions. The histogram shows the change in gain for each channel of the array as a result of the presence of the beam. The average change is 2.5%.

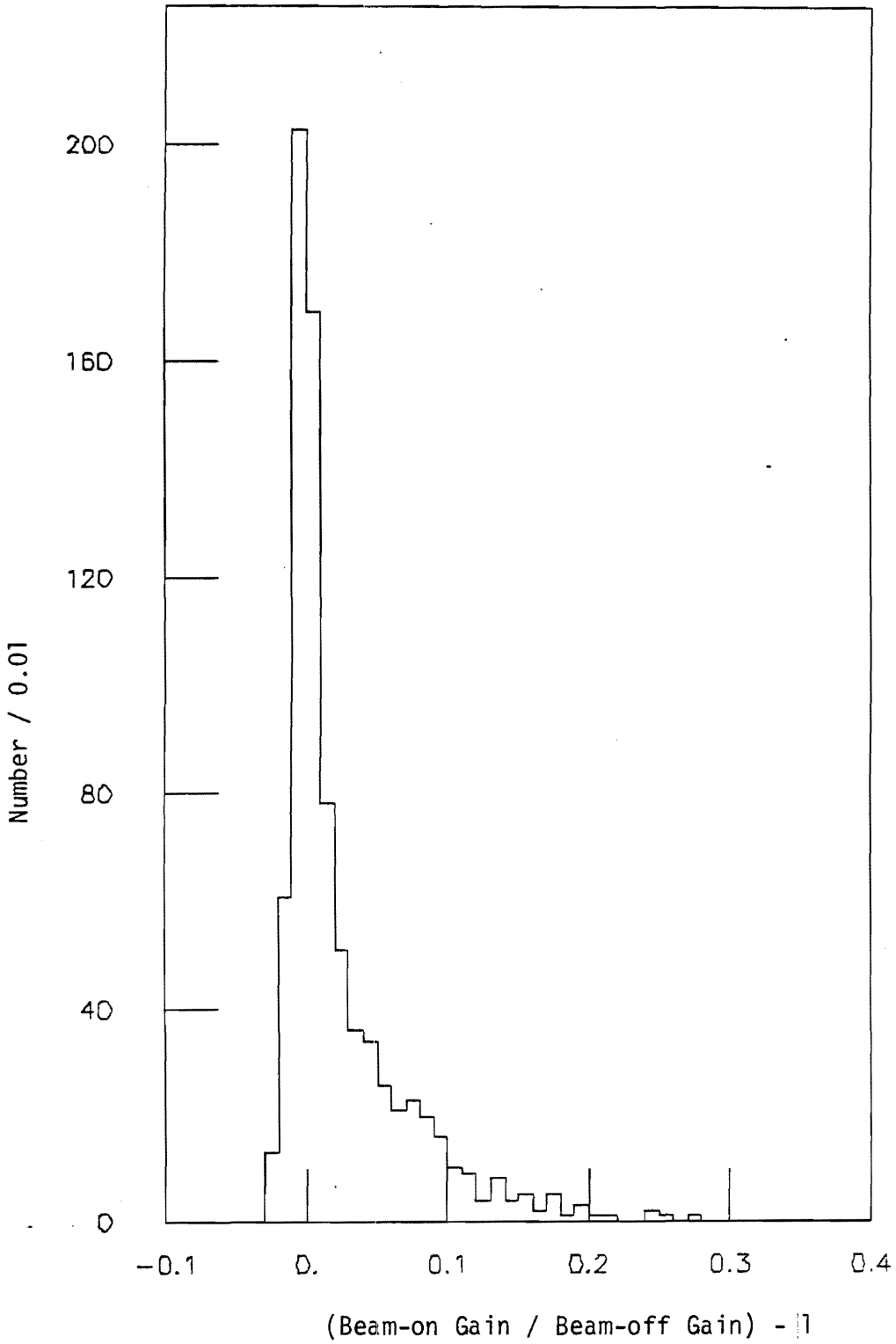
200
160
120
80
40
0
Number / 0.01
-0.1
0.
0.1
0.2
0.3
0.4
(Beam-on Gain / Beam-off Gain) - 1

Figure 16. The variation of the gain with time within the spill, for randomly selected channels. The gain changes in the presence of the beam and immediately starts to relax to its quiescent value. Depending on the individual phototube, the gain as a function of time can take on different forms.

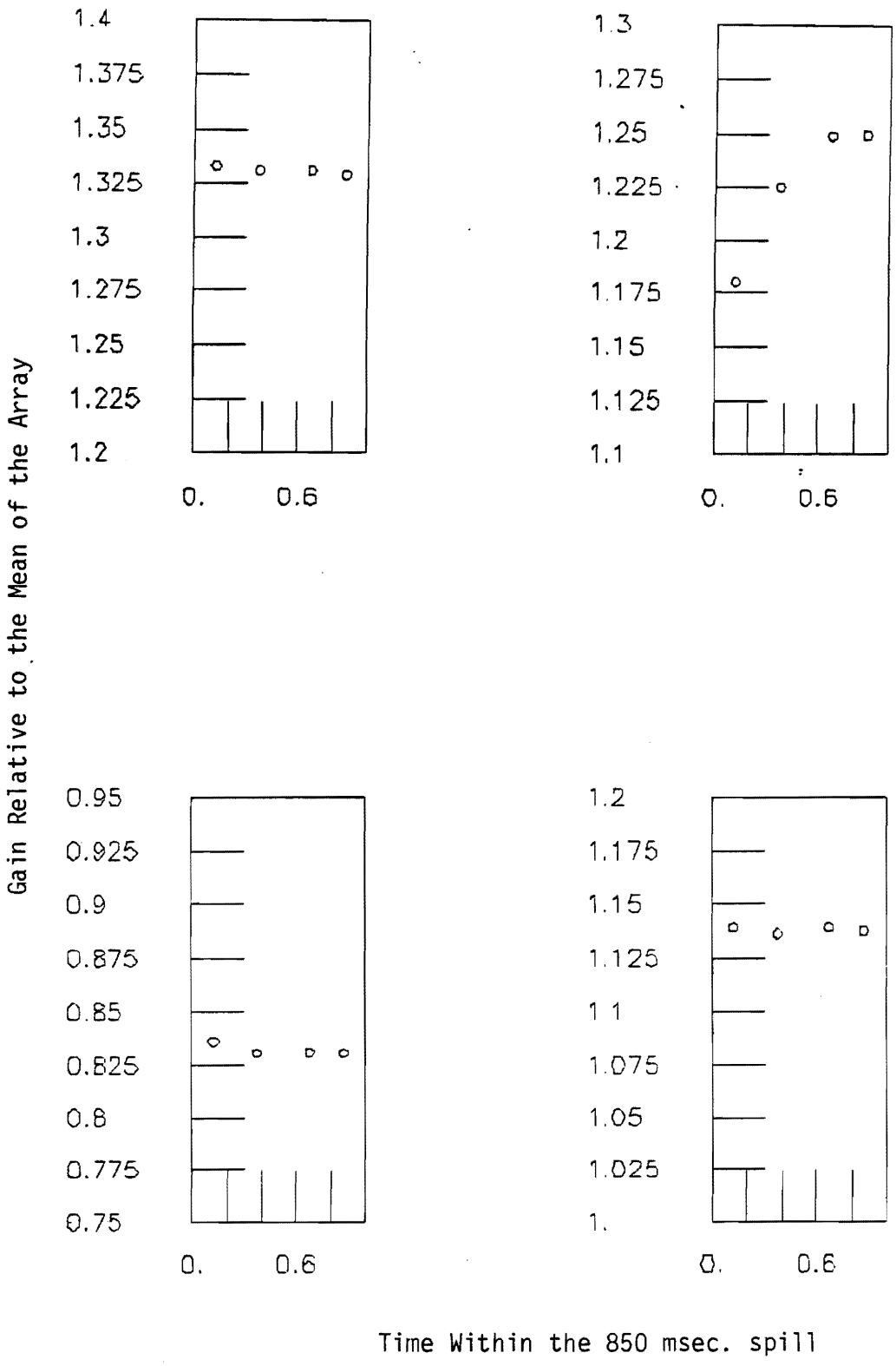
Gain Relative to the Mean of the Array
1.4
1.375
1.35
1.325
1.3
1.275
1.25
1.225
1.2
0.
0.6
1.3
1.275
1.25
1.225
1.2
1.175
1.15
1.125
1.1
0.
0.6
0.95
0.925
0.9
0.875
0.85
0.825
0.8
0.775
0.75
0.
0.6
1.2
1.175
1.15
1.125
1.1
1.075
1.05
1.025
1.
0.
0.6
Time Within the 850 msec. spill

Figure 17. The standard deviation of the pedestals for a typical run. For each channel of the array, the mean and standard deviation of the pedestal over a three-hour run was computed; this plot shows the standard deviations.

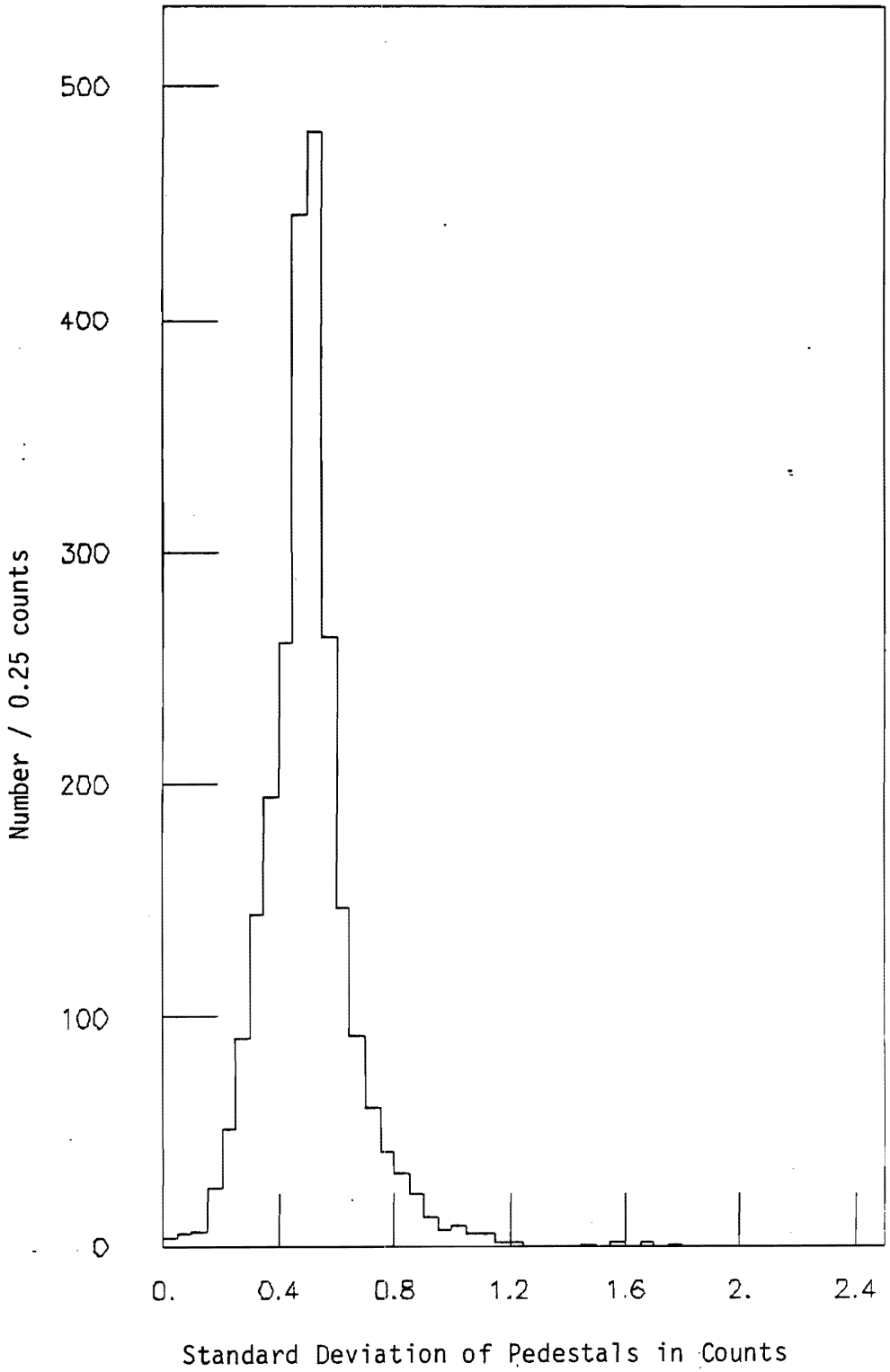
500
400
300
200
100
0
Number / 0.25 counts
0.
0.4
0.8
1.2
1.6
2.
2.4
Standard Deviation of Pedestals in Counts

Figure 18. A typical distribution of the lead glass response to a muon. A muon deposits roughly 40 counts in a block; the average depends on the gain of the individual channel.

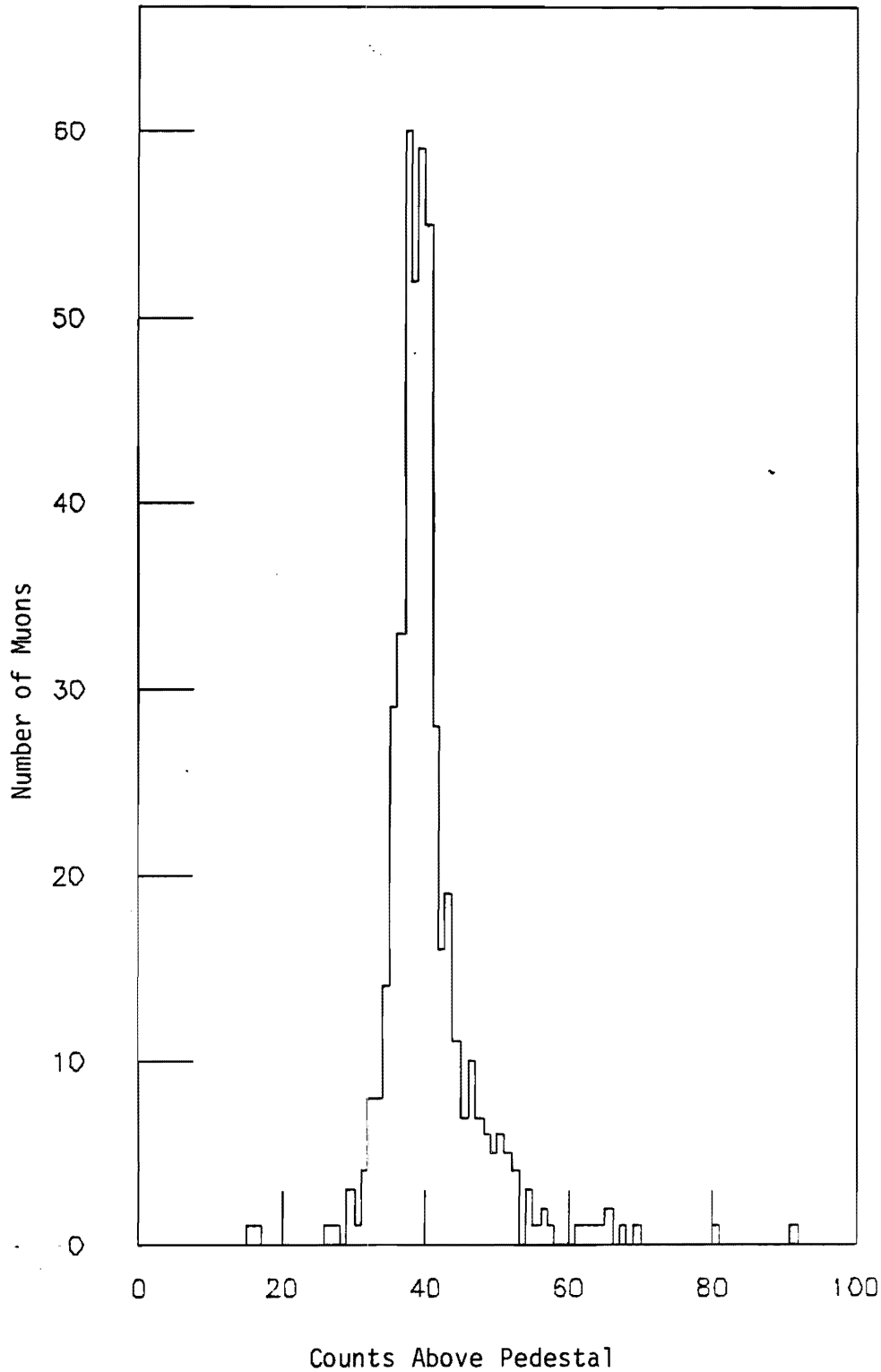
60
50
40
30
20
10
0
Number of Muons
0
20
40
60
80
100
Counts Above Pedestal

Figure 19. The average nonlinearity in the more nonlinear of the two neutral mode data sets. The nonlinearity is plotted as the percentage correction relative to the response at 450 counts above pedestal; hence, for 200 counts, the energy should be multiplied by 1.02 to remove the nonlinearity.

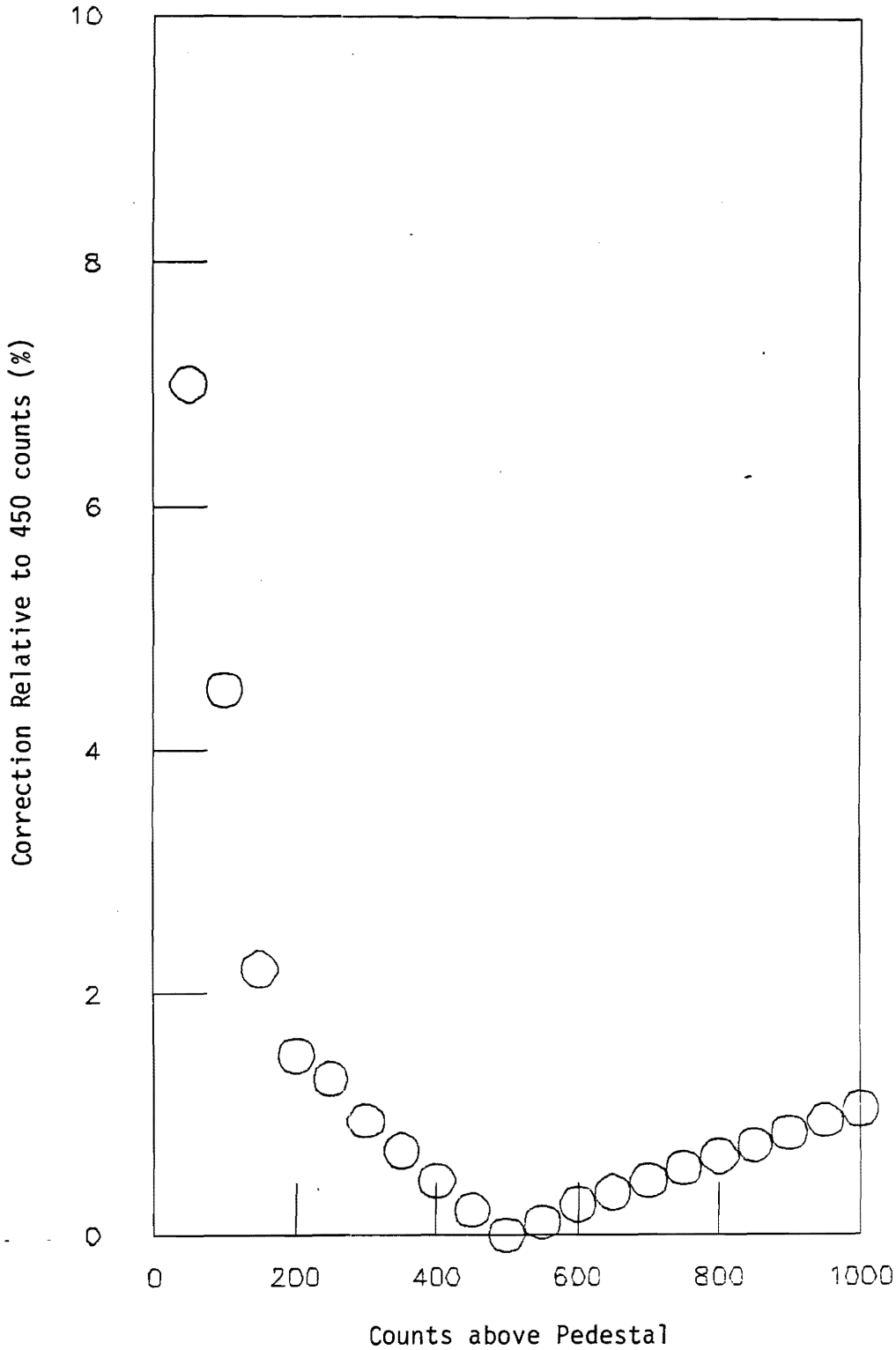
10
8
6
4
2
0
Correction Relative to 450 counts (%)
0
200
400
600
800
1000
Counts above Pedestal

variations, although the average shift was only 0.1%.

Our calibration then had to take into account slow drifts in gain, shifts with the presence of beam, and nonlinearity. We have used several techniques which compliment and check each other to calibrate the response over as wide a dynamic range as possible.

Before proceeding we must describe the calculation of the pedestals. The automatic pedestals subtracted by the ADC system were based on pedestals measured at the beginning of a two or three hour run of the experiment, and updated only occasionally within that time. As mentioned at the end of the preceding section, we measured the pedestals before and after each spill (we determined separately that there was no significant change in the pedestal during the spill and in the presence of beam). Fifty spills, or 100 of these pedestals, were averaged together and used to adjust the automatically subtracted pedestals in the offline analysis. Each of these 50-spill averages (about 10 minutes of data-taking) also had a standard deviation; a typical distribution of these standard deviations from one three-hour data tape appears in Figure 17. Eight runs with rapid pedestal changes were recalculated with 1-spill averages instead of 50-spill averages.

The simplest method of calibration used Cerenkov light from muons, which do not shower. They deposit approximately 40 counts, or the equivalent of a 2/3 Gev electromagnetic shower. To calibrate to muons we inserted a beamstop (about four meters of steel) around 100 meters from the target and used the muon bank to trigger. We then measured the response with the ADC's. A typical (pedestal-subtracted) ADC distribution for muons is shown in Figure 18; the peak is at about 40 channels. We took

the mean of the distribution between 20 and 100 counts to obtain the gain. The gain shift with the beam severely limited this method; however, we could use the 'muon gain' as a starting point for more sophisticated calibrations, and as a 'fall-back' if these methods lacked statistical power in an individual block. The muon gains were used extensively during the run to analyze the data offline.

If the time-dependence of the gains and gain shifts with the beam were the only problems, we could have corrected for them using our monitoring system. The nonlinearity mentioned at the beginning of this section dwarfed these problems. Our calibration method used the data themselves; hence we did not worry about beam-on/beam-off shifts. The .1% average change during the spill did not significantly contribute to the resolution and we ignored it. The remainder of this section will examine our two methods of calibration and how they attacked the problem of nonlinearity.

Before proceeding let us quote the size of the nonlinearity and explain why it is a problem. Our neutral mode data was divided into two sets, as we shall describe in Chapter V. Figure 19 shows the average nonlinearity measured over all channels for the more nonlinear of the two sets. At energies from 10-20 GeV, the average nonlinearity takes the form

$$E_{meas} = E_{true} \times (1 - .004 E_{true}) \tag{4.5}$$

so a 20 GeV photon is mismeasured by 4% relative to a 10 GeV photon. The nonlinearity is a problem because our reconstruction algorithms are sensitive to the energy measurements. We now explain the essence of the reconstruction method to clarify the problem. Consider a π^o decaying into two photons z meters from the lead glass. Then using

the small-angle approximation

$$m_{\pi^o}^2 = 2E_1E_2(1-\cos\theta_{12}) \approx 2E_1E_2(1-(1-\frac{{r_{12}}^2}{2z^2})) = E_1E_2\frac{{r_{12}}^2}{z^2} \tag{4.6}$$

where E_1 and E_2 are the photon energies and ${r_{12}}^2$ is the distance between the photons at the lead glass. The z-vertex is then given by

$$z^2 = E_1E_2\frac{{r_{12}}^2}{m_{\pi^o}^2} \tag{4.7}$$

It is clear that a shift in the energies biases the z-vertex measurement. Our reconstruction method, developed in Chapter VII, uses equation (4.7). Hence a 1% mistake in the energies becomes a 1% mistake in z-vertex , or about 0.7 meters (the upstream end of the decay region is 74 meters from the glass). But 70 cm. is 5.5% of the 13 meter decay region! A software cut in z-vertex therefore induces a 5.5% error in the rate of accepted K_L for only a 1% error in the energy scale. The error does not necessarily cancel from K_L to K_S because the upstream end of the regenerated beam is defined in hardware through the RA. We must therefore understand this nonlinearity and correct for it.

The first method of calibration uses the electron-positron pair from the converted photon. The energy in the glass (E) is compared to the momentum measured in the chambers (p) and the ratio E/p is formed. This method has several advantages. First, there are approximately 20000 pairs for each data tape; we found we could recalibrate the experiment every 14 hours of running. Second, the track momenta are accurately measured. Finally, the data and the calibration are taken simultaneously.

This disadvantage of this method arises from the effect of bremsstrahlung. As soon as the pair is created in the lead converter it begins to lose energy. The photons then

travel along the electron's trajectory and strike the glass near the point that the unconverted photon would have struck. The tracks are bent away from this point by the magnet in the x-direction; multiple scattering further changes their impact point. If the tracks are well-separated from the bremsstrahlung and from each other, measuring E/p provides an accurate calibration; if the tracks are too close, the showers overlap both with the random bremsstrahlung and each other and the calibration is imprecise. These effects become significant for 10 GeV electrons; the usable momentum spectrum does not extend past 15 GeV/c. Since many of the photons from $K \rightarrow 2\pi^o$ decay were 20 GeV or more, this is a significant limitation.

One of the difficulties of lead glass calibration is that one must sum over many blocks to obtain the shower energy. We avoided the problem by using only the central block of the shower and then requiring that a constant fraction of the shower energy be deposited in the central block. This was accomplished by demanding the track extrapolate to within the central quarter of the struck block. Figure 20 shows the fraction of deposited energy in a block as a function of the impact point of the shower; we corrected for the variation in the containment over the central quarter of the block .

The number of counts in the ADC for that block was then divided by the track momentum. A table of the mean of this ratio for each channel as a function of the number of channels was then formed. The table was reformed approximately every seven runs, or 14 hours of data-taking.

The E/p distribution of electrons in our $K \rightarrow \pi^o\pi^o$ sample after the calibration is shown in Figure 21. The high end shape seen in the Figure is affected by the extra

Figure 20. The fraction of energy deposited in a block as a function of the impact point of the electromagnetic shower.

.614	.615	.605	.584	.549	.441
.753	.751	.736	.719	.668	.549
.806	.801	.792	.768	.719	.584
.832	.826	.818	.792	.736	.605
.843	.840	.826	.801	.751	.615
.847	.843	.832	.806	.753	.614

block center

Figure 21. The energy in the glass divided by the the momentum in the chambers for electrons from the $K \rightarrow \pi^o \pi^o$ data sample. The low end tail arises largely from misreconstructed tracks; the high end shape is affected by the presence of bremsstrahlung showers fusing with the showers from the electrons.

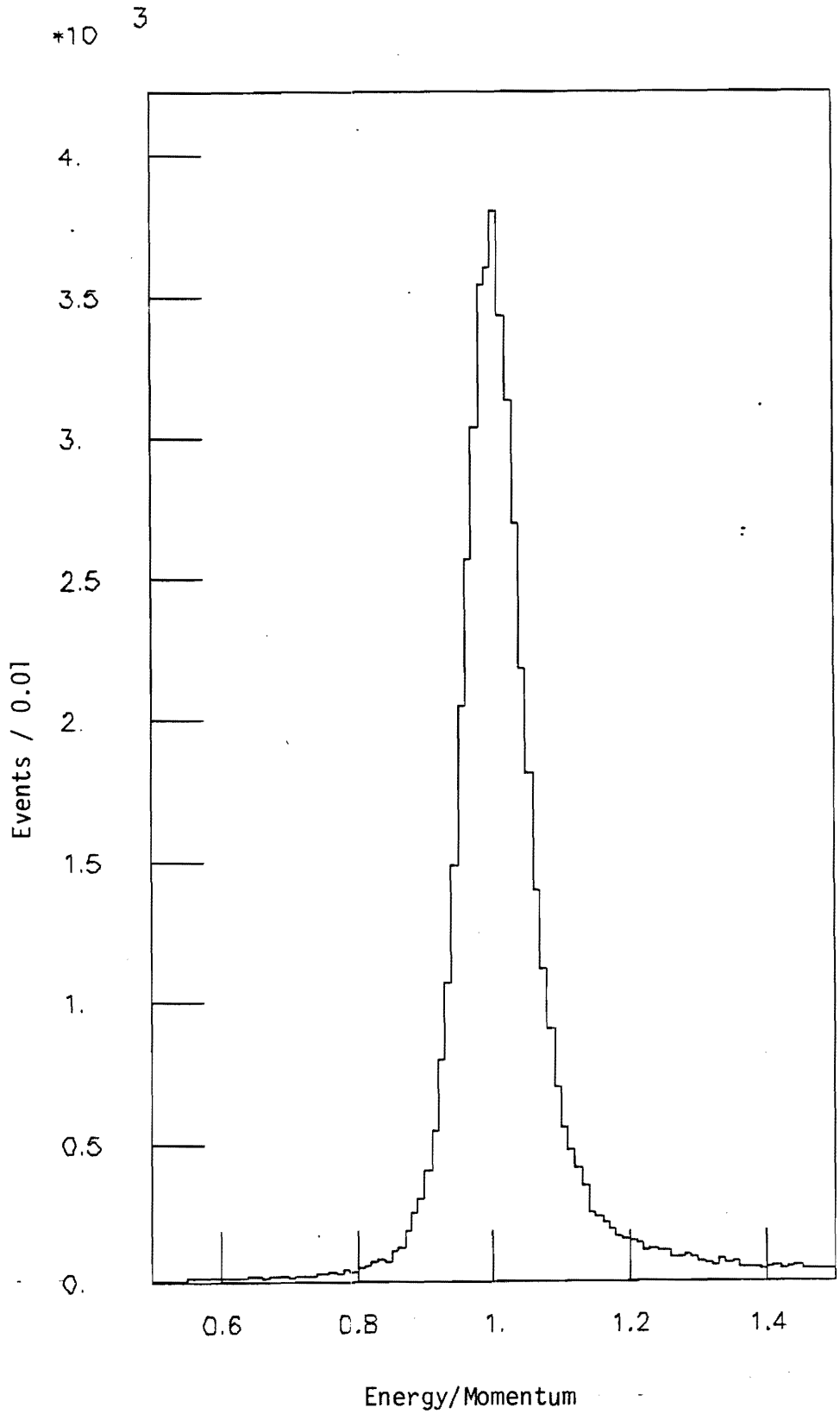
*10 3
4.
3.5
3.
2.5
2.
1.5
1.
0.5
0.
Events / 0.01
0.6
0.8
1.
1.2
1.4
Energy/Momentum

Figure 22. The $FWHM$ / E of E/p vs. $1/\sqrt{E}$ for electrons. E (energy) measured in the glass is divided by p (momentum) measured in the chambers and a plot similar to Figure 21 is formed as a function of momentum; the FWHM is computed for each of several momentum bins. The results are presented in the plot.

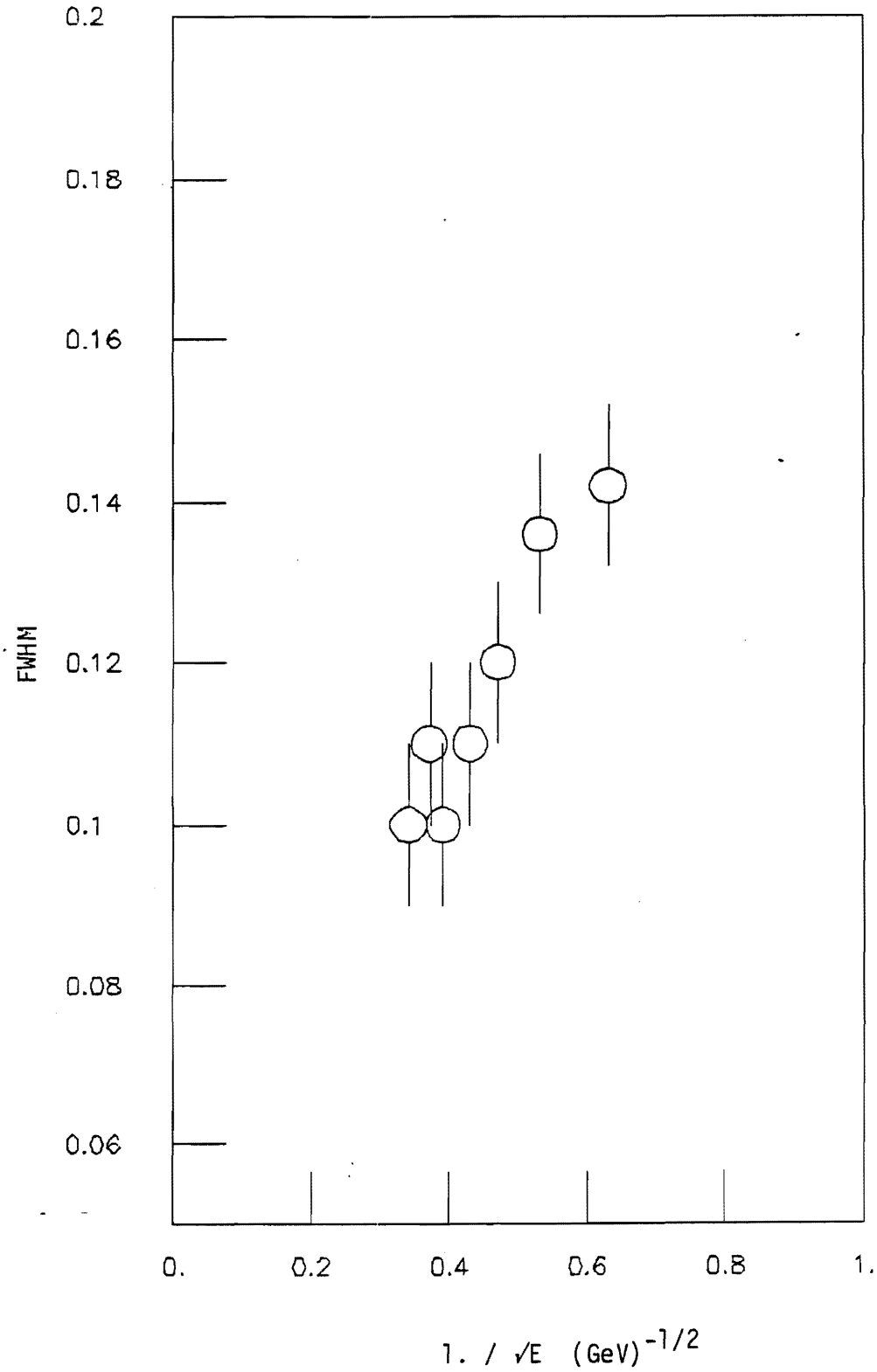
0.2
0.18
0.16
0.14
0.12
0.1
0.08
0.06
FWHM
0.
0.2
0.4
0.6
0.8
1.
1. / √E (GeV)^-1/2

energy from the bremsstrahlung while the low end tail is due to misreconstructed tracks. Figure 22 is a plot of $FWHM/\sqrt{E}$ vs. $1/\sqrt{E}$ in the range of electron calibration. A fit yields $6\%/\sqrt{E} + 2\%$, both typical of lead glass and in agreement with our naive expectations.

Before examining the next method, we must discuss a correction to the data. Recall that a five-count threshold determined which channels were read out by the ADC. In practice, this leads to blocks with finite energies in good showers not being read out. Figure 23 shows two showers, one at 20 GeV and one at 4 GeV. A typical number of channels for a real shower is shown in each of the blocks. The 20 GeV shower only loses 0.6% of its energy while the 4 GeV shower loses 6% ! A shower shape measured from the data was used to calculate the 'missing block' correction. We did not concern ourselves with this correction in the electron calibration; there we had enough data to cut on the central portion of the block, making this correction just an overall constant.

The final method calibrated the array to photons.[43] Neutrons interacting in the lead converter would occasionally make a π^o and two tracks, which then triggered the apparatus. These event have a known z-vertex, that of the converter. Equation (4.6) then gives us the π^o mass. The distance between the photons is well-measured (the algorithm is discussed in Chapter VII) and is only weakly dependent on the gains. We therefore measured the gains iteratively, adjusting the gains as a function of counts in the ADC to minimize the width of the π^o mass peak. We only had 600 π^o events per tape, as opposed to 20000 electron-positron pairs. Therefore we could not cut on impact point and had to apply the missing block correction to calculate the energies.

The photons from π^o decay have a mean energy of 15 GeV and provide adequate statistical power from 10 to 40 GeV, which compliments the range of electron energy well. The π^o mass peak after the calibration is shown in Figure 24. Finally, in Figure 25 we plot the π^o mass as a function of π^o energy for the more nonlinear of the two neutral mode data sets. The top half of the graph is based on an electron calibration assuming linearity; the bottom half is the same plot using the π^o calibration. The improvement is dramatic. The two methods of calibration were then combined[44] to determine the final set of gains.

Figure 23. Two showers, one at 20 GeV and one at 4 GeV. The boxes represent blocks and the contained numbers represent counts above pedestal, as in Figure 12. These two typical showers show how the readout threshold can cause a significant, energy-dependent loss in the measured energy of a shower.

Not read out →	0	2	3	2	0
	3	8	20	8	0
	3	100	1250	50	2
	2	8	20	8	2
Not read out →	0	0	1	0	0

20 GeV shower;
miss 0.6% of energy

Not read out →	0	0	0	0	0
Not read out →	0	1	4	1	0
	0	20	250	10	0
Not read out →	0	1	4	1	0
Not read out →	0	0	0	0	0

4 GeV shower
miss 6.1% of energy

Figure 24. The π^o mass peak, after calibration. The mean of the plot is at the π^o mass of .13496 MeV/c ^{2}.

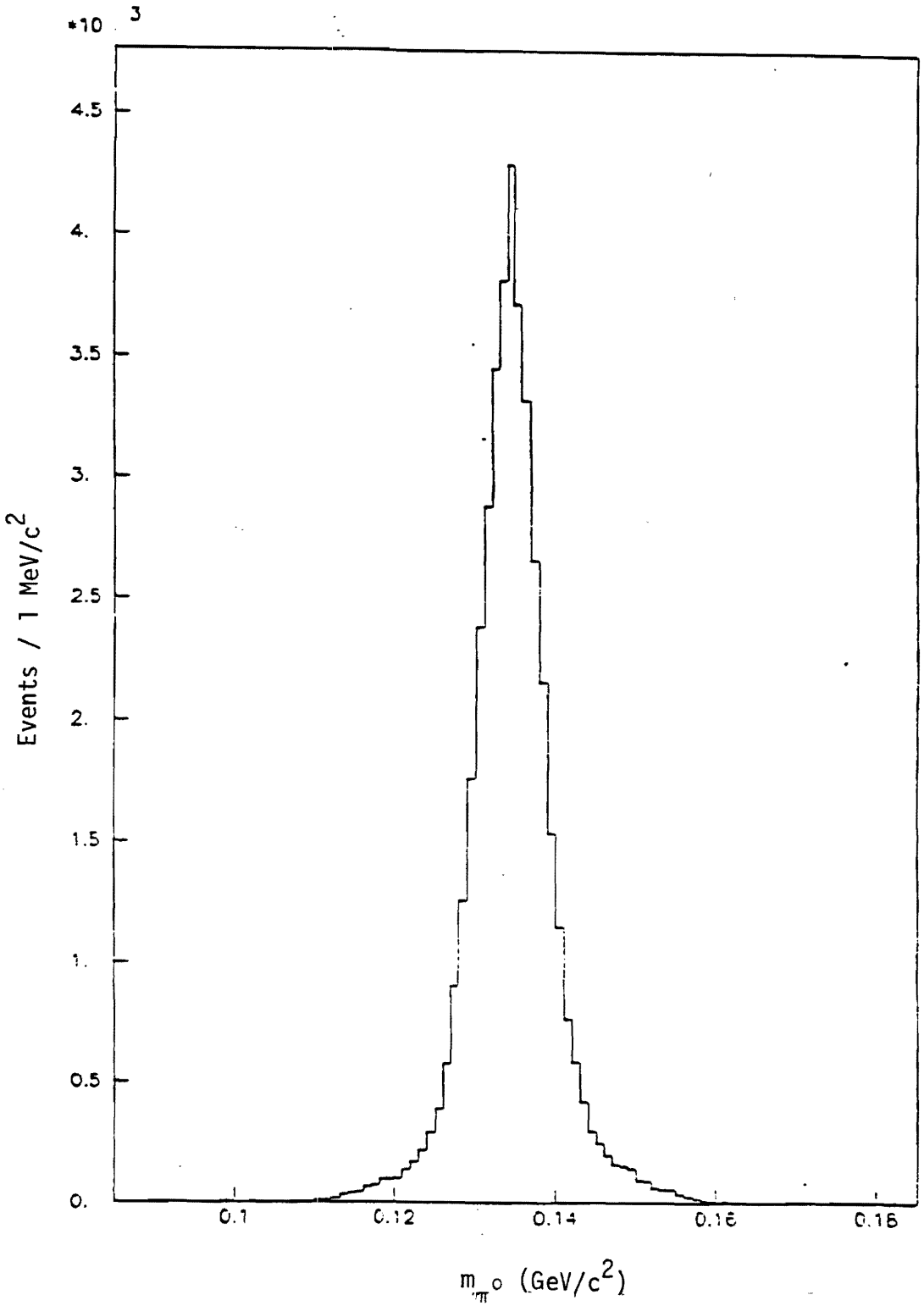
*10 3
4.5
4.
3.5
3.
2.5
2.
1.5
1.
0.5
0.
Events / 1 MeV/c2
0.1
0.12
0.14
0.16
0.18
mπo (GeV/c2)

Figure 25. The π^o mass as a function of π^o energy for the more nonlinear of the two neutral mode data sets before and after calibration. The slight rise at π^o energies near 40 GeV is due to merged showers from the two daughter photons; the effect will be explained in Chapter VI, Section B.1.

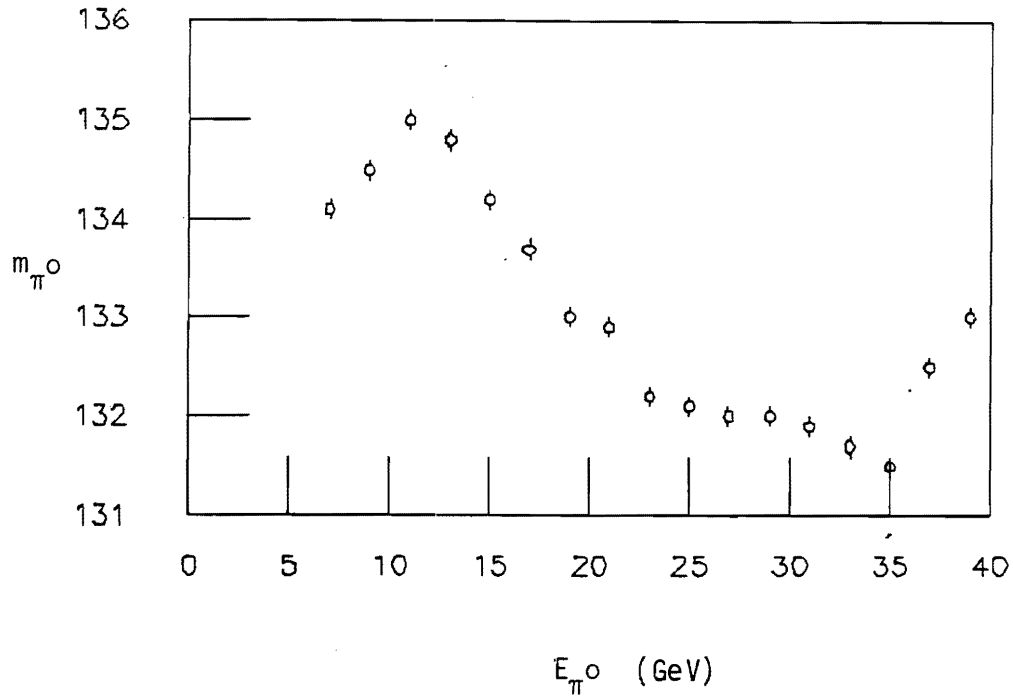
136
135
134
133
132
131
m_{π^o}
0
5
10
15
20
25
30
35
40
E_{π^o} (GeV)

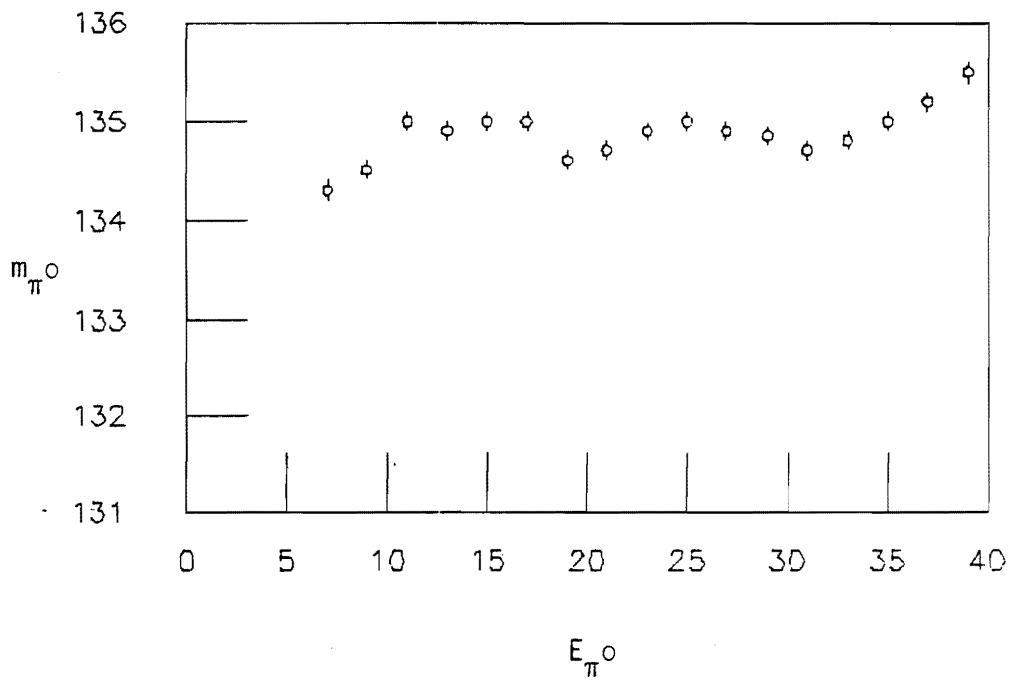
136
135
134
133
132
131
m_{π^o}
0
5
10
15
20
25
30
35
40
E_{π^o}

CHAPTER V

DATA COLLECTION AND ONLINE MONITORING

This chapter will discuss the data-taking for the experiment. We will describe the different data sets and typical running conditions. The second half of this Chapter will explain the on-line monitoring of the apparatus.

A. Data Sets and Running Conditions

The data were taken from January to June of 1982 in the M3 neutral beam line at FNAL. Since the neutral and charged mode data were taken separately, we had to perform small changes to the spectrometer and beam line. To change from neutral to charged mode data-taking we had to : (1) remove the lead converter and A counter from the conversion hodoscope, and (2) move the lead curtain in front of the G-bank. In order be as compatible as possible with other experiments sharing our production target, in the charged mode running we had to change the targeting angle of the primary proton beam and change the absorber (the absorber upstream of the two-hole collimator) to adjust for the increased neutron flux.

As we explained in the previous Chapter, the lead curtain was in place for only part of the charged mode running. The 'unbiased' data was also intended for a precision

semileptonic decays could not be rejected in the trigger.

In both the neutral and charged data-taking the primary proton beam delivered 3-5 $\times 10^{12}$ protons per pulse, as measured by a secondary emission monitor, in a 850 msec. spill every 10-15 seconds. In the neutral mode we collected about 40 triggers per pulse (we detected on average one $K_L \rightarrow 2\pi^o$ decay every 80 spills) and in the charged mode we collected about 70 triggers per pulse (with one detected $K_L \rightarrow \pi^+\pi^-$ decay every 12 spills). The limitation on the useful flux in both the neutral and charged modes was the instantaneous rate in the drift chambers; we ran with beam-on currents of the order of 100-200 μA. Significantly higher currents caused the chamber voltages to sag, decreasing the chamber efficiency ; the higher rates also produced too many accidental hits.

The data were recorded on 1600 BPI tapes; a typical tape took between two and three hours to fill and had about 40000 triggers in the neutral mode and 80000 triggers in the charged mode. In the neutral mode approxiamtely half the triggers were electron-positron pairs. Table 3 summarizes the data samples.

In addition to the charged and neutral mode data sets we performed a measurement of the radiative width of the $K^{o*}(890)$[45]; none of this data was used in the η_{oo}/η_{+-} analysis. As mentioned in Chapter IV, muon calibration runs, for which we inserted our beam stop and triggered using the muon bank, were interspersed within the data.

B. Online Monitoring

During all data-taking a number of checks were made to insure that the apparatus was working properly. We used alarms to indicate when tanks of Helium or chamber gas were running low, or various malfunctions had occurred. We used the end of data tapes to visually check the beam line and to plot a variety of raw and scaled rates, such as the relative rates of various subtriggers or their rates scaled to the proton flux. We could catch the failure of individual logic elements as well as monitor the targeting of the primary beam.

Our on-line computing system used MULTI.[46] We could define and monitor a wide variety of histograms and define new ones when necessary. For example, the number of times each scintillation counter was struck was plotted for each scintillation bank. Several histograms were used to monitor the performance of the drift chambers. We monitored the distribution of the number of times each wire was hit, providing graphic indications of 'hot' or dead wires. The number of hits in each chamber was checked, allowing us to monitor their efficiencies. We plotted the distribution of drift times relative to the scintillator trigger; this distribution should be flat and run from zero to the maximum drift time in a cell. Changes in this distribution, and especially distortions around the edges, indicated problems with the chamber gas. Finally we monitored the performance of the mean timers by plotting the hardware calculated mean time.

We monitored a variety of characteristics of the lead glass. The distribution in the number of times each ADC channel was read out was followed, providing analogous information to the hit distribution of the wires; in addition, drifting pedestals would

often cause spikes in this distribution because of the five-count threshold for reading out blocks. The values and standard deviations of the last seven pedestals for each channel were frequently scanned, as well as the average response to the flashers over the last seven-spill period. The pedestals were updated whenever the beam was interrupted or we noticed a pedestal drift. Finally, the distributions of E_T, E_X, and E_2 from the mass box were checked throughout the runs.

TABLE 3

DATA SETS USED IN THE ANALYSIS

Tapes	Triggers($\times 10^6$)	Reconstructed Events ($\times 10^6$)
η_{+-}, unbiased, Set I	32	2.39
η_{+-}, unbiased, Set II	38	3.06
η_{+-}, biased	71	3.44
η_{00}, Set I	117	3.75
η_{00}, Set II	121	3.91

CHAPTER VI

CHARGED MODE RECONSTRUCTION

AND

BACKGROUND SUBTRACTIONS

In order to identify and reconstruct $K_{L,S} \rightarrow \pi^+\pi^-$ decays we must detect the tracks of the pions and reconstruct their trajectories and momenta; in order to extract the observed number of K_L and K_S we must measure and subtract the backgrounds. This chapter will cover both of these procedures. A detailed account of the track reconstruction algorithm and of subtleties in the chamber alignment can be found in Reference 31.

A. Event Reconstruction

1. Drift Chamber Alignment

The relative location and orientation of the chambers has to be determined before tracks can be reconstructed. The positions along the beam line were carefully measured but the transverse offsets were best determined from the data. The drift velocities and the arrival times of hits on wires (drift times) must be known as well. The drift velocity varied from chamber to chamber and changed with time

because of irregularities in the flow of chamber gas. The details of the readout system resulted in the measured drift times systematically shifting with shifts in the Fermilab-supplied RF, already discussed in Chapter IV. All of these effects were measured by running the pattern reconstruction program on selected events; muon calibration runs, which gave clean single tracks passing through the spectrometer, were especially useful for determining the positions of the chambers.

In order to determine the transverse position of each chamber in each view, the tracks were fit to the other three chambers; the fitted track was then projected to the fourth, chosen chamber and the 'residual', the signed distance between the fitted track and the measured location of the hit in the chamber, was plotted as a function of the position of the hit. Figure 26 shows the effect of an overall spatial offset, an error in the measured drift time, and nonuniformities in the drift velocity. We corrected for each of these effects every few tapes, or eight to ten hours of data-taking; discrete changes in spatial position were tracked down to a specific tape. The final chamber positions were known to $\pm 50\mu$ and the systematic error in the drift times was less than 1.3 nsec (63μ).

2. Track Fitting and Kinematic Analysis

Using the above determinations, struck wires and drift times were converted into hits in space. The tracks were then fit in the two views, the top view and the side view: the top view refers to the trajectory in x and is the view in which tracks

are bent by the magnet; the side view is the y, up/down view. In the top view the tracks are fit to three parameters: the track slopes in the front and back halves of the spectrometer and a common point in the center of the magnet. In the side view the tracks were fit to a single line (a small correction was made for a p_T kick of the magnet in this view). The details of this correction and of the reconstruction algorithm can be found in Reference 31. The tracks were then correlated: using the split chamber, which told us to which side of the spectrometer a given y-view track belonged, each y-view track was assigned to a specific x-view track. The G-bank was used to correlate the tracks if both of them fell on the same side of the split chamber.

The track momenta were then calculated using the measured field map and the angle between the front and back half track segments. The scale of the field map was determined by applying it and then requiring that the reconstructed kaon mass have its nominal value. The error on this normalization is less than .01%.

The decay vertex was then determined. The method finds the shortest perpendicular segment between the two tracks; the distance of closest approach is defined to be the length of this segment. The two points of intersection of this segment with the two tracks were weighted by the square of their momentum and averaged to obtain the vertex. Figure 27 is a plot of the distance of closest approach for all pairs of tracks in the $\pi^+\pi^-$ sample; we cut at 3 cm., removing misreconstructed tracks. Figure 28 and 29 show the z-vertex distribution for each of the vacuum and regenerated beams. The peaks at 406 and 420 meters in the vacuum beam are

due to neutron interactions in the region of the regenerator anticounters and conversion hodoscope respectively.

The decay was then assigned to one of the beams. The decay vertex, determined above, does not cleanly separate between the two beams because incoherently produced K_S are created at a finite angle to the beam. Hence a K_S can leave both beams or cross from one beam to the other before decaying, as shown in Figure 30. We perform the separation by extrapolating the kaon trajectory to the xy vertex at the z-plane of the regenerator anticounters (z_{RA}). We have two points with which to determine the kaon's path: one is the decay vertex and the other is the center of momentum of the two tracks at the magnet. The line between these two points is the kaon trajectory through the spectrometer; Figure 3 showed the K_S decay vertex extrapolated back to z_{RA}.

Having separated the beams, we next calculate the q^2 of the event. The calculation is illustrated in Figure 31. The line from the meson target to the xy vertex at the regenerator is drawn and its angle relative to the kaon trajectory through the spectrometer is computed. The q^2 of the event is then $p^2\sin^2\theta$, where θ is the angle just defined and p is the sum of the track momenta (The location of the target was determined by extrapolating the kaon trajectory in the spectrometer back to the meson target for coherently produced K_S).

The mass of the event was calculated assuming the decay products were pions:

$$M^2_{\pi\pi} = 2m_\pi{}^2 + 2(E_1E_2 - \vec{p_1} \cdot \vec{p_2}) \tag{6.1}$$
$$E_i^2 = p_i^2 + m_\pi{}^2$$

B. Cuts Used in the Analysis

Before attempting to perform a background subtraction we imposed a variety of cuts on the sample to minimize the background; this section will describe these cuts and their effects.

The first set of cuts eliminated the effects of known problems with the drift chambers. Recall that the chambers had a central hole for the passage of the beam pipe. Wires which otherwise would have passed through the pipe were terminated on a central box suspended from the outer frame of the chamber. The chambers were inefficient near the box because of the resultant irregularity in the electric fields. For similar reasons, the chambers were inefficient along their outer edge. Rather than attempting to understand the inefficiency and correct for it with a Monte Carlo, we cut 3 cm. away from the central box and 3 cm. away from the outside edge of the chamber; events with a track passing through either of these zones were cut. The split chamber had a identical difficulty along a central strip constituting the split; we cut at $\pm$ 3 cm. from the strip.

The second cut was required by the pattern recognition program which reconstructed the tracks. The program did not work well when the two tracks were close in either the top or side view; a track separation cut of 2 cm. in each view

Figure 26. The effect of systematic errors on the drift chamber residuals. The mean residual is plotted as a function of position within the cell for four cases: (1) no errors, (2) the chamber position is wrong and should be translated, (3) the t_o relative to the true time of particle passage is incorrect by an offset in time, and (4) the drift velocity is incorrect; the error may be due to variation with drift velocity over the cell.

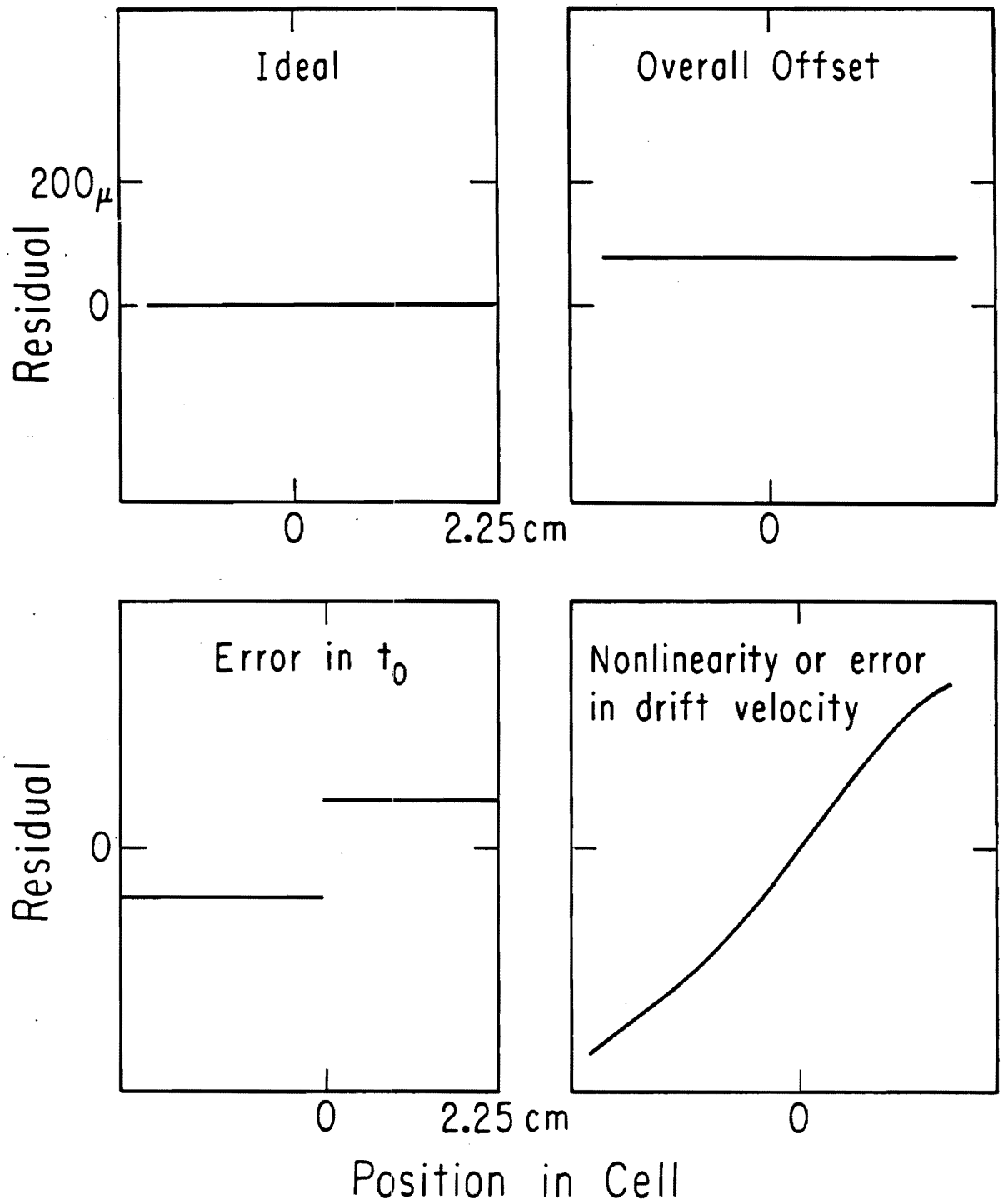
Ideal
Overall Offset
200μ
0
Residual
0
2.25 cm
0
Error in t_0
Nonlinearity or error in drift velocity
0
Residual
0
2.25 cm
0
Position in Cell

Figure 27. The distance of closest approach for charged tracks. We cut the sample at 3 cm. in this distance.

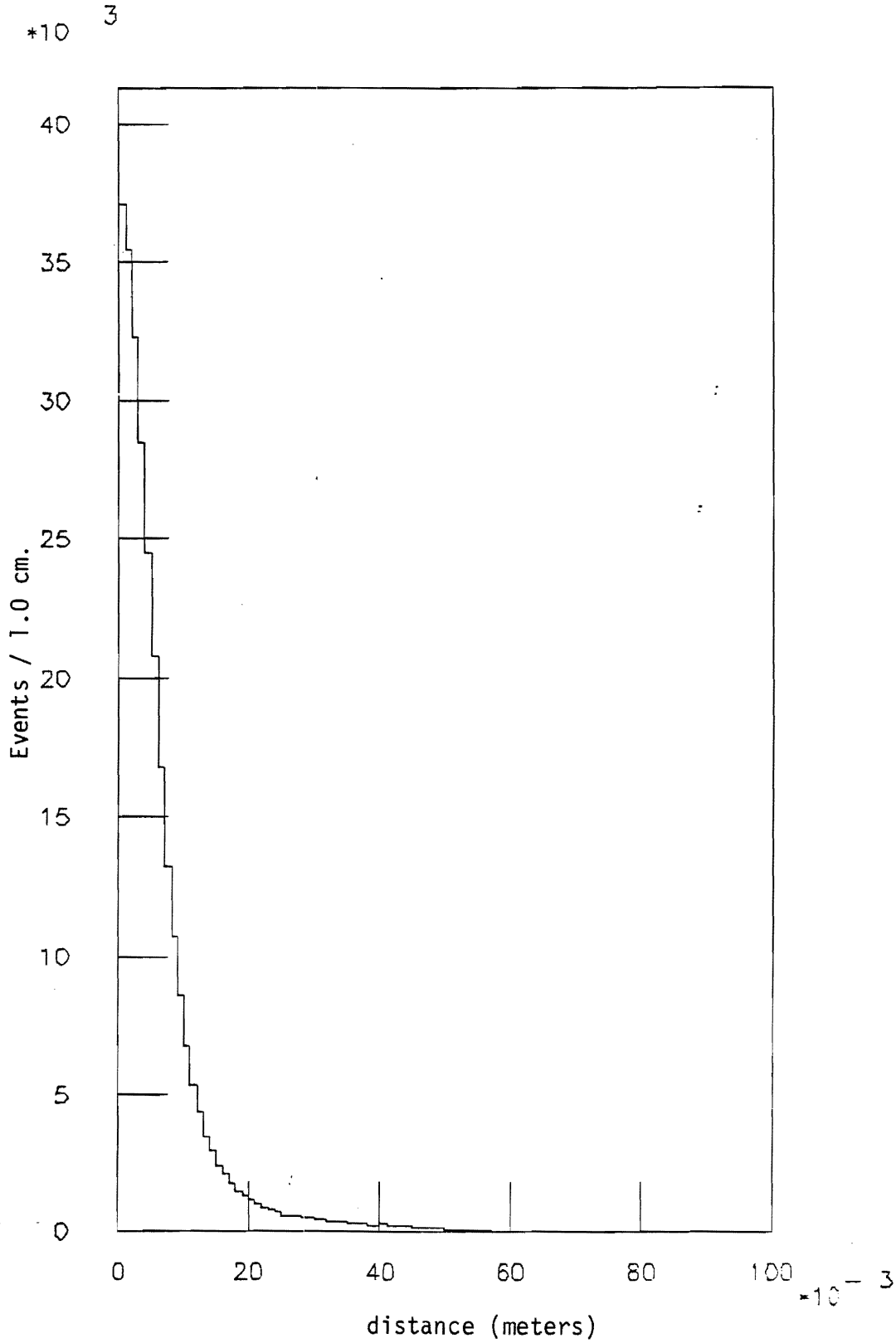
*10 3
40
35
30
25
20
15
10
5
0
Events / 1.0 cm.
0
20
40
60
80
100
*10 - 3
distance (meters)

Figure 28. The z-vertex distribution for the $K_L \rightarrow \pi^+\pi^-$ sample. The peaks at 406 and 420 meters arise from neutron interactions in the air and windows at either end of the decay region.

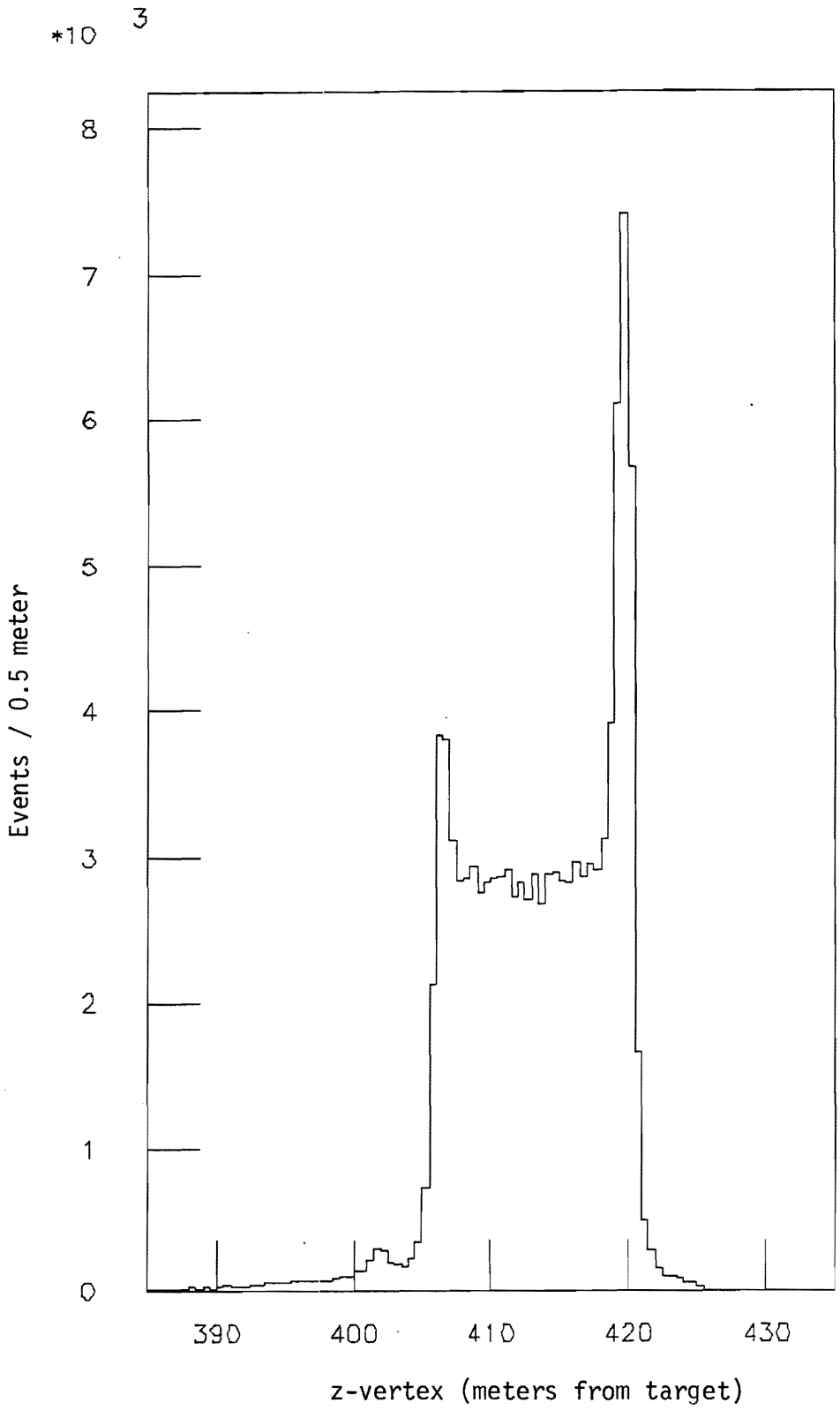
*10 3
8
7
6
5
4
3
2
1
0
Events / 0.5 meter
390
400
410
420
430
z-vertex (meters from target)

Figure 29. The z-vertex distribution for the $K_S \rightarrow \pi^+\pi^-$ sample. The exponentially falling distribution reflects the K_S lifetime.

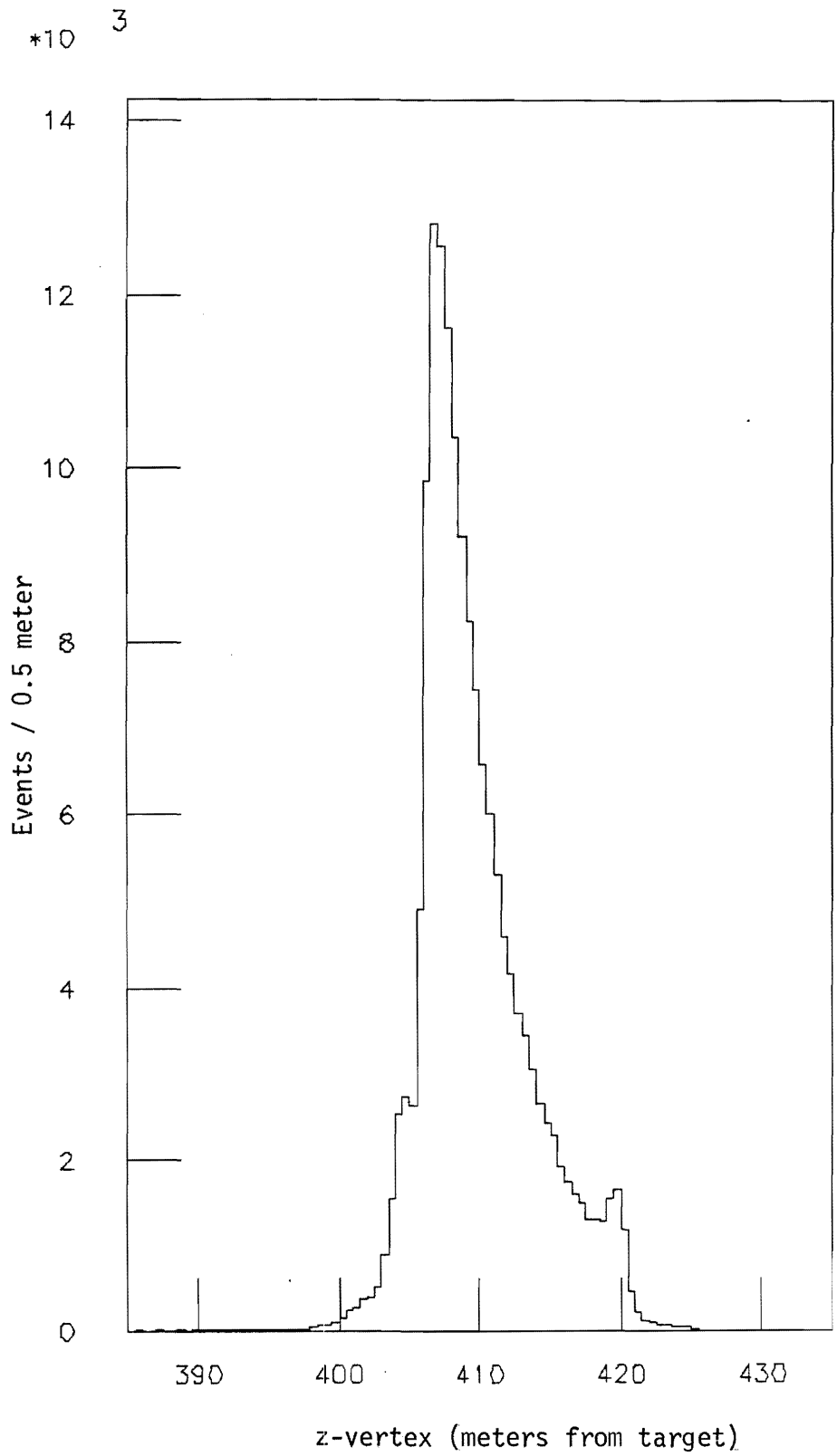
*10 3
14
12
10
8
6
4
2
0
Events / 0.5 meter
390
400
410
420
430
z-vertex (meters from target)

Figure 30. An inelastically produced K_S crossing between the beams before decaying.

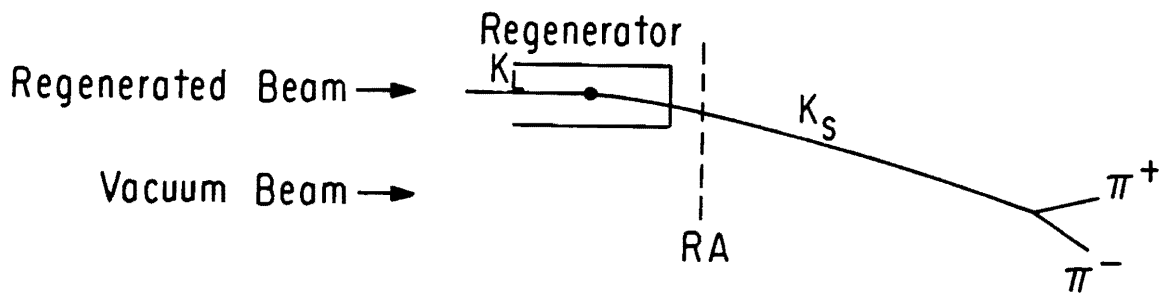
Regenerator
Regenerated Beam
K_L
K_S
Vacuum Beam
π^+
RA
π^-

Figure 31. The calculation of q^2 in the charged mode.

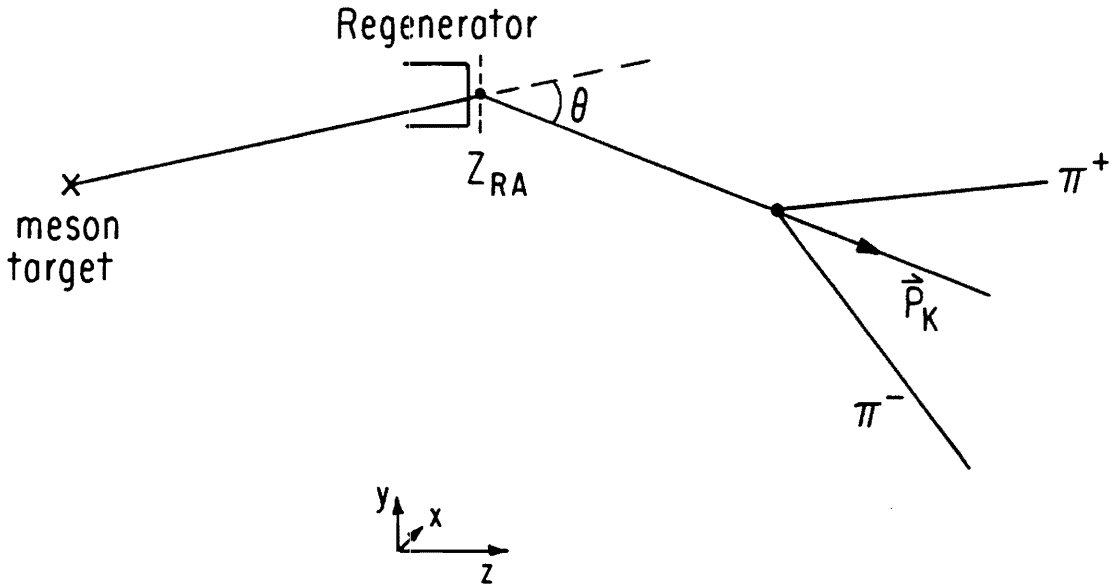

$$q^2 = p_K^2 \ \mathrm{SIN}^2 \theta$$

was imposed.

The next cut eliminated tracks which would 'range out' due to energy loss in the muon filter. We demanded all tracks have more than 10 Gev/c of momentum, insuring 90% efficiency for rejecting muons.

The above three cuts were used to ensure that the tracks were well measured and could be properly identified. The next set of cuts will remove electrons and muons from the data sample, allowing us to analyze the biased and unbiased data together. A contamination from Λ^o decay will also be removed.

The first cut removes muons; the muon latches had been written to tape and we cut on them in both the biased and unbiased data.

The elimination of electrons used the lead glass. We have studied in considerable detail the calibration of the glass in the neutral mode. In the charged mode the resolution was far less important and the procedure was correspondingly simpler; each of the two unbiased sets was calibrated as a whole and we did not correct for nonlinearity. The technique used electrons from $Ke3$ decay and calibrated with E/p as in the neutral mode; in the charged mode data the lead converter had been removed and so bremsstrahlung presented no difficulties. The ratio E/p was formed using the nine central blocks of the shower (the nine blocks closest to the impact point of the electron as measured by the chambers); the gains were altered iteratively to minimize the width of E/p. The E/p distribution after calibration is shown in Figure 32. The peak near zero is due to noninteracting pions; the shoulder extending out to high E/p comes from pions which interacted

in the glass, and the peak near unity is the electron signal. We required $E/p < 0.8$ to eliminate electrons.

The next cut removed Λ^o decays from both the unbiased and biased data sets. If the higher momentum track was positively charged we assumed it was a proton and calculated $m_{P\pi}$ for the event analogously to our earlier calculation of $m_{\pi\pi}$. Figure 33 shows $m_{P\pi}$ for these events, revealing a clear Λ signal. We cut by eliminating events with $1105 < m_{P\pi} < 1125$ Mev/c ^{2}.

The final cut eliminated decays upstream of the decay region; we simply demanded neither regenerator anticounter had fired. No software cut in z-vertex was applied since the edge of the decay region was defined with the hardware.

C. Isolation and Measurement of the Backgrounds

Figures 34 and 35 show the vacuum $K\pi 2$ sample with the above cuts in two momentum bins for q^2 less than 300 (MeV/c) ^{2}. A clear $K\pi 2$ signal is observed with some residual background at the level of a few percent of the peak. The background clearly varies with momentum; this structure must be understood to arrive at the observed numbers of K_L and K_S.

The remaining background was fit using measured distributions of identified sources of background where possible; hence we did not rely on a Monte Carlo to simulate the mass and q^2 dependence of the background. The $K\mu 3$ and $Ke3$ backgrounds were handled in this way. The remaining background was due to neutron interactions and was measured separately. We first discuss how the sources of

Figure 32. E/p for electrons after calibration in the charged mode. The peak at unity is the electron signal. The peak near zero arises from pions which do not interact in the lead glass and the broad shoulder comes from those which do.

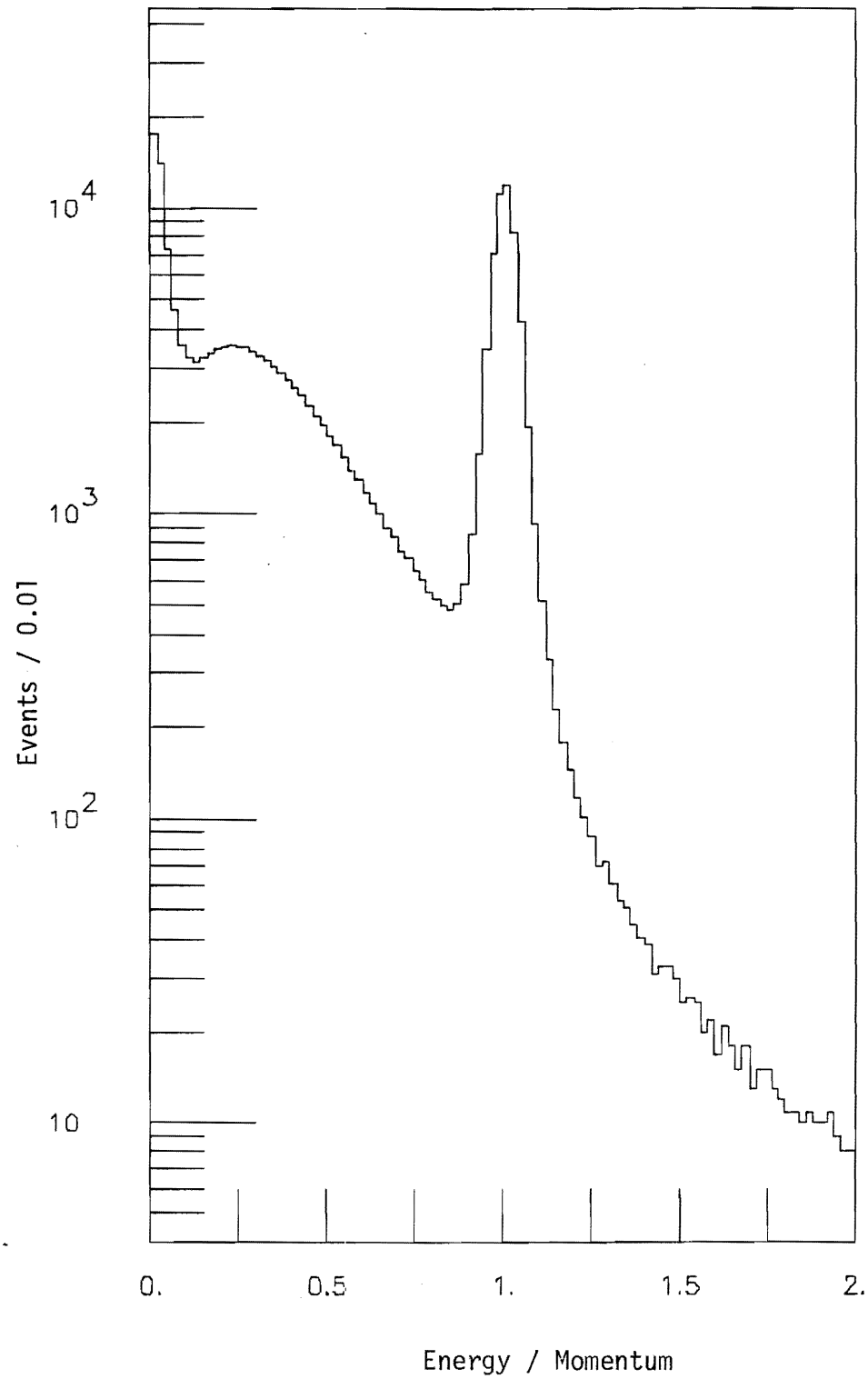
10^4
10^3
10^2
10
Events / 0.01
0.
0.5
1.
1.5
2.
Energy / Momentum

Figure 33. The $m_{P\pi}$ distribution, showing a clear Λ^o peak.

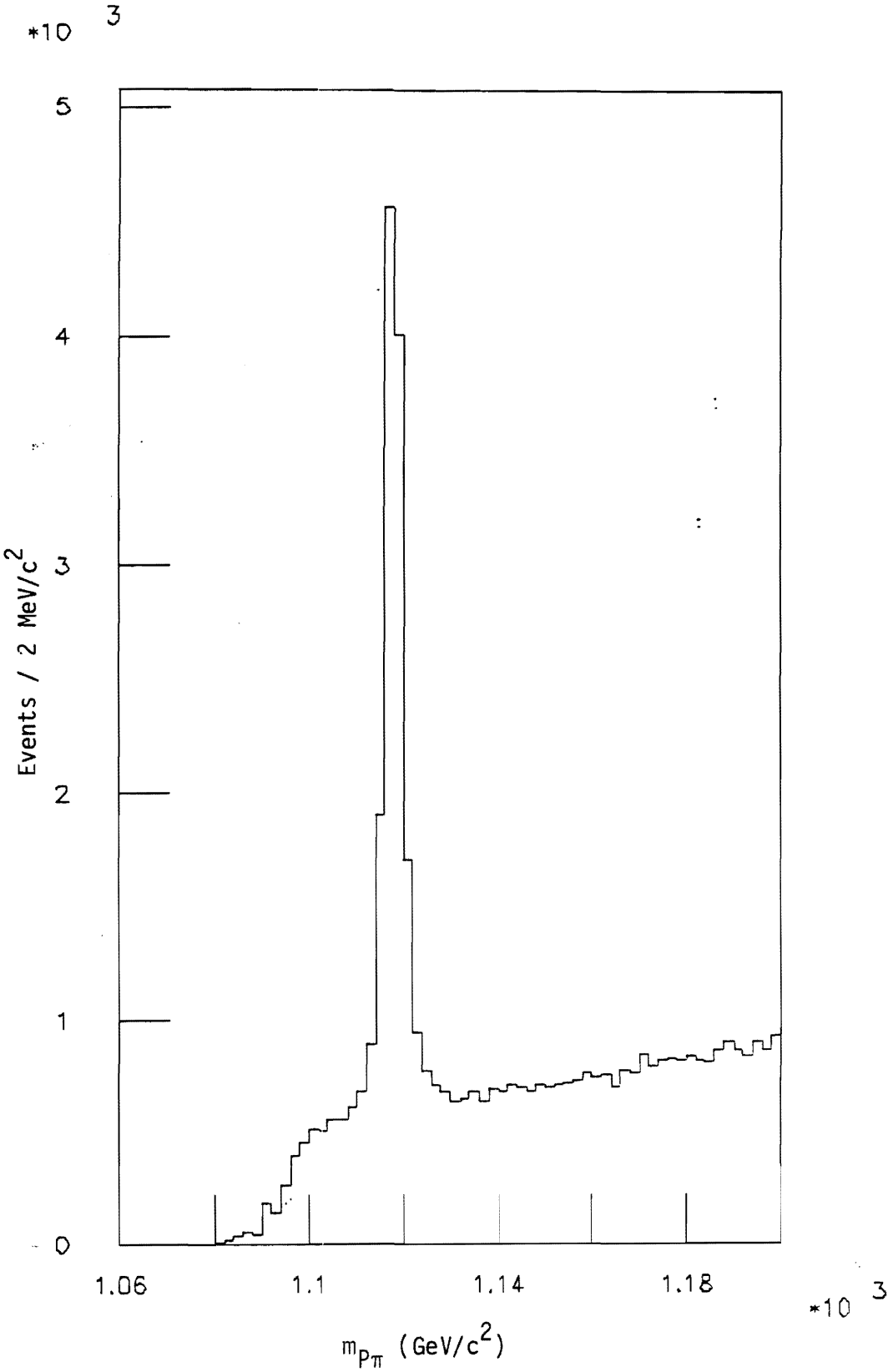
*10 3
5
4
3
2
1
0
Events / 2 MeV/c2
1.06
1.1
1.14
1.18
*10 3
mPπ (GeV/c2)

Figure 34. The vacuum $K\pi 2$ sample for 30 GeV/c $< p_K <$ 40 GeV/c.

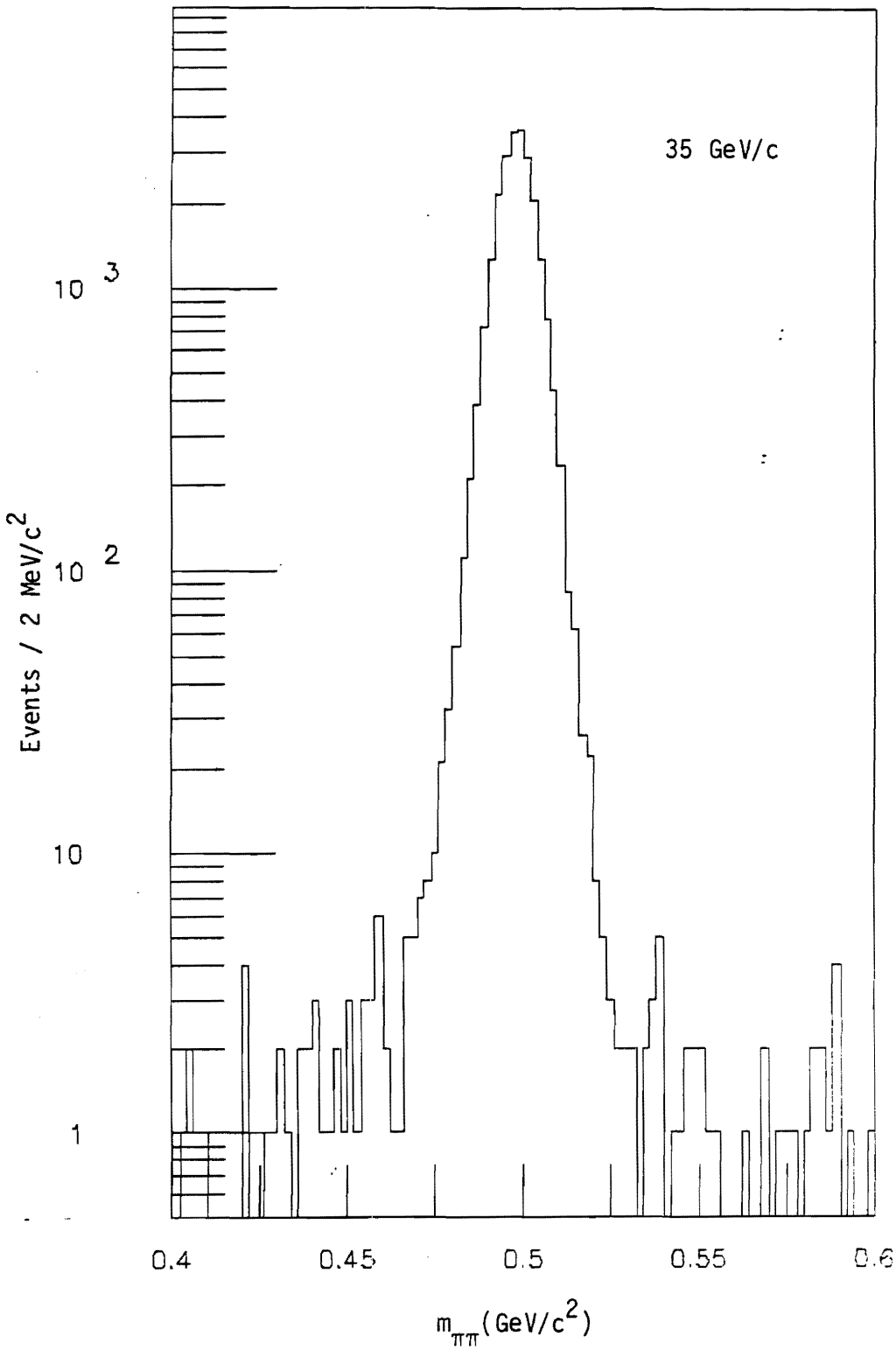
35 GeV/c
Events / 2 MeV/c^2
10^3
10^2
10
1
0.4
0.45
0.5
0.55
0.6
$m_{\pi\pi}$(GeV/c^2)

Figure 35. The distribution shown in Figure 34 for $50 < p_K < 60$ GeV/c.

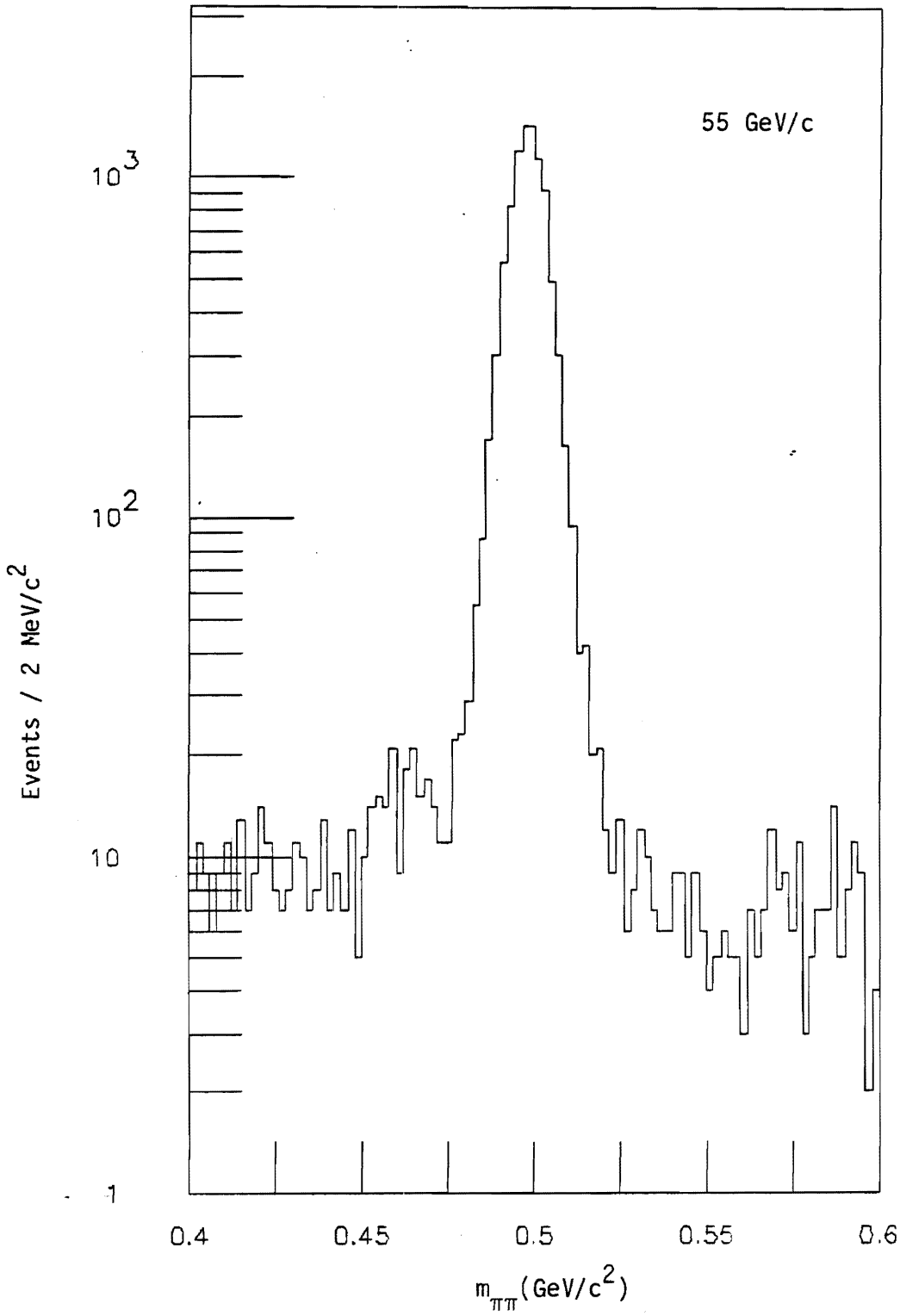
55 GeV/c
10^3
10^2
10
1
Events / 2 MeV/c^2
0.4
0.45
0.5
0.55
0.6
$m_{\pi\pi}$(GeV/c^2)

backgrounds were identified and their characteristics measured; then we discuss the fits and results.

In identifying the semileptonic backgrounds we first demanded the reconstructed z-vertex be from $407.5 < z < 418.5$ meters from the target. This vertex requirement cut away from the edges of the decay region; recall from Figure 28 that there is a significant contribution from neutron interactions at 406 and 420 meters.

The $K\mu 3$ sample was isolated by demanding that a muon counter fired. To eliminate $Ke3$ decays in which a pion had 'punched-through' the muon filter, we cut demanding neither track had $E/p > 0.8$.

Having guaranteed that one of the particles was a muon we now required the other to be a pion. We identify the muon track in the glass by requiring that one track deposit less than 1 GeV of energy (recall that a muon deposits 2/3 GeV). We search for a showering pion by requiring the other track to deposit more than 2 GeV (recall that E/p must be less than 0.8). This completed the identification of $K\mu 3$ events.

The $Ke3$ sample required that the no muon counter fired for the event. We required one track have $0.9 < E/p < 1.1$ to identify the electron. We placed the same requirements as in the $K\mu 3$ case on the other track to ensure it belonged to a pion.

We have now identified samples of the $K\mu 3$ and $Ke3$ backgrounds. The next step in the background subtraction was to prepare tables in $M_{\pi\pi}$ and q^2 for each

sample in several momentum bins (recall from Chapter II that the experiment will be analyzed in bins of momentum; the data will ultimately be analyzed in these same bins). The $K\mu 3$ and $Ke3$ distributions summed over all momenta appear in Figures 36 and 37.

D. Isolation of the Signal; Background Subtractions

We have used these tables to measure the variation of the $K\mu 3$ and $Ke3$ backgrounds with mass and q^2; we shall determine the scale of the subtraction from the $K\pi 2$ sample itself. The first step is to define the mass and q^2 region that contains the signal. Figure 38 shows a $M_{\pi\pi}$ vs. q^2 plot for the vacuum beam data. We cut in mass from 480 to 520 Mev/c ^{2} and at 300 (Mev/c) ^{2} preserving approximately 90% of the signal.

We must next determine the normalization of the background. We fit the $K\pi 2$ sample from 400 to 460 Mev/c ^{2} and from 540 to 600 MeV/c ^{2} in mass, thus excluding the region of the mass peak, and summed each mass bin over the range from 0 to 10000 (MeV/c) ^{2} in q^2. We made the same cuts in the $K\mu 3$ and $Ke3$ samples. We then determine the scale of the background by minimizing the following χ^2 in each bin of momentum (we suppress the momentum dependence):

$$\chi^2 = \sum_m \frac{(K\pi 2(m) - \alpha K\mu 3(m) - \beta Ke3(m))^2}{\sigma^2(m)} \tag{6.2}$$

where $K\pi 2(m)$ is the mass distribution for the $K\pi 2$ sample, and similarly for $K\mu 3(m)$ and $Ke3(m)$; $\sigma(m)$ is the statistical error in each bin of the $K\pi 2(m)$ table. Hence the dependence of the backgrounds in mass and q^2 are fixed but the

Figure 36. The $m_{\pi\pi}$ vs. q^2 distribution for the identified $K\mu 3$ sample.

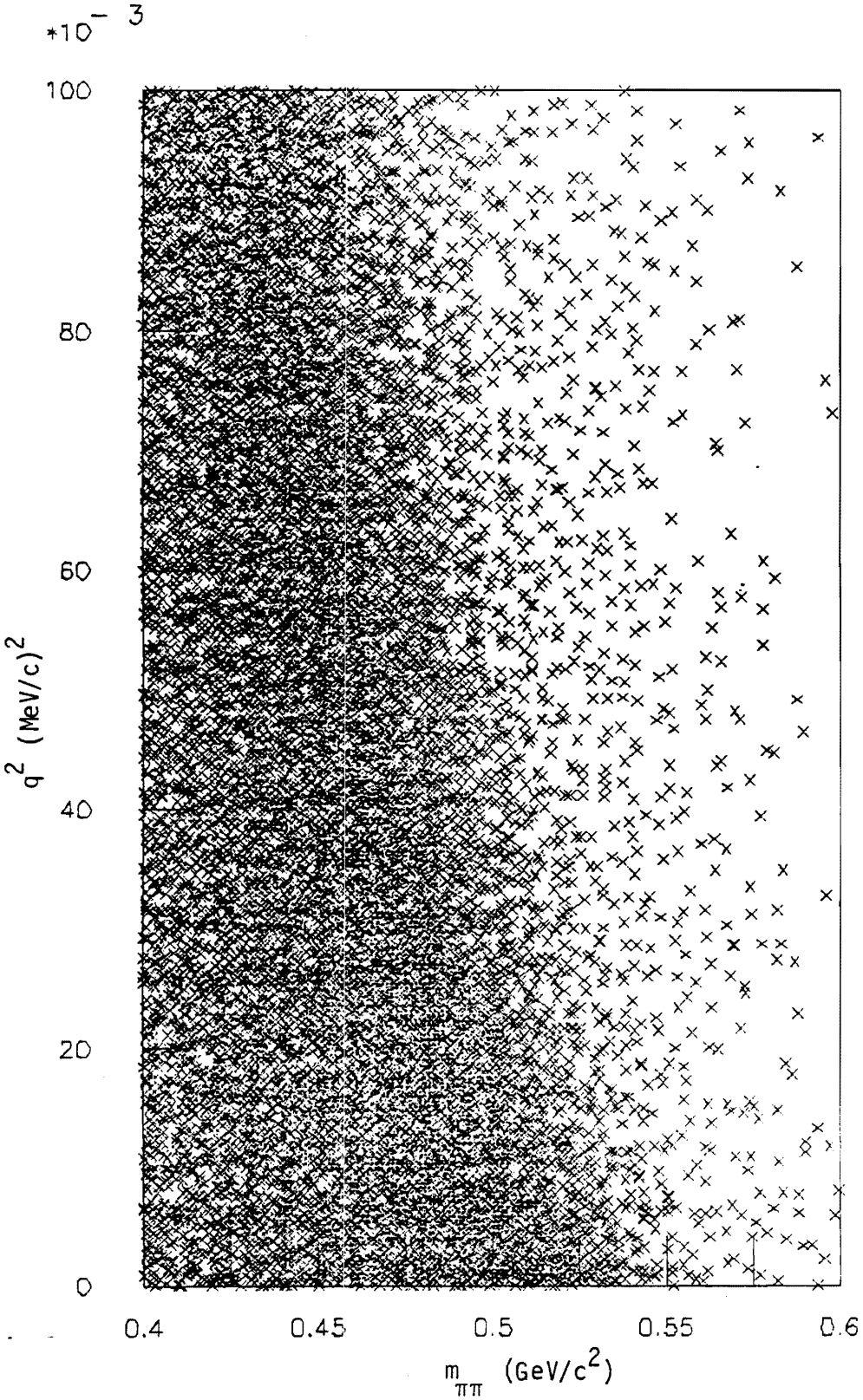
*10^-3
100
80
60
40
20
0
q^2 (MeV/c)^2
0.4
0.45
0.5
0.55
0.6
m_ππ (GeV/c^2)

Figure 37. The $m_{\pi\pi}$ vs. q^2 distribution for the identified $Ke3$ sample.

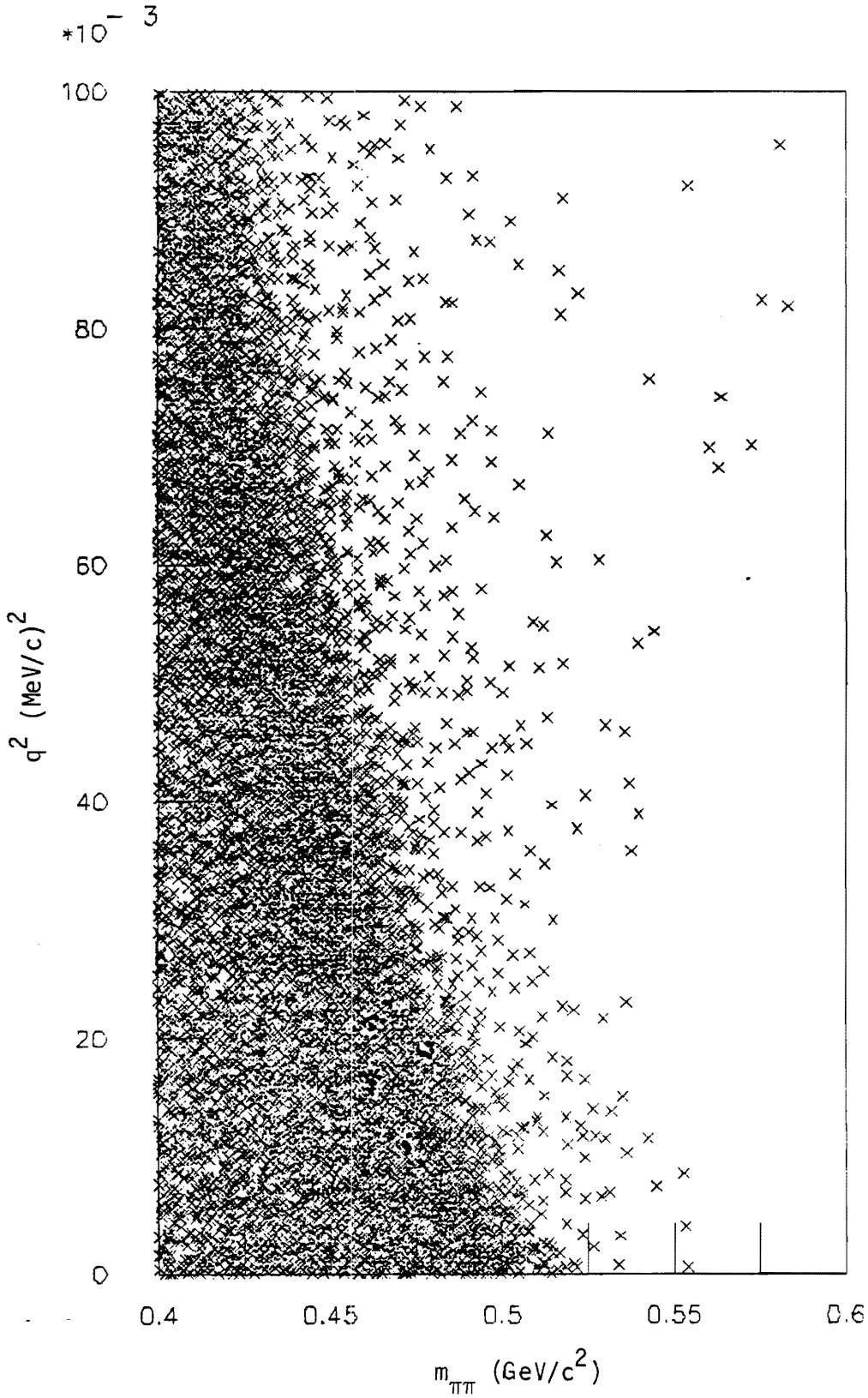
*10^-3
100
80
60
40
20
0
q^2 (MeV/c)^2
0.4
0.45
0.5
0.55
0.6
m_ππ (GeV/c^2)

Figure 38. The $m_{\pi\pi}$ vs. q^2 distribution for the vacuum $K\pi 2$ sample.

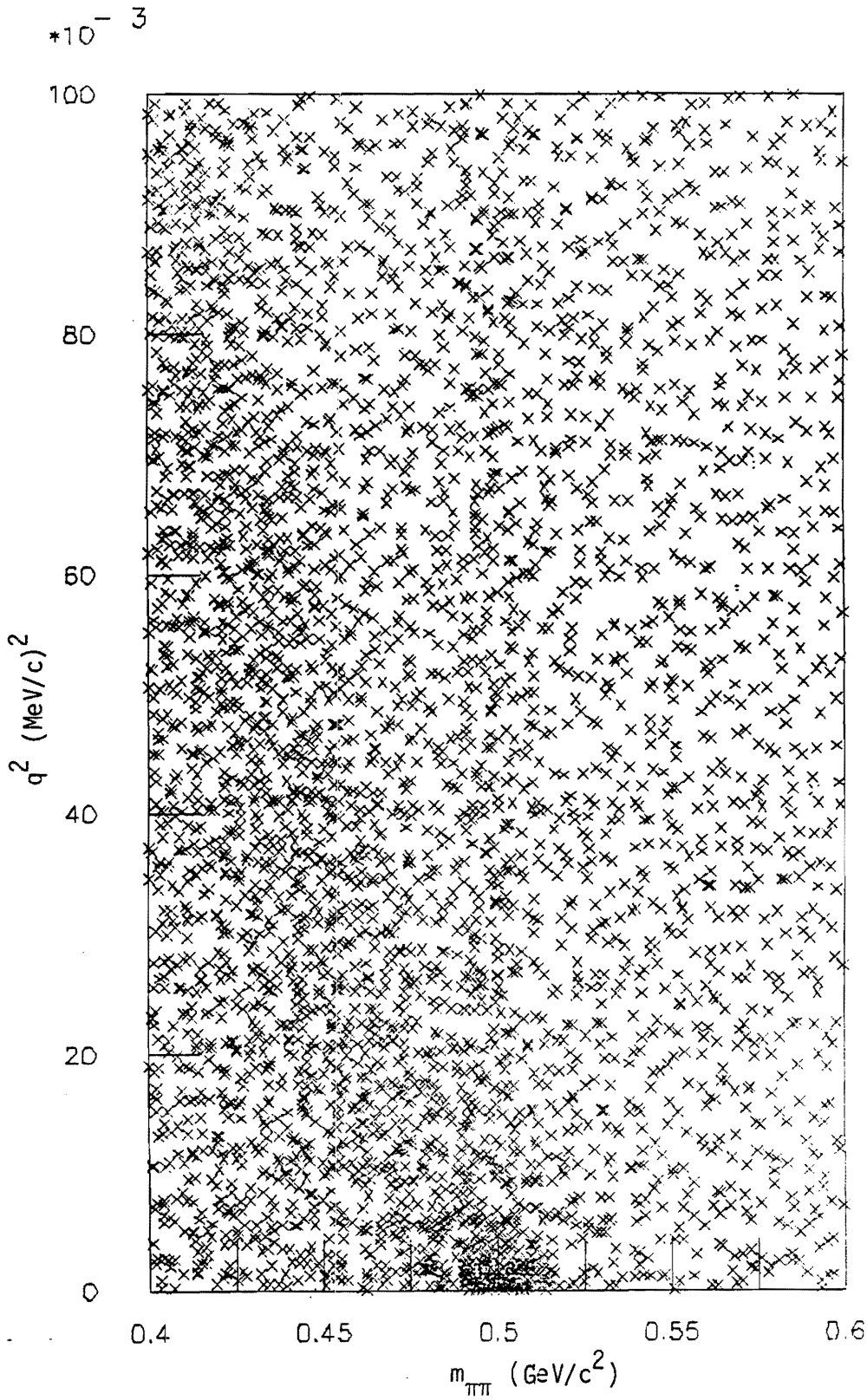
*10^-3
100
80
60
40
20
0
q^2 (MeV/c)^2
0.4
0.45
0.5
0.55
0.6
m_ππ (GeV/c^2)

overall size of the backgrounds was varied. The shape of the two backgrounds summed over all momenta appear in Figures 39 and 40.

The magnitude and shape of the backgrounds have now been determined; the samples were cut at 300 (MeV/c) ^{2} in q^2 and the backgrounds were subtracted bin-by-bin in mass.

Neutron interactions were not treated by this method because was no comparably clean way of isolating them. We fit the mass distribution after the $K\mu3$ and $Ke3$ subtractions had been performed to the form $(\alpha + \beta m + \gamma m^2)$ over the mass range used above: 400 to 460 MeV/c ^{2} and 540 to 600 MeV/c ^{2}. The quadratic was interpolated under the mass peak to perform the subtraction.

Figure 41 shows the final fit to the $K\pi2$ mass spectra in each bin of momentum summed over the three sources of background. Table 4 gives the number of $K\pi2$ events in the vacuum beam before and after the subtraction along with the contribution of each source of background. The agreement, as shown in the Figure, is excellent. The quality of the fits indicate the backgrounds are understood.

E. Incoherent K_S Background Subtractions

We have discussed the subtraction of backgrounds induced by sources other than $K\pi2$ decays. Since we are measuring the rate of K_L decays relative to coherent K_S decays we must subtract the incoherent background discussed in Chapter I. There is also a small contamination of inelastically produced K_S in the vacuum beam; interaction of neutrons in the counters or windows can produce K_S

TABLE 4

NUMBER OF $K_L \to \pi^+\pi^-$

p_K	Raw	Background	Background Subtracted	Final
35	1029	50.6	978.4	974.5 ±32.8
45	1795	57.9	1737.1	1730.2±43.0
55	2116	48.7	2067.3	2059.0±46.5
65	1927	50.6	1876.4	1869.0±44.5
75	1596	41.6	1554.4	1548.2±40.5
85	1170	40.8	1129.2	1124.7±34.8
95	723	17.3	705.7	702.9±27.2
105	429	7.40	421.6	419.9±20.9
115	220	10.0	210.0	209.2±15.2
Σ	11005	324.9	10680.1	10637.6

Figure 39. The mass distribution for the identified $K\mu 3$ sample for $q^2 < 300$ $(\mathrm{MeV/c})^2$.

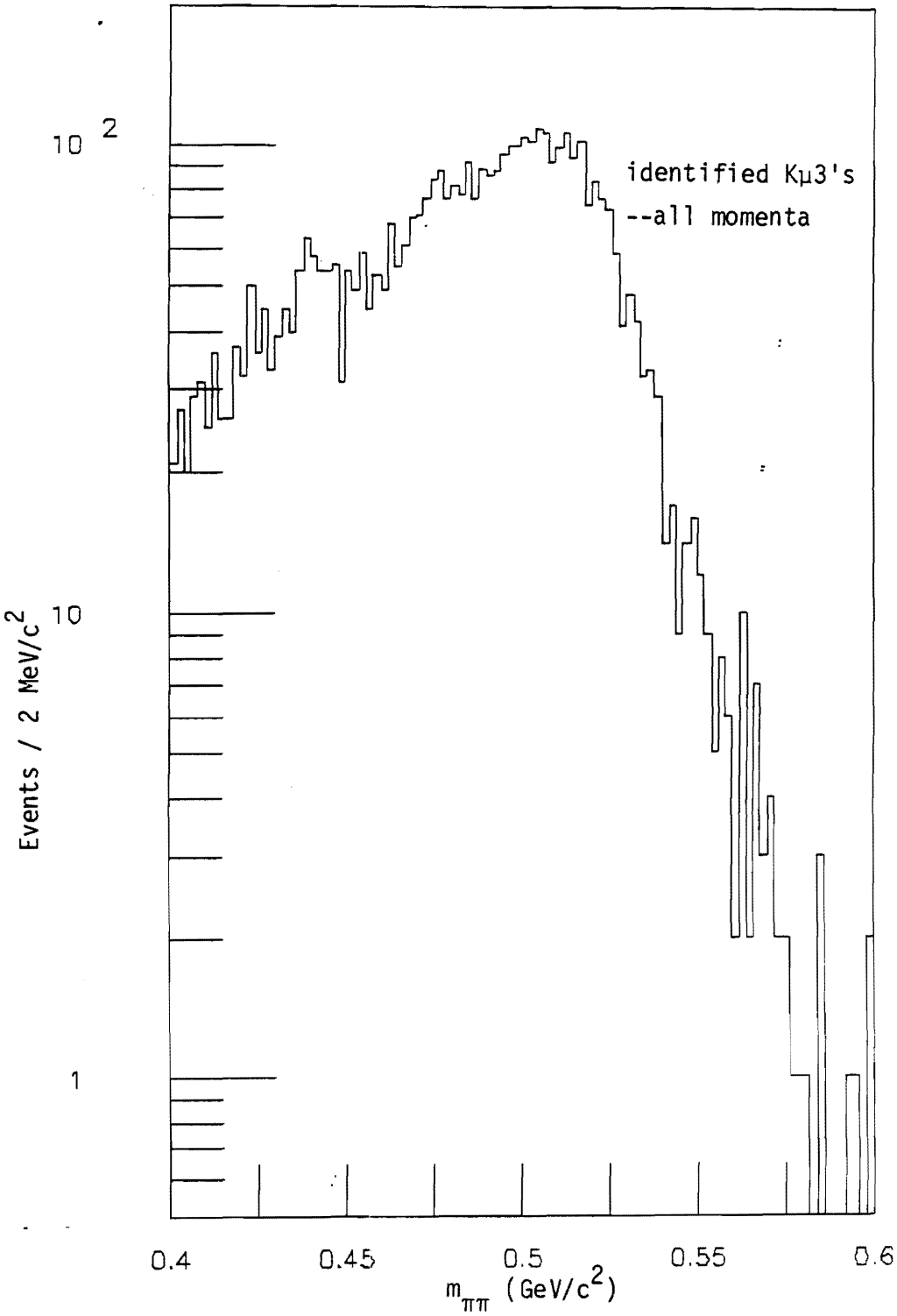
identified Kμ3's
--all momenta
Events / 2 MeV/c^2
10^2
10
1
0.4
0.45
0.5
0.55
0.6
$m_{\pi\pi}$ (GeV/c^2)

Figure 40. The distribution of Figure 39 for the identified *Ke*3 sample.

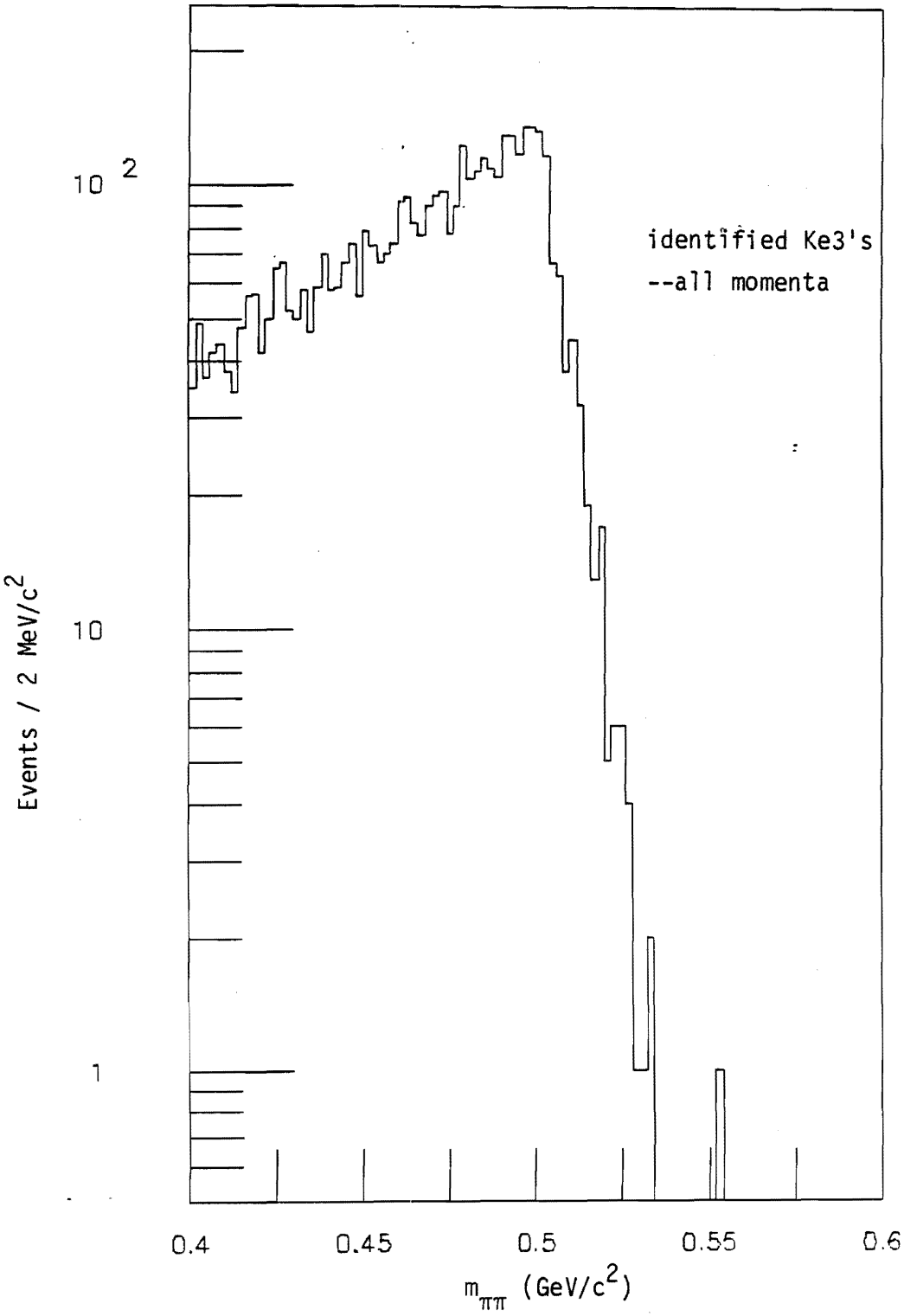
identified Ke3's
--all momenta
Events / 2 MeV/c^2
10^2
10
1
0.4
0.45
0.5
0.55
0.6
$m_{\pi\pi}$ (GeV/c^2)

Figure 41. The mass distribution for the vacuum $K\pi 2$ sample summed over momentum. The fit to the background, discussed in the text, is shown by the dots.

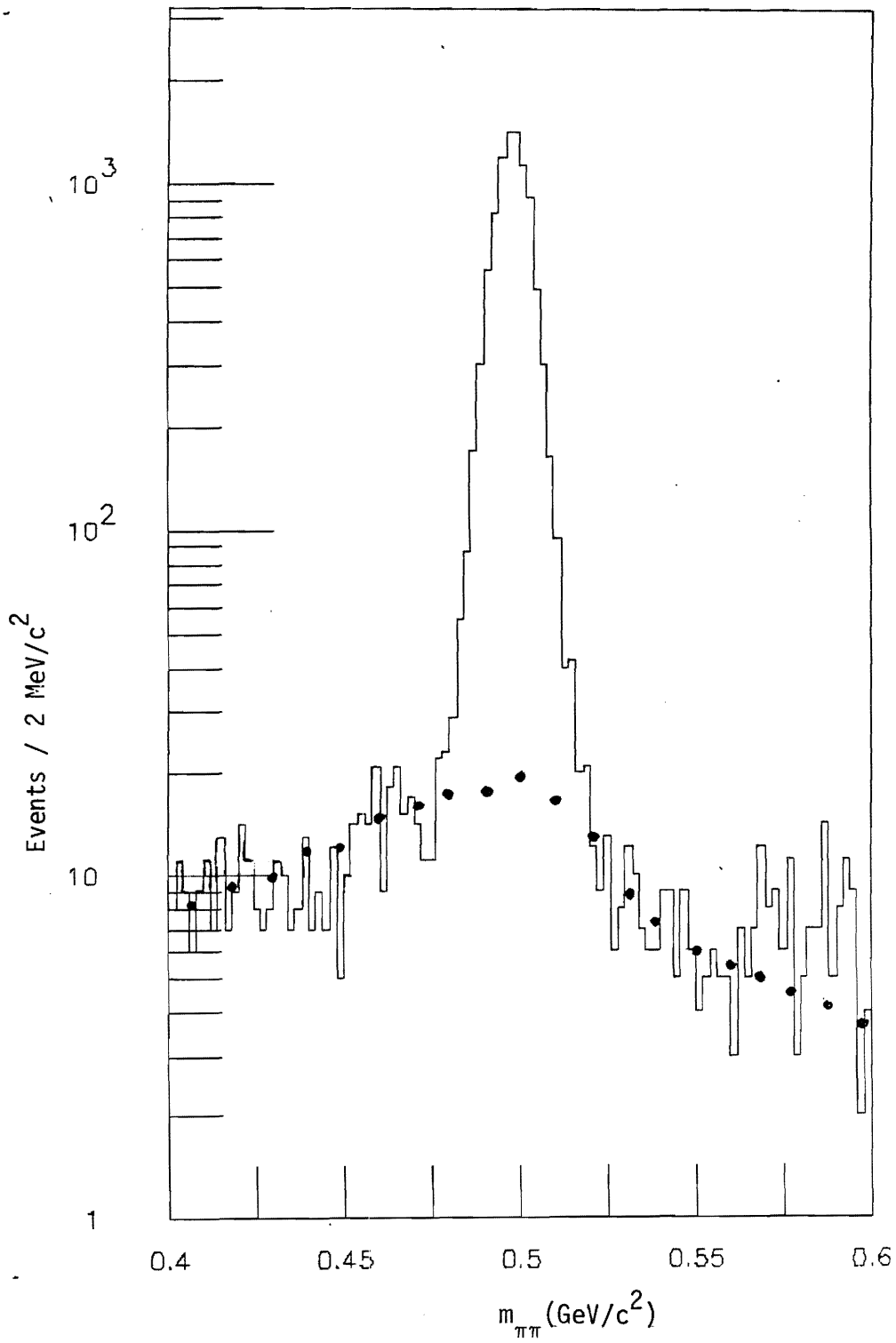
Events / 2 MeV/c^2
10^3
10^2
10
1
0.4
0.45
0.5
0.55
0.6
$m_{\pi\pi}$(GeV/c^2)

Figure 42. The $m_{\pi\pi}$ vs. q^2 distribution for the regenerated $K\pi 2$ sample.

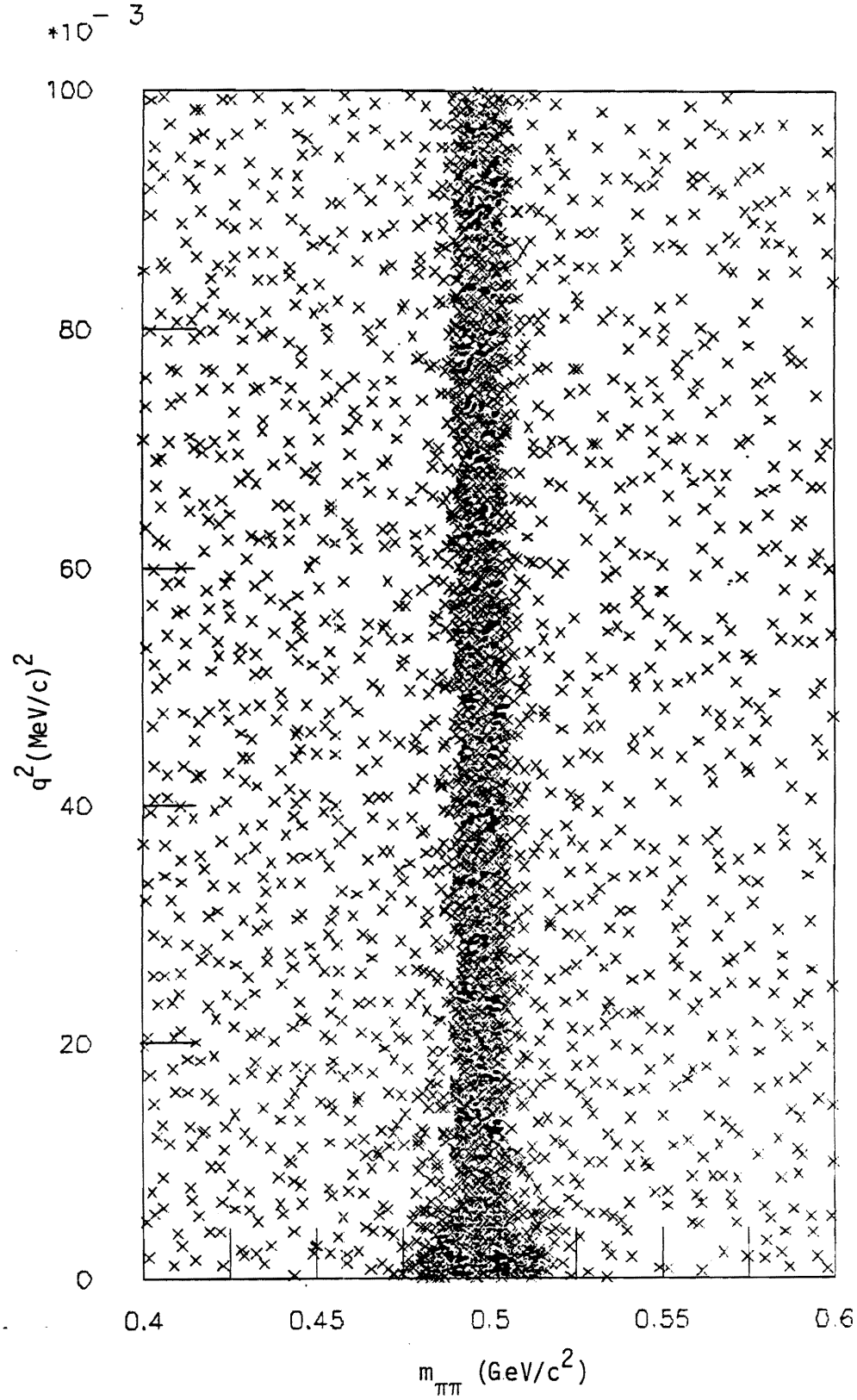
*10^-3
100
80
60
40
20
0
q^2(MeV/c)^2
0.4
0.45
0.5
0.55
0.6
m_ππ (GeV/c^2)

which then decay; the extrapolation to z_{RA} correctly assigns these decays to the vacuum beam.

The background subtraction procedure described in Section D was repeated in 300 (MeV/c) ^{2} bins of q^2 out to 10^4 (MeV/c) ^{2} for both the vacuum and regenerated beams. We show in Figure 42 the $M_{\pi\pi}$ vs. q^2 distribution for regenerated beam events over all momenta. In Figure 43 we show for each momentum bin the number of signal events from $480 < M_{\pi\pi} < 520$ in each bin of q^2, along with an exponential fit determined between 2000 and 10000 (MeV/c) ^{2}. No acceptance corrections have been made. Figure 44 shows the extremely clean K_S mass peaks; a small background subtraction performed identically to the vacuum data is made. The results in the various momentum bins are given in Table 5, corrected for the inelastic contamination at small q^2. The final numbers of K_S along with the statistical error and the size and error of the subtractions are quoted. The error on the q^2 subtraction is the statistical error on the subtraction combined with the error from extrapolating the fit to $q^2 = 0$.

A similar fit was performed in the vacuum beam; the subtraction is much smaller and consistent with a momentum independent subtraction of 0.4%. The final numbers of $K_L \rightarrow \pi^+\pi^-$ events, along with the statistical and fit errors, are quoted in Table 4.

TABLE 5

NUMBER OF $K_S \to \pi^+\pi^-$

p_K	Raw	After $K\mu 3$, $Ke3$ subt.	Inelastic Sub.	Final
35	1348	1343.8	25.7±3.6	1318.±36.8
45	3518	3511.1	72.7±5.4	3439.±59.5
55	4671	4664.7	83.6±5.6	4581.±68.5
65	5078	5070.1	76.8±5.2	4994.±71.4
75	4270	4264.2	70.9±5.0	4193.±65.5
85	3390	3383.9	52.7±4.6	3331.±58.4
95	2037	2034.9	34.7±3.6	1999.±45.3
105	1221	1216.7	23.3±3.5	1204.±35.0
115	702	700.8	9.0±1.9	692.±26.5
Σ	26235	26190.2	439.2	25751.

Figure 43. The q^2 distribution of the regenerated $K\pi 2$ sample in each bin of momentum. An exponential fit to the inelastic contribution is indicated.

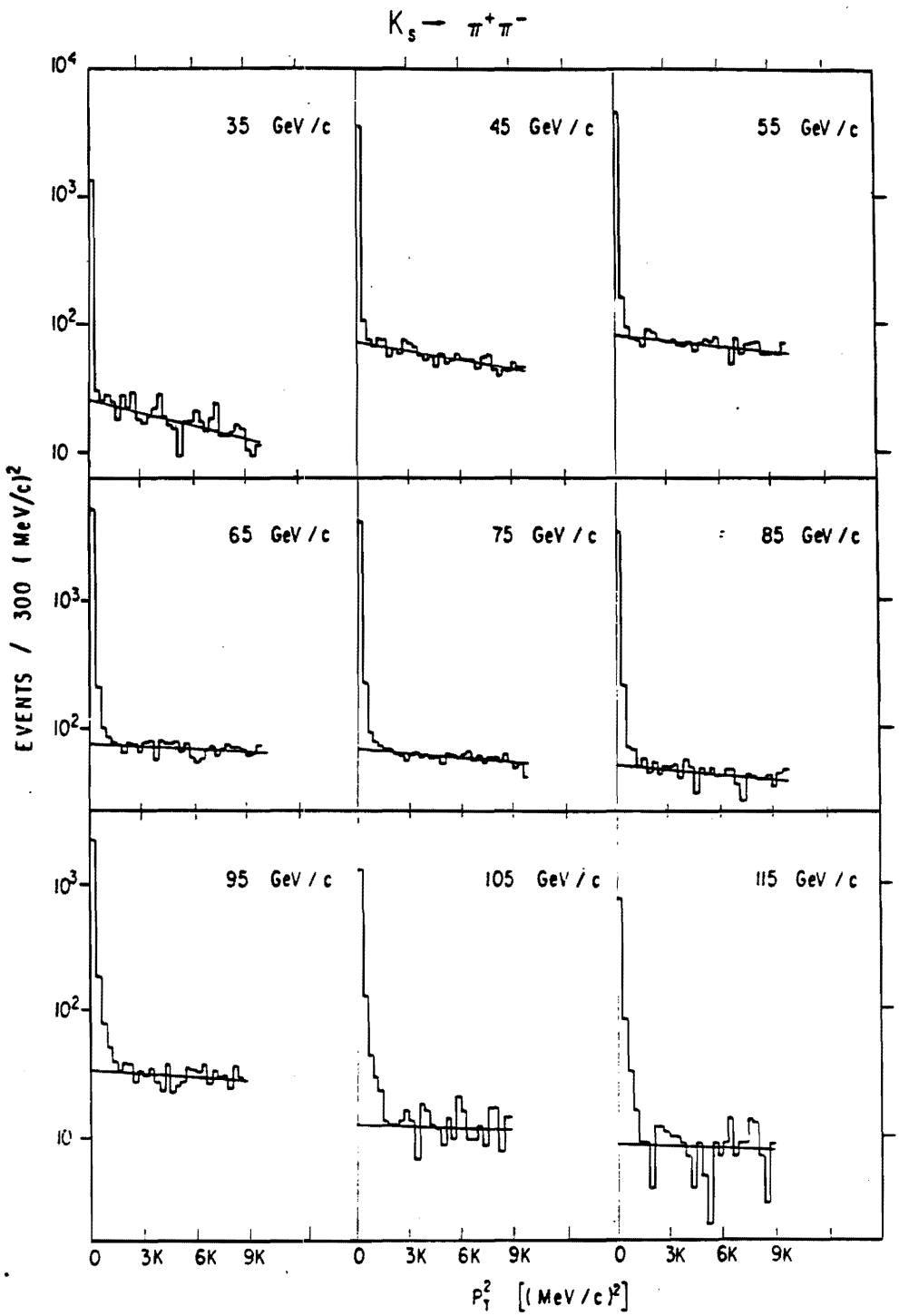
$K_s \to \pi^+\pi^-$
35 GeV/c
45 GeV/c
55 GeV/c
65 GeV/c
75 GeV/c
85 GeV/c
95 GeV/c
105 GeV/c
115 GeV/c
EVENTS / 300 (MeV/c)^2
10^4
10^3
10^2
10
0
3K
6K
9K
P_T^2 [(MeV/c)^2]

Figure 44. The mass distribution of the regenerated $K\pi 2$ sample in each bin of momentum.

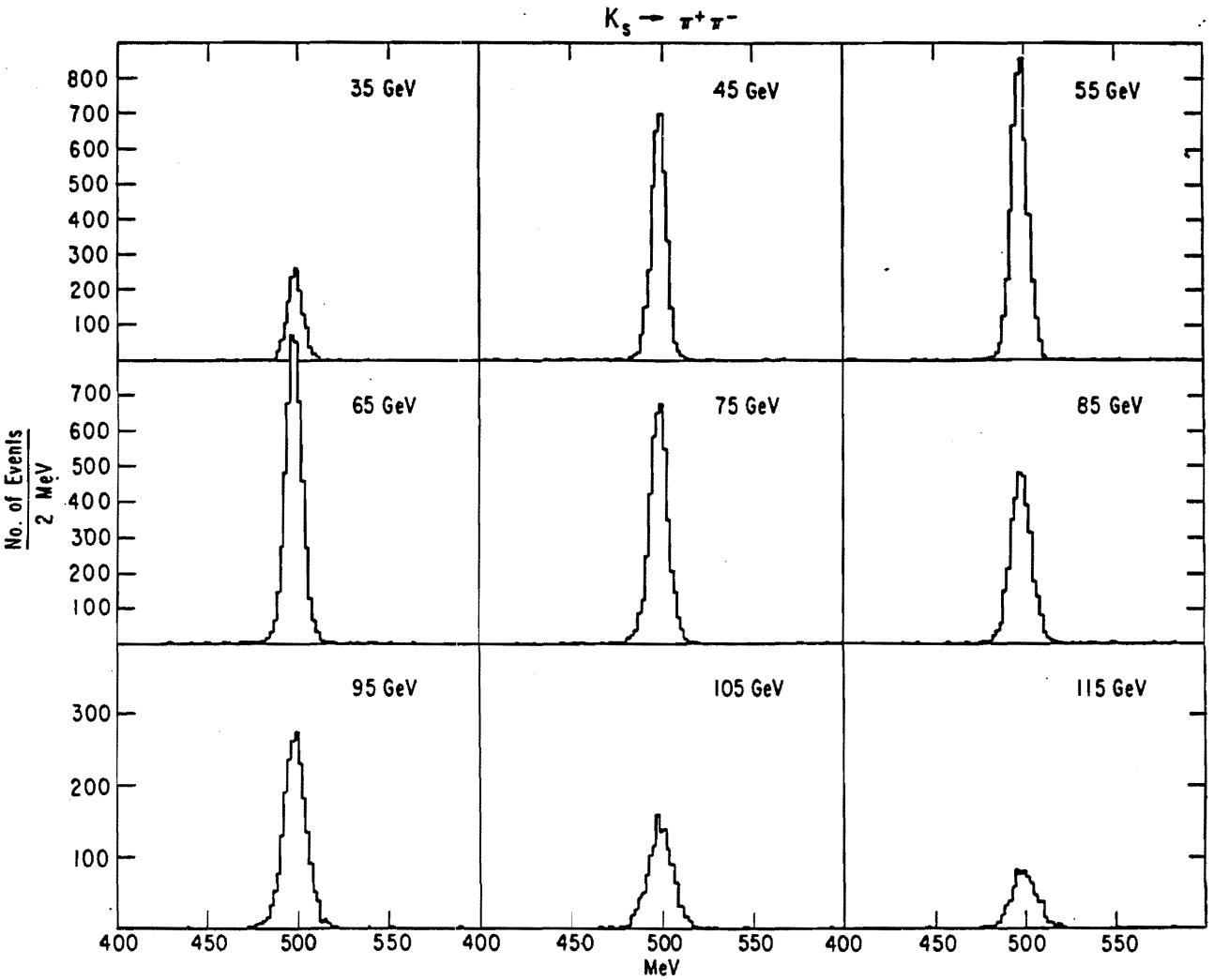
$K_s \rightarrow \pi^+\pi^-$
35 GeV
45 GeV
55 GeV
65 GeV
75 GeV
85 GeV
95 GeV
105 GeV
115 GeV
No. of Events / 2 MeV
MeV
400
450
500
550
100
200
300
400
500
600
700
800

CHAPTER VII

NEUTRAL MODE RECONSTRUCTION

AND

BACKGROUND SUBTRACTIONS

The reconstruction of the neutral mode data was the most exacting and complicated portion of the analysis. It required the detailed scrutiny of the signals from the lead glass as well as a subtle algorithm for track reconstruction. The reconstruction of kaon decays from electromagnetic showers involved a subtle algorithm with intricate systematic biases. The backgrounds proved intractable using Monte Carlo techniques and could not be separately measured as in the charged mode.

This Chapter is divided into five parts. In the first we consider the reconstruction of the electron and positron tracks. We then explain how electromagnetic showers are isolated and their energies and locations are determined; the reconstruction of the energy and trajectory of the converted photon will receive special attention. This leads us to our reconstruction algorithm: how the mass, vertex, and q^2 of the event are calculated. Finally we discuss the background subtractions: first the backgrounds from sources other than $K \rightarrow 2\pi^o$ decay and then

the inelastic contaminations.

A. Track Reconstruction

The alignment and calibration of the chambers was discussed in Chapter VI. In this Chapter we concentrate on the neutral mode reconstruction algorithm. Recall that in the charged mode we cut tracks which were closer than 2 cm. to each other; in the neutral mode most of the events would be cut by this criterion. The electron-positron pair formed at the converter, initially separated by multiple scattering, is only separated by a few centimeters or less at the spectrometer; the dead time then causes hits to be lost. The result is that in the side (non-bend) view we often see only a swath of hits consisting of hits from both tracks, and in the top view the tracks are similarly fused until they are bent apart by the magnet. The reconstruction algorithm must successfully pick the best tracks out of this confusion. We illustrate in Figure 45 two close tracks passing through the y-view of the spectrometer; there is a strong tendency to lose half the hits because each of the offset planes sees the hits for one of the track and is dead when the signal from the other track arrives.

How can we reconstruct two tracks when the tracks are close? We first followed the method of the charged mode by fitting all possible combinations of hits to 'segments' in the front and back halves of the spectrometer and demanding that the segments meet within some tolerance at the magnet center to qualify as a track. We fitted the candidate tracks and projected them back to the conversion hodoscope. In the absence of multiple scattering and with perfect chamber

Figure 45. Two close tracks passing through the spectrometer. In the upper drawing, the two tracks pass within the same cell; sense wires close to one of the tracks see the hits from that track and are dead when the hits from the further track arrive. In the lower drawing, the tracks are in different cells and are 1 cm. apart; track 1 is slightly closer to the middle plane of sense wires than is track 2 and hence the center plane is dead when the hits from track 2 arrive.

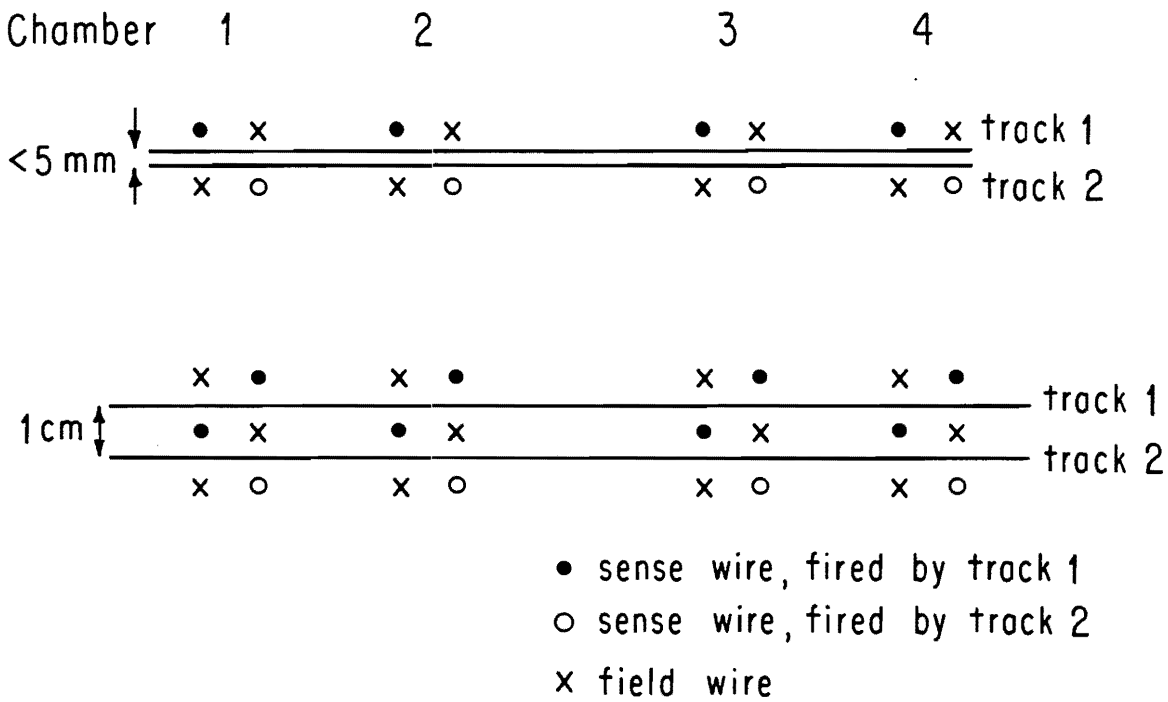
Chamber 1 2 3 4
<5 mm
track 1
track 2
1 cm
track 1
track 2
• sense wire, fired by track 1
o sense wire, fired by track 2
x field wire

resolution, the true track will project to within the counter; hence the distance from the counter center to the projected location should be under half a counter. Ideally, one could demand that the reconstructed tracks point to within this distance. Scattering and the finite chamber resolution makes this too stringent a test for candidate tracks. We found from Monte Carlo studies of the reconstruction algorithm that our effective 'resolution' was about 2.5 cm.; a track projecting outside this distance was probably spurious but we could not use the distance from the counter to distinguish among tracks closer than this distance. The tracks were hence grouped into two categories: those projecting outside a fixed distance (or 'road') of 2.5 cm. from the center of the struck counter and those projecting within this distance.

The tracks projecting farther out than this distance were sorted to find the two closest to the counter center. If there were no tracks within the road, the two tracks closest to the counter center were chosen; if there were closer tracks, any track projecting within the road was chosen over any track projecting outside the cut. The tracks projecting within the cut were sorted again; the two tracks with most hits were chosen. In case of a tie, a third criterion was employed: the RMS deviation of the hits from the fitted track was computed and the track with the better fit was picked.

(With the above algorithm it was possible that the tracks were 'copies' of each other; perhaps seven of eight possible hits were identical for two tracks and the eighth was a hit and its mirror image on the other side of a wire. We avoided

this problem in the x-view by requiring that the tracks bend in opposite directions and in the y-view by forcing the two final tracks to fire separate wires in the most downstream chamber.)

The algorithm was allowed to find only one track in the side view and the final top view tracks could share a common segment in the front half of the spectrometer. A hand-scan of nearly three hundred events by two physicists was used to check the final algorithm.

B. Cluster Finding; Energy and Position Determinations

1. Cluster Finding; Energy of a Cluster

'Cluster-finding' means isolating electromagnetic showers in the lead glass. We wish to both identify the impact point of the shower and measure its energy. The method was simple; it searched for local maxima of energy on a block-by-block basis, where the maximum block had to contain at least 300 MeV of energy. The algorithm then associated each block with the adjacent block containing the most energy, stopping at the local maximum. All of these blocks constituted a 'cluster'. The cluster energy was the sum of the energies of the individual blocks, corrected for 'missing blocks' as explained in Chapter IV. A cluster typically had more than 90% of its energy contained in a 3×3 set of blocks centered on the shower axis. Low energy clusters of a few GeV or less often only had three blocks read out; it was not unusual for clusters of 15 GeV or more to have more than

Figure 46. Energy mismeasurement in 'fused' clusters. A 3×3 set of blocks for two clusters is shown in the upper drawing; the number in each block represents the number of counts above pedestal. In the lower drawing, the clusters have overlapped; their centers are in the centers of the second and fourth row. The third row shares energy from both clusters, which the algorithm assigns to the more energetic shower.

True Distribution

1	5	3
5	100	20
10	50	10

True Energy, Shower I

194 cts ~ 3.2 GeV

5	25	15
25	500	100
50	250	50

True Energy, Shower II

970 cts ~ 16.2 GeV

Observed Distribution

1	5	3
5	100	20
15	75	25
25	500	100
50	250	50

Measured Energy, Shower I

= 134 cts ~ 2 GeV

Measured Energy, Shower II

= 1090 cts ~ 18.1 GeV

Shower I, Measured Energy / True Energy = 0.63

Shower II, Measured Energy / True Energy = 1.12

twenty blocks with a measurable energy deposit.

The algorithm did not work well if two clusters overlapped. Figure 46 shows how the energies of two showers can be mismeasured when they start to merge; the higher energy cluster tends to pick up energy at the expense of the lower energy cluster. We shall cut events with 'fused' clusters in the analysis.

2. Position Measurement and Track Correlation

The xy position of an electromagnetic shower in the glass can be determined from the sharing of energy among the blocks in a cluster. We examined the sharing among a 3×3 set of blocks centered on the central block of a shower. The algorithm first determines which of the two columns not containing the central block has the greater energy; define this energy to be A_2 (the explanation is for the x-view; for the y-view, the method works with rows instead of columns). Next we divide this energy by the energy contained in the central column (A_1). The ratio A_2 / A_1 was measured for many showers; if we assume the distribution of impact point is uniform over the face of a block, we may integrate the distribution of A_2 / A_1 to obtain the impact point as a function of this ratio. The result of the analysis is shown in Figure 47, which plots the difference between the reconstructed position and the extrapolated impact point in the glass as determined from the chambers for electrons. The width σ as determined from the FWHM is under 4 mm.

The position and orientation of the glass relative to the drift chambers were then determined using tracks from the converted pairs. Define δx and δy as the signed differences between the reconstructed glass position and the extrapolated chamber determination for the two views. Then a plot of δx vs. x_{glass} or δy vs. y_{glass} will be a straight line with a slope given respectively by the pitch or yaw of the glass; a plot of δx vs. y or δy vs. x gives the roll. The pitch, yaw, and roll of the glass were all negligible. The overall transverse position of the array was determined from the means of the δx and δy distributions. The determination of the glass position in z was more subtle. The reconstructed x and y positions of showers in the glass do not correspond to the entry point at the front edge; rather they correspond to a point within the glass which is a function of the shower development. Again using electrons, we plotted δx vs. θ_x, where θ_x is the x-view slope of the track after the magnet. This plot revealed a straight line with a slope equal to the distance from the magnet to the 'best-z' in the glass, because:

$$x_{glass} = x_{magnet} + \theta_x(z_{best} - z_{magnet}) \tag{7.1}$$
$$x_{chamber} = x_{magnet} + \theta_x(z_{glass} - z_{magnet})$$
$$x_{glass} - x_{chamber} = \theta_x(z_{glass} - z_{best})$$

where z_{glass} is the physical front edge of the array. A measurement of the slope results in a best-z 15 cm. into the front face of the glass. This plane was used as the z-location of the array throughout the analysis.

We correlated the side view and top view tracks in the chambers using the glass. The different combinations of x and y-view tracks were projected into the glass and the combinations closest to clusters were found. Two tracks were

Figure 47. The position resolution of the lead glass. The position in the glass, extrapolated from the drift chambers for electrons, is compared to the position of the shower measured within the glass.

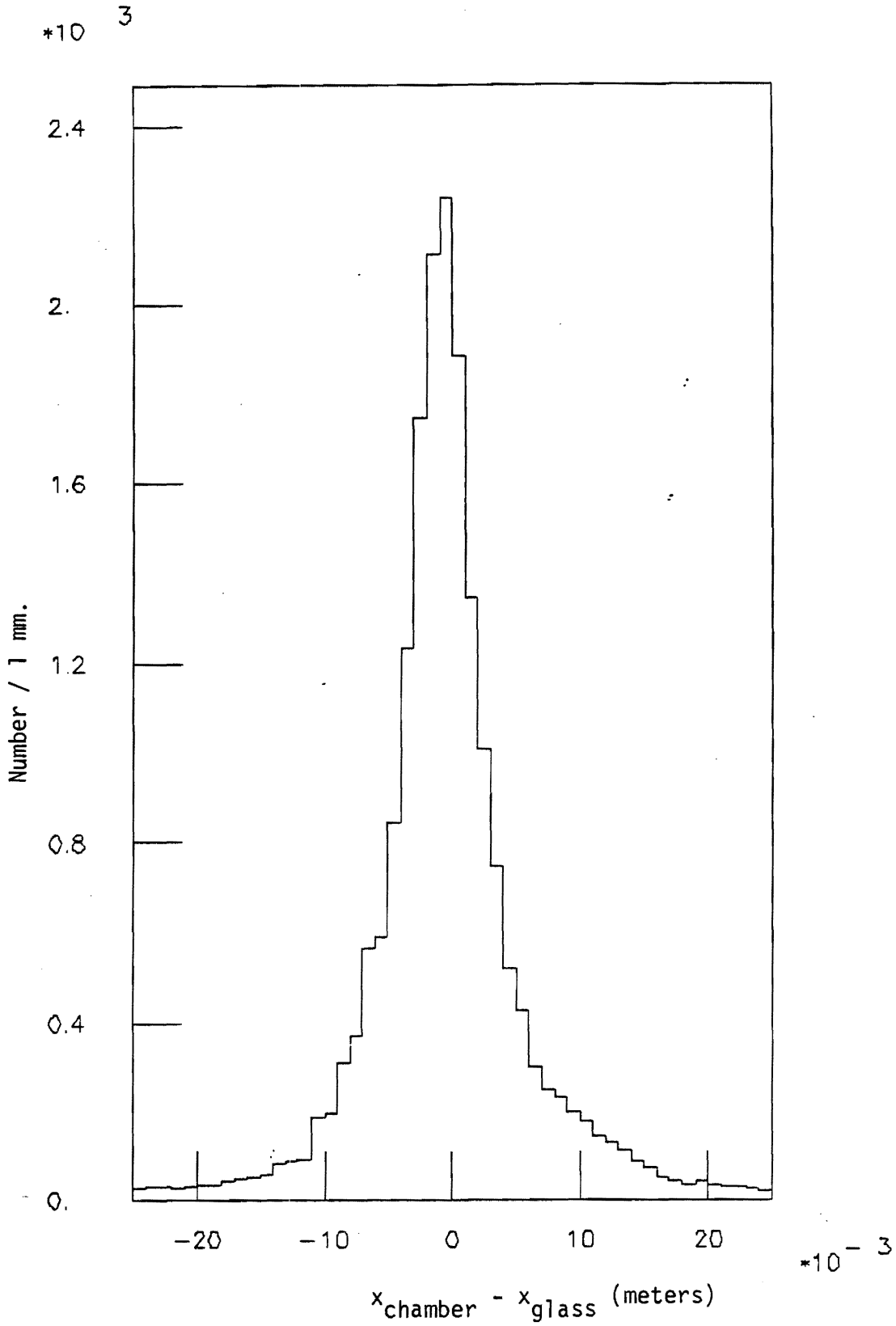
*10 3
2.4
2.
1.6
1.2
0.8
0.4
0.
Number / 1 mm.
-20
-10
0
10
20
*10 - 3
x chamber - x glass (meters)

allowed to share a single cluster since high momentum tracks would often land within a block of each other and were indistinguishable in the glass.

C. Definition of Photons and the Analysis of Bremstrahlung

Clusters which were not associated with tracks, 'neutral' clusters, were assumed to be photons. The electron-positron pair and their bremsstrahlung were combined into a 'pseudo-photon'. We determined the position of the neutral clusters from the above algorithm; we determined the position of the pseudo-photon using the drift chambers. The trajectories as measured in the front half of the spectrometer were extrapolated into the glass; we assigned the position of the pseudo-photon to

$$\vec{X}_\gamma = \frac{\vec{x}_1 {p_1}^2 + \vec{x}_2 {p_2}^2}{{p_1}^2 + {p_2}^2} \tag{7.2}$$

which assumes the positions of the tracks are 'measurements' of the trajectory of the converted photon with errors given by multiple scattering.

We determined the energy of the pseudo-photon by adding the bremsstrahlung energy to the glass-determined energy of the pair. We use the energy in the glass as opposed to the more precisely determined momentum from the chambers in order to include any bremsstrahlung that landed within clusters. We searched for bremsstrahlung separate from the clusters in two ways. First we determined the 1σ error on $\vec{X}_\gamma$ from Gaussian multiple scattering beginning halfway through the lead converter. We searched for any cluster within twice this distance from $\vec{X}_\gamma$; if there was one with an energy less than 60% of the energy of the

pair, we assumed the cluster was a bremsstrahlung. After any clusters were found we searched a 3 $\times$ 3 box around $\vec{X}_\gamma$ and then summed the blocks in a 3$\times$3 box around the most energetic block in the box.

D. Event Reconstruction

As in the charged mode, we must determine the mass and q^2 of an event and determine in which of the two beams the K originated. The problem is significantly more complicated than in the charged mode because we do not have the trajectories of the unconverted photons; we only know their transverse position at the plane of the glass.

We will use equation (4.7) to reconstruct the z-vertex which allows us to calculate the mass; we will use the converted pair to obtain the transverse vertex.

Consider a $K \rightarrow 2\pi^o$ decay. Each π^o decays into two photons and so four photons are detected in the glass (one is actually the pseudo-photon constructed from the electron-positron pair). We wish to know which photons came from which π^oin order to use equation (4.7). There are three possible combinations of the photons: (12) (34), (13) (24), and (14) (23), where (ij) (kl) means photons i and j came from one π^o and photons k and l came from the other. For any of these arrangements we can use equation (4.7) to calculate two z-vertices, z_{ij} and z_{kl}. The principle is illustrated in Figure 48, where we have indicated pairs of z-vertices for each of the three arrangements; only one, the correct pairing, gives a consistent z-determination. We may make this method precise by defining an average z-vertex

Figure 48. Photon pairings and the calculation of the z-vertex in the neutral mode. As explained in the text, there are three possible pairings of photons to make 2 π^0's from the four photons. One of them, the true pairing, provides a consistent z-vertex since the two π^0's originated from a K at this location. The three pairings are indicated; the top two, incorrect, pairings give inconsistent z-determinations. The third, bottom pairing is correct.

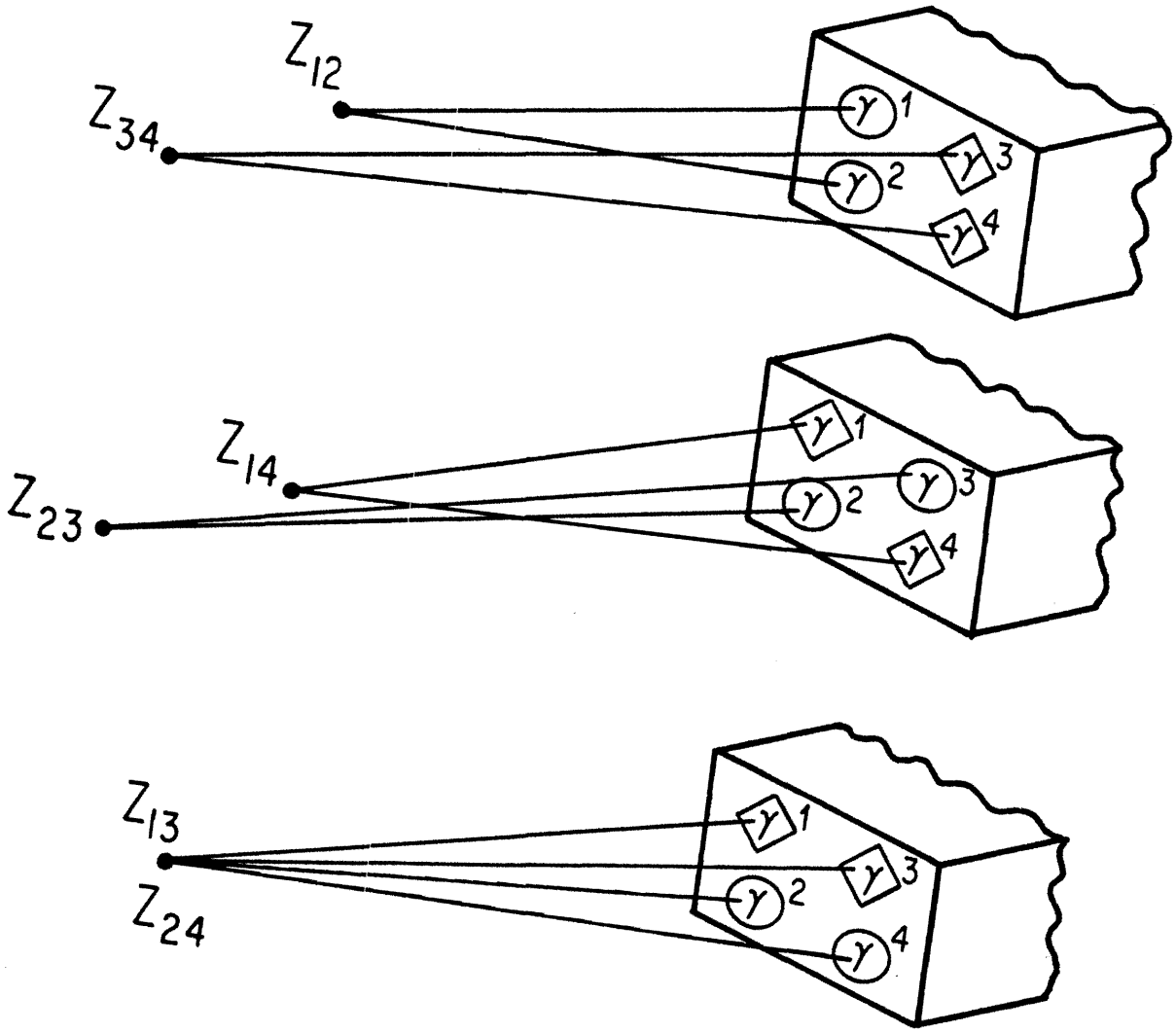

$$Z_{ij} = \frac{\sqrt{E_i E_j r_{ij}^2}}{M_{\pi^0}}$$

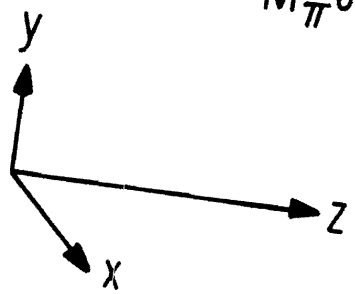

and χ^2 for each pairing:

$$Z_{AV} = \frac{\frac{z_{ij}}{\sigma_{ij}^2} + \frac{z_{kl}}{\sigma_{kl}^2}}{\frac{1}{\sigma_{ij}^2} + \frac{1}{\sigma_{kl}^2}} \tag{7.3}$$

$$\chi^2 = \frac{(Z_{AV} - z_{ij})^2}{\sigma_{ij}^2} + \frac{(Z_{AV} - z_{kl})^2}{\sigma_{kl}^2} \tag{7.4}$$

We choose the pairing with the smallest χ^2 and use Z_{AV} as the z-vertex.

The errors σ_{ij} are given by the position and energy resolution for the photon and pseudo-photon. We assumed an energy resolution of $((6\%/\sqrt{E})^2 + (3\%)^2)^{1/2}$ for both the photons and electrons. The position resolution of the photons was taken to be 4 mm. The position resolution of the pseudo-photon is dominated by multiple scattering of the pair while still in the converter; the scattering produces a large deviation of $\vec{X}_\gamma$ from the unscattered impact point of the converted photon when extrapolated over the 60 meters to the glass. Figure 49 shows the χ^2 distribution for the $K_S \rightarrow \pi^o \pi^o$ sample, compared to the χ^2 distribution for one degree of freedom.

After we have determined Z_{AV} we may calculate the kaon mass from

$$m_K^2 = \sum_{i>j} \frac{E_i E_j r_{ij}^2}{Z_{AV}^2} \tag{7.5}$$

The method can easily be extended to $K_L \rightarrow 3\pi^o$ decays where all six photons (again one pseudo-photon) strike the glass. In this case there are fifteen combinations of six photons but otherwise the algorithm is identical. These $K_L \rightarrow 3\pi^o$ decays are invaluable; we collected about 2×10^5 of them and hence they can be used for

checking any part of the analysis with considerable statistical power.

Figure 50 shows the reconstructed K_L mass for $K_L \rightarrow 3\pi^o$ decays; the FWHM is about 10 MeV/c ^{2}. The z vertex resolution is about 1.8% for both two and three pion decays independent of the z-vertex or q^2. The z-vertex distribution for all $2\pi^o$ events with $\chi^2 < 5$ is shown for the vacuum beam in Figure 51 and for the regenerated beam in Figure 52.

In order to determine the q^2 of an event we must determine the transverse point at the regenerator. In the charged mode we calculated the kaon trajectory using a line determined by the center of momentum of the tracks at the magnet and by the decay vertex. In the neutral mode we will use the center of energy of the kaon as reconstructed in the glass to replace the center of momentum of the tracks. The decay vertex cannot be determined using the distance of closest approach as in the charged mode since all the pairs originate at the converter; instead we use the information from the z-vertex combined with the converted photon's trajectory determined from the pair.

Figure 53 illustrates how the converted pair is used to determine the decay vertex. We take the converted photon trajectory and extrapolate it back to Z_{AV}; this point is the decay vertex. We then use the center of energy of the kaon in the glass and the decay vertex exactly as we used the center of momentum of the tracks and the decay vertex in the charged mode to determine first the position at the regenerator and then the q^2 of the event. Before showing the results of the calculation we explain how the converted photon trajectory is determined from the

Figure 49. The χ^2 distribution for the $K_S \rightarrow \pi^o \pi^o$ sample, compared to the χ^2 distribution for 1 d.o.f.

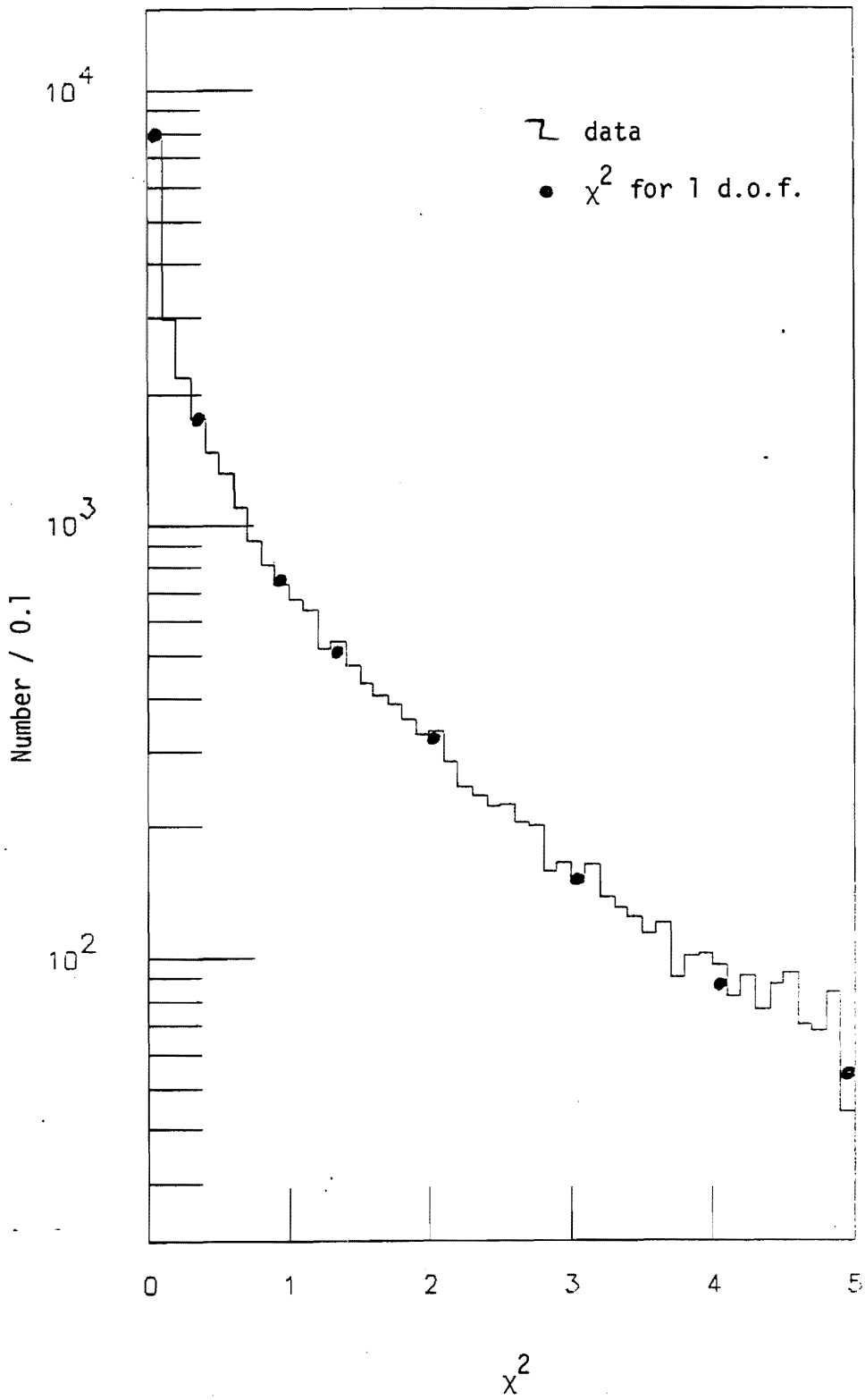
data
χ^2 for 1 d.o.f.
10^4
10^3
10^2
Number / 0.1
0
1
2
3
4
5
χ^2

Figure 50. The $K_L \rightarrow 3\pi^0$ mass peak. The sample was collected in about eight hours of data-taking.

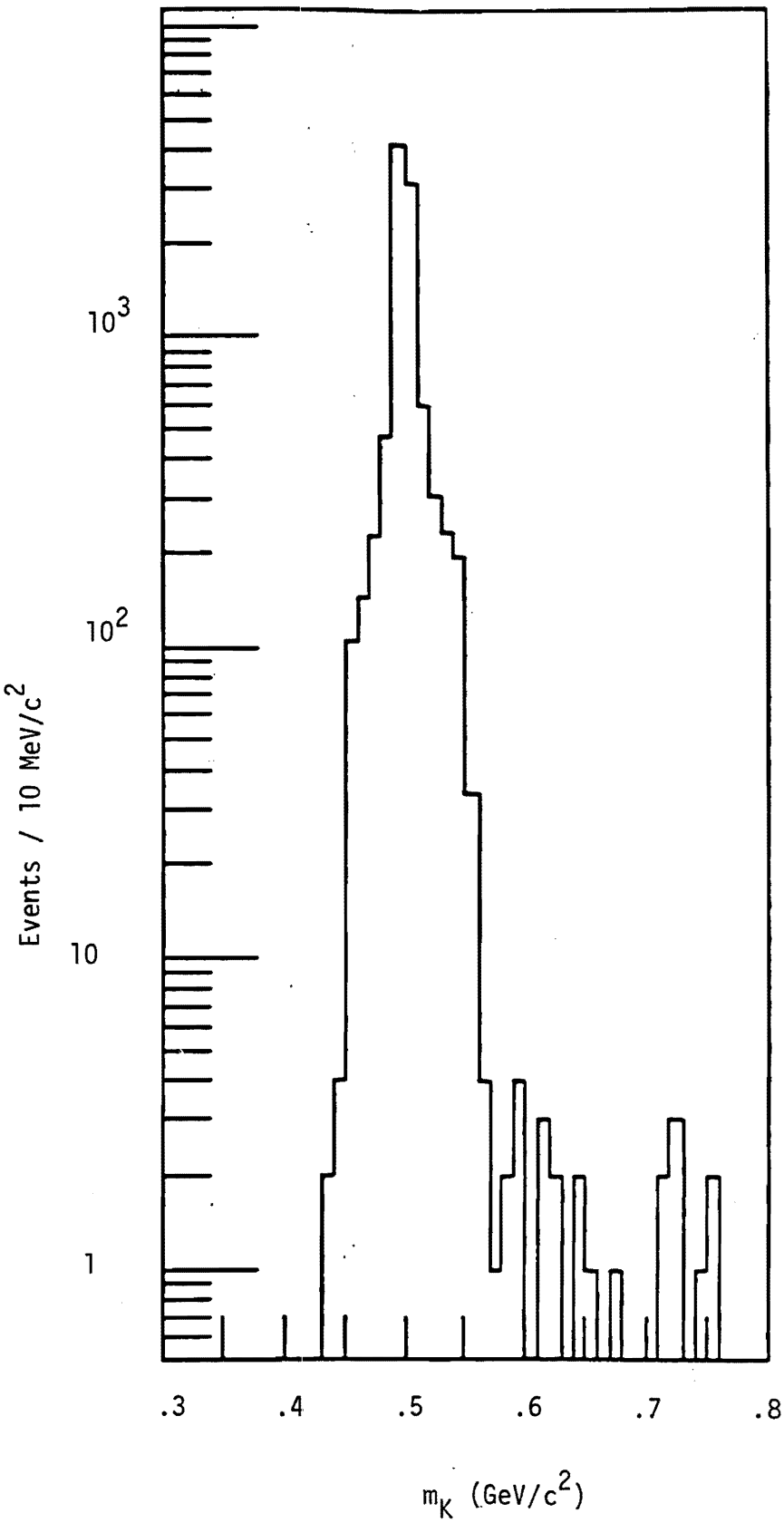
10^3
10^2
10
1
Events / 10 MeV/c^2
.3
.4
.5
.6
.7
.8
m_K (GeV/c^2)

Figure 51. The z-vertex distribution for the $K_L \rightarrow \pi^o \pi^o$ sample; as in Figure 28, the peaks at 406 and 420 meters arise from neutron interactions at either end of the decay region.

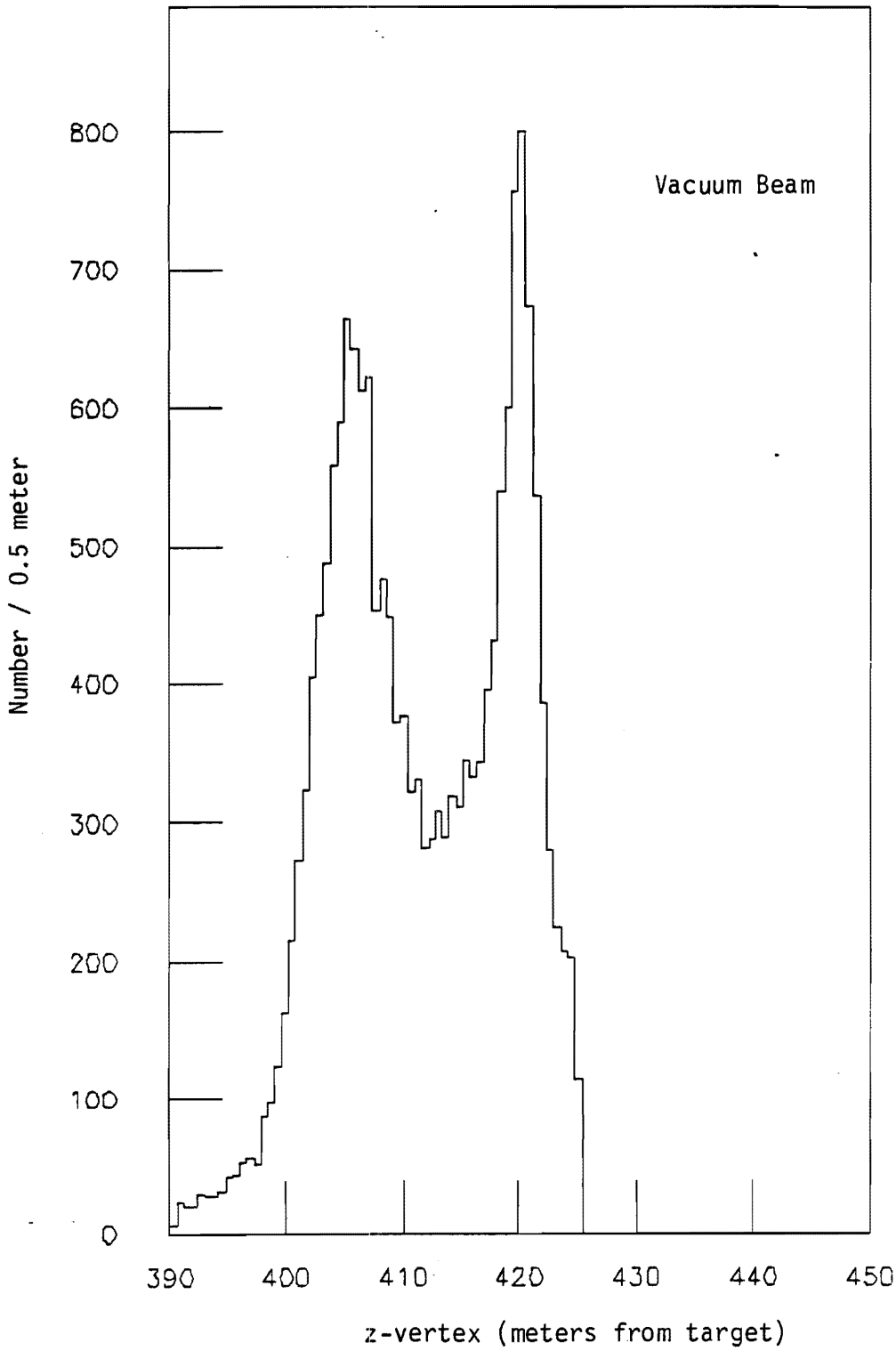
Vacuum Beam
Number / 0.5 meter
800
700
600
500
400
300
200
100
0
390
400
410
420
430
440
450
z-vertex (meters from target)

Figure 52. The distribution of Figure 51 for the $K_S \rightarrow \pi^o \pi^o$ sample; as in Figure 29, the exponentially falling shape reflects the K_S lifetime.

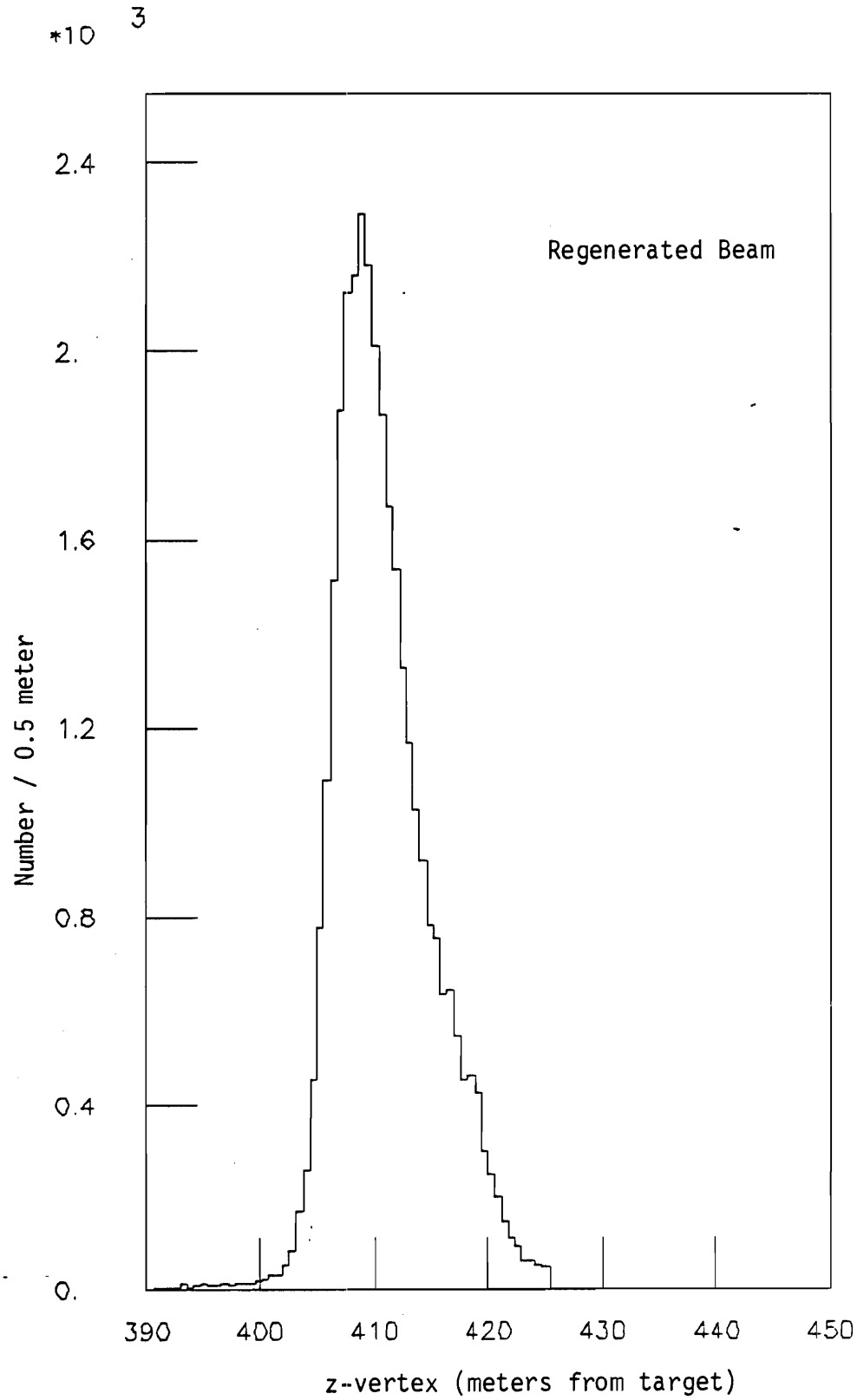
*10 3
2.4
2.
1.6
1.2
0.8
0.4
0.
Number / 0.5 meter
Regenerated Beam
390
400
410
420
430
440
450
z-vertex (meters from target)

converted pair.

The trajectories of the electron and positron within the spectrometer are well determined; these trajectories can be combined to determine the trajectory of the converted photon. We saw that multiple scattering in the lead converter deflected the pair from the trajectory of the parent photon inducing an error in $\vec{X}_\gamma$; scattering in the thin window at the end of the separation pipe degrades our resolution when we attempt to extrapolate in the other direction to the regenerator. Recall that there are about .005 radiation lengths of material in the region of the window; the induced error in x or y at the hodoscope is about 5.3 cm./p, which is typically a centimeter for our tracks. We can significantly reduce our sensitivity to scattering in the window by using the struck counter in the H or V banks. We used it once in the track reconstruction as a test; now we will use it as a measurement of the location of the conversion point. The intrinsic resolution of the counter is $\sqrt{w^2/12}$, where w is the counter width, yielding $\sigma = 0.37$ cm. independent of momentum. We have combined the information from the counter with the track projections using a likelihood technique. The xy position at the hodoscope then provides one point on the trajectory of the converted photon; the other is $\vec{X}_\gamma$. These line determined by these two points is extrapolated to Z_{AV} to determine the transverse vertex.

The technique allows us to cleanly distinguish between the beams. Figure 54 shows the distribution at the regenerator for the coherent K_S decays; as in the charged mode, we use the extrapolation to z_{RA} to distinguish between the beams.

We now have the same information as in the charged mode to calculate q^2 and the calculation proceeds identically (in the neutral mode the target position was determined from fully reconstructed $K_L \rightarrow 3\pi^o$ decays).

E. Cuts Used in the Analysis

The cuts used in the neutral mode analysis fell into three categories. The first used the information from the spectrometer to determine whether the tracks were properly reconstructed and whether they were likely to have been an electron-positron pair. The second category examined the information from the lead glass to determine whether the event had the topology of a $K \rightarrow 2\pi^o$ decay and to eliminate events with especially problematic clusters. The third category used reconstructed quantities other than the mass and q^2 to eliminate as many $3\pi^o$ events as possible before performing the background subtractions.

1. Track Requirements

We required the tracks have at least 2/3 GeV/c of momentum. Hand-scans indicated tracks below this momentum were often spurious, and in addition the cluster-finding routine had difficulty finding showers below this energy. The next cut specifically eliminated misreconstructed tracks. Figure 55 shows the xy deviation of the tracks from the centers of the struck hodoscope counter. There is a symmetric distribution about zero deviation produced by multiple scattering; we also see tails extending along δx or $\delta y = 0$. Multiple scattering is uniform in angle;

Figure 53. The use of the converted pair in determining the vertex and in calculating q^2.

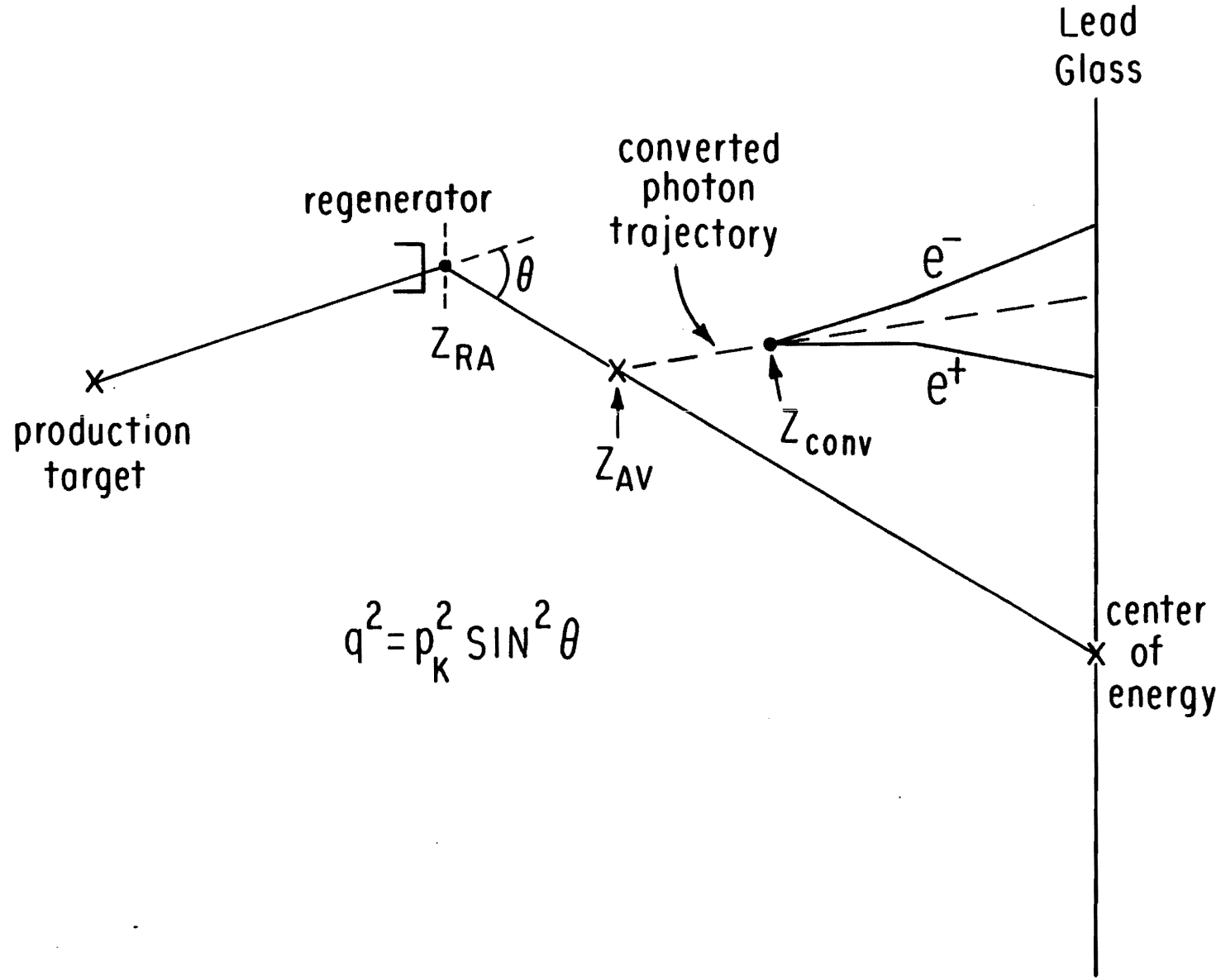

$$q^2 = p_K^2 \, \mathrm{SIN}^2 \theta$$

Figure 54. The transverse vertex distribution for the coherent $K_S \rightarrow \pi^o \pi^o$ sample. As in Figure 3, the regenerator is in the west beam for the left-hand picture and the east beam for the right-hand one.

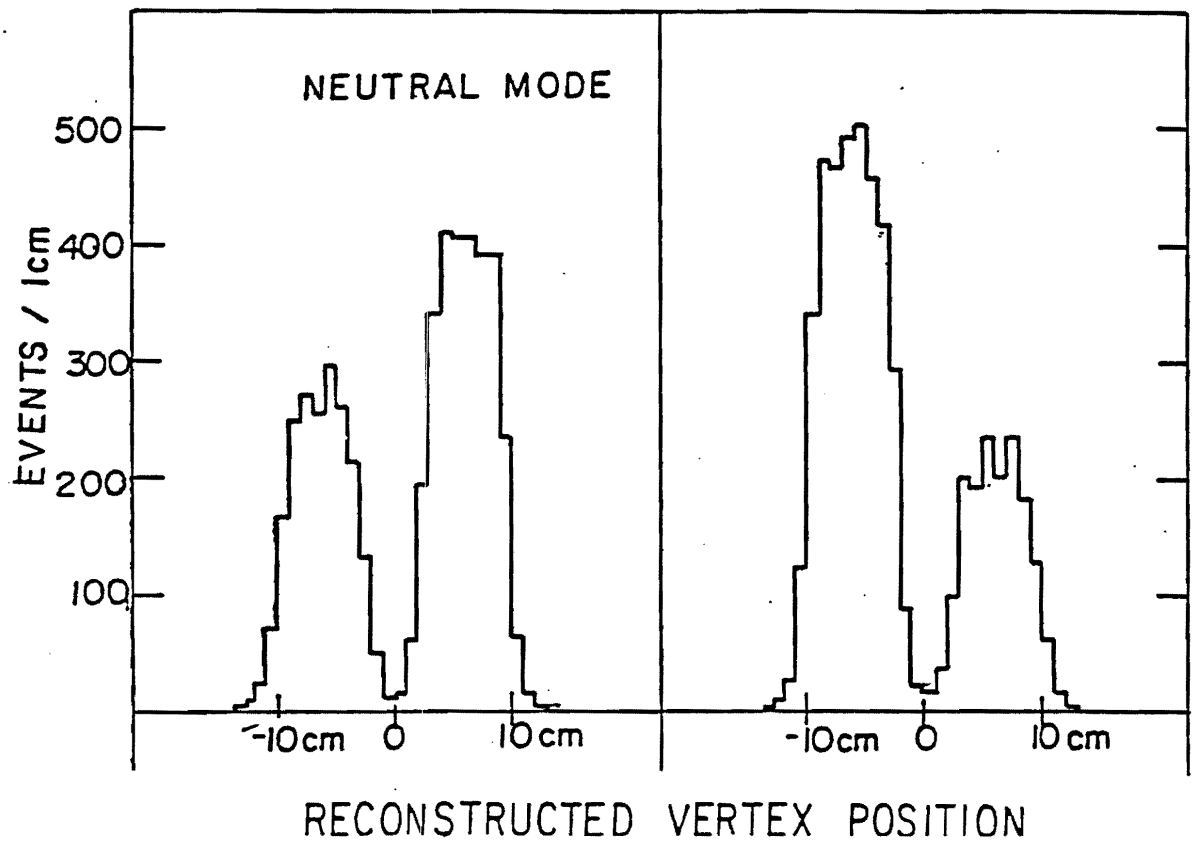
NEUTRAL MODE
500
400
300
200
100
EVENTS / 1cm
-10cm
0
10cm
-10cm
0
10cm
RECONSTRUCTED VERTEX POSITION

these tails are produced by misreconstructed tracks. We cut tracks deviating by more than 3 cm. in either view.

We have stressed that the electron-positron pair is only separated by multiple scattering before the magnet. We can use this characteristic to recognize electron-positron pairs and eliminate hadrons independently of the information from the lead glass. For Gaussian multiple scattering the RMS separation of the tracks at the magnet center is given by

$$((\delta x)^2 + (\delta y)^2)^{1/2} = .021 l \left(\frac{1}{p_1^2} + \frac{1}{p_2^2}\right)^{1/2} (z_{magnet} - z_{conversion\ plane}) \qquad (7.6)$$

where p_1 and p_2 are the track momenta and l is the number of radiation lengths. Define the momentum-independent quantity

$$SEP2 = \frac{(\delta x^2 + \delta y^2)}{\frac{1}{p_1^2} + \frac{1}{p_2^2}} \qquad (7.7)$$

We cut events with $SEP2 > 1$, which is about 18 σ for the scattering, to require the tracks to have the topology of a converted pair. Figure 56 shows a $SEP2$ distribution; the cut is clearly in the broad, flat tail due to hadrons.

2. Cluster Finding and Cluster Reconstruction Cuts

An accepted $K \rightarrow 2\pi^o$ decay deposits three photons and a converted pair in the glass. After the cluster-finding algorithm had decided which of the clusters belonged to the converted pair and handled any bremsstrahlung, the remaining neutral clusters were required to have more than 3 GeV of energy. If we found

exactly three such clusters, the event was passed on to the next step of the analysis. This cut was made because the minimum energy requirement largely eliminated 'out-of-time' showers occurring within our 175 nsec. gate; an 'out-of-time' shower would increase the number of neutral clusters to four and a good $K \rightarrow 2\pi^o$ decay would be rejected. We found the cut at 3 GeV maximized the yield of $K \rightarrow 2\pi^o$ decays. Any neutral cluster with an energy less than 3 GeV was ignored in further analysis.

We have now selected events with the topology of $K \rightarrow 2\pi^o$ decays. The next pair of cuts examined the location of clusters to ensure their energies were properly measured and their positions well determined. We first eliminated events with clusters whose centers were in a block on the inner or outer edge of the array, since a significant amount of energy may not have been deposited in the glass. Recall that no event should have a cluster centered on the inner edge of the glass because of the collar anti.

We have mentioned that the cluster-finding algorithm encountered difficulties with 'fused', or overlapping, clusters. We demanded no neutral cluster be within 15 cm. in either x or y of any other neutral cluster or either track. The cut insured that a 3×3 set of blocks centered on each cluster was uncontaminated by other clusters; more than 95% of a cluster's energy is contained in such a set of blocks, insuring any sharing of energy is small.

Figure 55. The xy deviation of tracks at the conversion hodoscope. The deviation is defined to be the distance from the center of the struck counter to the position of the extrapolated track. The distribution near zero is symmetric in angle and arises from resolution and multiple scattering; the tails extending out along x and y are due to misreconstructed tracks.

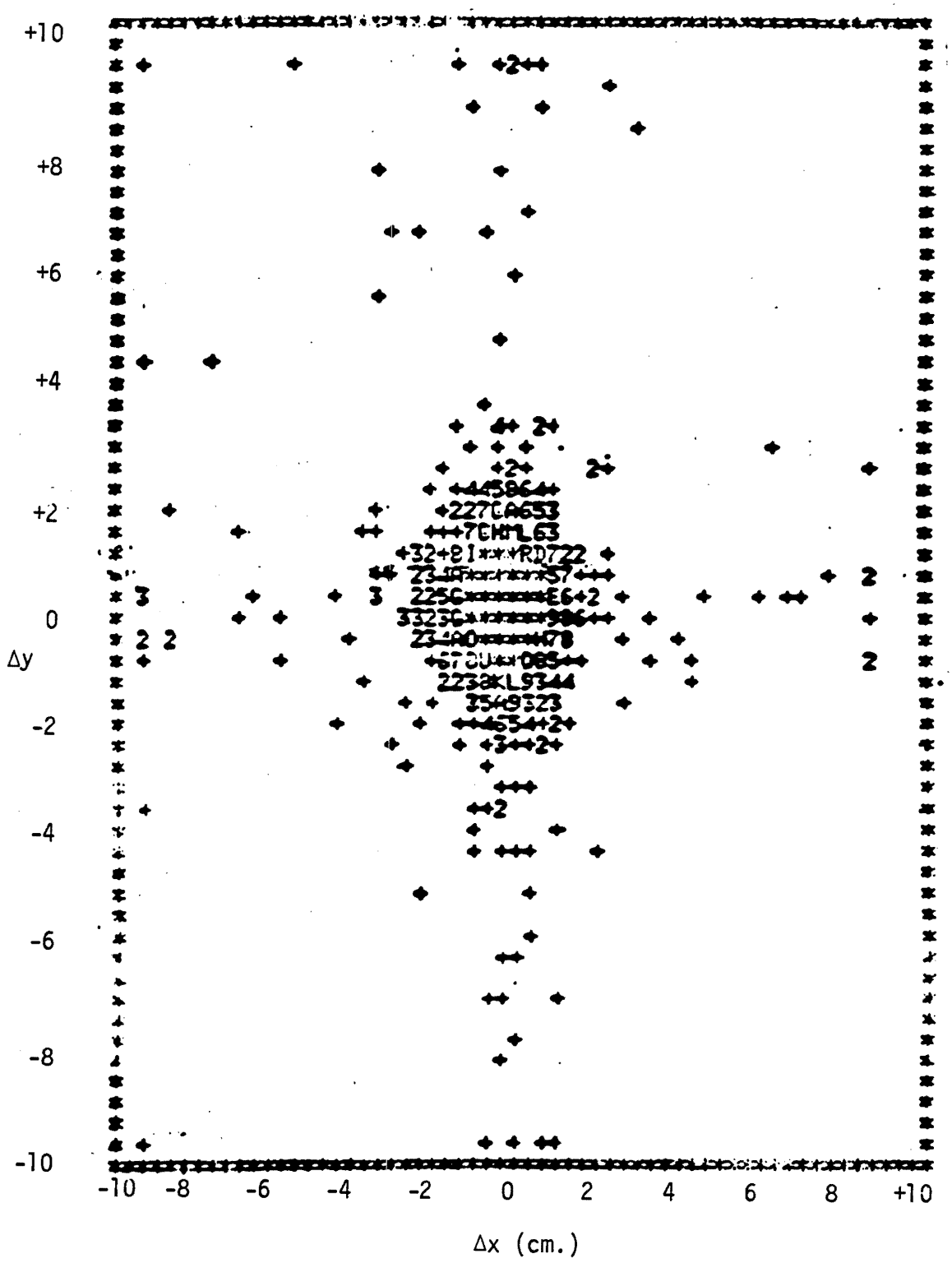
+10
+8
+6
+4
+2
0
Δy
-2
-4
-6
-8
-10
-10 -8 -6 -4 -2 0 2 4 6 8 +10
Δx (cm.)

Figure 56. A typical *SEP*2 distribution. There are roughly 14000 events entered on the plot and 6000 overflows.

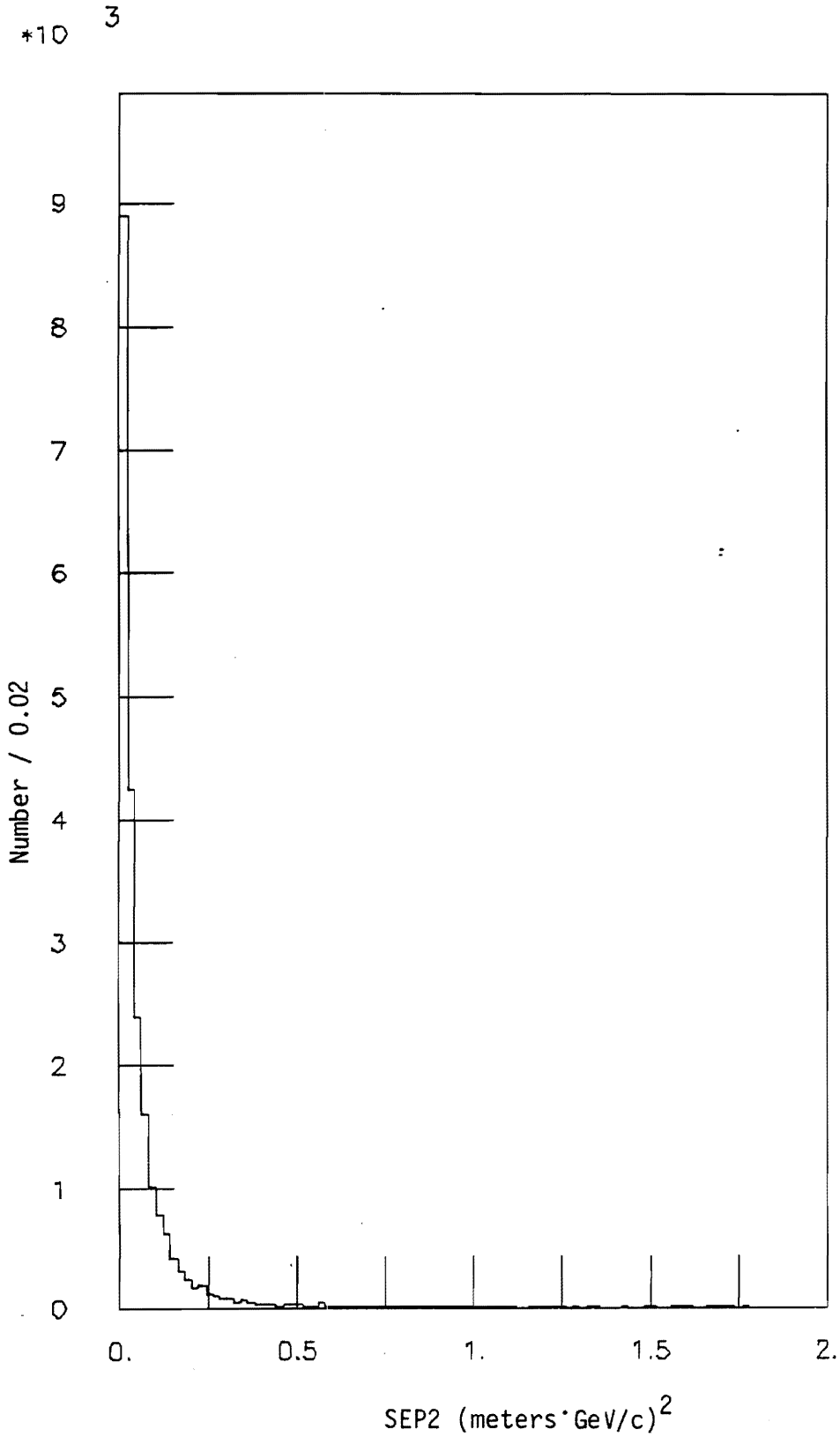
*10 3
9
8
7
6
5
4
3
2
1
0
Number / 0.02
0.
0.5
1.
1.5
2.
SEP2 (meters·GeV/c)2

3. Kinematic Reconstruction Cuts

Events which survived the track reconstruction and cluster cuts were fully reconstructed. The first reconstruction cut examined the electron-positron pair to check that E as measured in the glass agreed with p as measured by the chambers. We eliminated events in which either track had $E/p<0.7$; we summed the track momenta and compared it to the energy of the pseudo-photon, rejecting events with $E_{pseudo}/(p_1 + p_2) > 2$. Events with low E/p were generally due to misreconstructed tracks while events with large E_{pseudo}/p were often the result of unresolved neutral clusters fusing with the pair.

After these cuts were made the mass and q^2 calculations were performed. As described earlier, from Z_{AV} we then calculated the decay vertex and assigned the event to one of the beams.

Next we cut on the reconstructed z-vertex. The decay region ran from 406.26 to 420.6 meters; we cut requiring $390 < Z_{AV} < 425$ meters. In making a software cut on the z vertex we must guarantee that we are insensitive to systematic shifts in Z_{AV} resulting from nonlinearities in the energy measurements. Recall that the conversion hodoscope is at 420.1 meters and that our vertex resolution is about 1.25 meters in the decay region; hence the downstream cut removes practically no $K \rightarrow 2\pi^o$ decays. The acceptance, as discussed in Appendix II, is such that a cut at 390 meters removes a negligible fraction of the events. We are thus insensitive to any small nonlinearity remaining after the calibration. With these

z-vertex cuts we also accept a large number of $K_L \rightarrow 2\pi^o$ decays occurring alongside and upstream of the regenerator in the vacuum beam, increasing our yield by 1/3 as referred to in Chapter II.

Finally we cut on any anticounter having fired; the fraction of events lost at this level of the analysis was about 5%.

The mass vs. q^2 distributions over all momenta after all cuts is shown for the K_L beam in Figure 57 and for the K_S beam in Figure 58. The K_L mass distribution for q^2 less than 2500 (MeV/c) ^{2} has roughly an 8% background arising from $3\pi^o$ decays and neutron interactions. In the K_S beam we see no significant contamination in mass; in q^2, there is approximately a 15% contamination of inelastically produced K_S for q^2 less than 2500 (MeV/c) ^{2}. The next section describes the subtraction of these backgrounds.

F. Background Subtractions

In the charged mode we were able to identify and measure the sources of the background in order to perform the subtraction. This was not necessary in the neutral mode; instead we have fit the backgrounds in regions of mass and q^2 nearby to but offset from the signal and interpolated the fit to perform the subtraction. We first discuss the K_L subtractions: the subtraction of the $3\pi^o$ background and of the background due to neutron interactions in our spectrometer. In the K_S beam we subtracted the contribution of inelastically produced K_S. Finally we return to the K_L data and subtract a small contamination of inelastically pro-

Figure 57. The $m_{\pi\pi}$ vs. q^2 distribution for the $K_L \rightarrow \pi^0\pi^0$ sample.

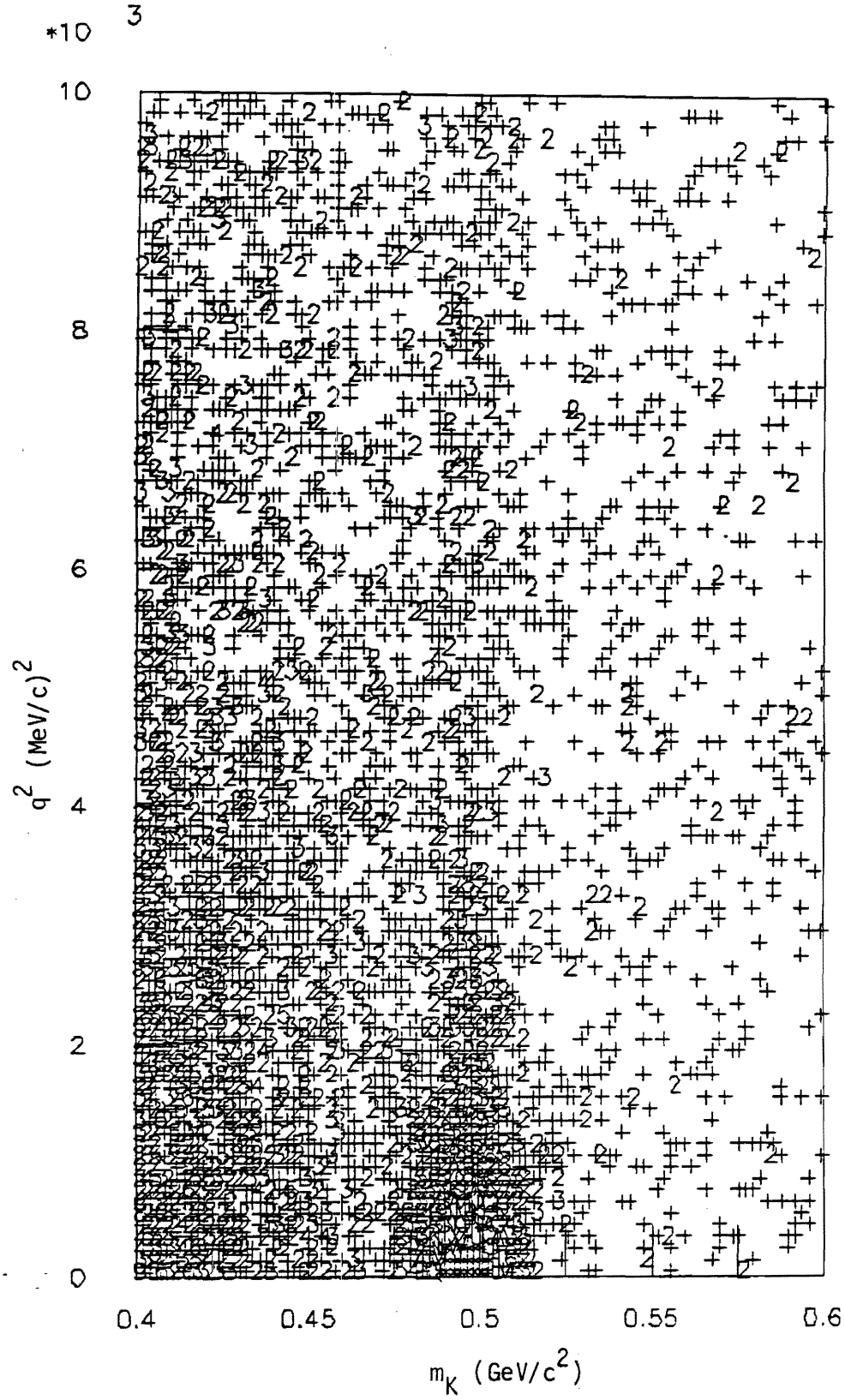
*10 3
10
8
6
4
2
0
q^2 (MeV/c)^2
0.4
0.45
0.5
0.55
0.6
m_K (GeV/c^2)

Figure 58. The $m_{\pi\pi}$ vs. q^2 distribution for the $K_S \rightarrow \pi^o\pi^o$ sample.

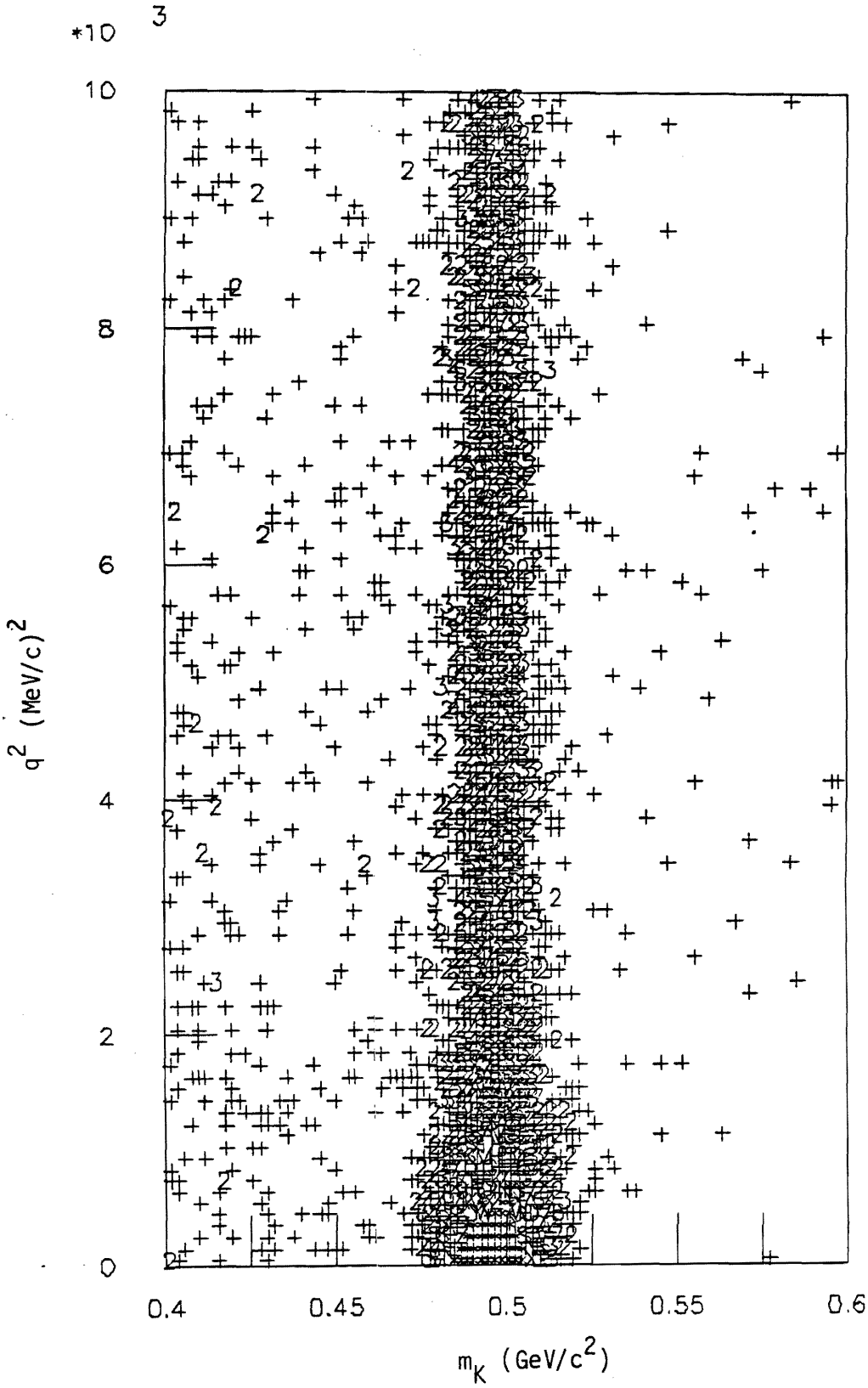
*10 3
10
8
6
4
2
0
q^2 (MeV/c)^2
0.4
0.45
0.5
0.55
0.6
m_K (GeV/c^2)

duced K_S in this beam as well.

We have used the maximum likelihood technique for our fits. The method requires a probability distribution both for the signal distribution and any background. We have fitted the K_L mass distribution in nine bins of momentum to the form:

$$P(m) = \alpha\, S(m) + (1 - \alpha)\, B(m) \tag{7.8}$$

where $S(m)$ is a normalized probability distribution for the $K_L \rightarrow 2\pi^o$ signal and $B(m)$ is a trial distribution for the background. We shall measure $S(m)$ from the data and vary α and $B(m)$ to fit the backgrounds.

We measured $S(m)$ from the data using the clean K_S peak; Figures 59 through 67 show the K_S mass distribution for q^2 less than 2500 (MeV/c) ^{2} in each momentum bin. Each of these histograms was transformed into a probability distribution between 470 and 520 MeV/c ^{2}: first the histogram was smoothed to lessen any statistical fluctuations and then each 1 MeV/c ^{2} bin of mass was assigned a probability. The method has the significant advantage of using the measured K_S mass distribution to fit both the K_L and K_S data(the K_S and K_L mass shapes should be identical) instead of relying on a Gaussian or some artificially constructed function.

The two sources of background in the K_L beam, the $K_L \rightarrow 3\pi^o$ decay and neutron interactions, were fitted to exponentials. The background distribution then had the form ($\beta_{3\pi}$ and β_n refer to the $3\pi^o$ and neutron backgrounds):

$$b(m) = e^{-\beta_{3\pi} m} + \gamma e^{-\beta_n m} \tag{7.9}$$
$$B(m) = \frac{b(m)}{\int b(m) dm}$$

where γ reflects the relative size of the two sources of background. The two slopes and γ were varied in performing the fits.

How did we arrive at this trial form? We did not Monte Carlo the $3\pi^o$ background because it took too much computer time to generate a useful sample, nor could we extract it from the data as in the charged mode; however, this simple form fit the data well. We were more fortunate with the neutron background. The typical q^2 of neutron-induced interactions is $\approx 10^5$ (MeV/c) ^{2} (a typical momentum transfer of 300 MeV/c) which is large compared to the resolution of the coherent K_L signal. We therefore assumed that the mass distribution varied slowly with q^2 near q^2=0. We found that fitting an exponential in mass, independent of q^2, gave an adequate fit to the data from q^2 of 50000 (MeV/c) ^{2} to 100000 (MeV/c) ^{2}. The slopes obtained by fitting for $q^2 \geq 100000$ (MeV/c) ^{2} gave identical results within the errors, indicating the variation was indeed slow. A typical mass distribution is shown in Figure 68 for one momentum bin. We fit each bin to the form

$$P(m) = \alpha S(m) + (1 - \alpha) \frac{e^{-\beta_n m}}{\int e^{-\beta_n m} dm} \tag{7.10}$$

which is the same as equation (7.8) without the $3\pi^o$ contribution. The $3\pi^o$ background is negligible at this value of q^2 in the region of the kaon mass. The clear $K \rightarrow 2\pi^o$ mass peak is due to inelastically produced K_S made in the vacuum beam;

Figure 59. The mass distribution of the $K_S \rightarrow \pi^o \pi^o$ sample for $50 < p_K < 60$ GeV/c. The irregularities in the shape arise from the smoothing algorithm mentioned in the text.

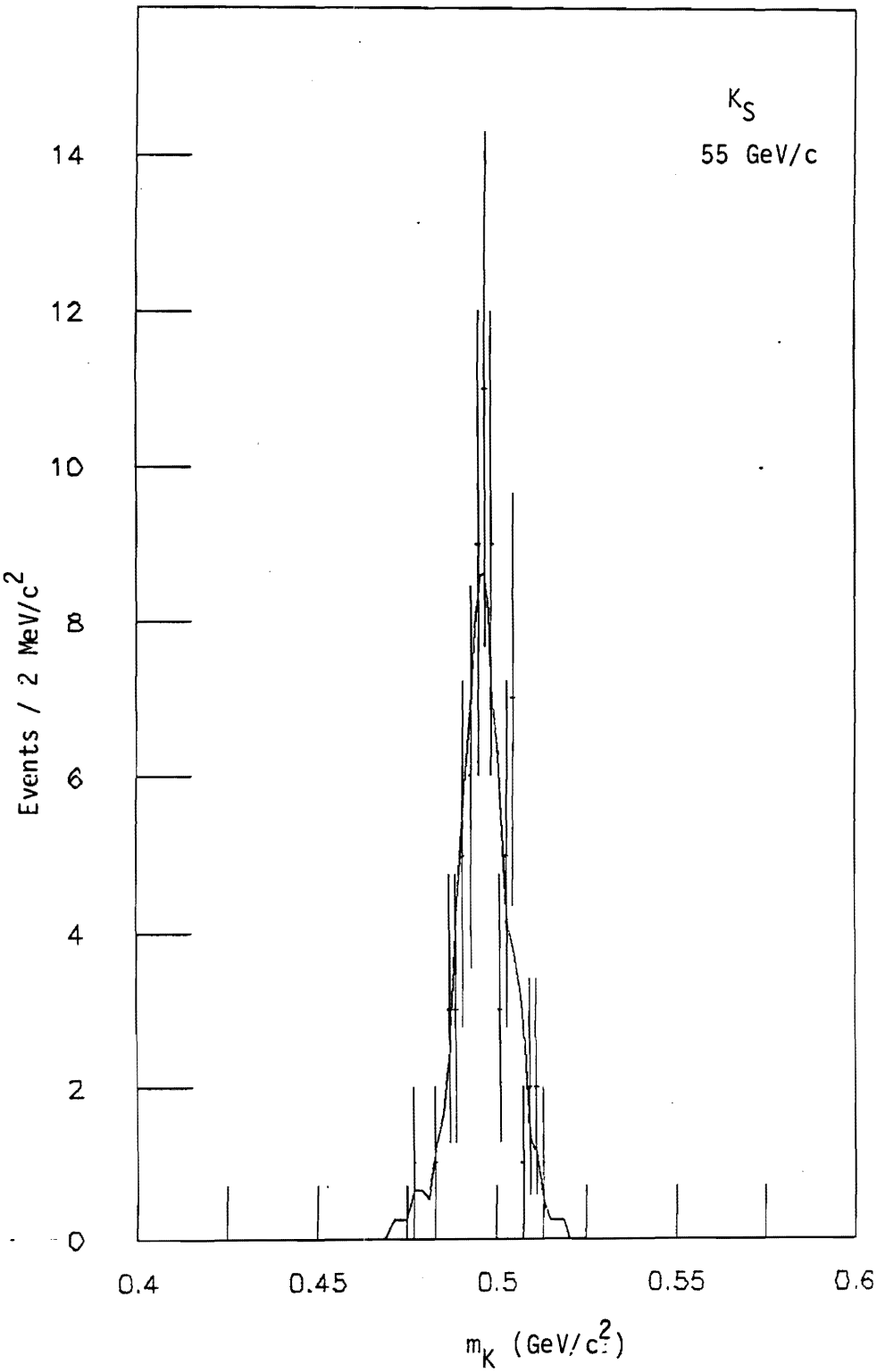
K_S
55 GeV/c
14
12
10
8
6
4
2
0
Events / 2 MeV/c^2
0.4
0.45
0.5
0.55
0.6
m_K (GeV/c^2)

Figure 60. The distribution of Figure 59 for 60 $< p_K <$ 70 GeV/c.

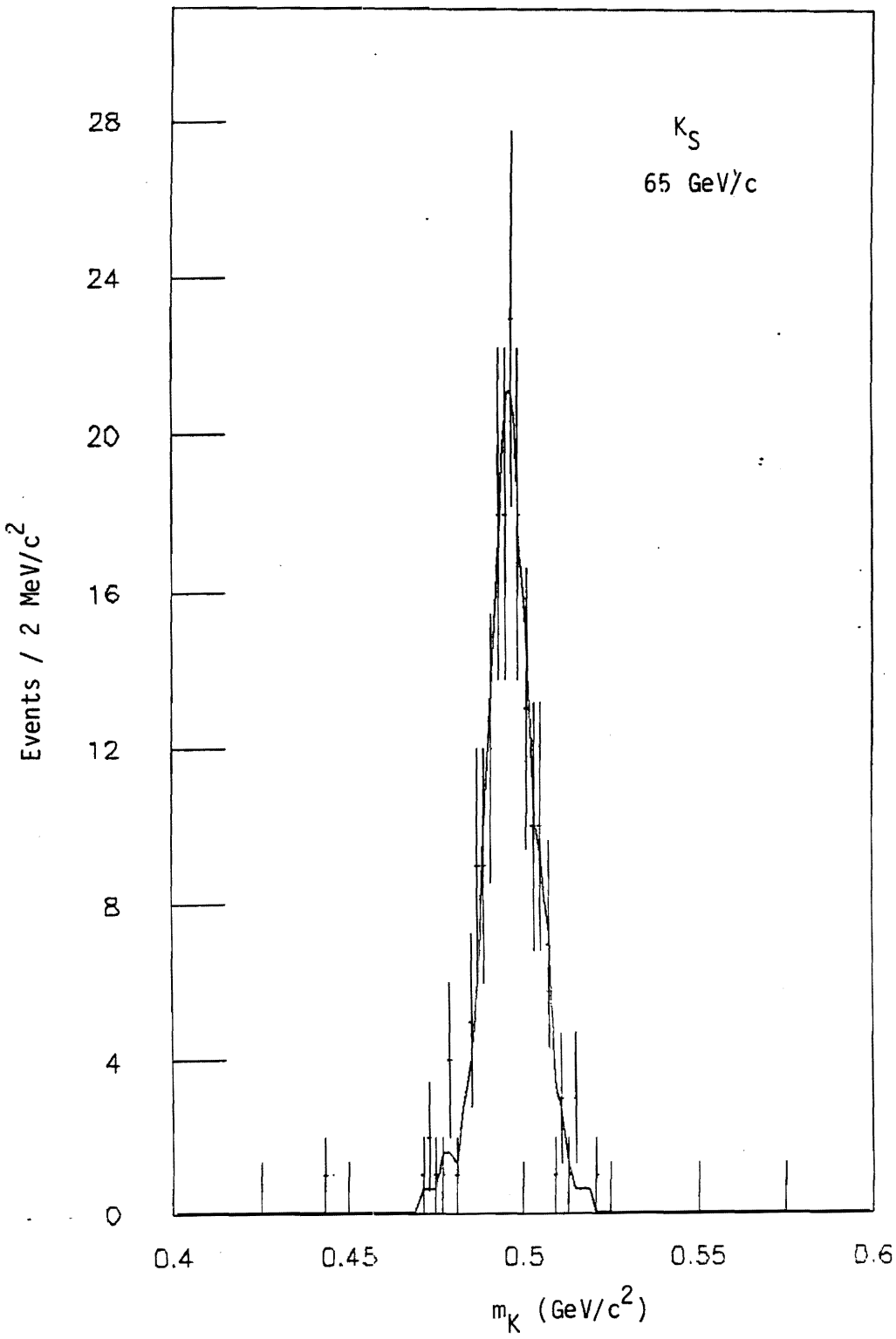
K_S
65 GeV/c
Events / 2 MeV/c^2
28
24
20
16
12
8
4
0
0.4
0.45
0.5
0.55
0.6
m_K (GeV/c^2)

Figure 61. The distribution of Figure 59 for 70 $< p_K <$ 80 GeV/c.

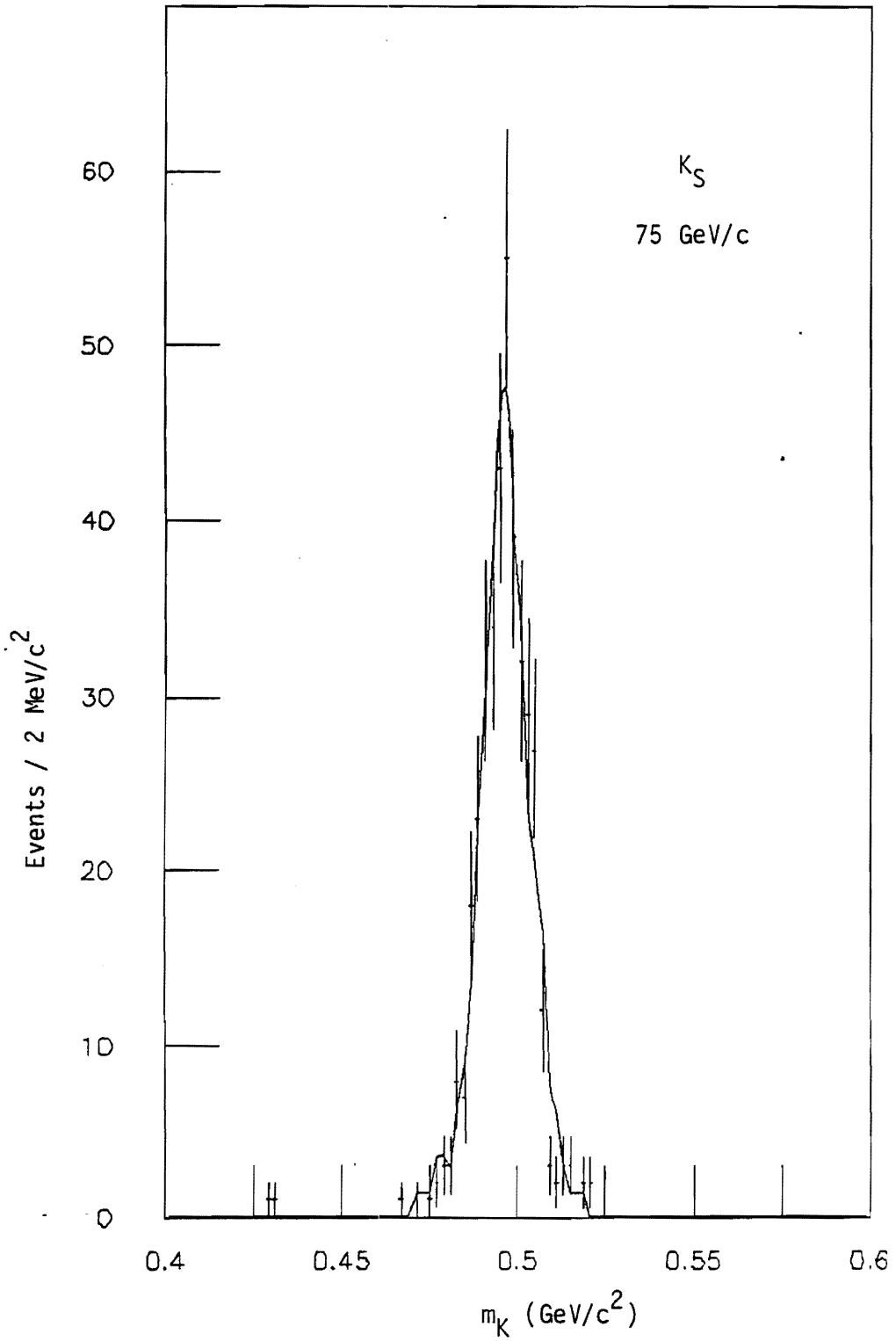
K_S
75 GeV/c
60
50
40
30
20
10
0
Events / 2 MeV/c^2
0.4
0.45
0.5
0.55
0.6
m_K (GeV/c^2)

Figure 62. The distribution of Figure 59 for 80 $< p_K <$ 90 GeV/c.

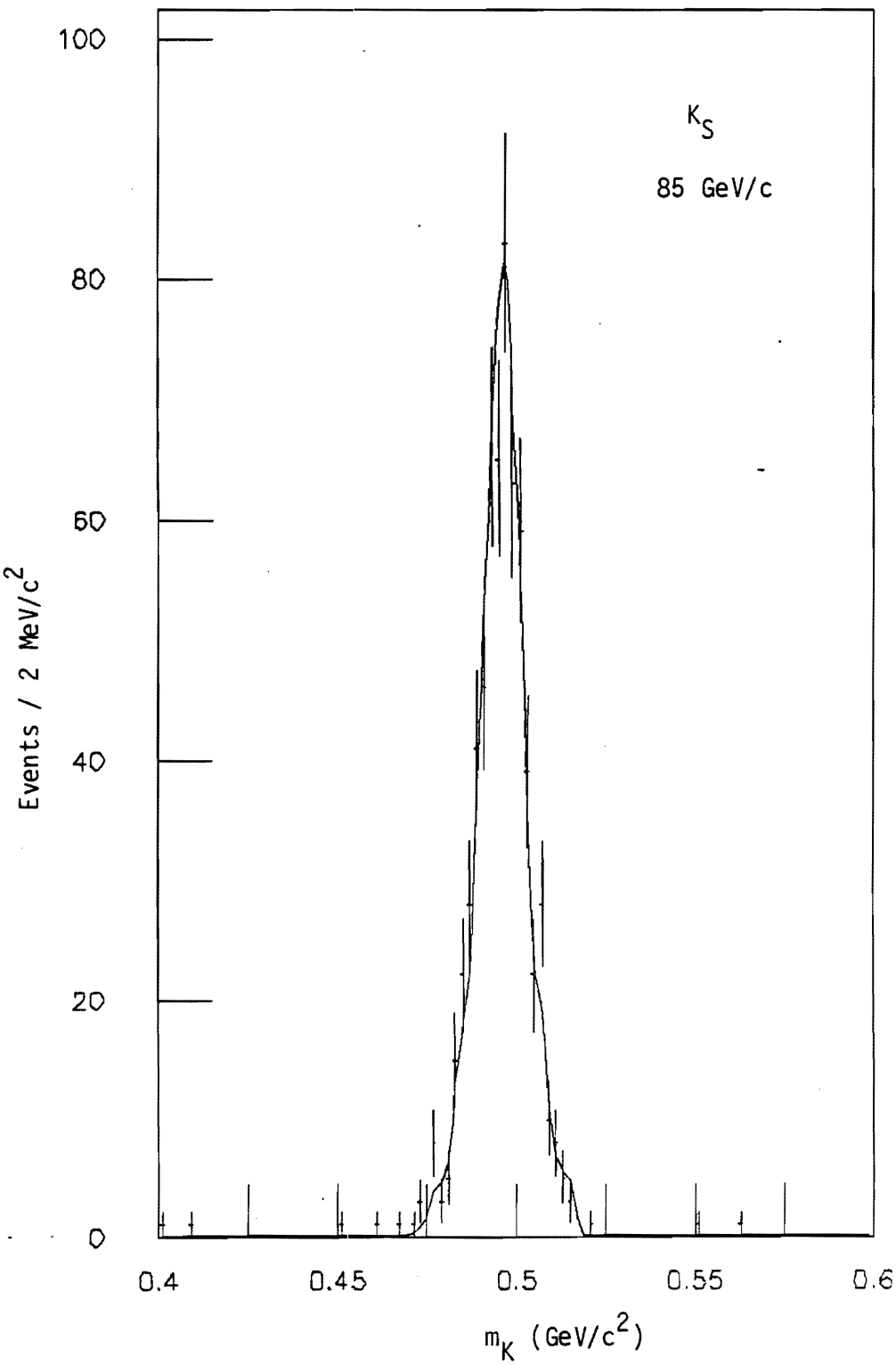
100
80
60
40
20
0
Events / 2 MeV/c^2
K_S
85 GeV/c
0.4
0.45
0.5
0.55
0.6
m_K (GeV/c^2)

Figure 63. The distribution of Figure 59 for 90 $< p_K <$ 100 GeV/c.

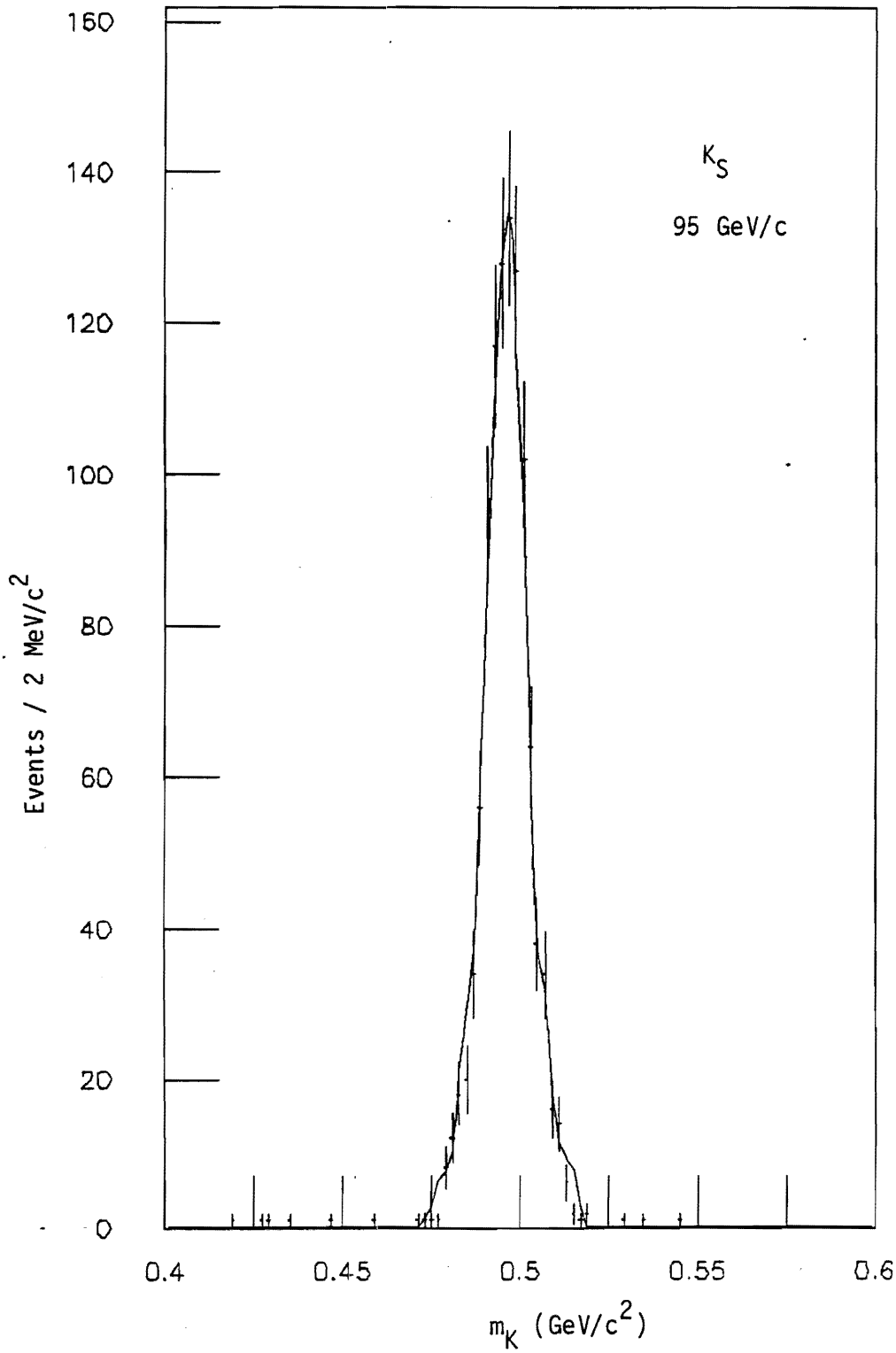
160
140
120
100
80
60
40
20
0
Events / 2 MeV/c^2
K_S
95 GeV/c
0.4
0.45
0.5
0.55
0.6
m_K (GeV/c^2)

Figure 64. The distribution of Figure 59 for 100 $< p_K <$ 110 GeV/c.

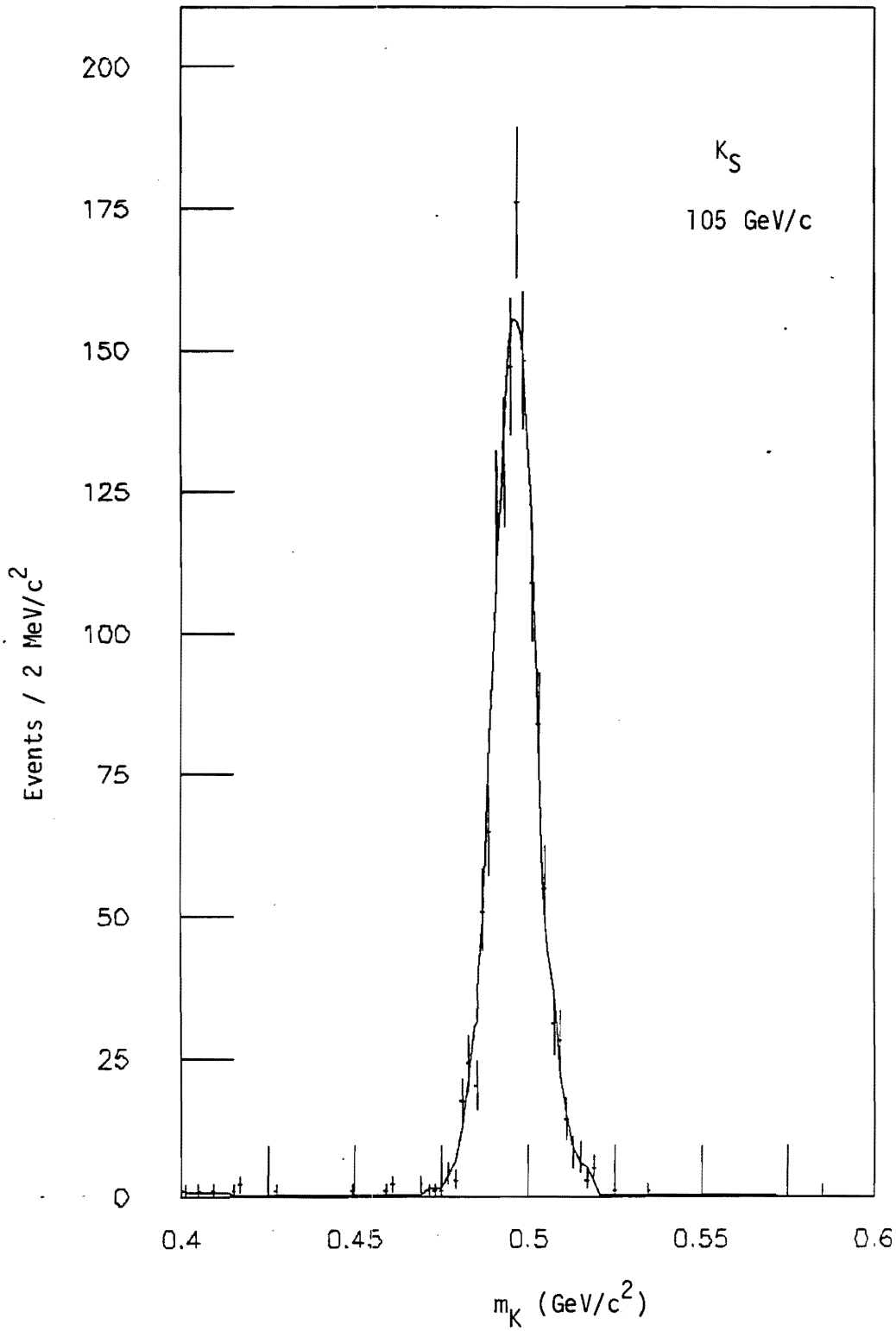
K_S
105 GeV/c
Events / 2 MeV/c^2
200
175
150
125
100
75
50
25
0
0.4
0.45
0.5
0.55
0.6
m_K (GeV/c^2)

Figure 65. The distribution of Figure 59 for 110 $< p_K <$ 120 GeV/c.

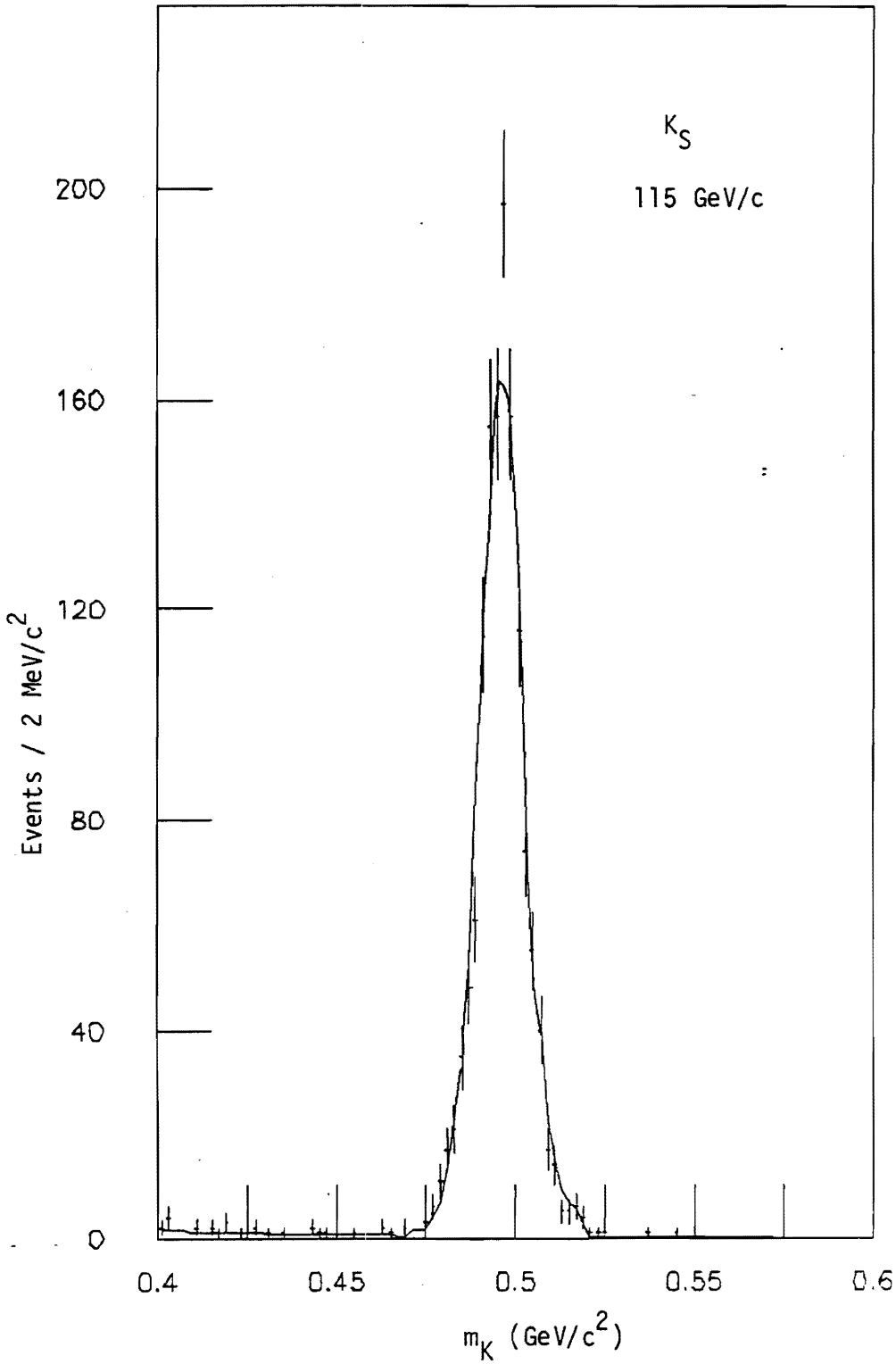
K_S
115 GeV/c
200
160
120
80
40
0
Events / 2 MeV/c^2
0.4
0.45
0.5
0.55
0.6
m_K (GeV/c^2)

Figure 66. The distribution of Figure 59 for 120 $< p_K <$ 130 GeV/c.

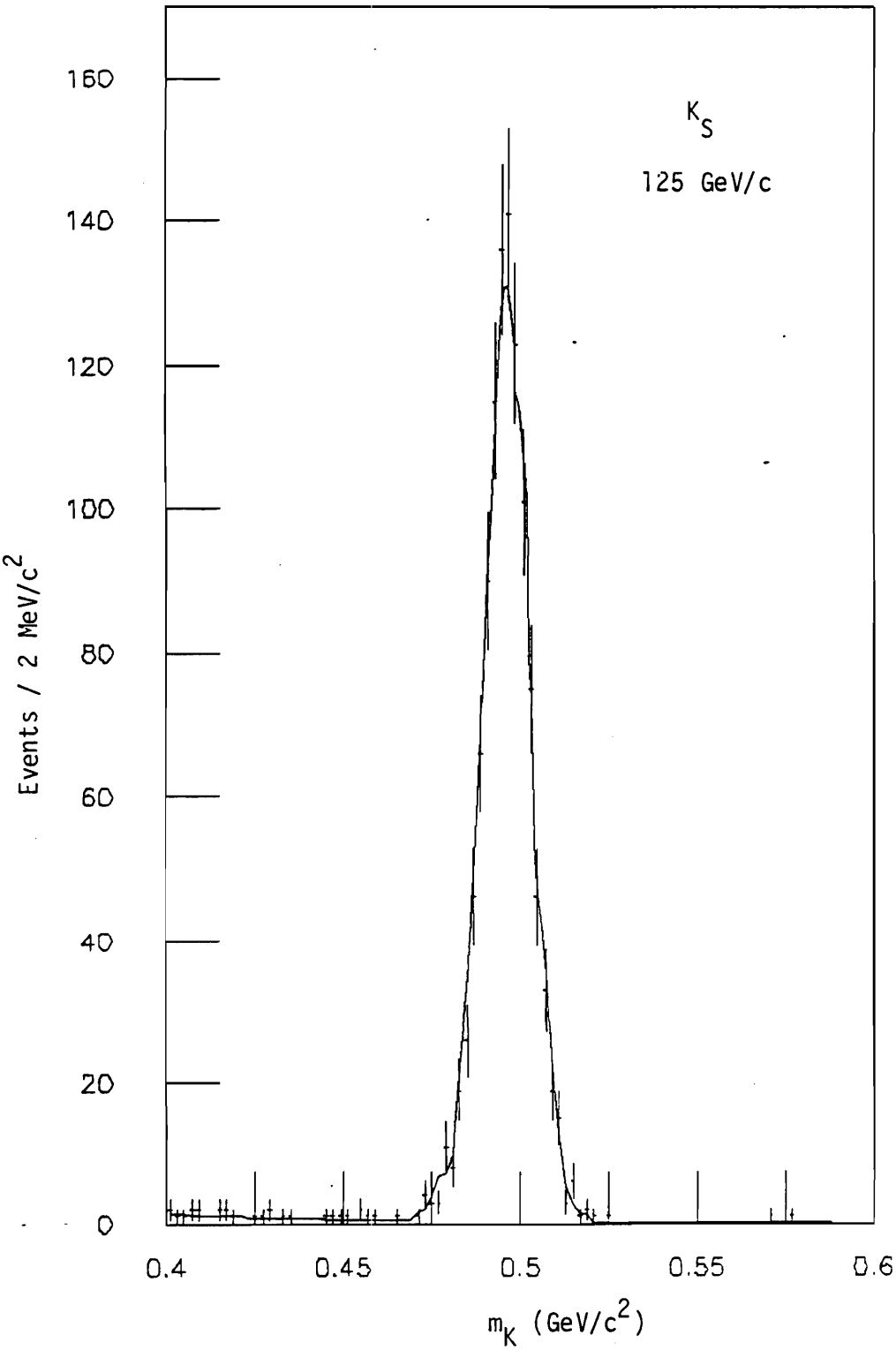
K_S
125 GeV/c
160
140
120
100
80
60
40
20
0
Events / 2 MeV/c^2
0.4
0.45
0.5
0.55
0.6
m_K (GeV/c^2)

Figure 67. The distribution of Figure 59 for 130 $< p_K <$ 140 GeV/c.

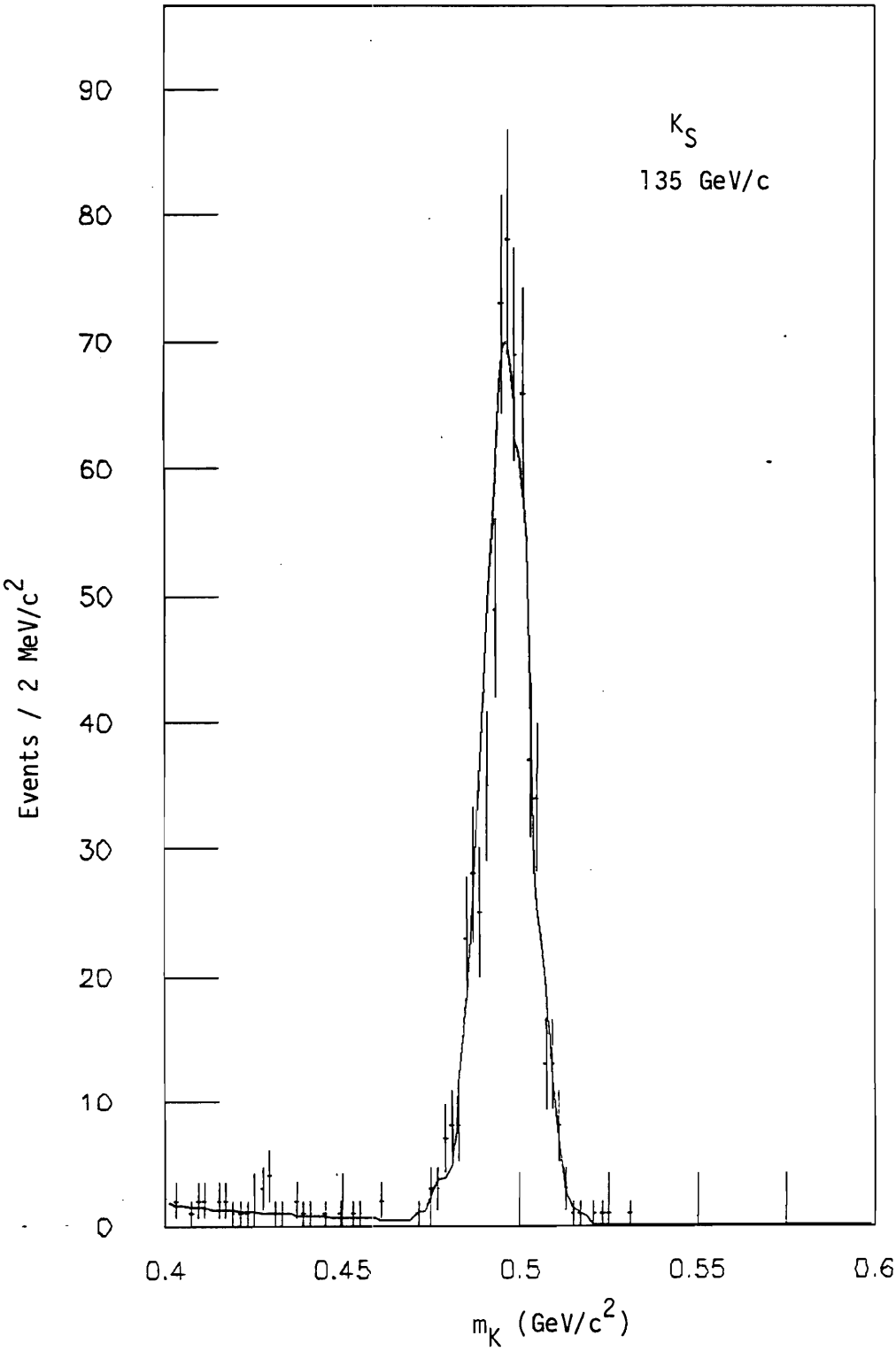
K_S
135 GeV/c
Events / 2 MeV/c^2
90
80
70
60
50
40
30
20
10
0
0.4
0.45
0.5
0.55
0.6
m_K (GeV/c^2)

Figure 68. The mass distribution of the $K_L \rightarrow \pi^o \pi^o$ sample for $70 < p_K < 80$ GeV/c and $10000 < q^2 < 50000$ (MeV/c)^2.

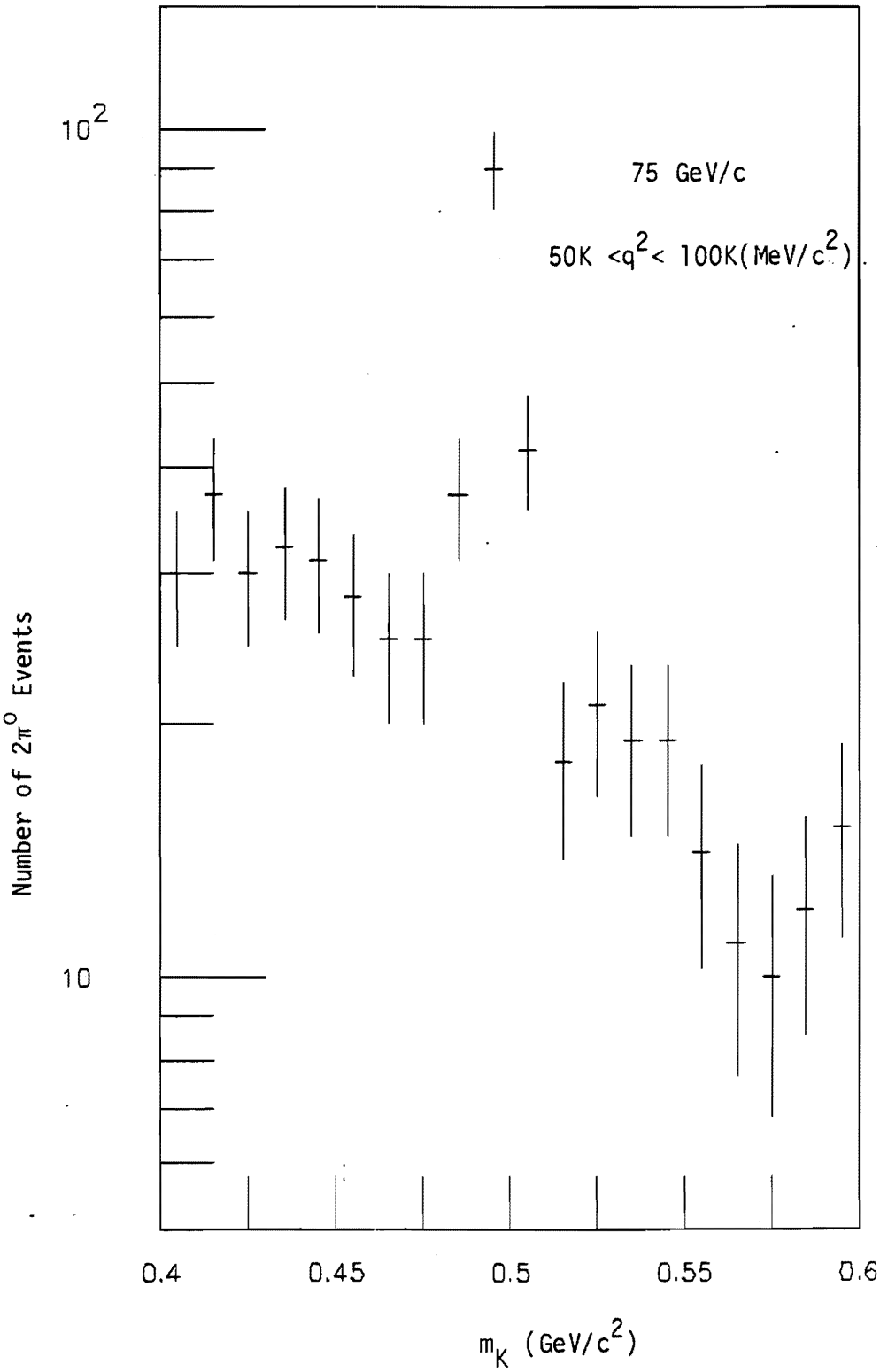
75 GeV/c
50K <q^2< 100K(MeV/c^2)
10^2
10
Number of 2π^0 Events
0.4
0.45
0.5
0.55
0.6
m_K (GeV/c^2)

Figure 69. The dependence of the shape of the neutron background upon momentum.

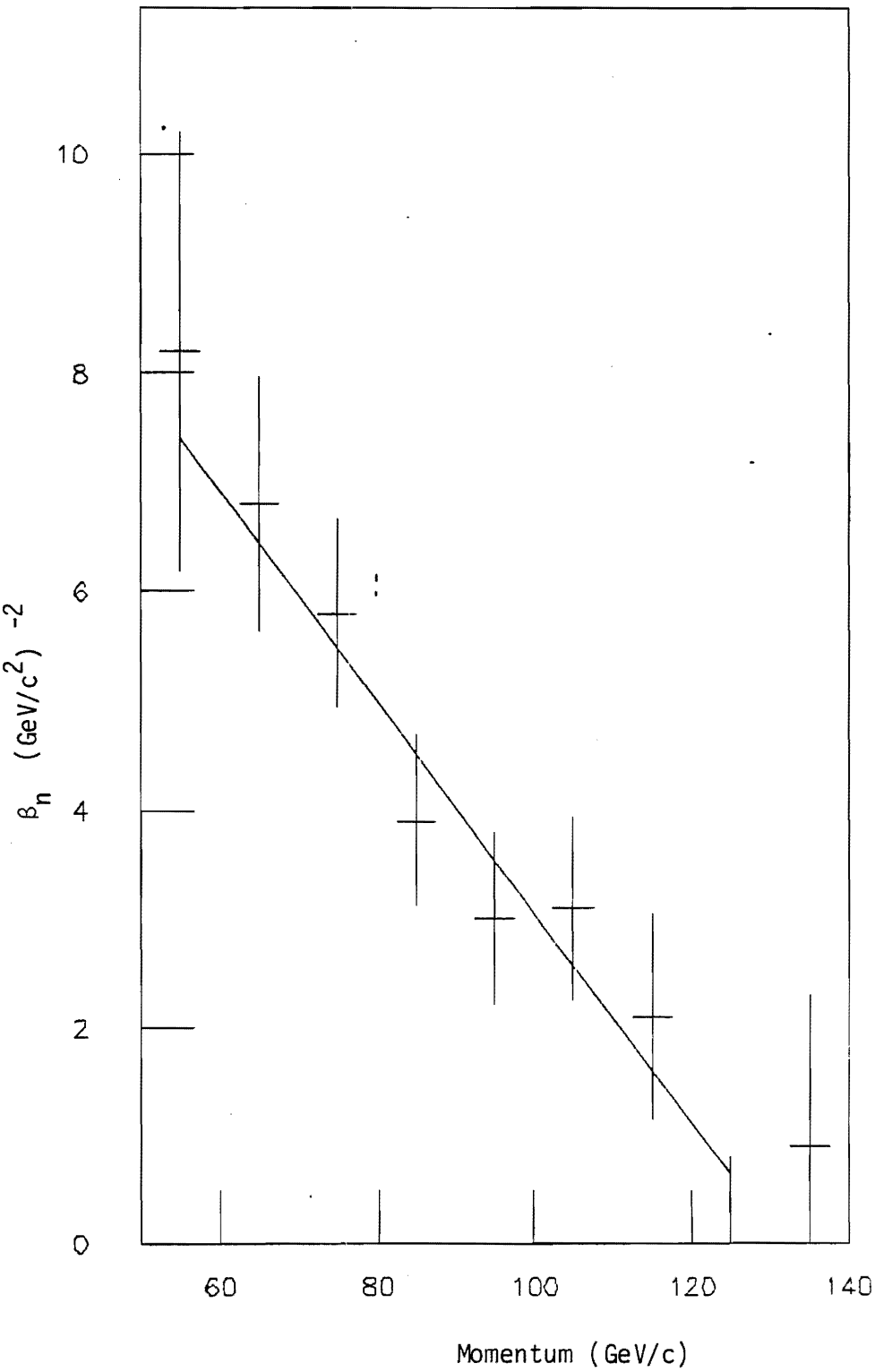
10
8
6
4
2
0
β_n (GeV/c^2) $^{-2}$
60
80
100
120
140
Momentum (GeV/c)

Figure 70. The dependence of the shape of the $3\pi^0$ background upon momentum.

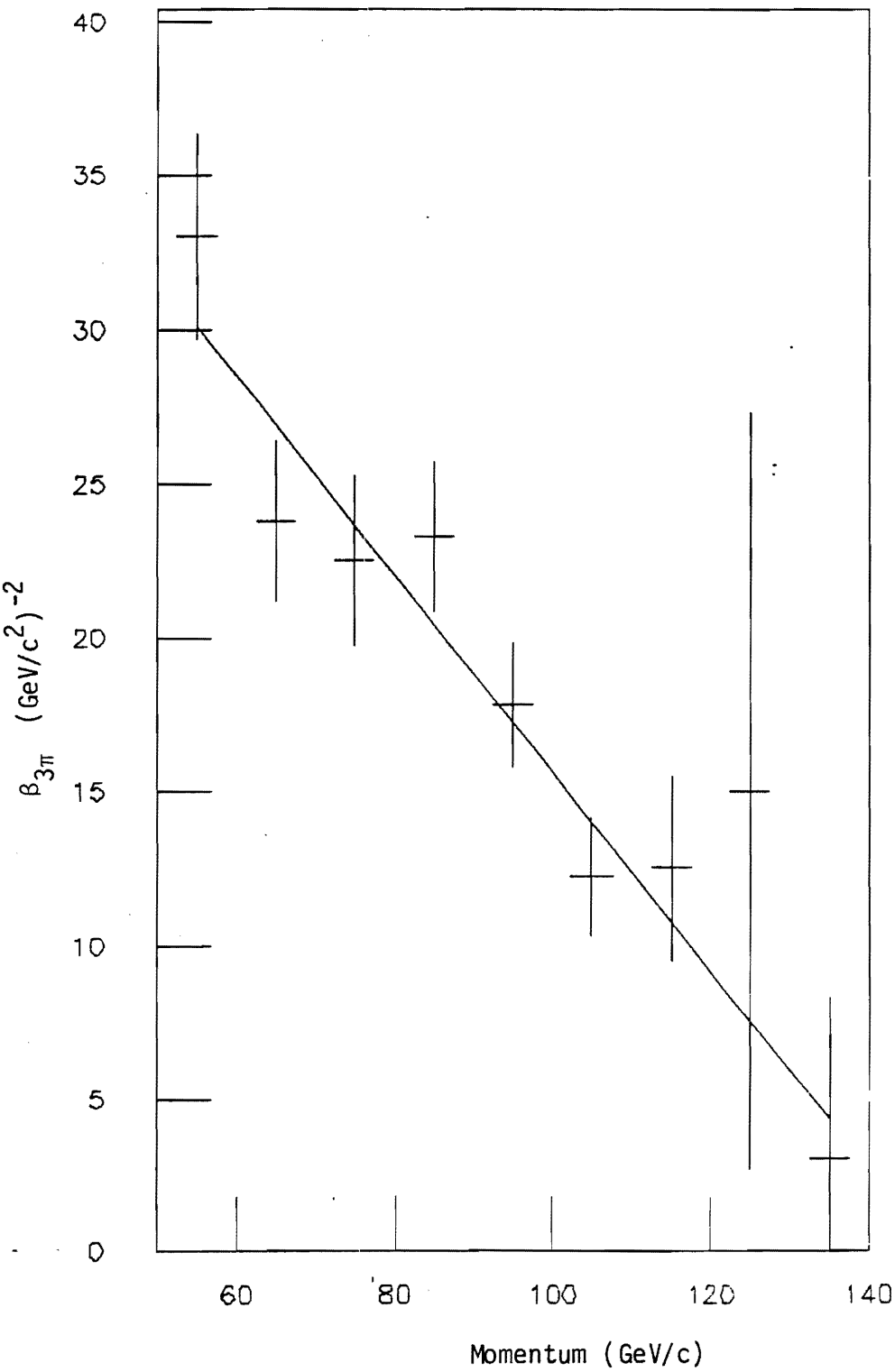
40
35
30
25
20
15
10
5
0
$\beta_{3\pi}$ $(GeV/c^2)^{-2}$
60
80
100
120
140
Momentum (GeV/c)

we discussed these events in Chapter VI. The value of β_n as a function of momentum is displayed in Figure 69 along with a fitted line. The values of β_n were taken from the fit and applied to the final K_L subtraction.

After determining the shape of the neutron-induced background we returned to the dominant $3\pi^o$ contamination. We used the measured $S(m)$ and β_n and allowed γ and $\beta_{3\pi}$ to vary. The resultant values of $\beta_{3\pi}$ as a function of momentum are shown in Figure 70, along with a fitted line. Just as in the neutron case we took the values of the slopes from the fit and refit the data. In the final fit the only parameter allowed to vary was α, the fraction of $K_L \rightarrow 2\pi^o$ signal in the distribution. The K_L data and the fit in each bin of momentum are shown in Figures 71-79. We show the distributions summed over momentum with the two sources of background indicated separately in Figure 80; Figure 81 is the same plot with the two sources summed. The agreement in all cases is excellent.

How can we check our fit to the $3\pi^o$ shape? We can think of no mechanism which would cause the distribution to flatten out or rise as the mass increases in the region of the kaon mass; it is harder to rule out a distribution which falls more rapidly than an exponential. The statistical power of the $3\pi^o$ fit at masses above the kaon mass is not great so it would be helpful to have some independent check of the fit. We have been able to use the Monte Carlo to check the distribution summed over momentum. The limitation on the power of the Monte Carlo was not our understanding of the experiment; rather it was the computer time necessary to generate an appreciable background sample. It took approximately one

second of Cyber 175 time to generate an accepted $3\pi^0$ decay; the statistics of our simulation represent roughly one thousand hours of Cyber 175 time. Figure 82 shows the mass distribution of Figure 81 with the Monte Carlo superimposed. The agreement is adequate within the statistics; the errors on the Monte Carlo and further checks will be discussed in the next Chapter. The number of K_L decays before the subtraction and the summed background subtractions are given in Table 6.

The K_S data, shown earlier, had relatively little contamination in mass. The important subtraction is that of incoherently produced K_S. We fit the K_S mass distribution to the same form as the K_L distribution but allowed an exponential q^2 dependence over the range 10000-50000 (MeV/c) ^{2} in q^2. The q^2 dependence of the number of K_S decays for each momentum bin in shown in Figure 83, along with the fitted exponential. The number of K_S decays for q^2 less than 2500 (MeV/c) ^{2} along with the size of the incoherent subtraction are given in Table 7. The errors quoted in the Table are the statistical errors combined with the fit errors, as described in Chapter VI. The reader will note the deviation of the q^2 distribution from an exponential for $5000 < q^2 < 10000$ (MeV/c) ^{2}; if the deviation is due to 'leakage' of the signal, there is no problem with the fit. If it is due to variations in the acceptance with q^2, our subtraction will be in error. We will return to this point in Chapter VIII.

The remaining subtraction is the subtraction of incoherent K_S from the K_L beam. The statistics for the high q^2 events is poor; we have rebinned that data

Figure 71. The mass distribution of the $K_L \rightarrow \pi^0\pi^0$ sample for $50 < p_K < 60$ GeV/c.

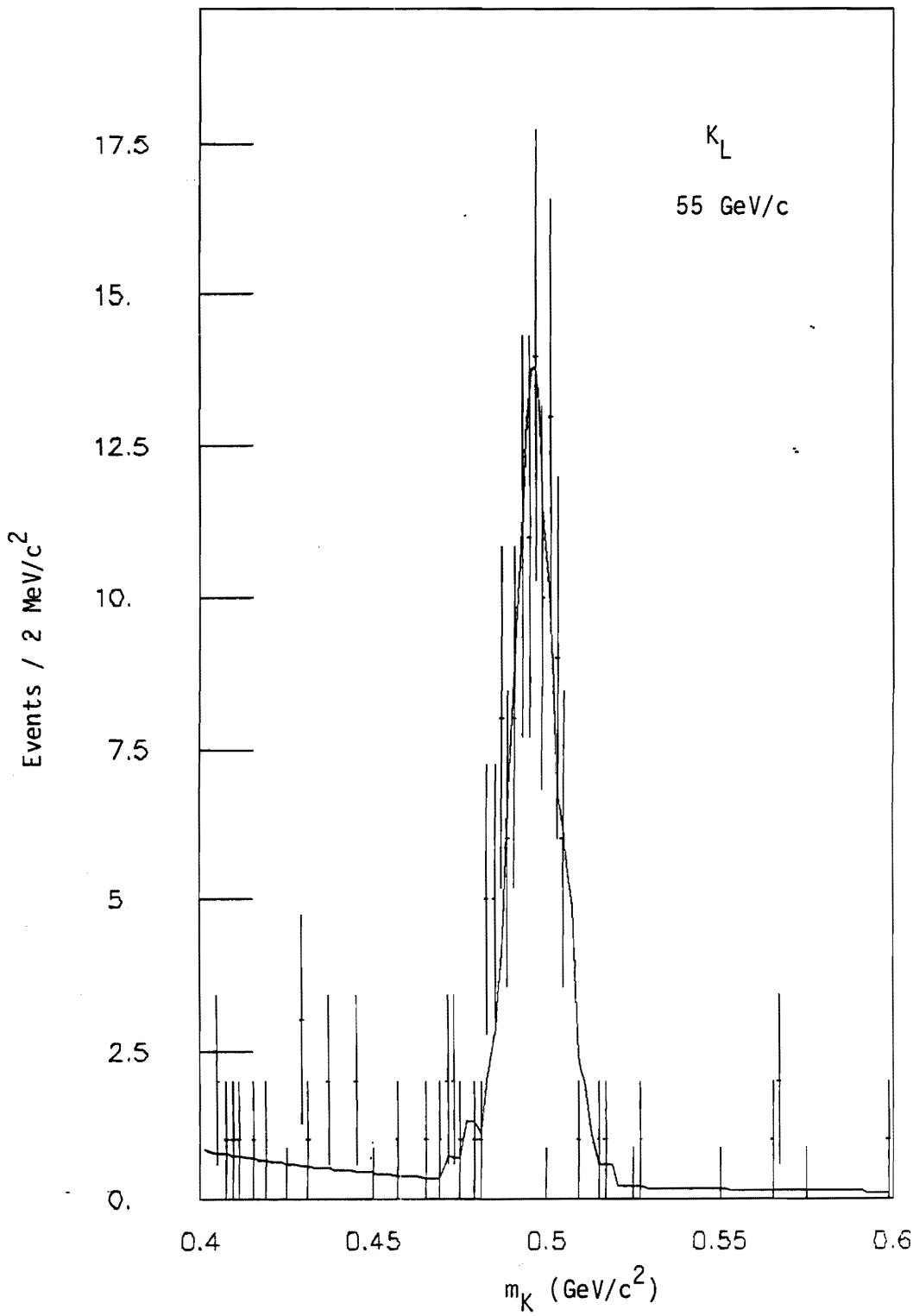
K_L
55 GeV/c
17.5
15.
12.5
10.
7.5
5
2.5
0.
Events / 2 MeV/c^2
0.4
0.45
0.5
0.55
0.6
m_K (GeV/c^2)

Figure 72. The distribution of Figure 71 for 60 $< p_K <$ 70 GeV/c.

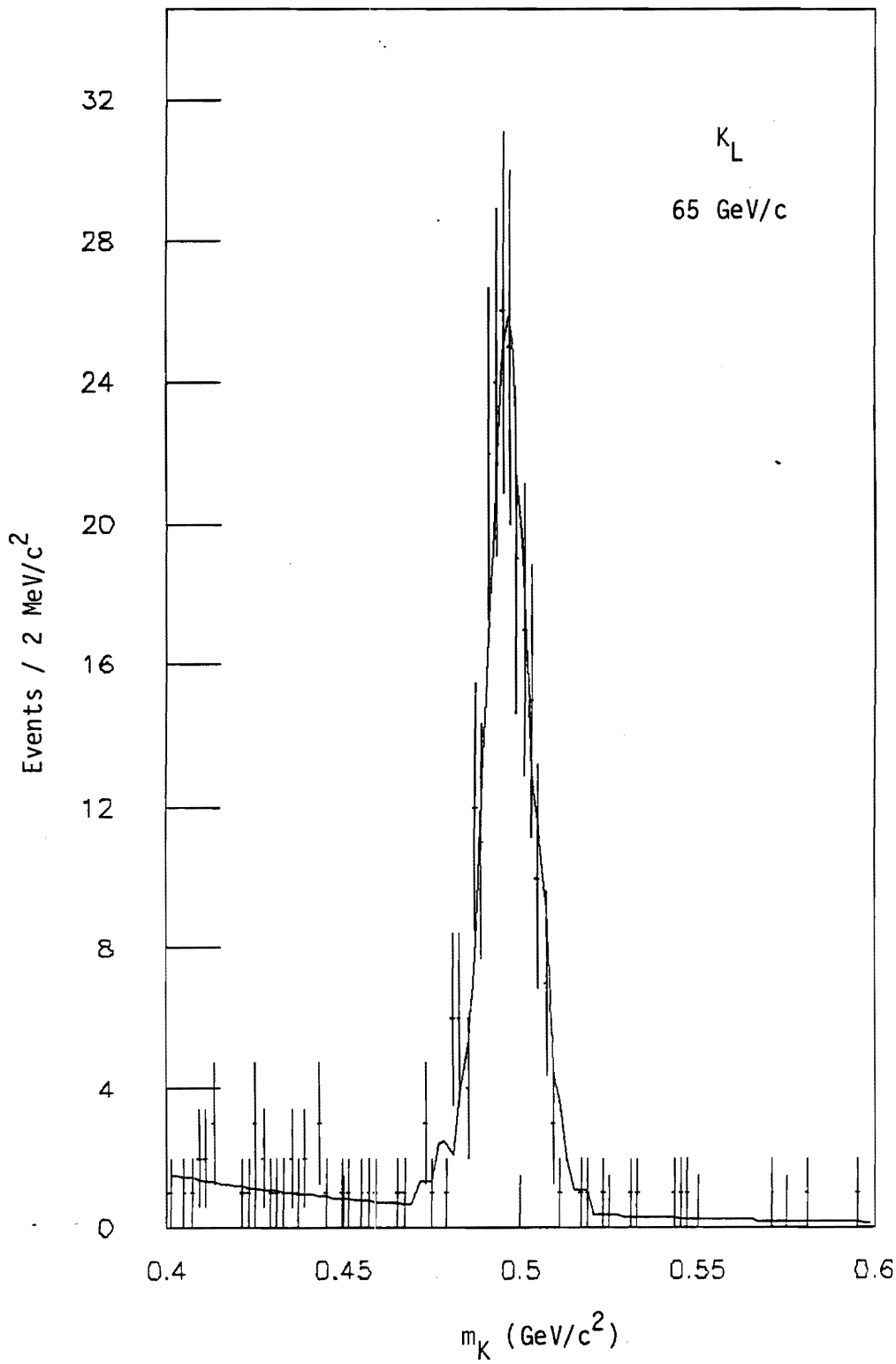
K_L
65 GeV/c
Events / 2 MeV/c^2
32
28
24
20
16
12
8
4
0
0.4
0.45
0.5
0.55
0.6
m_K (GeV/c^2)

Figure 73. The distribution of Figure 71 for 70 $< p_K <$ 80 GeV/c.

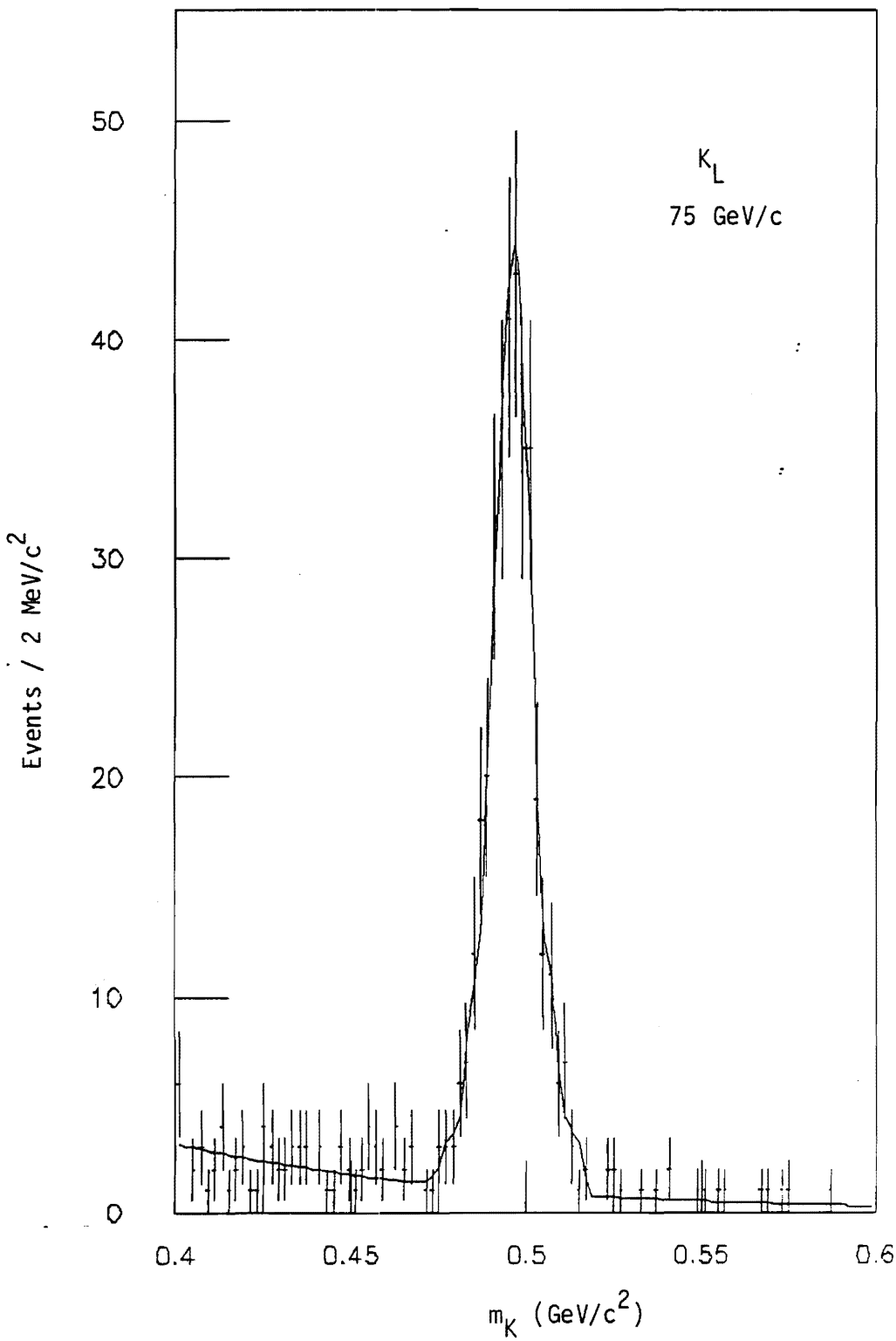
K_L
75 GeV/c
Events / 2 MeV/c^2
0
10
20
30
40
50
0.4
0.45
0.5
0.55
0.6
m_K (GeV/c^2)

Figure 74. The distribution of Figure 71 for 80 $< p_K <$ 90 GeV/c.

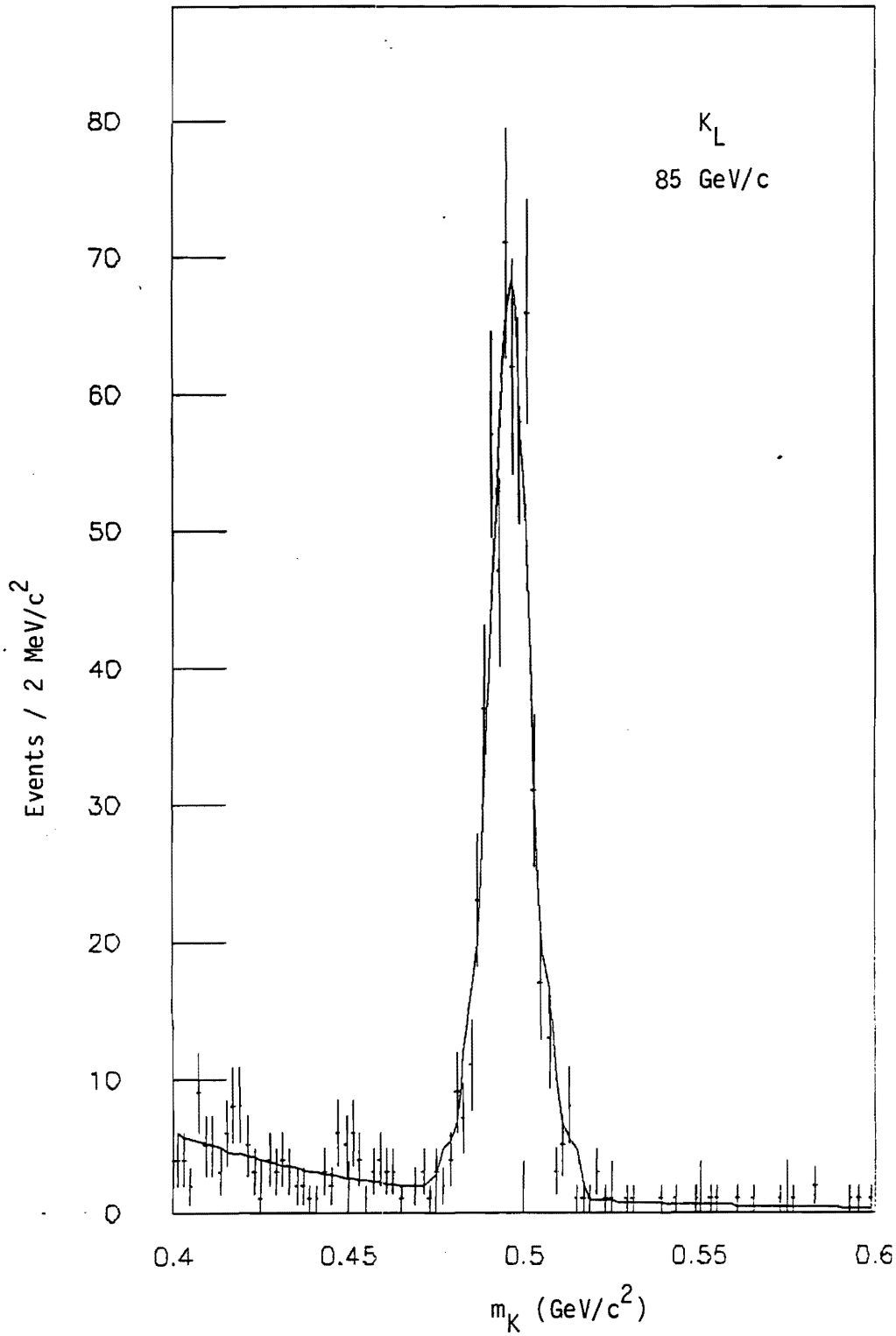
K_L
85 GeV/c
Events / 2 MeV/c^2
80
70
60
50
40
30
20
10
0
0.4
0.45
0.5
0.55
0.6
m_K (GeV/c^2)

Figure 75. The distribution of Figure 71 for 90 $< p_K <$ 100 GeV/c.

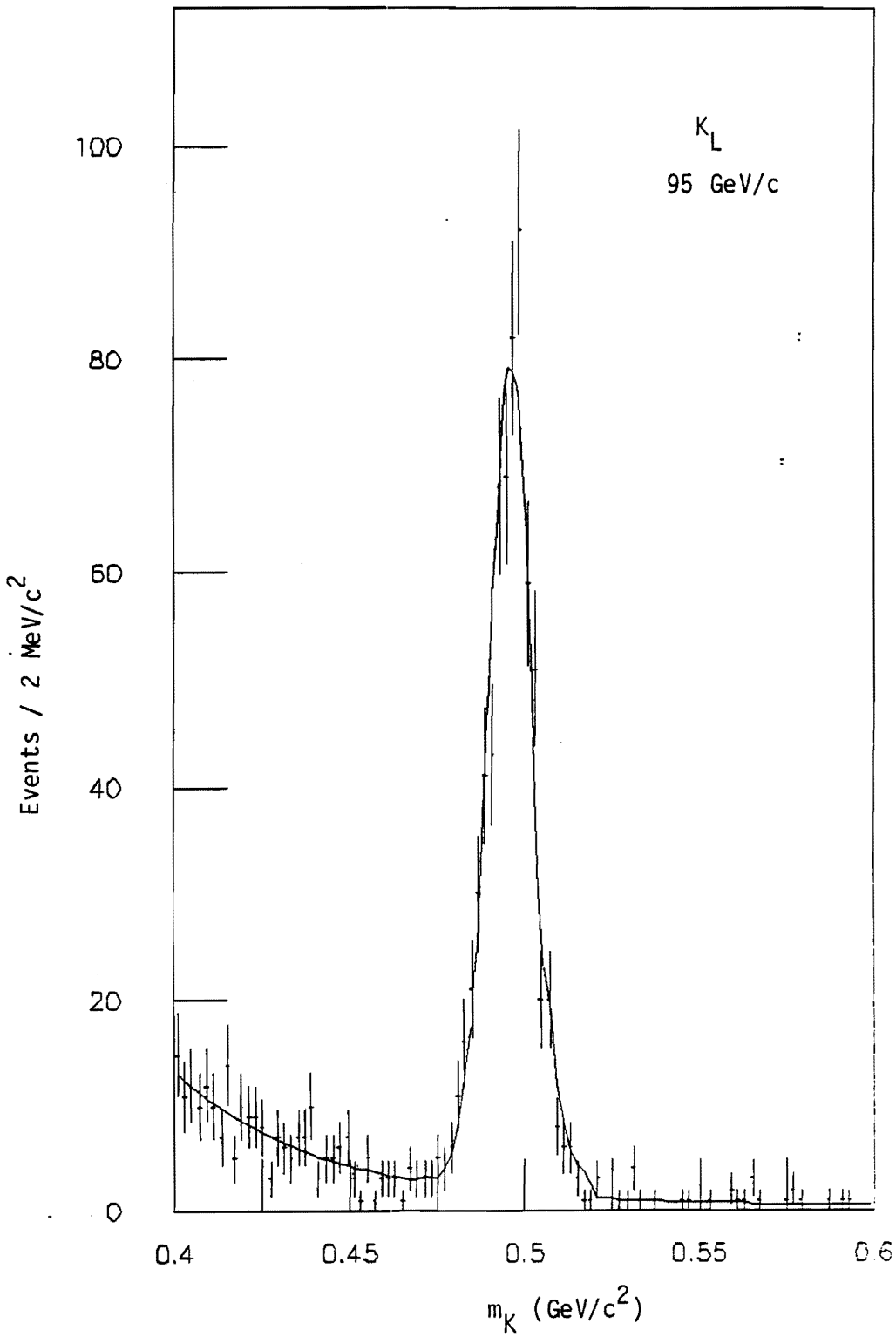
K_L
95 GeV/c
100
80
60
40
20
0
Events / 2 MeV/c^2
0.4
0.45
0.5
0.55
0.6
m_K (GeV/c^2)

Figure 76. The distribution of Figure 71 for 100 $< p_K <$ 110 GeV/c.

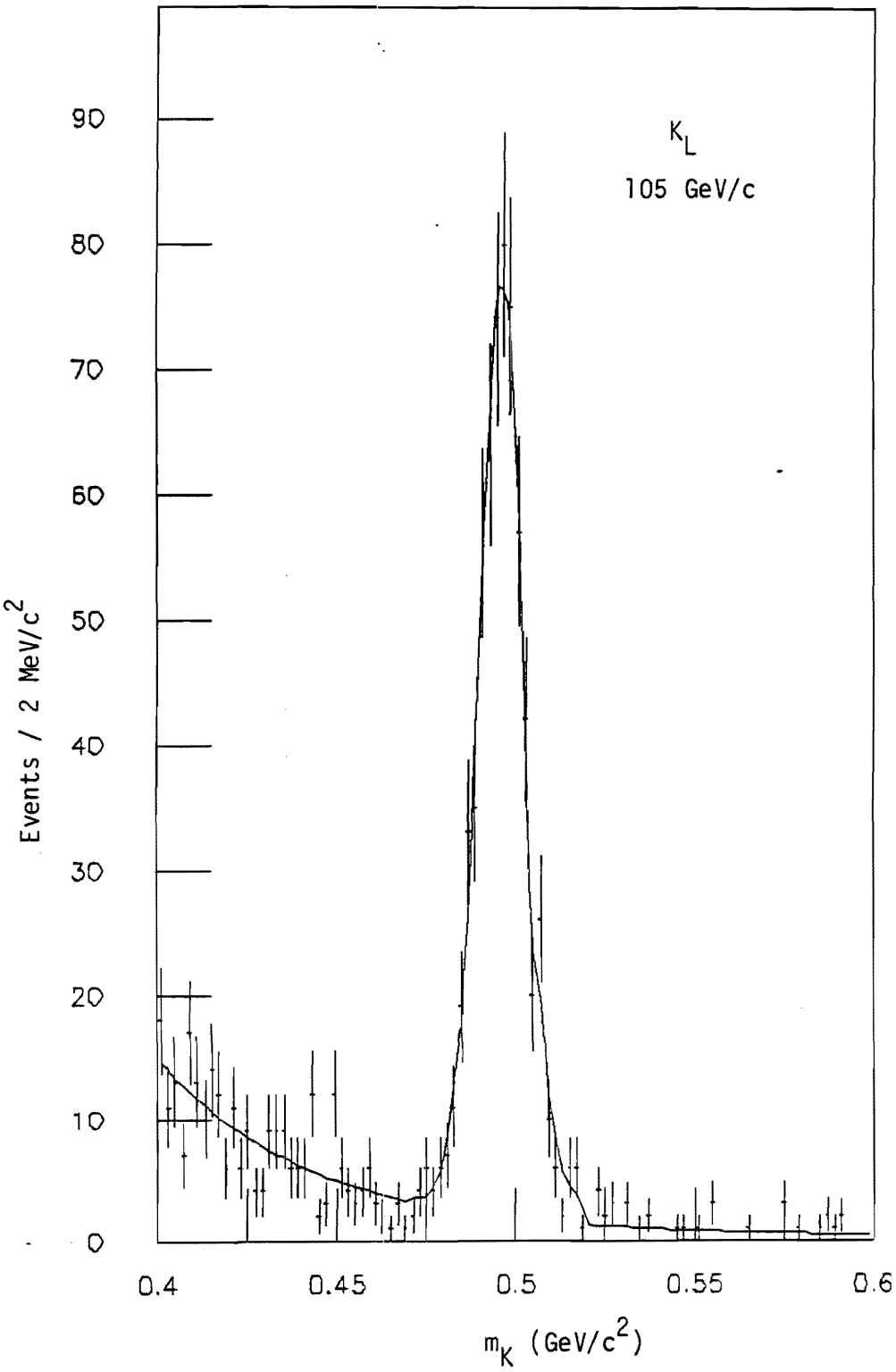
K_L
105 GeV/c
Events / 2 MeV/c^2
90
80
70
60
50
40
30
20
10
0
0.4
0.45
0.5
0.55
0.6
m_K (GeV/c^2)

Figure 77. The distribution of Figure 71 for 110 $< p_K <$ 120 GeV/c.

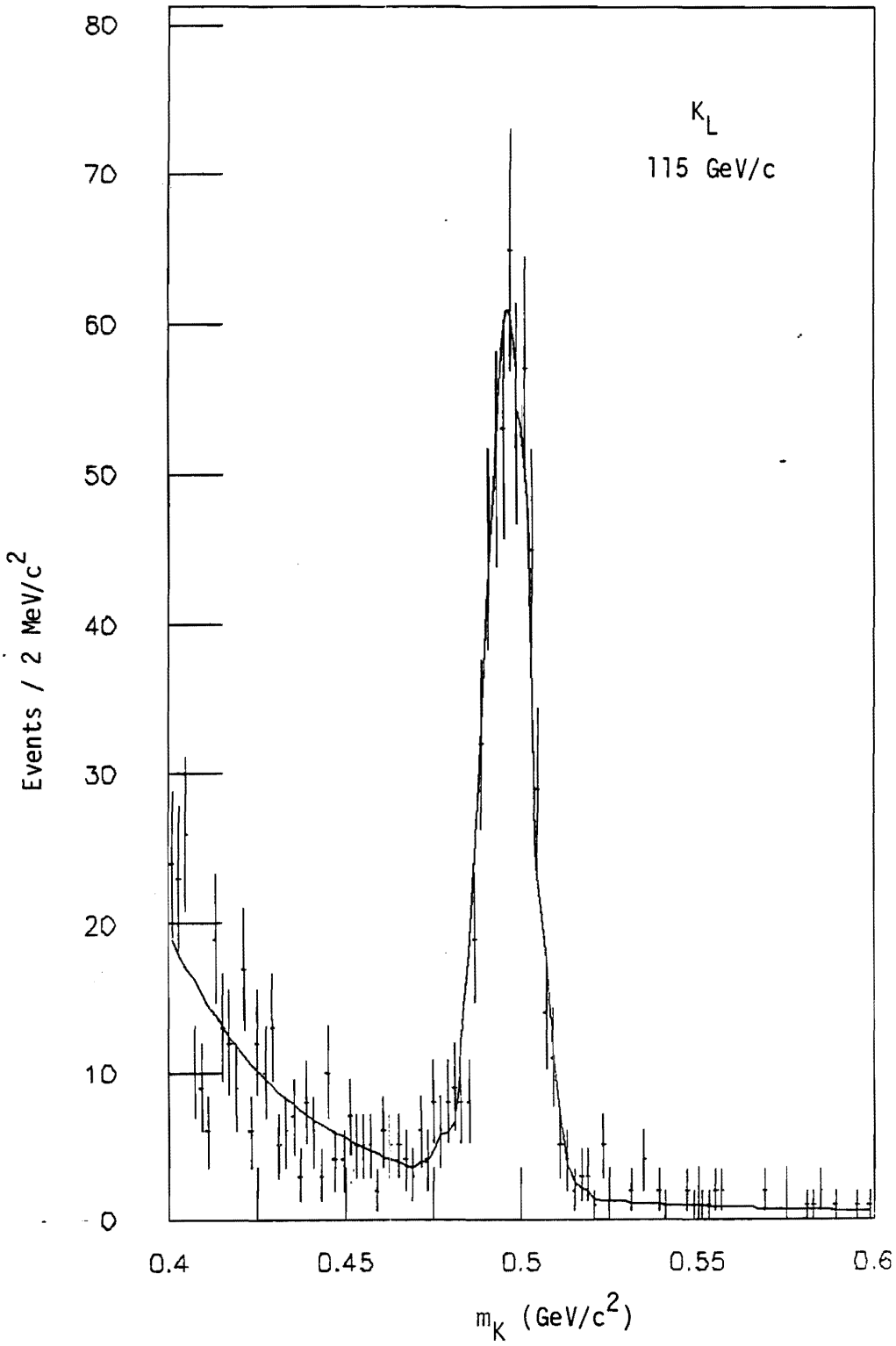
K_L
115 GeV/c
Events / 2 MeV/c^2
80
70
60
50
40
30
20
10
0
0.4
0.45
0.5
0.55
0.6
m_K (GeV/c^2)

Figure 78. The distribution of Figure 71 for 120 $< p_K <$ 130 GeV/c.

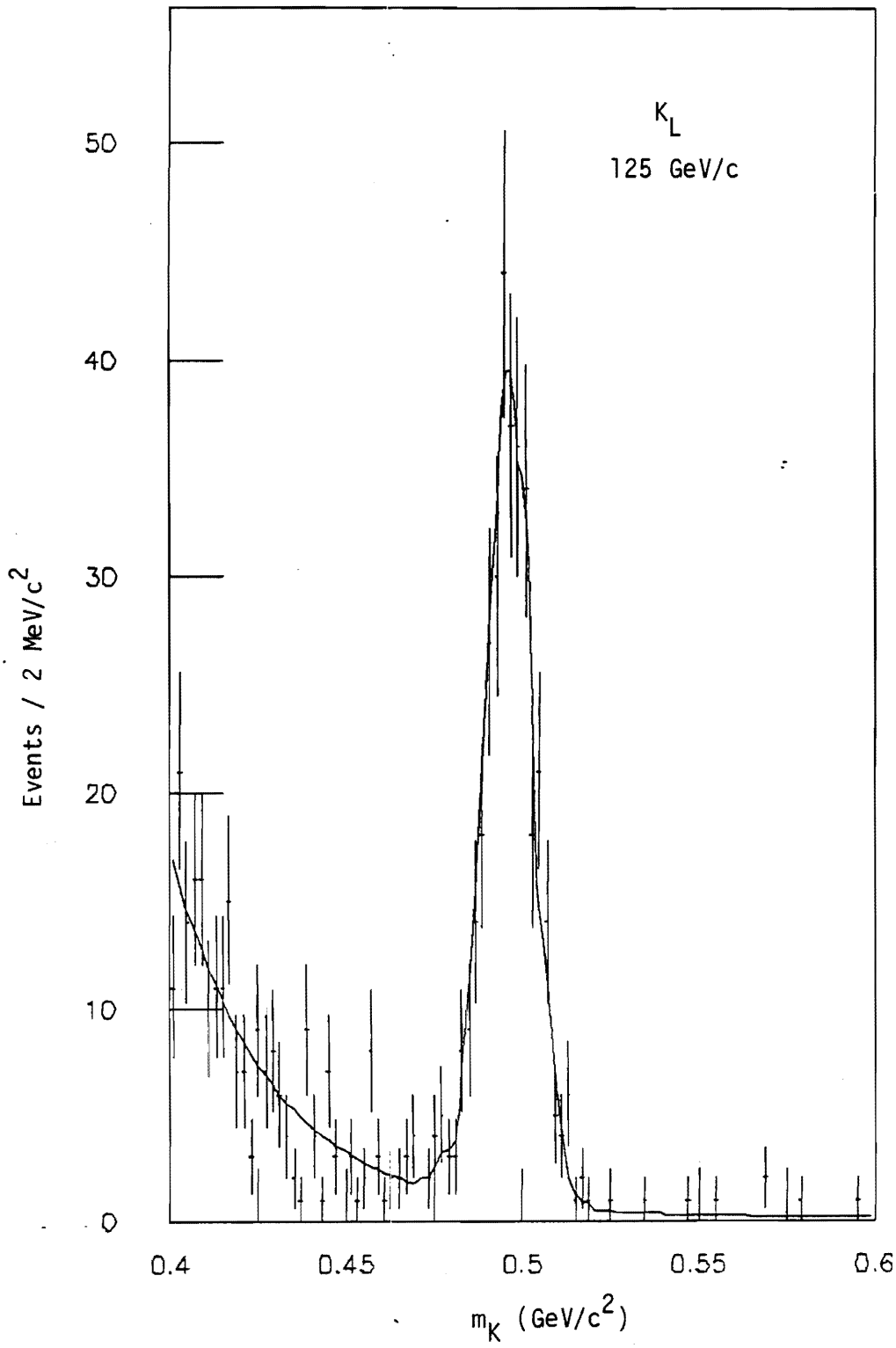
K_L
125 GeV/c
50
40
30
20
10
0
Events / 2 MeV/c^2
0.4
0.45
0.5
0.55
0.6
m_K (GeV/c^2)

Figure 79. The distribution of Figure 72 for 130 $< p_K <$ 140 GeV/c.

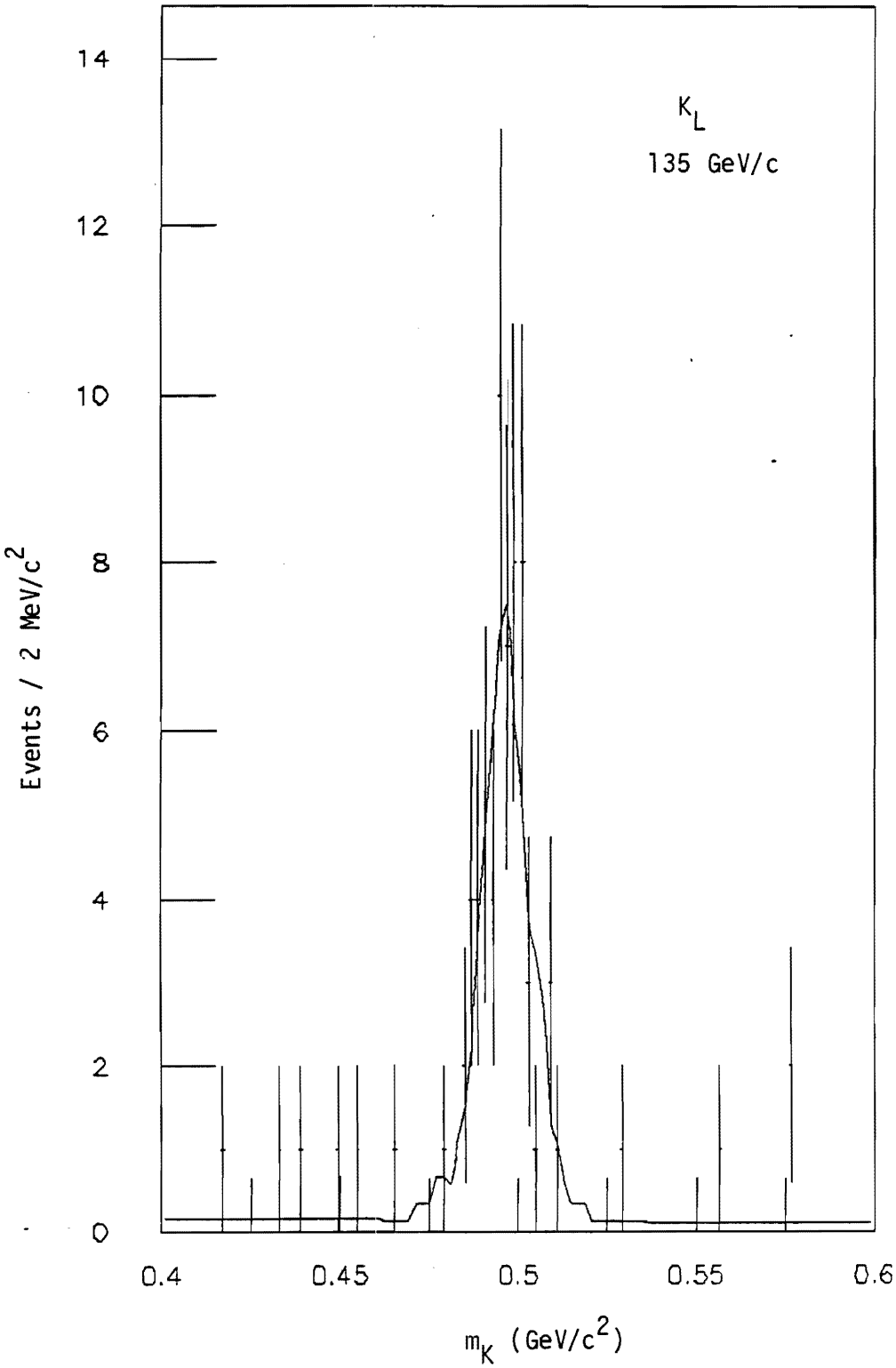
K_L
135 GeV/c
Events / 2 MeV/c^2
0
2
4
6
8
10
12
14
0.4
0.45
0.5
0.55
0.6
m_K (GeV/c^2)

Figure 80. The global $K_L \rightarrow \pi^0\pi^0$ distribution with the $3\pi^0$ and neutron backgrounds indicated separately.

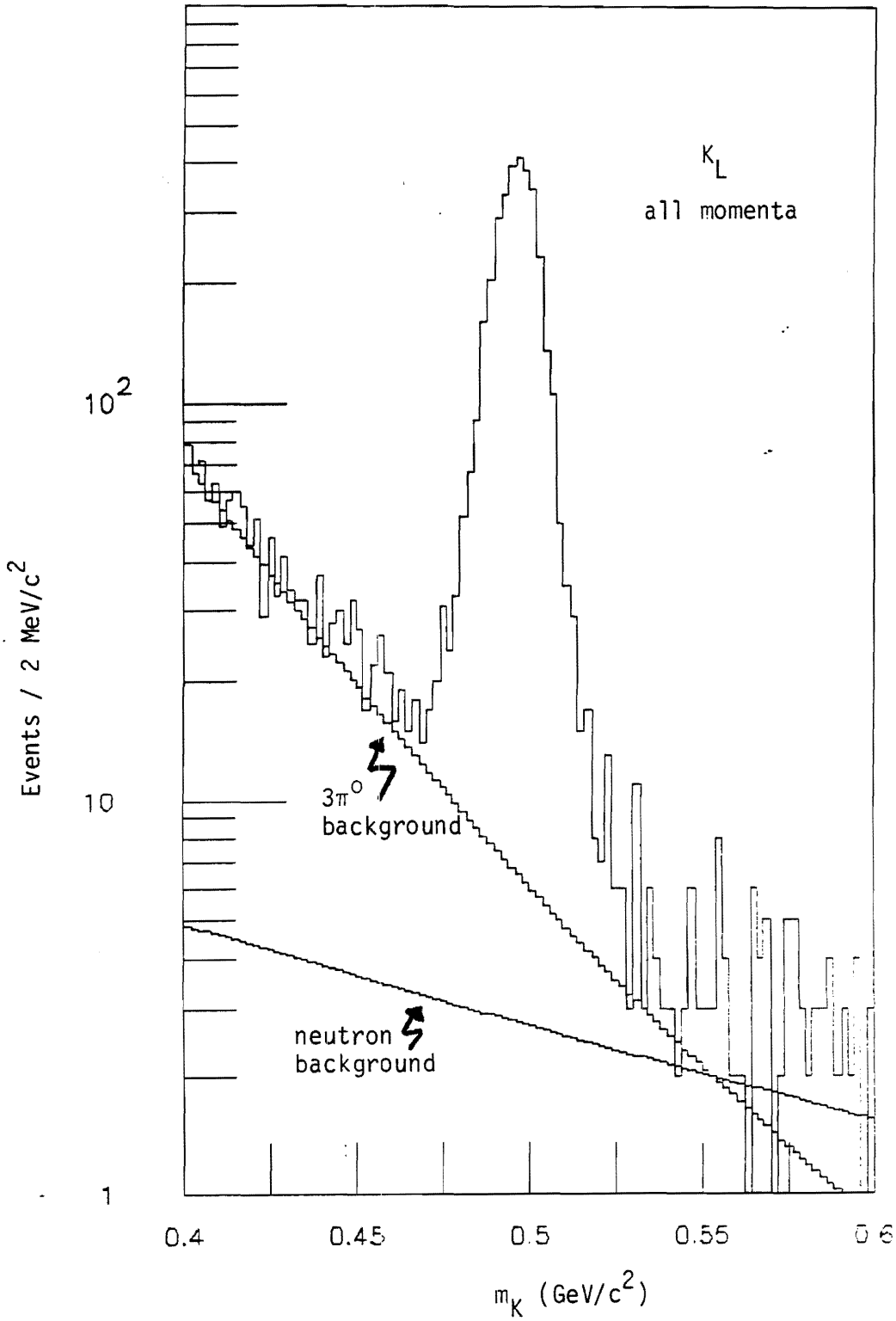
K_L
all momenta
10^2
10
1
Events / 2 MeV/c^2
$3\pi^0$
background
neutron
background
0.4
0.45
0.5
0.55
0.6
m_K (GeV/c^2)

Figure 81. The distribution of Figure 80 with the two sources of backgrounds summed.

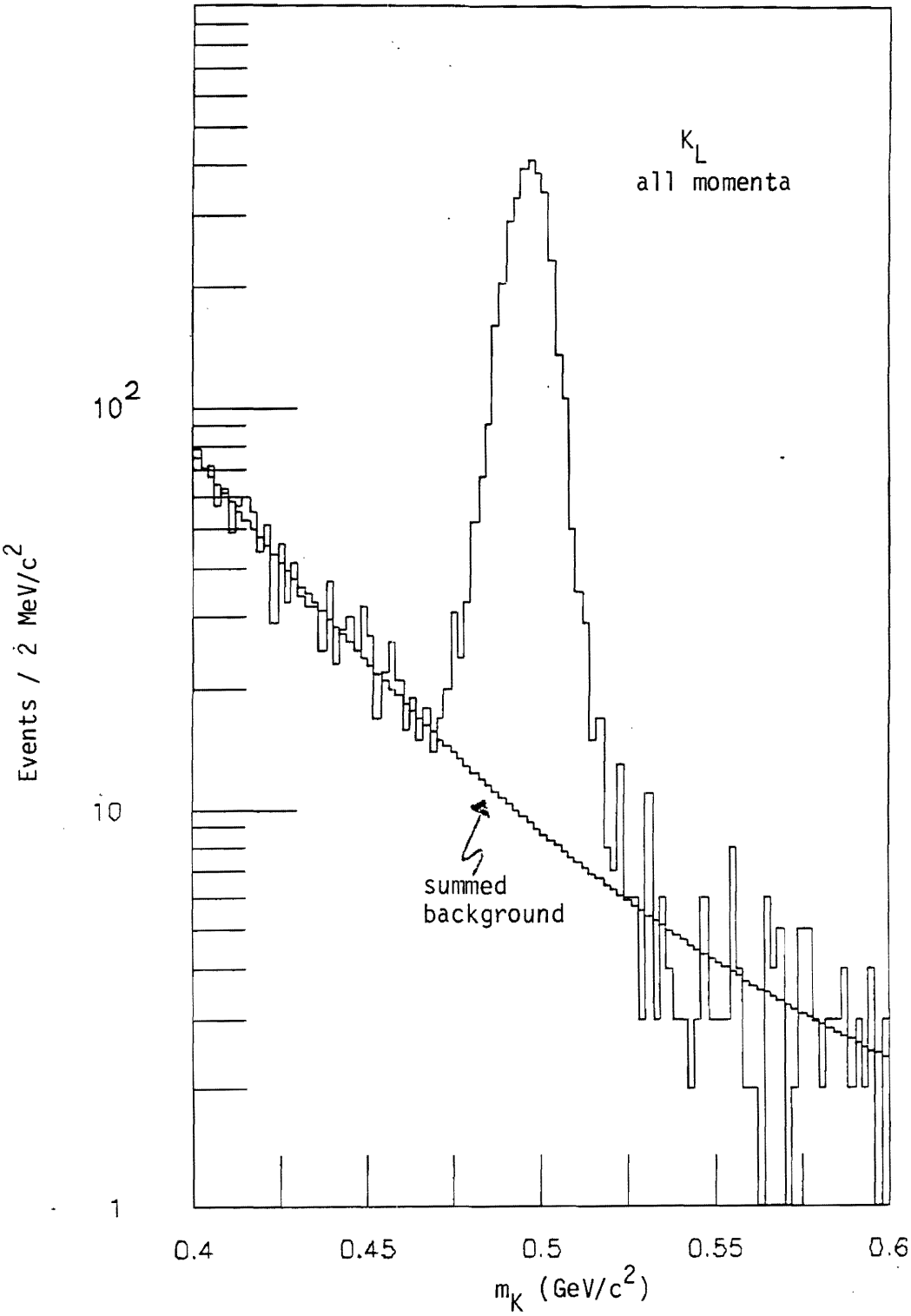
K_L
all momenta
summed
background
10^2
10
1
Events / 2 MeV/c^2
0.4
0.45
0.5
0.55
0.6
m_K (GeV/c^2)

Figure 82. The distribution of Figure 80, rebinned, with the Monte Carlo superimposed. The bins are now 10 MeV/c^2. The Monte Carlo has been scaled upwards by a factor of seven.

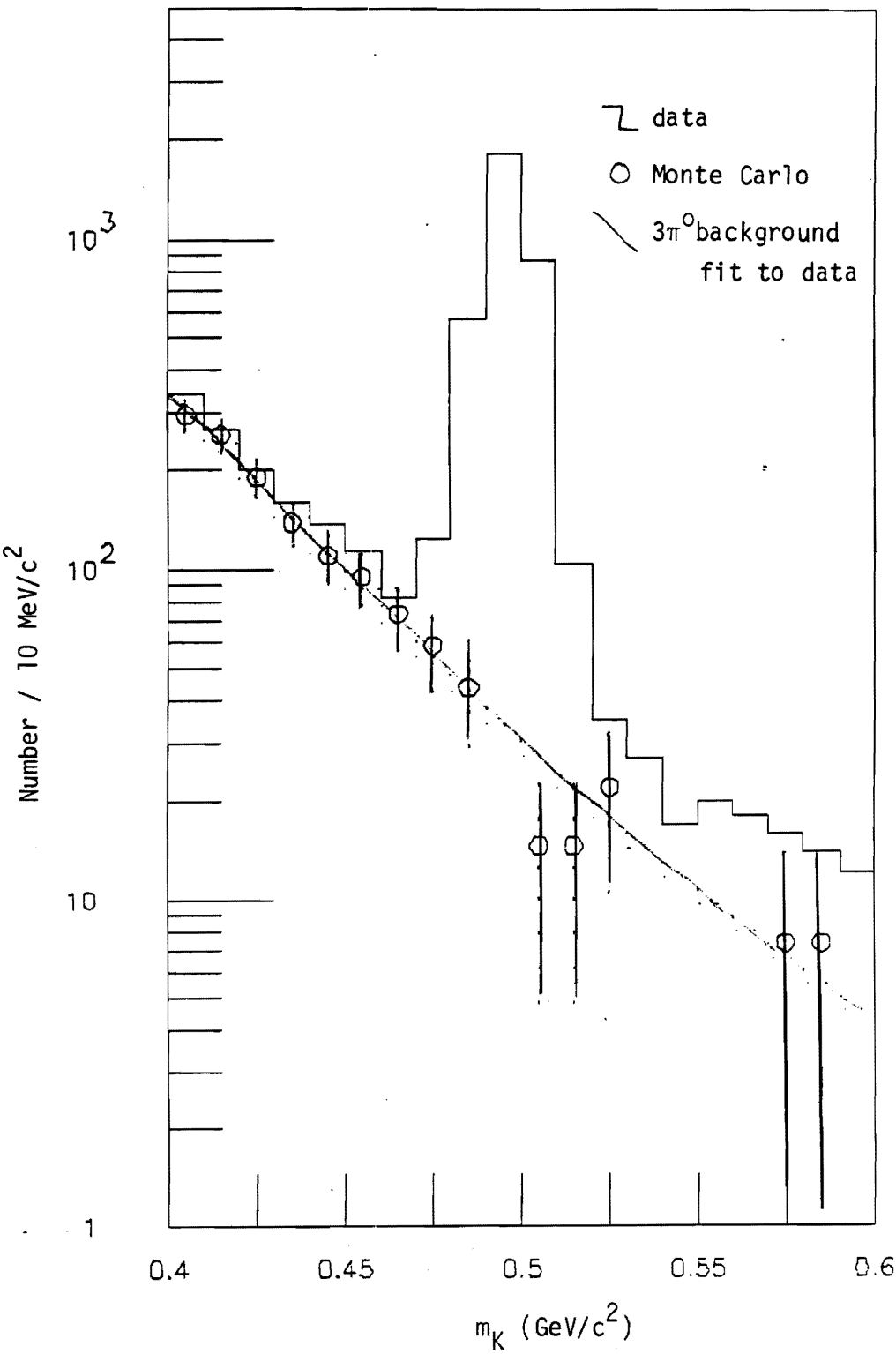
data
Monte Carlo
3π⁰background
fit to data
10³
10²
10
1
Number / 10 MeV/c²
0.4
0.45
0.5
0.55
0.6
m_K (GeV/c²)

Figure 83. The q^2 dependence of the $K_S \rightarrow \pi^o\pi^o$ sample in each bin of kaon momentum. An exponential fit to the inelastic contribution is indicated.

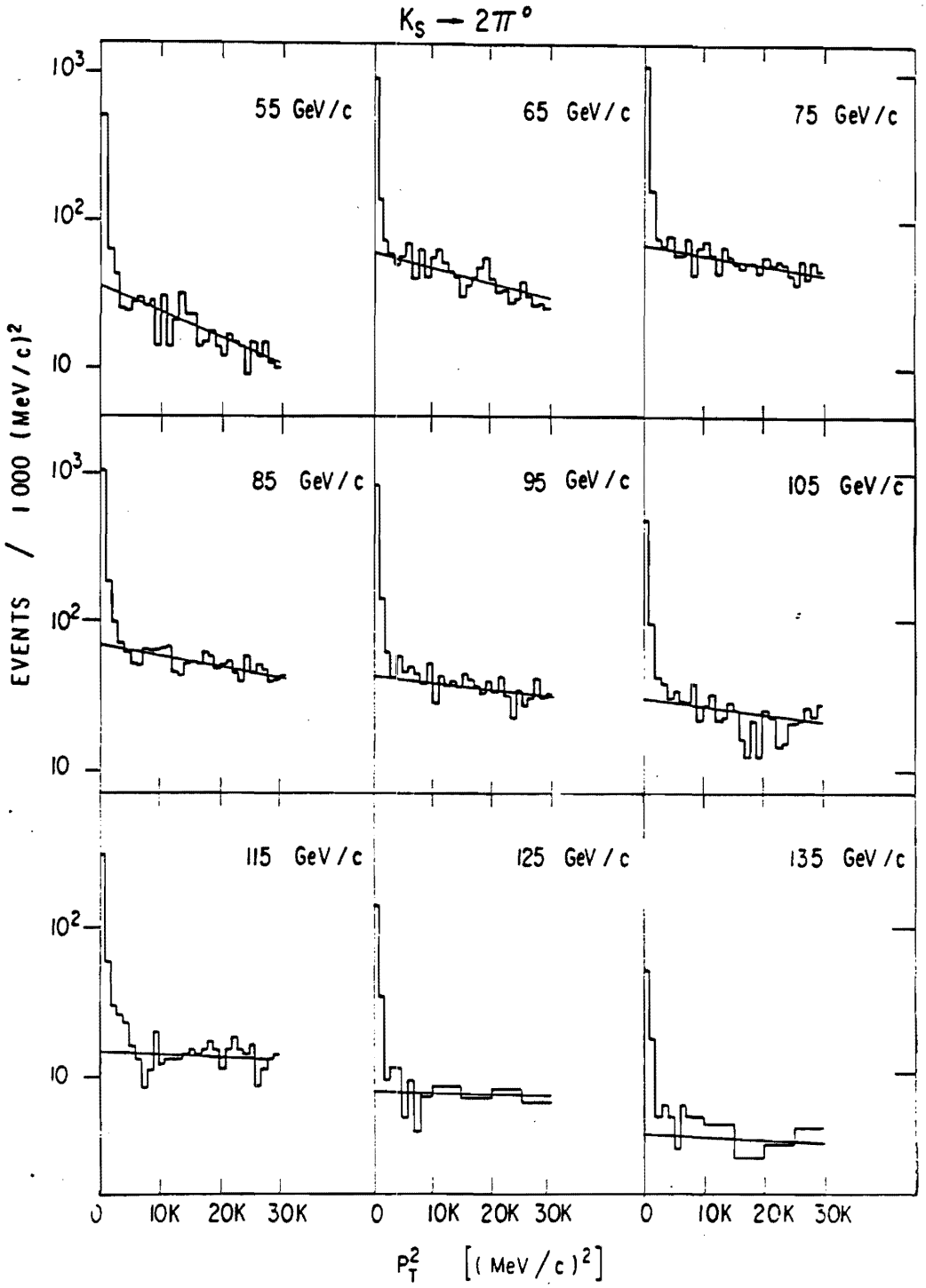
$K_S \to 2\pi^0$
55 GeV/c
65 GeV/c
75 GeV/c
85 GeV/c
95 GeV/c
105 GeV/c
115 GeV/c
125 GeV/c
135 GeV/c
EVENTS / 1 000 (MeV/c)^2
10^3
10^2
10
0
10K
20K
30K
P_T^2 [(MeV/c)^2]

Figure 84. The q^2 dependence of the $K_L \rightarrow \pi^o \pi^o$ sample for $70 < p_K < 90$ GeV/c.

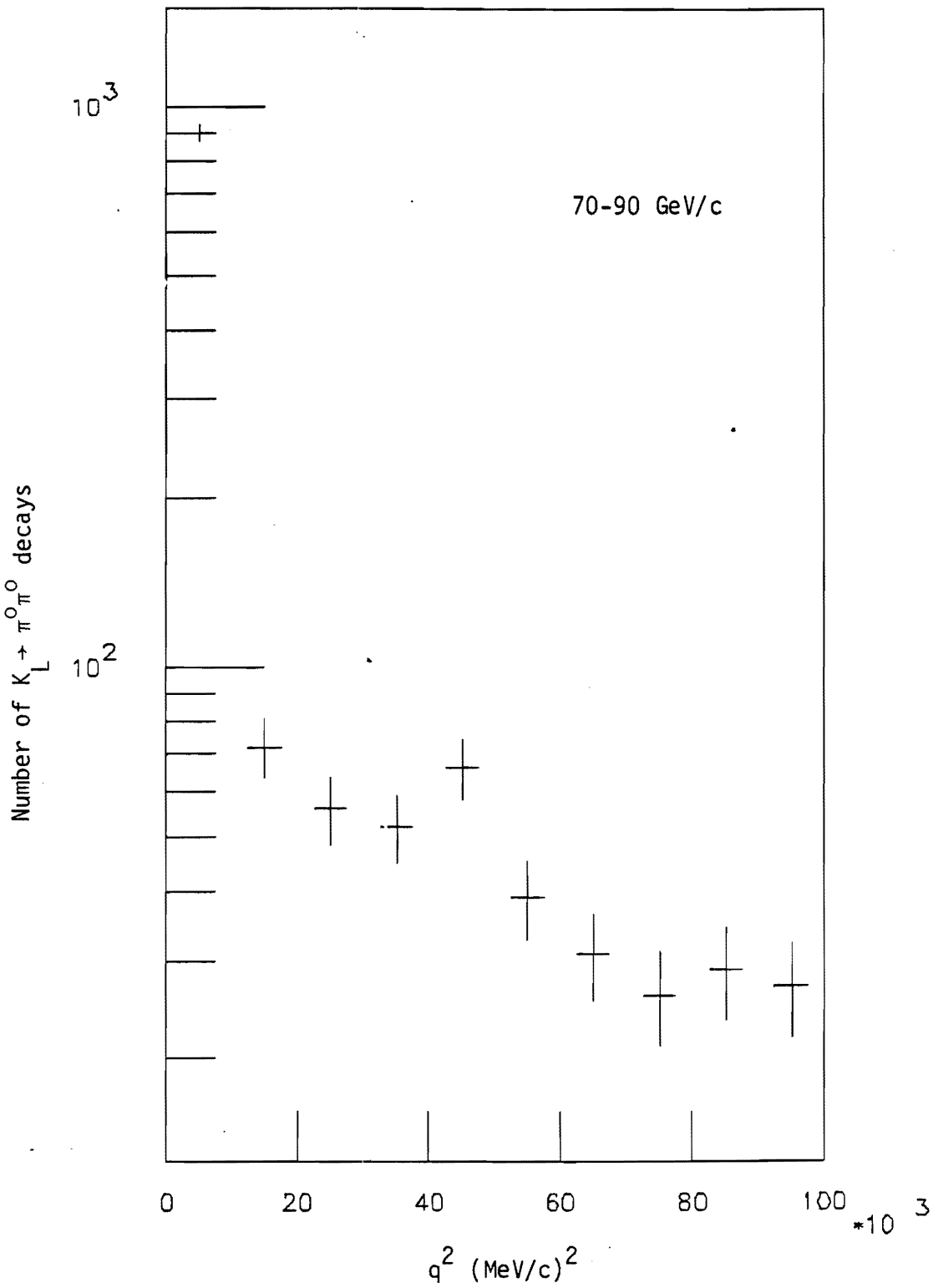
70-90 GeV/c
10^3
10^2
Number of $K_L \to \pi^0\pi^0$ decays
0
20
40
60
80
100
$*10^3$
q^2 $(MeV/c)^2$

into four momentum bins. A typical bin and the fit are shown in Figure 84. We measured an contamination of 2.8% in all momentum bins within statistical errors and have used this average to correct the data. The subtraction is larger than the 0.3% in the charged mode because the resolution requires we cut at 2500 $(\mathrm{MeV/c})^2$ in the neutral mode instead of the 300 $(\mathrm{MeV/c})^2$ of the charged mode. The final number of K_L with their statistical errors appear in Table 6.

TABLE 6

NUMBER OF $K_L \to \pi^0\pi^0$

p_K	Raw	Background	Background Subtracted	Final
55	344	24.5	319.5	310.5±19.2
65	544	55.4	488.6	474.9±24.5
75	652	51.6	600.4	583.6±26.5
85	670	49.9	620.1	602.7±26.8
95	548	36.7	511.3	497.0±24.2
105	355	23.9	331.1	321.8±19.5
115	216	13.0	202.9	197.2±15.1
125	115	7.63	107.4	104.4±11.1
135	62	3.02	59.0	57.3±8.1
Σ	3506	266	3240.3	3149.6

TABLE 7

NUMBER OF $K_S \rightarrow \pi^0\pi^0$

p_K	Raw	After $3\pi^0$,neutron subt.	Inelastic Sub.	Final
55	586	579.	84.6±8.6	494.4±25.6
65	1092	1086.	151.7±9.12	934.3±35.2
75	1319	1312.	168.2±8.9	1143.8±38.1
85	1252	1249.	170.7±9.2	1078.3±37.1
95	1031	1025.	107.1±6.9	917.9±32.7
105	623	619.	78.3±5.7	540.7±25.6
115	382	380.6	37.0±3.8	343.6±20.1
125	170	169.1	18.7±2.9	150.4±13.5
135	69	69.	9.43±1.92	59.6±8.52
Σ	6524	6488.7	825.7	5663.

CHAPTER VIII

EXTRACTION OF $|\epsilon' /\epsilon|$

We have now determined the numbers of $K \rightarrow 2\pi^o$ and $K \rightarrow \pi^+\pi^-$ decays in each of the two beams. This Chapter will use the technique described in Chapter II to determine $|\epsilon' /\epsilon|$. We will check our result by a variety of methods which will probe our sensitivity to various systematic errors. We conclude with a discussion of the systematic errors.

A. Determination of $|\epsilon' /\epsilon|$

Equations (2.7) and (2.8) allow us to determine $|\eta_{oo}/\eta_{+-}|$. Before fitting for the ratio we can determine ρ by assuming a value for η_{oo} and η_{+-}, and check that our value of ρ has the correct size and momentum dependence. In the analysis $(f - \bar{f})/k$, defined in Appendix I, is a more convenient quantity than ρ, because $(f - \bar{f})/k$ is only a function of the kaon momentum and the atomic weight of the regenerator; ρ is additionally dependent on the length and density of the particular regenerator. The relationship between $(f - \bar{f})/k$ and ρ is given in Appendix I. We can easily compare a measurement of $(f - \bar{f})/k$ to other determinations; a series of

measurements has obtained $|(f-\bar{f})/k|$ for a variety of materials (Gsponer *et.al.*[47]). Among these experiments was E82 at Fermilab, which determined $|(f-\bar{f})/k|$ for Carbon (some of the members of the present experiment performed those experiments as well). The result for all elements was that

$$|(f-\bar{f})/k| = 2.23\ A^{0.758\pm0.003}\ p^{-0.614}\ mb. \tag{8.1}$$

The momentum dependence of the regeneration amplitude is predicted by Regge theory to be the same for all elements[48] because the ω trajectory dominates the regeneration process but the atomic weight dependence is an empirical fit. For Carbon, equation (8.1) implies:

$$|(f-\bar{f})/k| = 14.67\ p^{-0.614}\ mb. \tag{8.2}$$

The phase of $(f-\bar{f})/k$ was determined[49] to be $\Phi = -(125\pm1.6)^o$. A plot of $|(f-\bar{f})/k|$ for Carbon as a function of momentum measured in E82 appears in Figure 85; note that since $|(f-\bar{f})/k|$ has a power law dependence on momentum, the points fall on a straight line on a log-log plot.

Recall that in the discussion of equations (2.7) and (2.8) we stressed that only ρ/η is determined. We must therefore assume a value for η in order to compare our results with those of the previous experiment; we use the value favored by E82, $\eta = 2.199\times10^{-3}$. The other constants used in the fit appear in Table 8. We have included the effect of the regeneration in the lead plug downstream of the regenerator[50] and of the absorption in the movable Carbon absorber in all of the fits to be discussed. Varying any of the 'standard' parameters such as Δm by 1σ produces a negligible change in our results so we have fixed these parameters at

their central values.

To perform the fits we need the acceptance-corrected ratios of vacuum to regenerated beam decays; the acceptances are given in Appendix II. The acceptance ratios for both the charged and neutral modes appear in Table 14 and 15. The statistical errors quoted in Tables 4-7 will determine the errors quoted in this section.

We begin by determining $|(f-\bar{f})/k|$ in each of the nine momentum bins of the charged mode data by using equations (2.8) and (8.2). The values appear in Table 9. We may then fit the dependence of $|(f-\bar{f})/k|$ on momentum to a power law; the fit yields:

$$|(f-\bar{f})/k| = (15.08 \pm 1.43)\ p^{-0.610 \pm 0.023}\ mb. \tag{8.3}$$

with a χ^2 of 10.9 for 7 degrees of freedom. The fit is displayed in Figure 86. The slope is in excellent agreement with equation (8.2) and increases our confidence that there are no large systematic errors in the charged mode. If, however, we freeze the power law to $p^{-0.614}$ then we find

$$|(f-\bar{f})/k| = (15.28 \pm 0.11)\ p^{-0.614}\ mb \tag{8.3a}$$

and the magnitude does not agree with the E82 value for Carbon. There are several differences in the analyses which make us think this difference is not significant. E82 normalized to semileptonic decays while we normalize to the $2\pi^0$ decay. Furthermore, a careful comparison of the magnitude would have to take into account systematic errors in the kaon absorption in both experiments. (For our experiment, a knowledge of the precise amount of absorption is not significant because the amount cancels between the charged and neutral modes.) Hence a com-

TABLE 8

CONSTANTS USED IN THE FITS

Constant	Value
Δm	0.5349×10^{-10} h sec^{-1}
τ_S	0.8923×10^{-10} sec $^{-1}$
η_{+-}	2.199×10^{-3}
Φ_ϵ	44.9^o
Φ_ρ, ^{12}C	125°
density of ^{12}C	1.73 g/cm^3
density of ^{207}Pb	11.35 gm/cm^3
$(f - \bar{f})/k$ for Pb	$150.7 p^{-0.654} e^{-i\, 122.2\pi/180}$
Absorption: σ_T, ^{12}C	188 mb.
Absorption: σ_T, ^{207}Pb	2050 mb.

The values for σ_T and $(f - \bar{f})/k$ are derived from References 28 and 49.

The values for η_{+-} and Φ_ρ also come from Reference 49.

TABLE 9

$|(f-\bar{f})/k|$(mb.) IN THE CHARGED AND NEUTRAL MODES

p_K	charged mode	neutral mode
35	1.746±0.045	--
45	1.466±0.026	--
55	1.272±0.020	1.286±0.061
65	1.219±0.020	1.201±0.044
75	1.077±0.019	1.057±0.0346
85	1.018±0.021	0.945±0.031
95	0.913±0.024	0.922±0.033
105	0.847±0.029	0.872±0.039
115	0.872±0.041	0.900±0.050
125	--	0.841±0.0675
135	--	0.742±0.086

Figure 85. $|(f - \bar{f})/k|$ for Carbon as measured by E82.

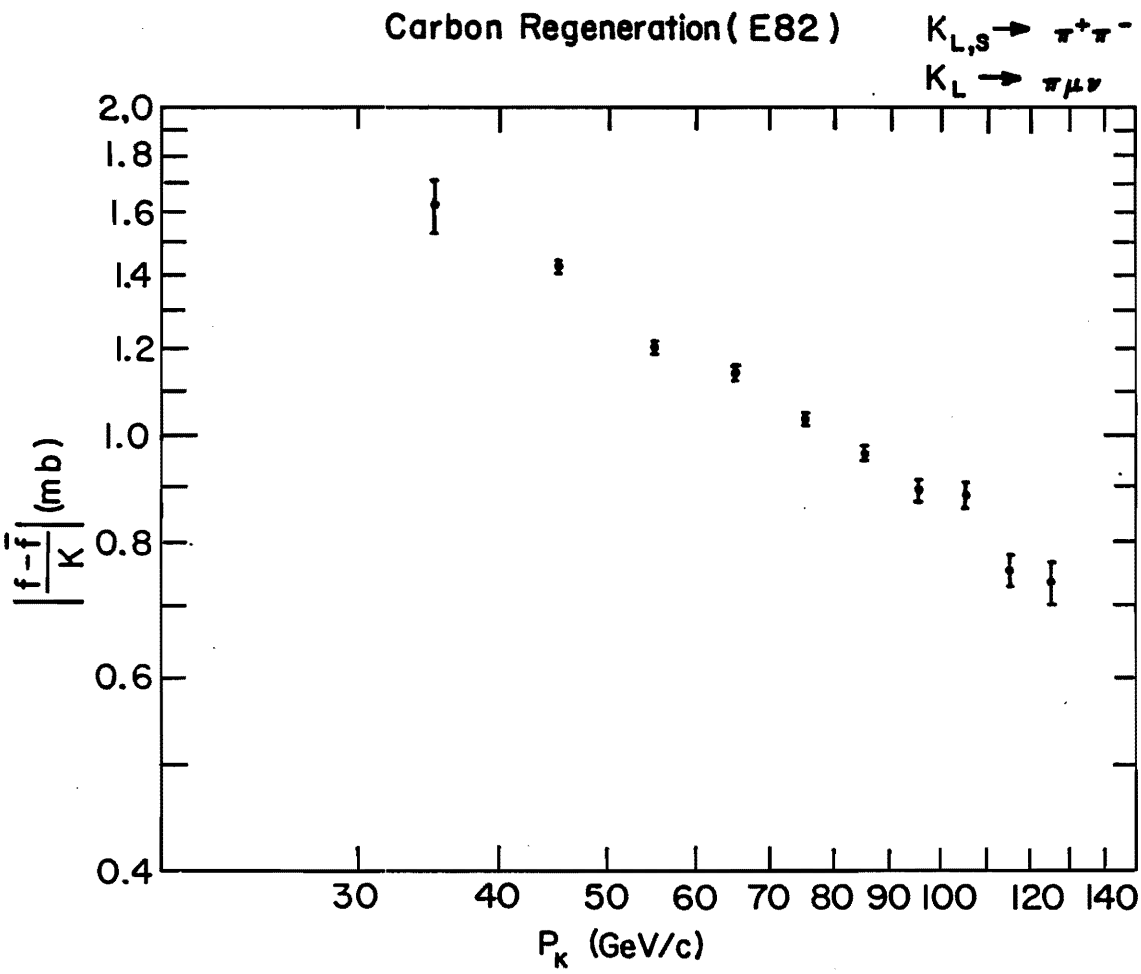
Carbon Regeneration (E82)
$K_{L,S} \rightarrow \pi^+\pi^-$
$K_L \rightarrow \pi\mu\nu$
2.0
1.8
1.6
1.4
1.2
1.0
0.8
0.6
0.4
$\left|\frac{f-\bar{f}}{K}\right|$ (mb)
30
40
50
60
70
80
90
100
120
140
P_K (GeV/c)

Figure 86. $|(f-\bar{f})/k|$ for Carbon as measured by the present experiment, in the charged mode.

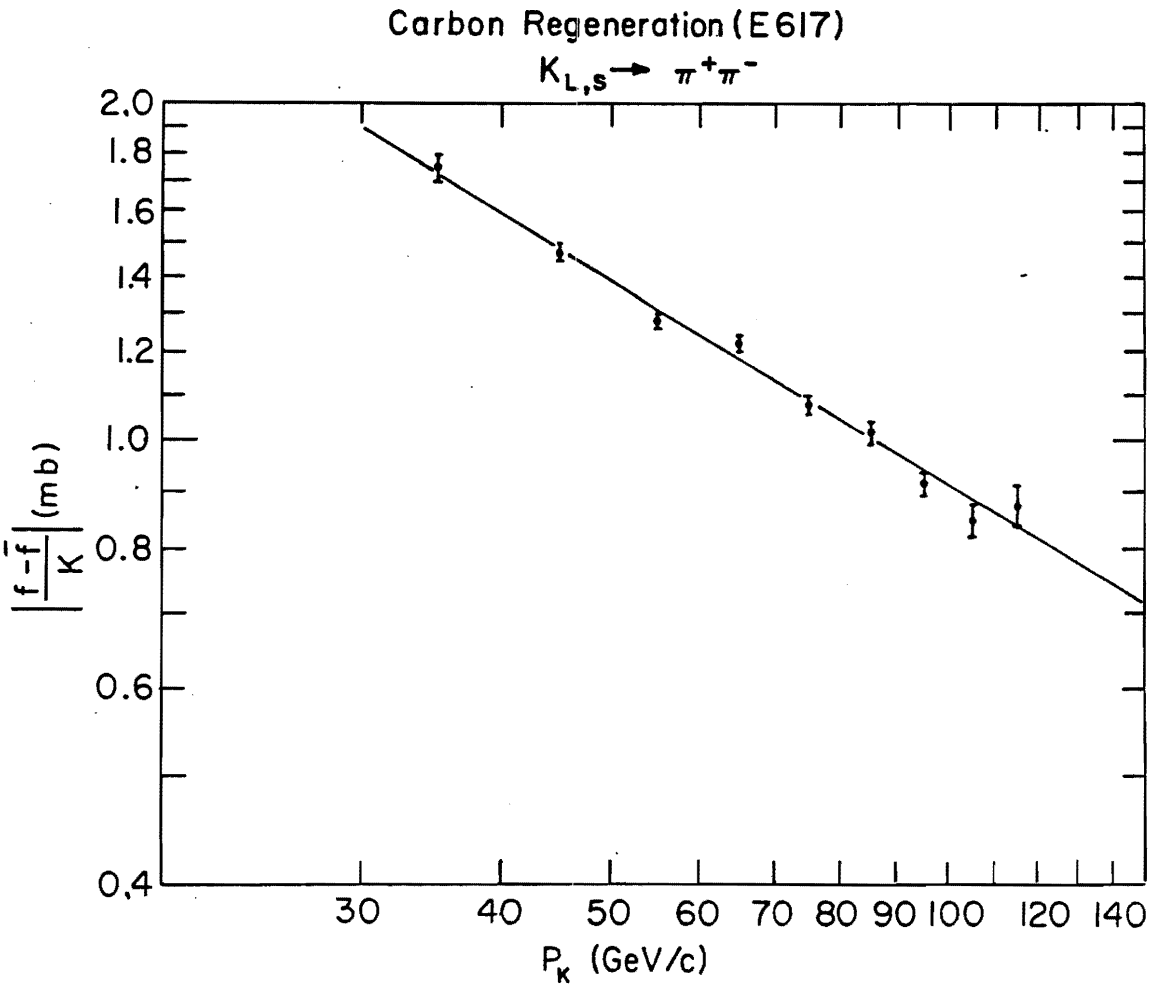
Carbon Regeneration (E617)
$K_{L,S} \rightarrow \pi^+\pi^-$
2.0
1.8
1.6
1.4
1.2
1.0
0.8
0.6
0.4
$\left|\frac{f-\bar{f}}{K}\right|$ (mb)
30
40
50
60
70
80
90
100
120
140
P_K (GeV/c)

Figure 87. $|(f-\bar{f})/k|$ for Carbon as measured by the present experiment, in the neutral mode.

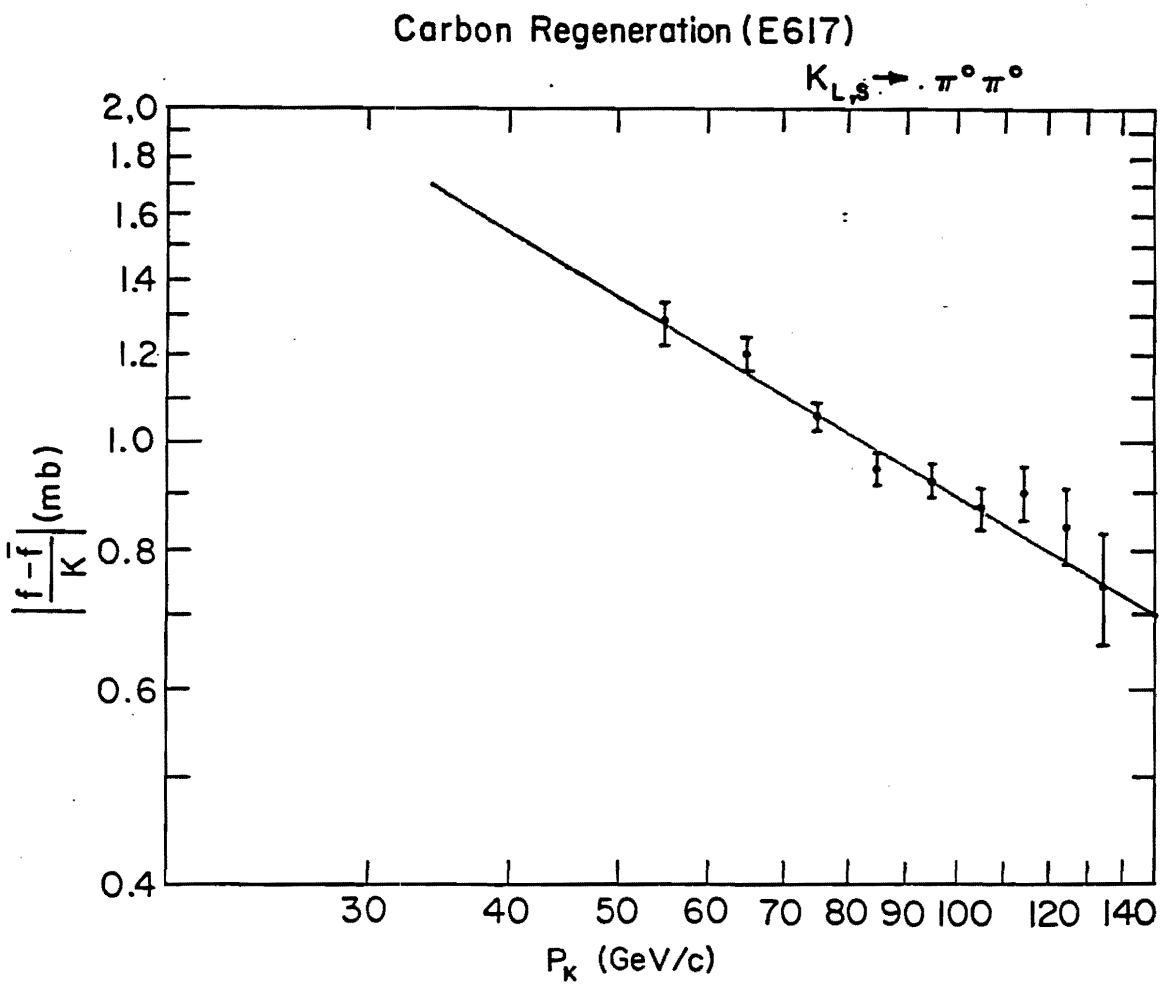
Carbon Regeneration (E617)
$K_{L,S} \rightarrow \pi^0 \pi^0$
2.0
1.8
1.6
1.4
1.2
1.0
0.8
0.6
0.4
$\left|\frac{f-\bar{f}}{K}\right|$ (mb)
30
40
50
60
70
80
90
100
120
140
P_K (GeV/c)

parison of the magnitude of $|(f-\bar{f})/k|$ has systematic errors which make it difficult to argue the difference in magnitude is a real physical effect.

We performed the corresponding fit in the neutral mode, again assuming $|\eta_{oo}| = 2.199\times10^{-3}$. The value of $|(f-\bar{f})/k|$ in each of the bins is given in Table 9. We find:

$$|(f-\bar{f})/k| = (12.49 \pm 3.98)p^{-0.572 \pm 0.072}\ mb. \tag{8.4}$$

with $\chi^2 = 5$ for 7 degrees of freedom. The fit is shown in Figure 87. Both the charged and neutral mode data show good agreement with the expected form of $|(f-\bar{f})/k|$.

We next used a more sophisticated procedure to extract $|\eta_{oo}/\eta_{+-}|$. We demanded that $|(f-\bar{f})/k|$ be the same in the charged and neutral modes and simultaneously fit to equations (2.7) and (2.8). The parameters varied in the fit were η_{oo} and the parameters of the power law, assuming the E82 value for η_{+-}. Again, the procedure is valid for obtaining $|\eta_{oo}/\eta_{+-}|$ independent of the value of η_{+-} because the fit is only sensitive to ρ/η. We obtain

$$|(f-\bar{f})/k| = (14.89 \pm 1.34)\ p^{-0.608 \pm 0.022} mb. \tag{8.5}$$

and

$$\left|\frac{\eta_{oo}}{\eta_{+-}}\right| = 1.015 \pm 0.017$$

with $\chi^2 = 16.5$ for 15 degrees of freedom.

The result is again in excellent agreement with equation 8.2. If we fix the power law to the more precisely determined value of $p^{-0.614}$, we obtain:

$$| (f - \bar{f})/k | = (15.28 \pm 1.05)\ p^{-0.614}\ mb. \tag{8.6}$$

and

$$|\frac{\eta_{oo}}{\eta_{+-}}| = 1.011 \pm 0.015$$

with $\chi^2 = 17.3$ for 16 degrees of freedom.

We can now extract $|\epsilon'\ /\epsilon|$. We use the phase for ϵ' quoted in Chapter I of 37.9^o. The power law is constrained to the E82 value. We use $\eta_{oo}=\epsilon - 2\epsilon'$ and $\eta_{+-} = \epsilon + \epsilon'$ to find:

$$|\frac{\epsilon'}{\epsilon}| = -0.0046 \pm 0.0053 \tag{8.7}$$

The significance of this result together with a comparison to previous measurements will be discussed in the final Chapter.

B. Checks of the Answer

The checks of our determination of $|\epsilon'\ /\epsilon|$ fall into two categories: first, there are consistency checks within the analysis described above. Second, we have checked the answer by binning the data in p and z separately. Both of these checks will attempt to uncover errors in the Monte Carlo calculation of the vacuum-to-regenerated acceptance ratios.

We have stressed many times that nonlinearities in the energy measurement can cause biases in the measured numbers of K_L or K_S ; our extremely loose cut on z-vertex has made us insensitive to small residual nonlinearities. We have also pointed out that the momentum bin analysis is dependent upon the Monte Carlo because we have included K_L events upstream of the regenerator where there are

no K_S. If we only accept events in the K_L beam which reconstruct downstream of the regenerator, we test our sensitivity to both effects. Here we have used a different method for calculating the z-vertex, described in Ref. 43. We refit the backgrounds and recalculated the inelastic subtraction in the K_L beam, which was 2.1% after the cut. The yields are given in Table 10. We used the identical method employed in obtaining equation (8.6) and found:

$$\left|\frac{\eta_{oo}}{\eta_{+-}}\right| = 1.015 \pm 0.017 \tag{8.7}$$

with a χ^2 of 15.8 for 16 degrees of freedom. We have cut roughly 1/3 of the events; the change in $|\eta_{oo}/\eta_{+-}|$ is within the statistical error induced by changing the number of events in the sample.

By binning the data in (p,z) bins we no longer rely on a Monte Carlo. We still must subtract the backgrounds in each bin and have performed the subtractions by making 'eyeball' fits. The numbers of events from the neutral and charged mode data binned in this way appear in Table 11.

There are two complications to this analysis which must be considered in calculating $|\eta_{oo}/\eta_{+-}|$. First, we cannot simply take the vacuum to regenerated ratios in order to extract $|\epsilon'/\epsilon|$ because of the interference term between ρ and η. Second, the resolution smearing among bins must be accounted for. To minimize our sensitivity to resolution smearing we have averaged the value of $|\eta_{oo}/\eta_{+-}|$ in each p bin over the different z bins:

$$\frac{\eta_{oo}}{\eta_{+-}}(p) = \frac{\sum_{z\text{-}bins} \eta_{oo}(z,p)\Delta z}{\sum_{z\text{-}bins} \eta_{+-}(z,p)\Delta z} \tag{8.8}$$

The value of $|\eta_{oo}/\eta_{+-}|$, uncorrected for interference, as a function of momentum is displayed in Figure 88 and the values are given in Table 12. We average over momentum to obtain

$$|\frac{\eta_{oo}}{\eta_{+-}}| = 1.014 \pm 0.017 \tag{8.9}$$

and correcting for the interference term we find

$$|\frac{\epsilon'}{\epsilon}| = -0.0044 \pm 0.0062$$

remarkably close to the value obtained by binning in momentum. We have not used a Monte Carlo, we have binned the data in a totally different way, and we have performed 'eyeball' subtractions instead of our measured fits, and have obtained a practically identical result in both methods.

A final check involves a subtlety of the double beam method. For the moment, we consider only the neutral mode. If the live time with the regenerator in the east beam is different from the live time with the regenerator in the west beam, we can write the number of observed decays in each beam for each regenerator position as

$$\begin{aligned} N_1 &= F_{R,E}\,\rho^2\,L_E \\ N_2 &= F_{R,W}\,\rho^2\,L_W \\ N_3 &= F_{V,E}\,L_E \\ N_4 &= F_{V,W}\,L_W \end{aligned} \tag{8.10}$$

F stands for flux and L for livetime. R or V denotes in which of the two beams the decay occurs, and E and W refer to the regenerator position. The number of decays is then the flux times the livetime for the appropriate beam, with a factor

TABLE 10

NUMBER OF $K_L \rightarrow \pi^0\pi^0$ IN THE DECAY REGION

p_K	Raw	Background	Background Subtracted	Final
55	311	25.4	285.6	279.6±17.7
65	449	52.3	396.7	388.3±21.6
75	507	41.0	466.0	456.2±22.6
85	478	31.9	446.1	436.7±22.0
95	340	22.0	322.0	315.2±18.5
105	222	14.8	207.2	202.8±14.9
115	123	6.3	116.7	114.2±11.1
125	53	4.9	48.1	47.1±7.22
135	25	0.4	24.6	24.1±5.0
Σ	2508	206.1	2313.	2264.2

TABLE 11
NUMBER OF EVENTS IN THE (p,z) BINS

Charged			Neutral			p_K
vacuum	regenerated	ratio	vacuum	regenerated	ratio	
467	1029	6.28±.33	40	225	5.63±.97	
366	1127	3.08±.19	41	137	3.34±.59	
408	632	1.55±.10	45	102	2.227±.41	55 GeV/c
354	326	0.921±.071	53	55	1.038±.201	
539	207	.384±.033	113	51	0.451±.077	
414	2927	7.07±0.39	72	420	5.83±.74	
373	1269	3.40±.21	59	262	4.44±.65	
324	725	2.24±.15	78	162	2.08±.29	65 GeV/c
347	476	1.37±.10	68	103	1.51±.24	
500	305	.61±.05	138	105	.76±.10	
388	2410	6.21±.37	96	490	5.10±.57	
285	1123	3.94±.27	89	301	3.38±.41	
301	605	2.01±.14	87	223	2.56±.32	75 GeV/c
261	414	1.59±.13	95	144	1.52±.20	
416	314	.754±.060	120	122	1.02±.14	
350	1844	5.27±.33	90	466	5.18±.60	
231	891	3.86±.29	92	330	3.59±.43	
187	543	2.90±.25	81	207	2.56±.33	85 GeV/c
210	339	1.61±.14	78	113	1.45±.22	
253	279	1.10±.10	131	111	.847±.110	
210	1162	5.53±.45	86	355	4.13±.50	
159	588	3.70±.34	73	294	4.03±.53	
148	364	2.46±.24	55	166	3.02±.47	95 GeV/c
130	193	1.49±.17	47	100	2.13±.38	
145	140	.966±.122	70	84	1.20±.20	

TABLE 11 (continued)

Charged vacuum	Charged regenerated	Charged ratio	Neutral vacuum	Neutral regenerated	Neutral ratio	p_K
158	738	4.68±.45	48	240	5.00±.80	
126	339	2.69±.28	46	157	3.41±.57	
67	185	2.76±.39	42	113	.269±.49	105 GeV/c
64	122	1.91±.29	40	57	.143±.29	
90	103	1.14±.17	36	47	1.31±.29	
82	438	5.34±.72	33	162	4.91±.94	
49	219	4.47±.71	22	100	4.54±1.07	
37	100	2.70±.52	28	53	1.89±.44	115 GeV/c
47	61	1.30±.25	21	31	1.48±.42	
55	40	.73±.15	18	22	1.22±.39	

The z-bins are (relative to the beginning of the decay region at 406.4 m.):

$$z < 3.5 \text{ m.}$$
$$3.5 \leq z < 6. \text{ m.}$$
$$6. \leq z < 8.5 \text{ m.}$$
$$8.5 \leq z < 11 \text{ m.}$$
$$z \geq 11 \text{ m.}$$

TABLE 12

$|\eta_{oo}/\eta_{+-}|^2$ AS A FUNCTION OF KAON MOMENTUM

p_K	$|\eta_{oo}/\eta_{+-}|^2$
55	0.9704 ± 0.1012
65	1.0156 ± 0.0816
75	1.069 ± 0.0743
85	1.083 ± 0.0784
95	0.9890 ± 0.0795
105	0.9485 ± 0.0975
115	1.0246 ± 0.1421

$$<|\eta_{oo}/\eta_{+-}|^2> = 1.028 +- 0.0383$$

Figure 88. $|\eta_{oo}/\eta_{+-}|^2$ as a function of kaon momentum.

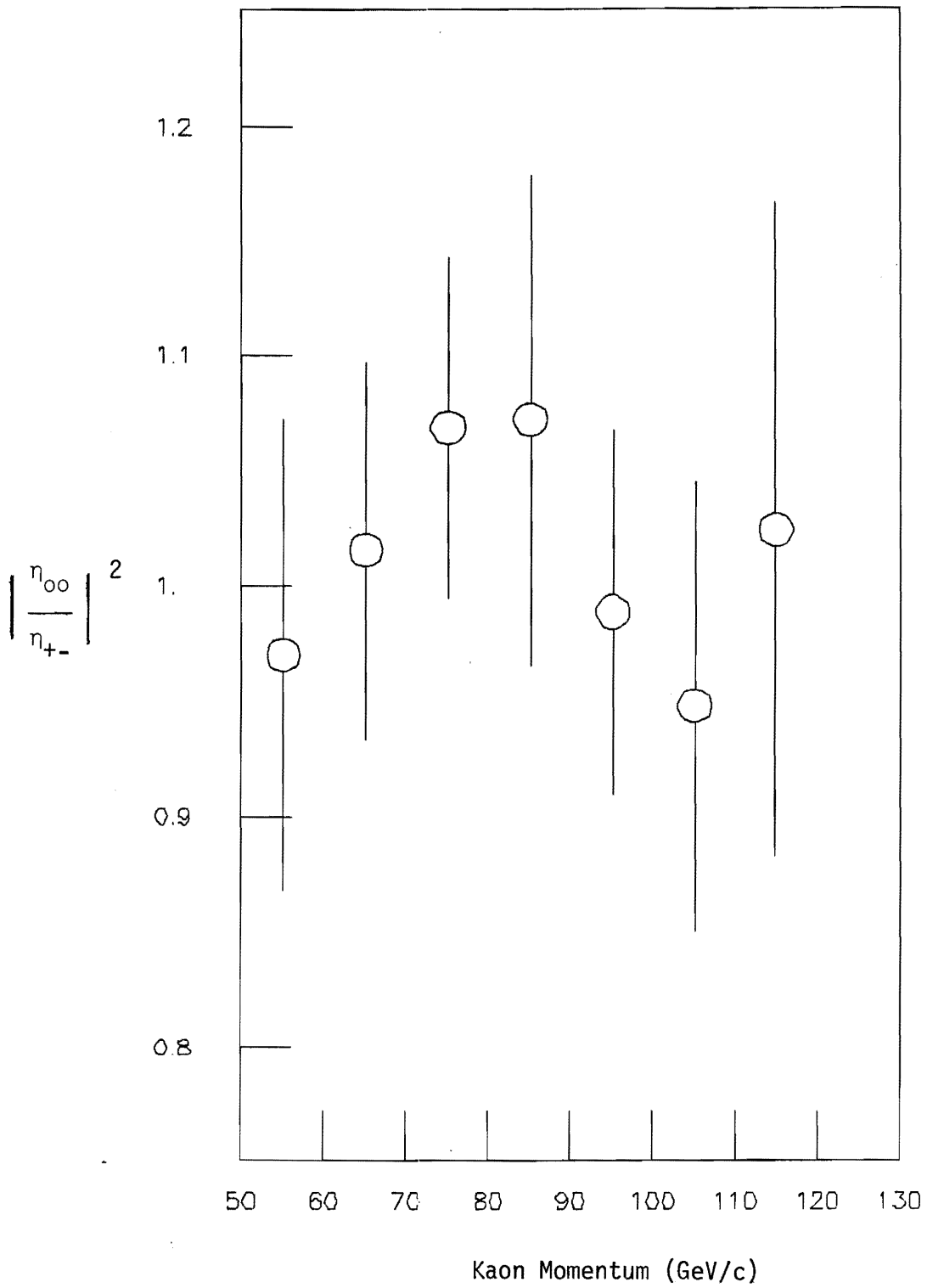
1.2
1.1
1.
0.9
0.8
$\left|\frac{\eta_{00}}{\eta_{+-}}\right|^2$
50
60
70
80
90
100
110
120
130
Kaon Momentum (GeV/c)

of ρ^2 for the regenerator. N_1 is the number of decays in the regenerated beam with the regenerator in the east position; N_2 is the number of regenerated decays with the regenerator in the west position. N_3 and N_4 are the corresponding number of decays in the vacuum beam. and our analysis then calculates

$$\frac{N_1 + N_2}{N_3 + N_4} = \frac{\rho^2 \left(F_{R,E}L_E + F_{R,W}L_W\right)}{\left(F_{V,E}L_E + F_{V,W}L_W\right)} \tag{8.11}$$

If $L_E = L_W$ then by alternating the regenerator between the two beams the fluxes cancel. If $L_E \neq L_W$ then the ratio does not reduce to ρ^2. If instead we form:

$$\frac{N_1 N_2}{N_3 N_4} = \frac{\rho^2 \, F_{R,E} \, L_E \, F_{V,W} \, L_W}{F_{R,W} \, L_W \, F_{V,E} \, L_E} \tag{8.12}$$

then the method of alternating the regenerator produces the desired cancellation. We have checked that the separation into the two configurations does not produce a significantly different result from the 'standard' analysis which uses equation (8.11). The change in η^2_{oo} is +0.59% of itself and the change in η^2_{+-} is similarly less than .01%, both well within the errors.

C. Estimates of Systematic Errors

The systematic errors in the experiment fall into two categories: those associated with the background subtractions and those associated with acceptance corrections. None of the background fits show any significant deviations from the data. Our decision was to assign a systematic error equal to the statistical error of the background subtraction: for example, a background subtraction of 100 events

would have a systematic error of ± 10 events.

The q^2 subtraction in the neutral beam is the only subtraction which may show some sign of a discrepancy. We have used two methods to estimate the maximum possible error: first we have acceptance-corrected the data, and second we have changed the region of the fit and recalculated the subtractions.

We calculated the acceptance as a function of q^2 and fit it using two different functional forms. After correcting the data with each form we refit the distributions of Figure 83 to exponentials; each of the two acceptance corrections gave a different value for the number of K_S from the uncorrected value. The difference in the number of K_S in the acceptance fit with the larger shift was 0.35%, a negligible change.

We refit the data without acceptance-corrections between 8000 and 25000 (MeV/c) ^{2}; we originally fit from 10000 to 50000 (MeV/c) ^{2}. We chose this region because the data clearly deviated from an exponential form in q^2 and so we regarded this as an extreme variation. The change in the number of K_S was -1.2% of itself, decreasing the number of K_S. However, the resolution-broadened coherent K_S signal 'leaks' into this region of q^2; residual nonlinearity in the calibration will distort the coherent K_S distribution. We therefore take this change in the fit as producing an 'extreme' variation which is certainly larger than our true systematic error, we have arbitrarily doubled the systematic error assigned to this subtraction to reflect this uncertainty.

The systematic errors due to the acceptance correction were estimated by systematically warping the momentum spectrum of K_L incident on the detector. In the charged mode the spectrum was directly multiplied by a power law which was varied until the measured and Monte Carlo spectra were in clear disagreement. In the neutral mode we changed the energy of the highest energy photon by 0.2% /GeV, which again produced a clear discrepancy in the momentum spectra. The measured shifts in η^2_{oo} and η^2_{+-} were 0.5% and 0.3% of themselves respectively.

A list of all systematic errors for each mode appears in Table 13. We have added the systematic errors in quadrature to obtain a final result of

$$\left|\frac{\epsilon'}{\epsilon}\right| = -0.0046 \pm 0.0053(stat.) \pm 0.0024(syst.)$$

TABLE 13

SYSTEMATIC ERRORS

mode	number	backgrounds	inelastics	total systematic error
$K_L \to \pi^0\pi^0$	3150	266±13	90.7±9.5	18.9
$K_s \to \pi^0\pi^0$	5663	35.3±5.9	825.7±28.7	58.0
$K_L \to \pi^+\pi^-$	10637.6	324.9±18.0	42.5±6.5	19.1
$K_S \to \pi^+\pi^-$	25751	44.8±6.7	439.2±21.0	22.0

Monte Carlo:

Charged 0.2%
Neutral 0.5%

Final Systematic Error in $|\eta_{00}/\eta_{+-}|^2$

$$\left[\left(\frac{18.9}{3150}\right)^2 + \left(\frac{58}{5663}\right)^2 + \left(\frac{19.1}{10637.6}\right)^2 + \left(\frac{22.0}{25751}\right)^2 + (.005)^2 + (.002)^2\right]^{1/2} = .0132$$

CHAPTER IX

COMPARISONS AND CONCLUSIONS

Our value of $|\epsilon' /\epsilon|$ is consistent with zero and with the three previous determinations of ϵ' . In this Chapter we describe the earlier measurements of $|\eta_{oo}/\eta_{+-}|$ and compare our method and results. We then explore the theoretical implications of our measurement.

A. Comparisons with Previous Measurements

The first experiment we discuss was performed by a Princeton group[51] at the Brookhaven AGS at a mean momentum of 6 GeV/c. The experiment used a single beam and measured the rates of each of the charged and neutral decays with and without a regenerator in four separate 'runs'. Flux monitoring, performed with a telescope at a finite angle to the beam, was then a significant contribution to the error. The regenerator data was taken with the regenerator in several locations in order to match the spatial distributions of K_L and K_S decays.

The neutral mode measurements converted one of the four photons and measured its trajectory and momentum. The positions of the other photons, but not their energies, were measured. In order to make the $3\pi^o$ background manageable the transverse momentum of the converted photon was required to be greater than

170 MeV/c; $3\pi^o$ decays have a kinematic cutoff at 168 MeV/c for the transverse momentum of a photon. The charged mode measurements were performed in the same beam line by removing the converter and using a Cerenkov counter and muon filter to reject electrons and muons respectively.

The experiment obtained a final result of $|\eta_{oo}/\eta_{+-}| = 1.03 \pm 0.07$. The largest error was the statistical error on the 124 collected neutral mode decays. The systematic and statistical errors were comparable.

The next experiment we examine was performed at the CERN PS by an Aachen-CERN-Torino group.[52] The experiment used a single beam and observed the four decays separately as did the Princeton group. Unlike the Princeton measurement, this experiment measured the energies of all the photons and converted at least two to measure their trajectories. The fluxes were monitored in the neutral measurement using $3\pi^o$ decays in the beam an improvement over the Princeton technique. The charged mode determinations used a different spectrometer but the same beam line and the same regenerator. Their result was $|\eta_{oo}/\eta_{+-}| = 1.00 \pm 0.06$, based on 167 $K_L \rightarrow 2\pi^o$ decays; as in the Princeton experiment, the systematic and statistical errors were comparable.

Both of the above experiments measured decays separately for K_L and K_S. The next experiment, performed by an NYU group at the Brookhaven AGS[53], worked in a conceptually different way; it was designed to measure the phases of η_{oo} and η_{+-} rather than their magnitudes. Both of the above experiments used a pure K_L beam and a regenerator, with the apparatus far from the target; this

experiment looked immediately downstream of the production point of the kaons; the resultant mixture of K^o and $\overline{K}^o$ is neither pure K_L nor pure K_S. The proper time distribution of $\pi\pi$ decays for such a mixture is given by:

$$I = e^{-\tau/\tau_S} + |\eta|^2 + 2D(p)|\eta|\cos(\Delta m\tau - \Phi_\eta)e^{-\tau/2\tau_S}$$

where $D(p)$ is the difference of K^o and $\overline{K}^o$ intensities divided by their sum. The proper-time distributions of $\pi\pi$ decays were fit in both the charged and neutral modes to obtain $|\eta_{oo}/\eta_{+-}|$, much like our fit of $|\ (f - \overline{f})/k\ |$. The analysis yielded $|\eta_{oo}/\eta_{+-}| = 1.00 \pm 0.09$.

The three previous results have been converted into measurements of $|\epsilon'\ /\epsilon|$ and compared with our result in Figure 89. The experiments are all in agreement; our error is a factor of four smaller than that of any of the previous measurements. The improvement in statistical power is only part of the reason for the improvement in precision; the two direct measurements had systematic errors of the order of 10% in $|\eta_{oo}/\eta_{+-}|^2$; we have an error of 1.3%, achieved by using the double beam, which freed us of flux monitoring and dead time induced errors. Further measurements will improve on the statistical errors; further improvement of the systematic errors will undoubtedly be far more difficult.

B. Comparisons with Theoretical Predictions

Our value for $|\epsilon' /\epsilon|$ is consistent with zero and with the superweak hypothesis: we have not seen a finite ϵ' . However, our result puts severe constraints on a variety of models and perhaps points the way to new ideas to explain CP-violation.

Our experiment was largely motivated by the Kobayashi-Maskawa model predictions for a non-zero $|\epsilon' /\epsilon|$ of the order of a percent or more. Figure 90 shows a result from a recent paper by Gilman and Hagelin[54] which presents a lower bound for $|\epsilon' /\epsilon|$ as a function of the mass of the top quark. Our result is two standard deviations from this lower bound for a top quark mass up to about 50 GeV/c ^{2}. Neither of the authors believe[55] the bound could be significantly lower and they are both sure that $|\epsilon' /\epsilon|$ must be positive within the Kobayashi-Maskawa model using the constraints quoted in Chapter I. The UA1 group has recently recently quoted[56] a range for the top quark mass of 30-50 GeV/c ^{2}; this further constrains the Kobayashi-Maskawa predictions.

It is of course possible that the phase δ in the Kobayashi-Maskawa matrix is zero; then we would have to look elsewhere for the source of CP-violation. The left-right symmetric models of Reference 2 predict a wide range of values of ϵ' /ϵ; the predictions are not yet precise enough to be tested by our measurement. The Weinberg multiple-Higgs model is almost certainly ruled out; our central value is nearly three standard deviations away from the upper bound of $|\epsilon' /\epsilon| \leq -0.02$ quoted in Reference 25.

Figure 89. A comparison of the value of $|\epsilon'/\epsilon|$ with previous measurements. The statistical and systematic errors have been added in quadrature for each experiment.

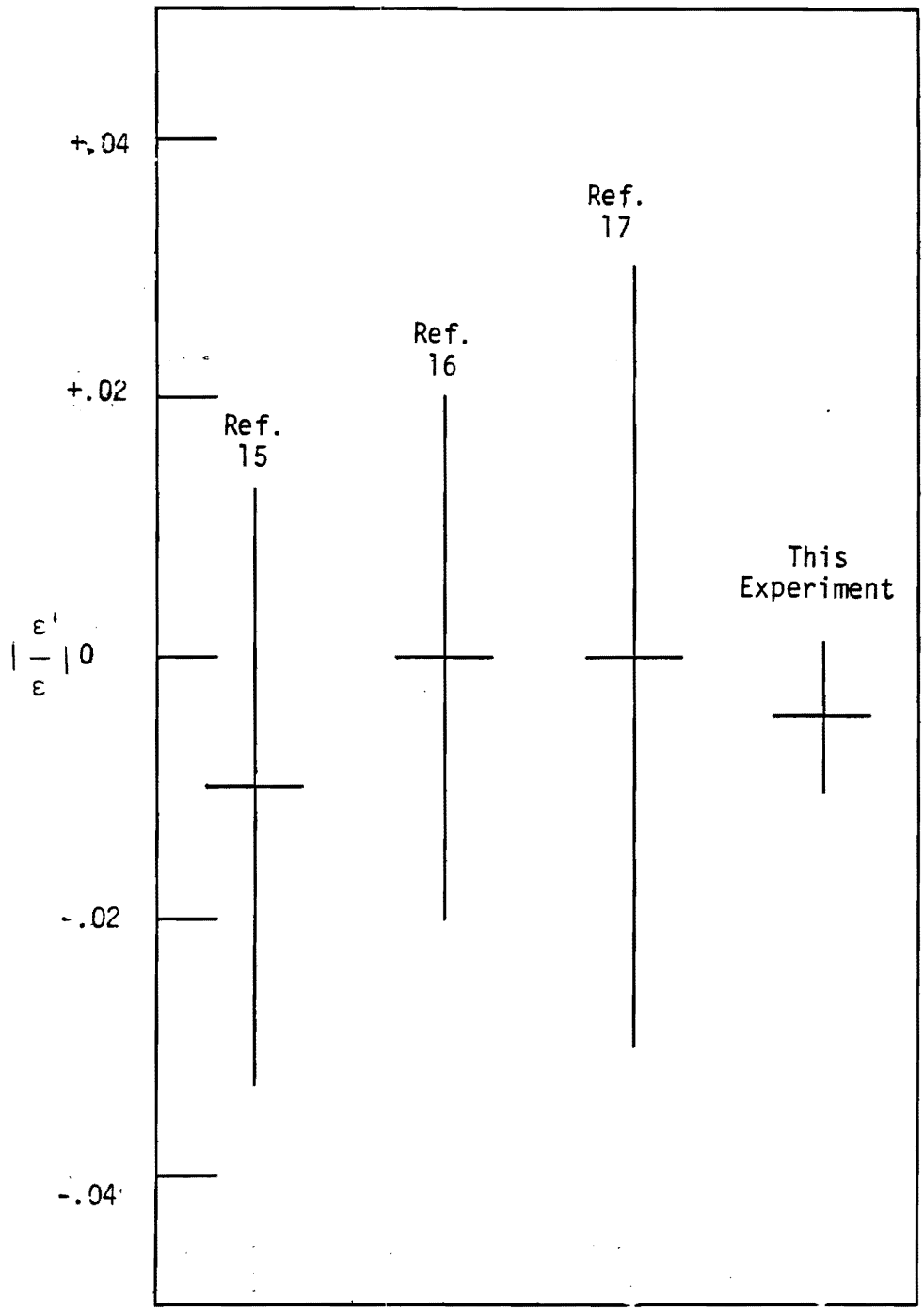
+.04
+.02
$\left|\frac{\varepsilon'}{\varepsilon}\right|$ 0
-.02
-.04
Ref. 15
Ref. 16
Ref. 17
This Experiment

Figure 90. A recent theoretical prediction for $|\epsilon'/\epsilon|$ in the Kobayashi-Maskawa model, from Gilman and Hagelin, 1983. The parameter B is the 'bag factor' and arises from QCD. For each value of B, a lower bound on $|\epsilon'/\epsilon|$ has been computed for three values of the b lifetime: for the solid line, 0.6×10^{-12}; for the dashed-dotted line, 0.9×10^{-12}; for the dashed line, 1.2×10^{-12}. The dotted line was a lower bound based on a calculation made before the b lifetime was measured. Note that for ranges of the top quark mass from 30-50 GeV/c^2, $\epsilon'/\epsilon > +.004$.

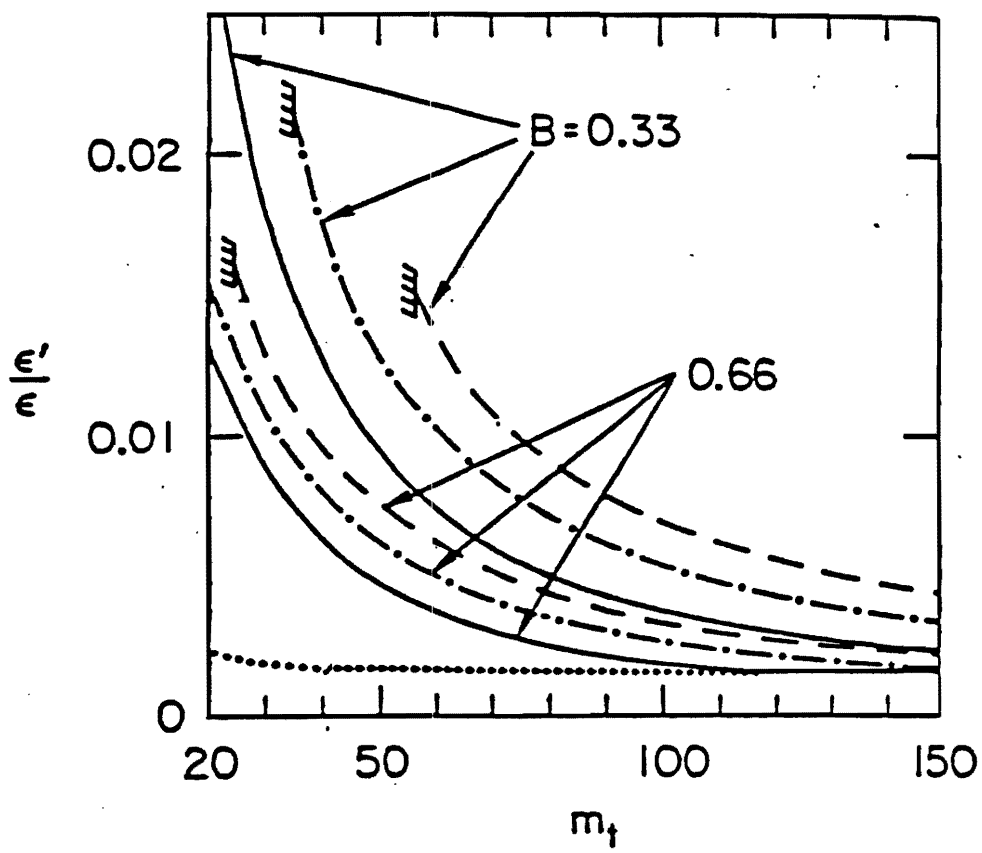
B = 0.33
0.66
0.02
0.01
0
20
50
100
150
m_t
$\frac{\epsilon'}{\epsilon}$

What else can be done to improve our understanding of CP-violation? Within the kaon system, more precise measurements of $|\eta_{oo}/\eta_{+-}|$ are already being planned at Fermilab[57] and at CERN[58]. A measurement of η_{+-0} (the amplitude ratio $K_S \to \pi^+\pi^-\pi^o / K_L \to \pi^+\pi^-\pi^o$) is already underway at Fermilab[59] and will provide new information which may constrain all of the models. Given the importance of CP-violation, both the experimental and the theoretical efforts will continue.

Our result for $|\epsilon' / \epsilon|$ is therefore tantalizing but far from conclusive. A negative value for $|\epsilon' / \epsilon|$ would rule out a promising and natural candidate for the source of CP-violation; therefore we must be doubly certain of the theoretical predictions and further sharpen the experimental evidence. It has been twenty years since the discovery of CP-violation, yet it remains a mystery.

APPENDIX A

REGENERATION

This appendix presents a sketch of regeneration phenomena. We begin by defining the quantity $|(f-\bar{f})/k|$. We then turn to a discussion of the scattering of K_L from a macroscopic target and define the regeneration amplitude ρ. Finally we derive some properties of ρ required by the text. An excellent discussion of regeneration, as well as many other topics covered in this work, may be found in Reference 28.

1. General Discussion of Regeneration; Definition of $|(f-\bar{f})/k|$

Recall the definition of the K-meson CP-eigenstates:

$$|K_1\rangle = \frac{|K^o\rangle + |\bar{K}^o\rangle}{\sqrt{2}} \qquad \text{(A1)}$$
$$|K_2\rangle = \frac{|K^o\rangle - |\bar{K}^o\rangle}{\sqrt{2}}$$

Denote the scattering amplitude for $K^oX \rightarrow K^oX$ as f/k and the analogous process for $\bar{K}^o$ by $\bar{f}/k$. We suppress the dependence of f on q^2 since we are ultimately only interested in phenomena at $q^2 = 0$. The amplitudes f and $\bar{f}$ are not identical because scattering in matter distinguishes the strong eigenstates K^o and $\bar{K}^o$. If an initially pure K_L beam scatters from matter, the outgoing state is (neglecting CP-violation):

$$|K^{out}\rangle = \frac{(f/k)\,|K^o\rangle - (\bar{f}/k)\,|\bar{K}^o\rangle}{\sqrt{2}} \qquad \text{(A2)}$$

Define

$$f_{12} = \frac{f - \bar{f}}{2k}$$

Then

$$|K^{out}> = \frac{f_{22}}{k}\,|K_L> + \frac{f_{21}}{k}\,|K_S> \tag{A3}$$

The appearance of K_S in an initially pure K_L beam arises from the difference in scattering amplitudes for K^o and $\overline{K}^o$; this is the phenomenon of regeneration.

2. Scattering of K_L from a Macroscopic Target

Consider the scattering of a K_L from a target of finite dimensions; the K_L is scattered with momentum transfer given by q^2.

There are three regimes of q^2, distinguished by the size of the scattering center. The first is called coherent regeneration, in which all scattering centers act coherently. The momentum transfer is of the order of $(h/target\ size)^2$. For a macroscopic regenerator, the momentum transfer is essentially zero; a measurement of the momentum transfer always yields a finite q^2 because of the finite resolution of any detector. The other two regimes involve progressively smaller scales: regeneration occurs from a specific nucleus or nucleon.

Coherent regeneration was originally described by Case and Good.[1] They showed that the probability per incident K_L for a K_S to emerge with $q^2 = 0$ from a target is:

$$P = |\rho|^2 e^{-L/\Lambda_I} \tag{A4}$$

where

$$\rho = 2\pi i N \frac{f - \bar{f}}{k}\, \delta(L) \tag{A5}$$

$$\delta(L) = \Lambda_S \frac{1 - e^{-\nu L/\Lambda_S}}{\nu} \quad \rightarrow L \ , \ L/\Lambda_S \rightarrow 0$$

and

$$k = P_K/h$$

$$\Lambda_S = \beta\gamma\tau_S$$

N is the number density of scatterers
L is the length of the regenerator
Λ_I is the interaction length of the target

$\nu = i\frac{\Delta m}{\Gamma_S} - 1/2$, where Δm is the K_L-K_S mass difference and Γ_S is $h/2\pi\tau_S$.

Next we state without proof the proper time distribution for 2π decays behind a regenerator. The expression includes the original K_L, the coherently regenerated K_S, and an interference term between them.

$$R(\tau) = |\rho|^2 e^{-\Gamma_S \tau} + |\eta|^2 e^{-\Gamma_L \tau} + 2|\rho||\eta|\ e^{-(\Gamma_S + \Gamma_L)\tau/2} \cos(\Delta m \tau + \Phi_\rho - arg\ \eta) \tag{A6}$$

where τ is the proper time, Γ_S and Γ_L are $1/\tau_S$ and $1/\tau_L$, and $|\rho|$ and Φ_ρ are the magnitude and phase of the regeneration amplitude, and $|\eta|$ and $arg\ \eta$ are the magnitude and phase of either η_{oo} or η_{+-}.

We stated in Chapter II that the the coherent production rate is maximized if the regenerator length L is twice the interaction length Λ_I. The amplitude is proportional to L but falls with absorption; hence

$$Y\ \alpha\ L^2 e^{-L/\Lambda_I} \tag{A7}$$

which has a maximum at $L = 2\Lambda_I$.

Chapter II also argued that we could maximize our K_S yield by choosing a

Chapter II also argued that we could maximize our K_S yield by choosing a regenerator of small atomic weight. This is true because of equation (A5) and the measured dependence of $(f - \bar{f})/k$ on the atomic weight of the regenerator, referred to in equation (8.1): $|(f - \bar{f})/k|$ is proportional to $A^{0.758}$ Combining (A5) with the measurement of $|(f - \bar{f})/k|$ gives:

$$\rho = 2\pi i NL(f - \bar{f})/k \tag{A8}$$

or

$$|\rho| = 2\pi NLA^{0.758}$$

but recall we are working with a fixed, two interaction length regenerator. Therefore NL is proportional to $2/\sigma_T$, which, from Reference 47, behaves as $A^{-0.84}$. Combining these facts gives:

$$|\rho| \quad \alpha \quad A^{-0.84}A^{0.758} \quad \alpha \quad A^{-0.08}$$

APPENDIX B

THE MONTE CARLO

In this Appendix we discuss the neutral and charged mode Monte Carlo programs and show the comparisons to the data which convinced us the Monte Carlo accurately simulated the experiment. We first discuss the neutral mode program and then turn to the charged. A full discussion of the neutral mode program can be found in Reference 43, and a discussion of the charged mode program is contained in Reference 31.

1. The Neutral Mode Monte Carlo

The Monte Carlo generated events according to the measured momentum spectrum for K_L incident on the detector. Every event was initially treated as if it were a K_L: the momentum and z-vertex were picked from the K_L distribution calculated from the incident momentum spectrum and the K_L lifetime. Each event was also assigned a weight which allowed us to treat it as if it occurred in the regenerated beam: equation (A6), which tells us the proper time distribution of decays behind a regenerator, was calculated for each event as used as a weight. Therefore we correctly modeled the distribution of events in the K_L beam and the K_S beam. The advantage of this method is that statistical fluctuations tend to cancel between the beams since we are really using the same events.

The π^o and the resultant photons were then propagated through the

apparatus. Multiple coulomb scattering, pair production, and bremsstrahlung were all simulated (we did not attempt to simulate a full electromagnetic shower for each particle; bremsstrahlung photons were allowed to pair-produce, but the daughter electrons were the last generation of the shower to be simulated.)

Hits in the chambers were digitized and smeared according to the measured resolution; the wire numbers and times were written out the same way as in the data, and the Monte Carlo events were passed through the data reconstruction program.

In the glass, we used the measured shower shape to deposit energy in each block and smeared the energy in each of the blocks to reflect the statistical error in the energy measurement and the error in the measurement of the gain.

We examined a variety of distributions to convince ourselves that the Monte Carlo accurately modeled the data. Here we used the fully reconstructed $K_L \rightarrow 3\pi^o$ decays to check the acceptance. Figures 91-94 show the Monte Carlo and data z-vertex distributions in four momentum bins: the agreement is excellent.

The $2\pi^o$ sample has lower statistics but is of course the more important test of the Monte Carlo. Figure 94 shows the data and Monte Carlo comparison in z-vertex for K_L and K_S in two momentum bins. There are no signs of any discrepancy. We have also compared the energy spectrum: Figure 95 compares the coherent K_S spectrum, and Figures 97 and 98 compare the unconverted and converted photon energies for the K_S sample. Again, no disagreement is evident. Since we cut on the distance between clusters to avoid 'merged' showers, we

compared the distance between photons in the data and Monte Carlo: as seen in Figure 99, the agreement, which reflects our understanding of the shower width, is excellent. Finally, we compare the χ^2 distribution of coherent K_S. Recall that χ^2 governs our event reconstruction and choice of z-vertex. Understanding the χ^2 requires an accurate understanding of the resolution of the lead glass. Figure 100 shows the comparison, which is nearly perfect over two orders of magnitude.

The acceptances in the neutral mode appear in Table 14. The quoted acceptances depend on the region over which decays are generated. The K_L sample was generated from 390 m. to 420 m. from the target; the K_S sample began at the regenerator anticounters. The acceptance is defined as the number of accepted events divided by the number of generated events; for the sample cut at the regenerator anticounters, the acceptance is defined as the number generated from 390 to 420 m. divided by the number accepted which also decayed downstream of the anticounters. The acceptance ratio for K_L and K_S decays which originate in the decay region is nearly unity, which is obscured by our definition of acceptance.

2. Charged Mode Monte Carlo

The charged mode Monte Carlo was considerably simpler than the neutral mode program: only two charged tracks were followed, instead of four photons and resultant electromagnetic showers. The tracks were propagated through the spectrometer and the wire numbers and times were written out the same way as in the

neutral mode. The pions were allowed to decay into muons and then continued through the apparatus.

As in the neutral mode, we examined many distributions to check that the Monte Carlo represented the data faithfully. Figure 101 shows the z-vertex comparison for K_L and K_S in two different momentum bins. As in the neutral mode, the agreement is excellent. The energy spectra agree as well: Figure 102 shows the comparison for the coherent K_S spectrum, which again shows no discrepancies. Reference 45 contains many other comparisons of the data and Monte Carlo, especially on the resolution of the spectrometer and reconstruction of the charged tracks. The acceptances for K_L and K_S decays appear in Table 15.

TABLE 14

ACCEPTANCES FOR $K_L, K_S \rightarrow \pi^0\pi^0$ (in %)

p_K	A_L	A_L, cut at z_{RA}	A_S	A_L/A_S	$A^{RA}{}_L/A_S$
55	.3992	.3571	.7533	.5299	.4740
65	.8901	.7460	1.874	.4749	.3981
75	1.397	1.095	3.074	.4545	.3562
85	1.674	1.214	3.553	.4711	.3417
95	1.702	1.134	3.480	.4891	.3259
105	1.550	.9120	2.895	.5354	.3150
115	1.254	.6603	2.126	.5898	.3106
125	.9096	.4048	1.333	.6824	.3037
135	.6045	.2239	.7619	.7934	.2939

(the pair-conversion probability is not included in the acceptance)

Figure 91. The $K_L \rightarrow 3\pi^o$ z-vertex distribution, $60 < p_K < 70$ GeV/c, data and Monte Carlo.

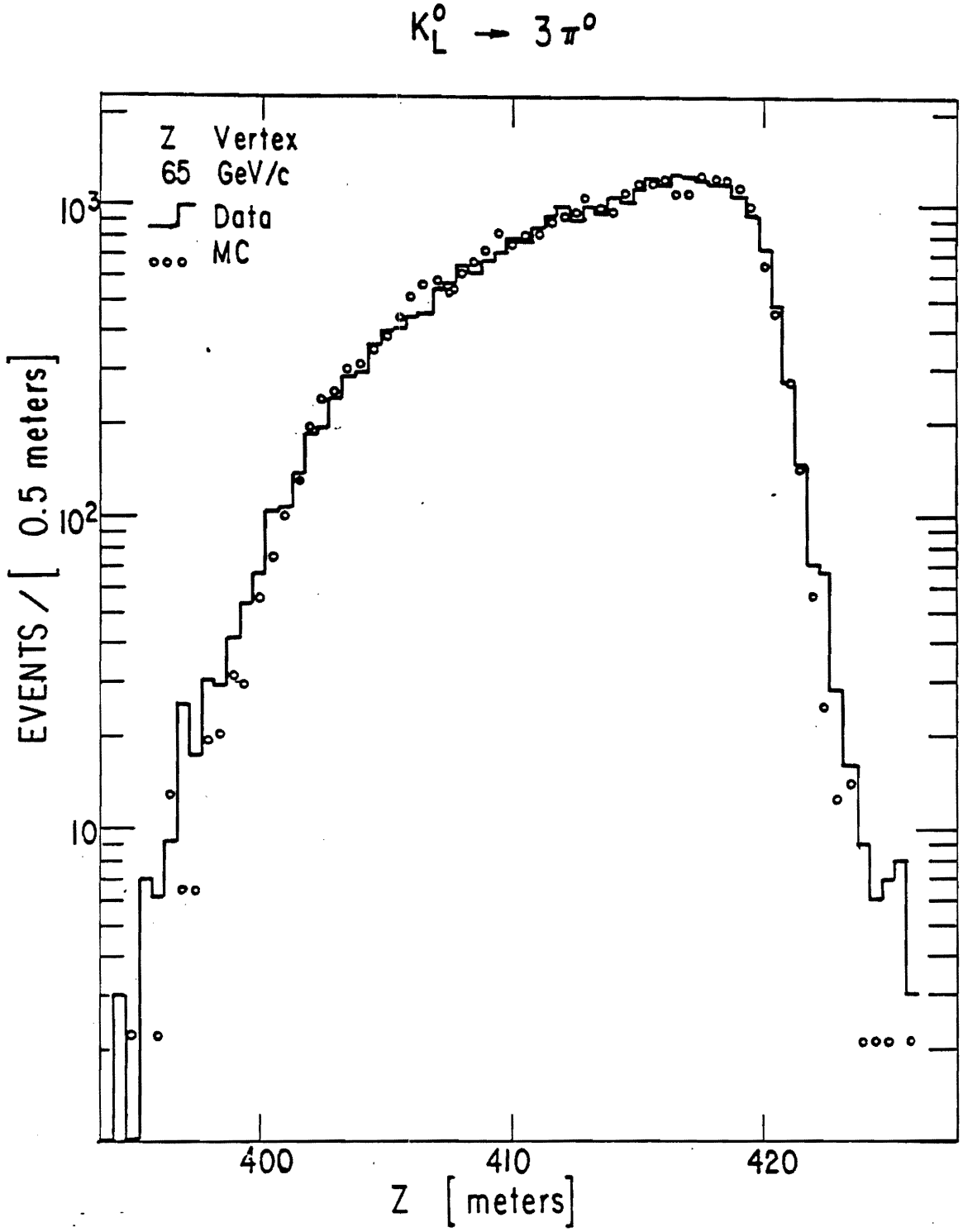
$K_L^0 \rightarrow 3\pi^0$
Z Vertex
65 GeV/c
Data
MC
EVENTS / [0.5 meters]
10^3
10^2
10
400
410
420
Z [meters]

Figure 92. The distribution of Figure 90, 70 $< p_K <$ 80 GeV/c.

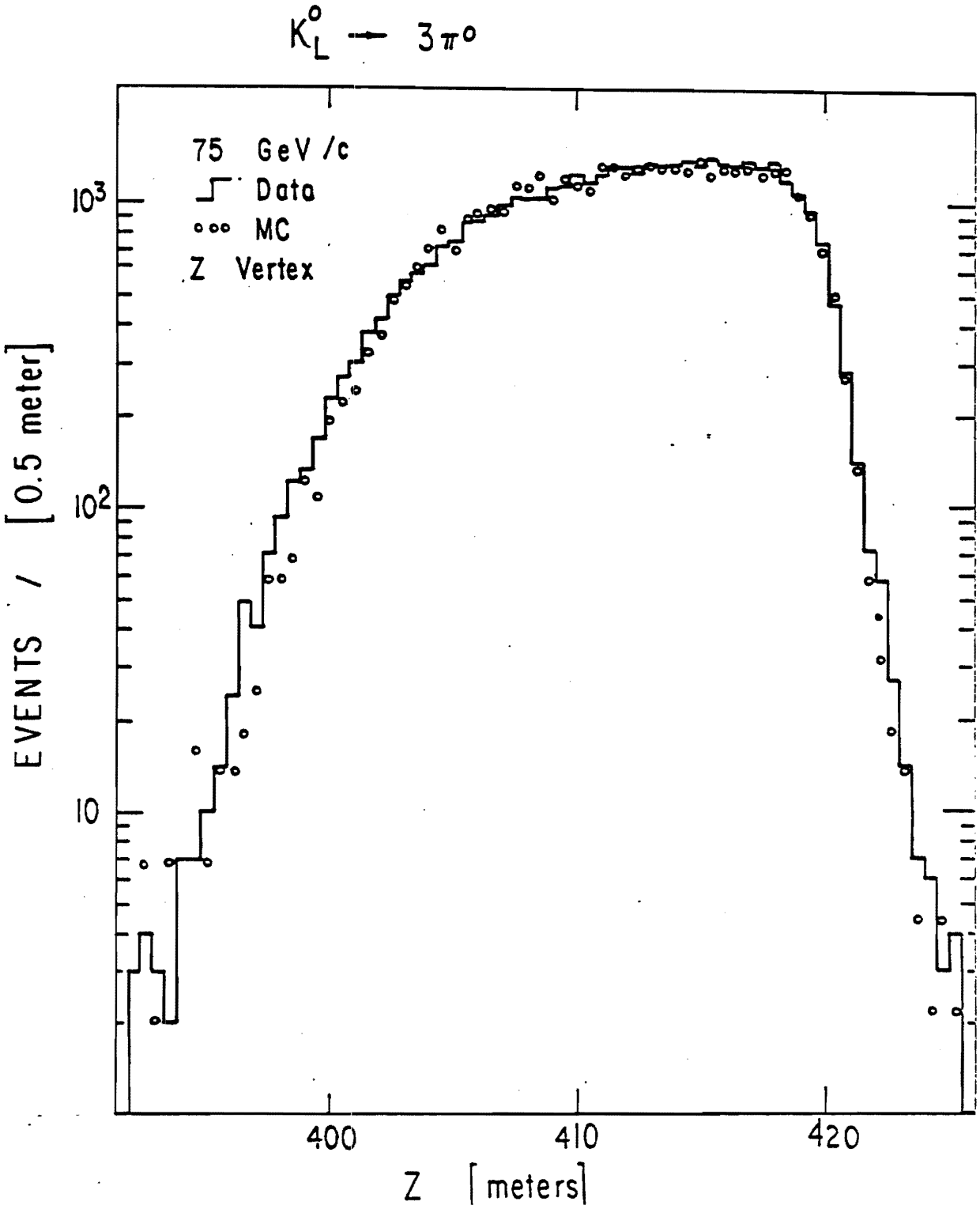
$K_L^0 \rightarrow 3\pi^0$
75 GeV/c
Data
MC
Z Vertex
EVENTS / [0.5 meter]
10^3
10^2
10
400
410
420
Z [meters]

Figure 93. The distribution of Figure 90, 80 $< p_K <$ 90 GeV/c.

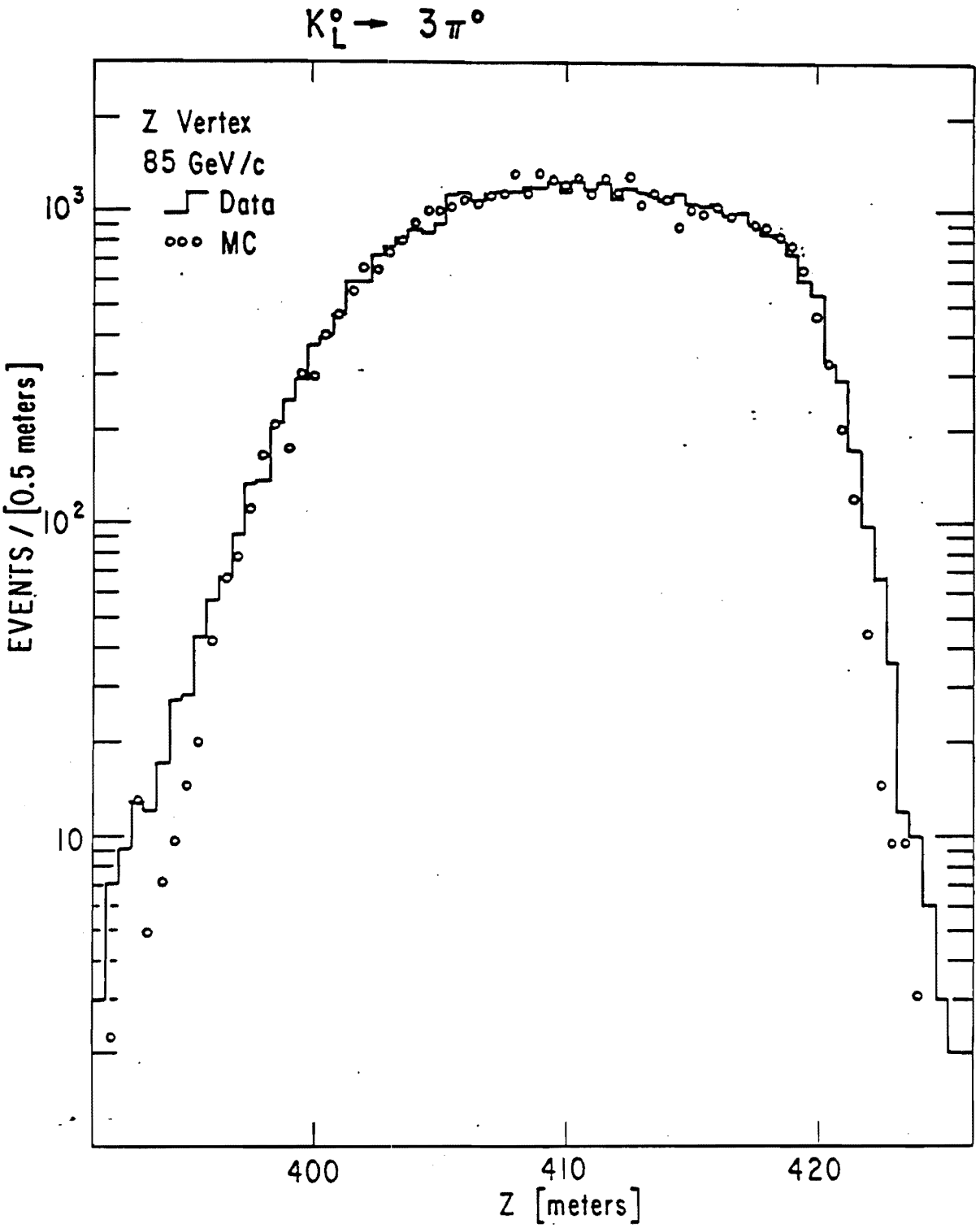
$K_L^0 \to 3\pi^0$
Z Vertex
85 GeV/c
Data
MC
EVENTS / [0.5 meters]
10^3
10^2
10
400
410
420
Z [meters]

Figure 94. The distribution of Figure 90, 90 $< p_K <$ 100 GeV/c.

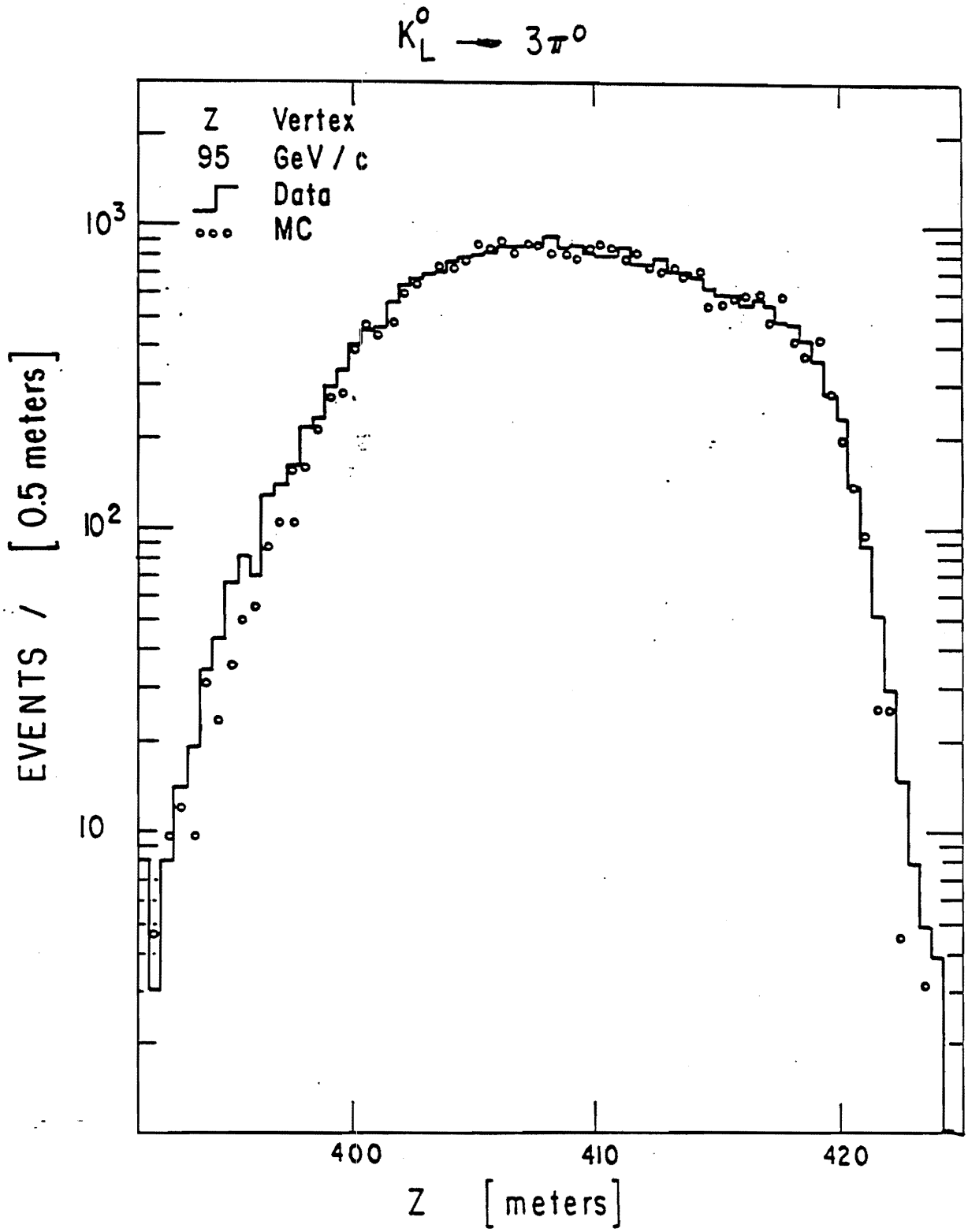
$K_L^0 \to 3\pi^0$
Z Vertex
95 GeV / c
Data
MC
10^3
10^2
10
EVENTS / [0.5 meters]
400
410
420
Z [meters]

Figure 95. The coherent K_S and K_L z-vertex distribution for $60 < p_K < 70$ GeV/c and $90 < p_K < 100$ GeV/c, data and Monte Carlo, in the neutral mode.

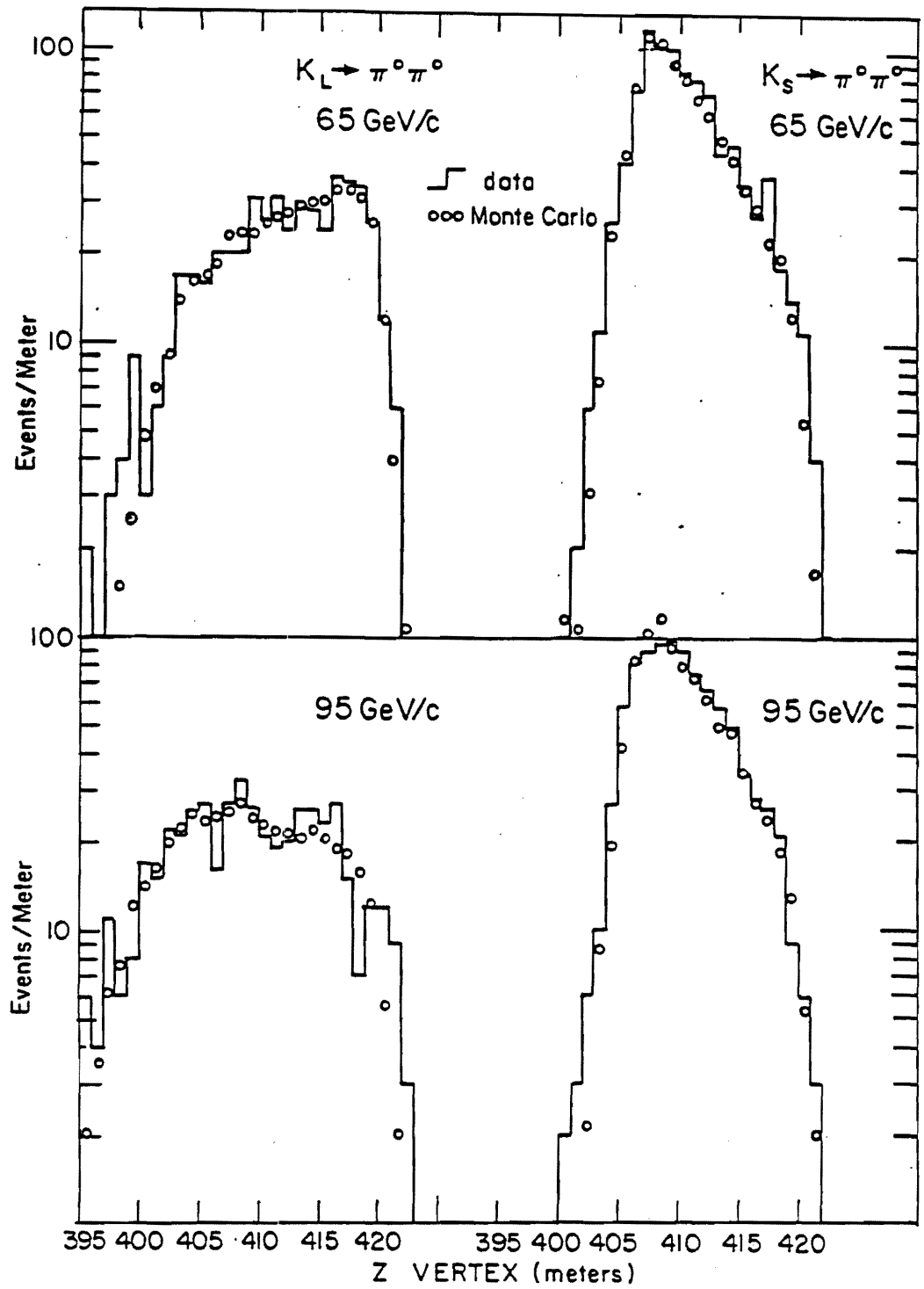
$K_L \rightarrow \pi^0\pi^0$
65 GeV/c
$K_S \rightarrow \pi^0\pi^0$
65 GeV/c
data
Monte Carlo
95 GeV/c
95 GeV/c
Events/Meter
100
10
100
10
395 400 405 410 415 420
395 400 405 410 415 420
Z VERTEX (meters)

Figure 96. The z-vertex distribution of all coherent K_S, data and Monte Carlo, in the neutral mode.

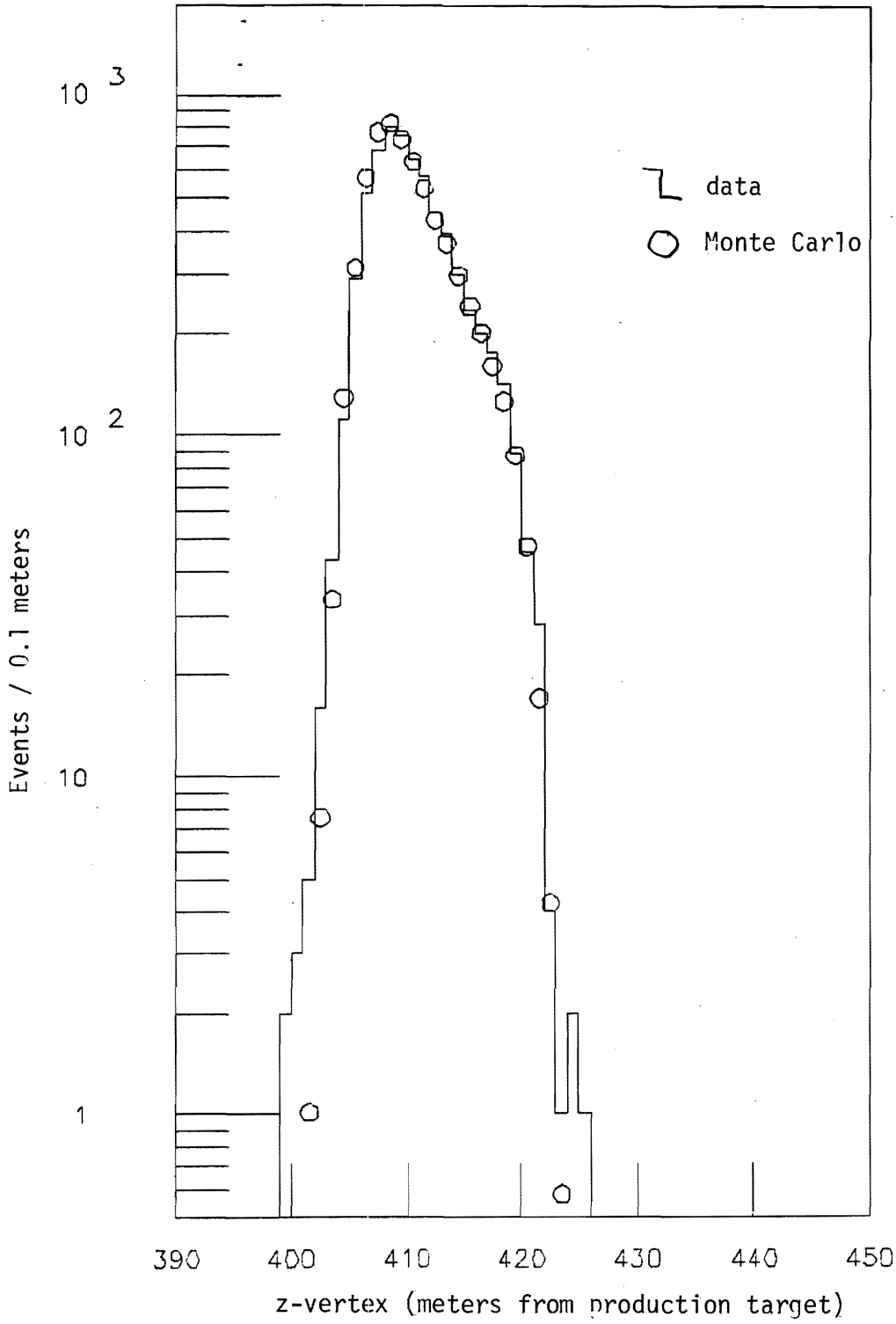
data
Monte Carlo
Events / 0.1 meters
10 3
10 2
10
1
390
400
410
420
430
440
450
z-vertex (meters from production target)

Figure 97. The coherent K_S energy spectrum, data and Monte Carlo, in the neutral mode.

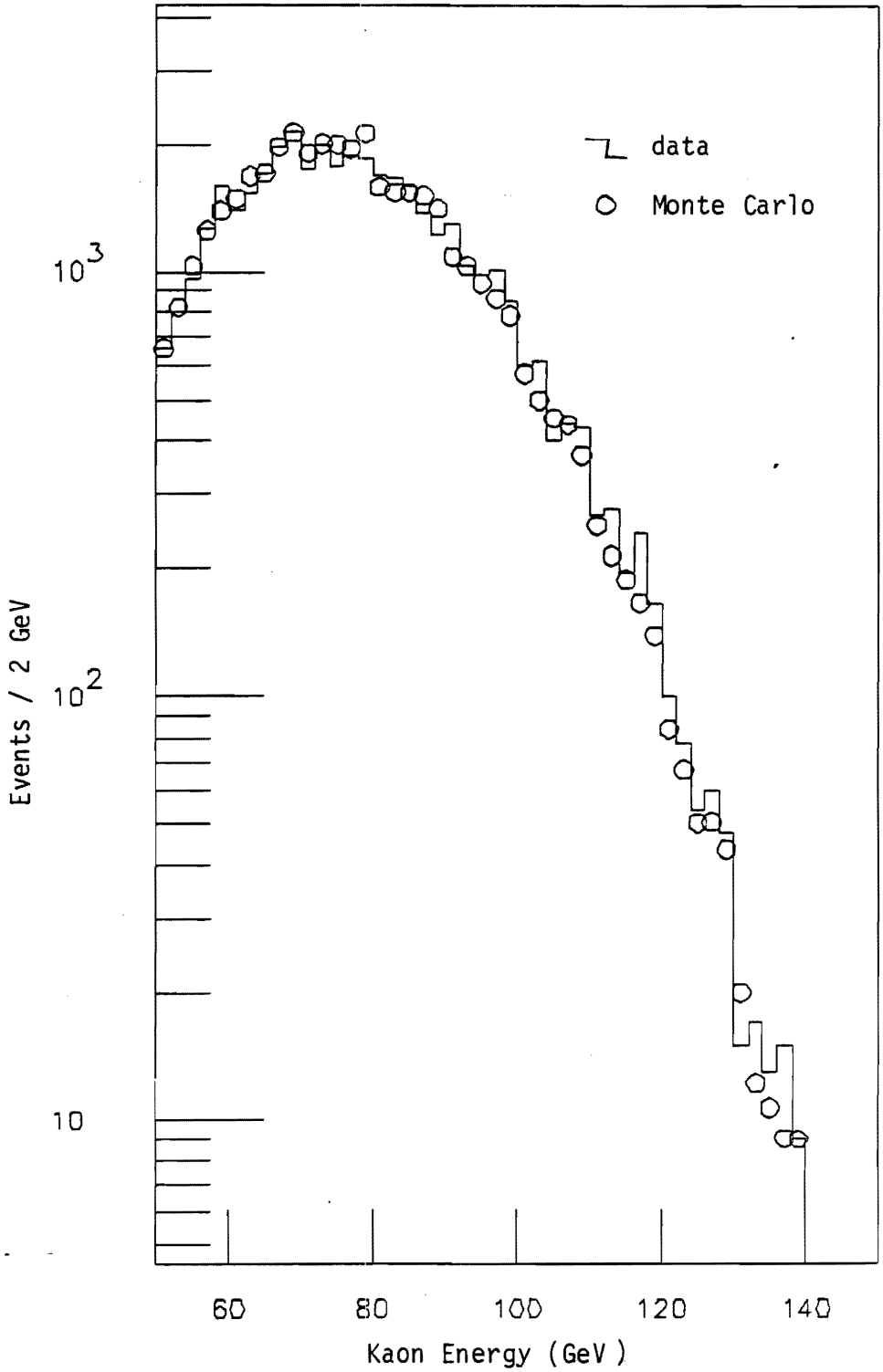
data
Monte Carlo
10^3
10^2
10
Events / 2 GeV
60
80
100
120
140
Kaon Energy (GeV)

Figure 98. The converted photon energy spectrum for coherent K_S, data and Monte Carlo, in the neutral mode.

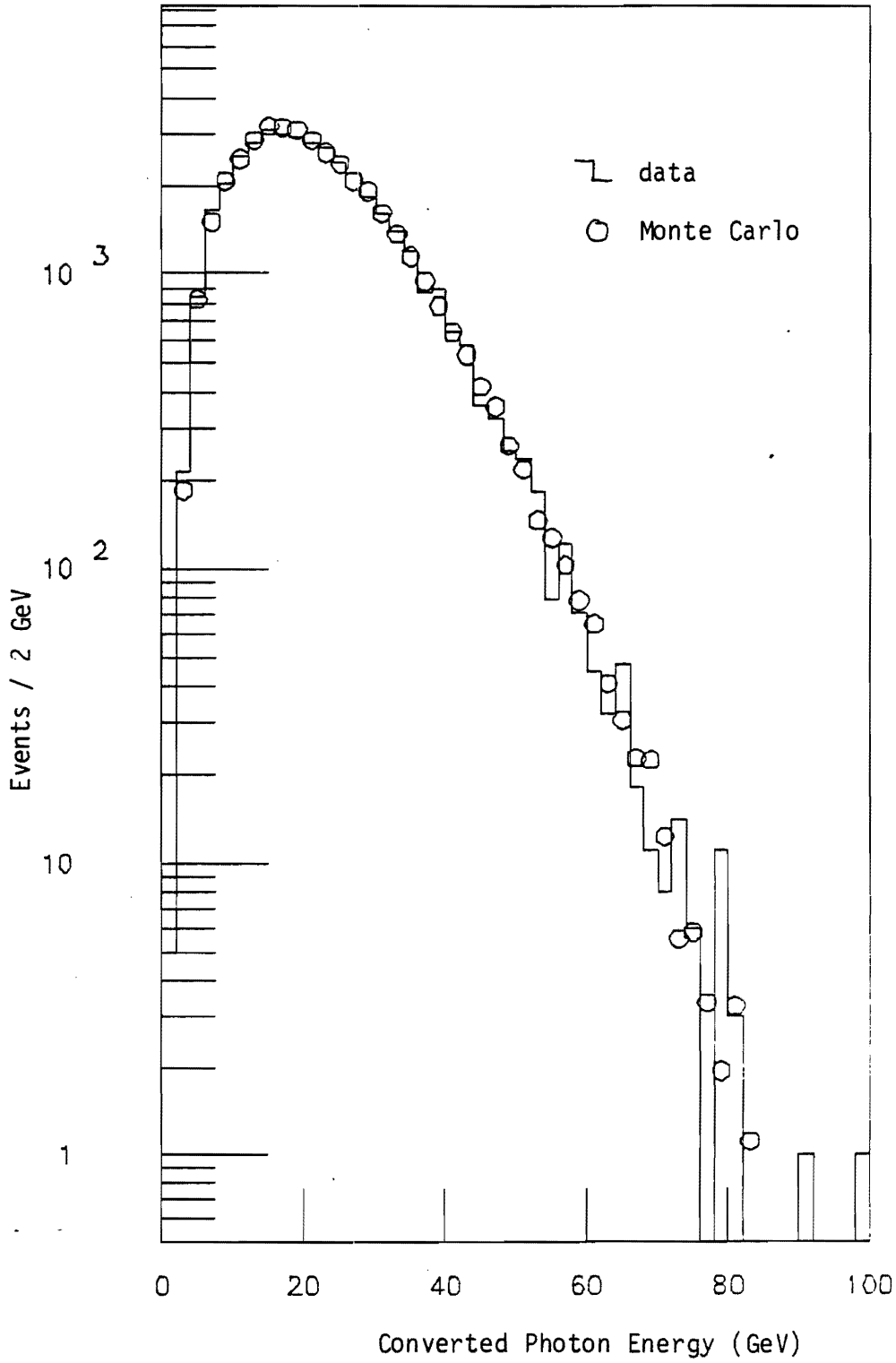
data
Monte Carlo
Events / 2 GeV
10 3
10 2
10
1
0
20
40
60
80
100
Converted Photon Energy (GeV)

Figure 99. The unconverted photon energy spectrum for coherent K_S, data and Monte Carlo, in the neutral mode.

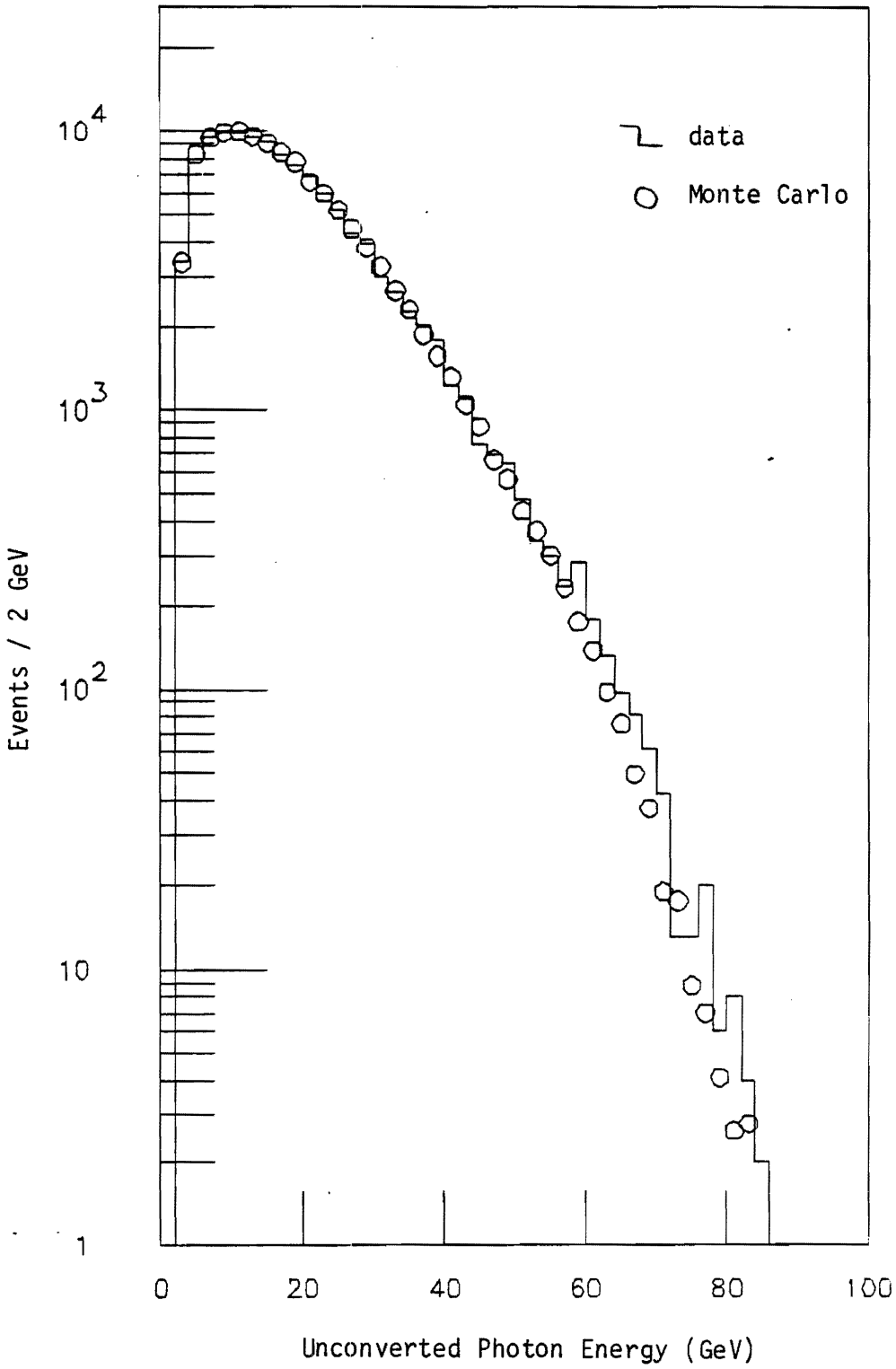
data
Monte Carlo
10^4
10^3
10^2
10
1
Events / 2 GeV
0
20
40
60
80
100
Unconverted Photon Energy (GeV)

Figure 100. The distance between photons for coherent K_S, data and Monte Carlo.

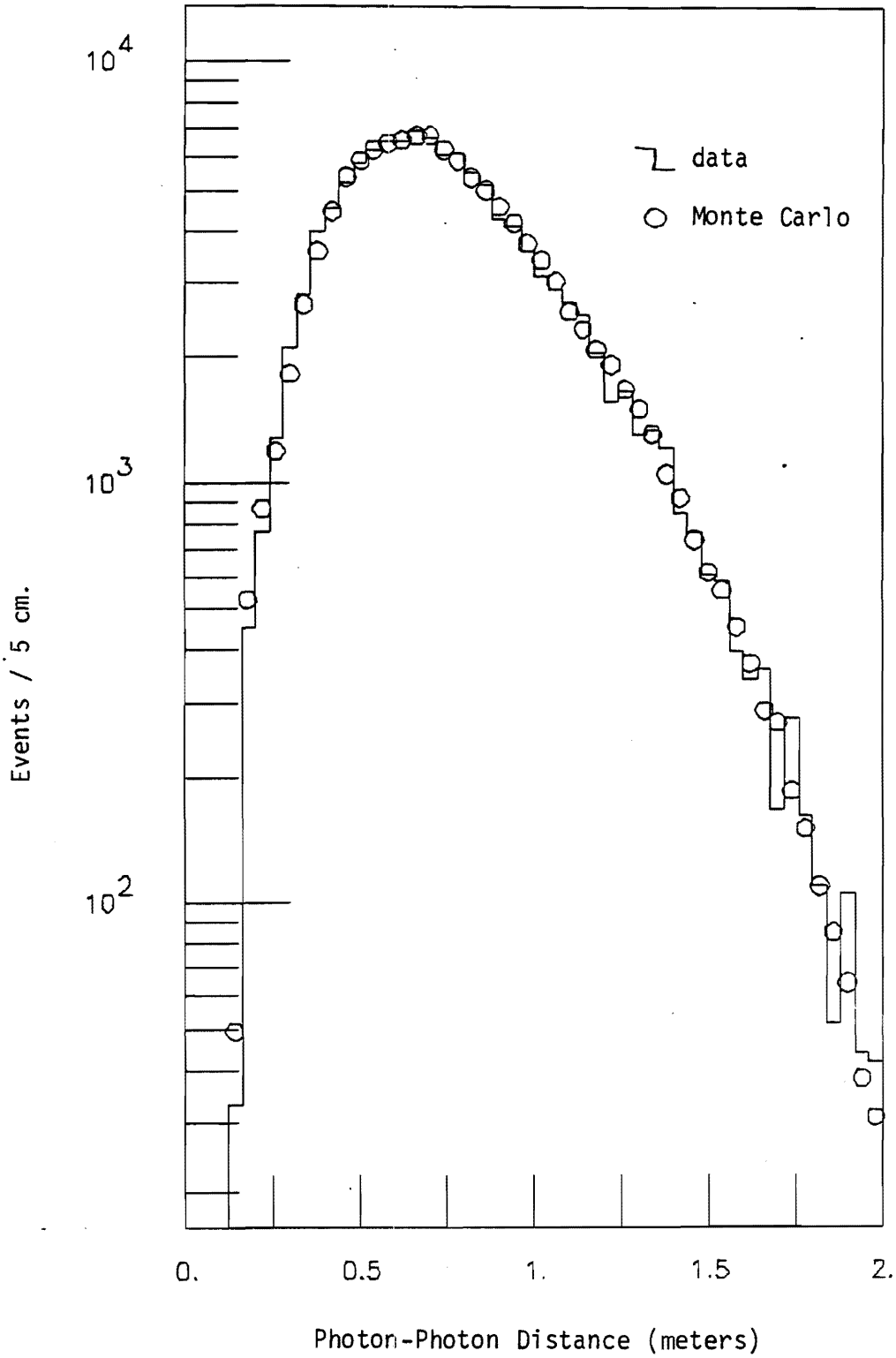
10^4
10^3
10^2
Events / 5 cm.
data
Monte Carlo
0.
0.5
1.
1.5
2.
Photon-Photon Distance (meters)

Figure 101. The χ^2 distribution of coherent K_S, data and Monte Carlo, in the neutral mode.

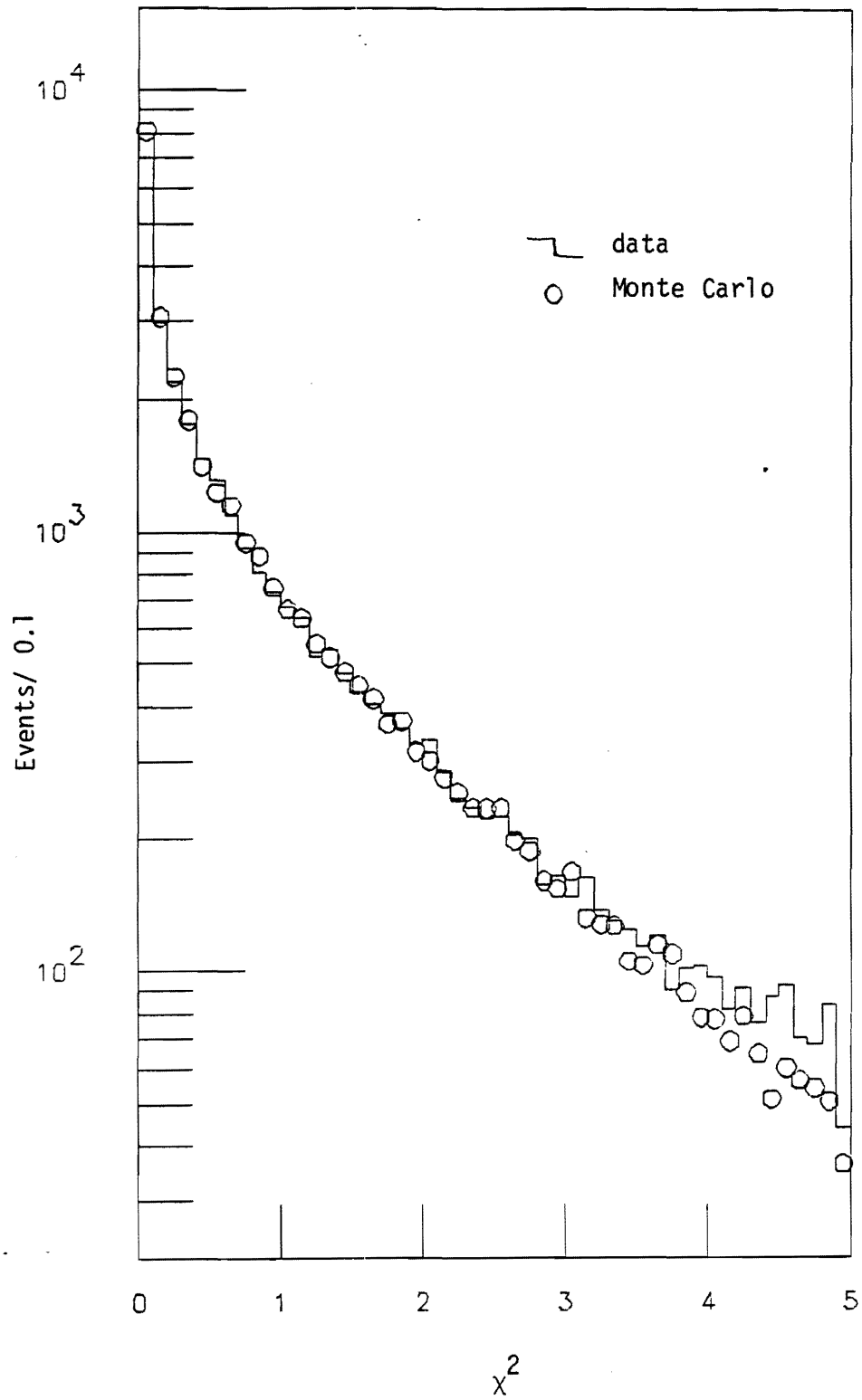
data
Monte Carlo
10^4
10^3
10^2
Events/ 0.1
0
1
2
3
4
5
χ^2

Figure 102. The coherent K_S and K_L z-vertex distribution, 60 $< p_K <$ 70 GeV/c and 90 $< p_K <$ 100 GeV/c, data and Monte Carlo, in the charged mode.

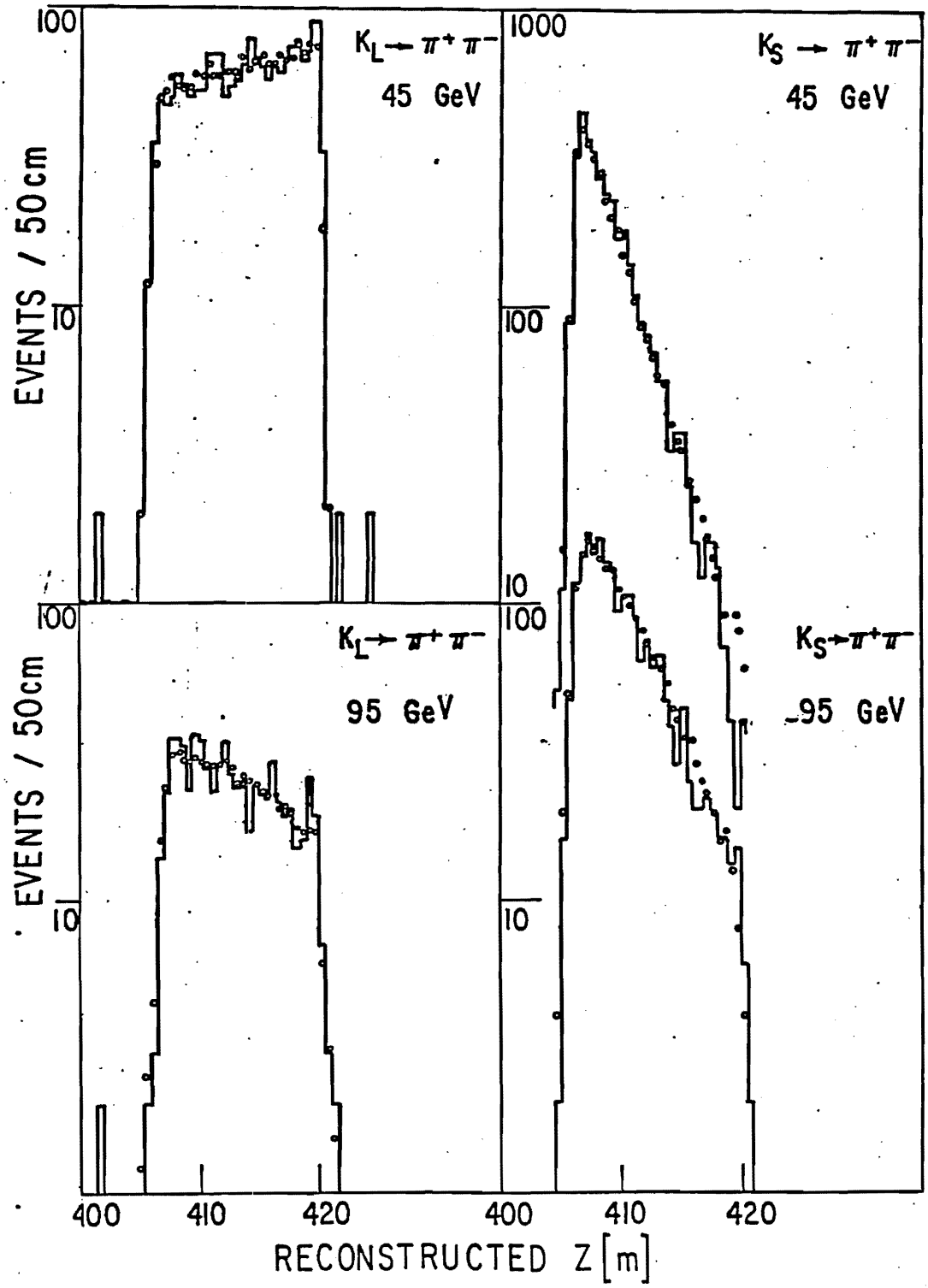
$K_L \to \pi^+\pi^-$
45 GeV
$K_S \to \pi^+\pi^-$
45 GeV
$K_L \to \pi^+\pi^-$
95 GeV
$K_S \to \pi^+\pi^-$
95 GeV
EVENTS / 50cm
EVENTS / 50cm
100
10
1000
100
10
100
10
100
10
400
410
420
400
410
420
RECONSTRUCTED Z [m]

Figure 103. The coherent K_S energy spectrum, data and Monte Carlo, in the charged mode.

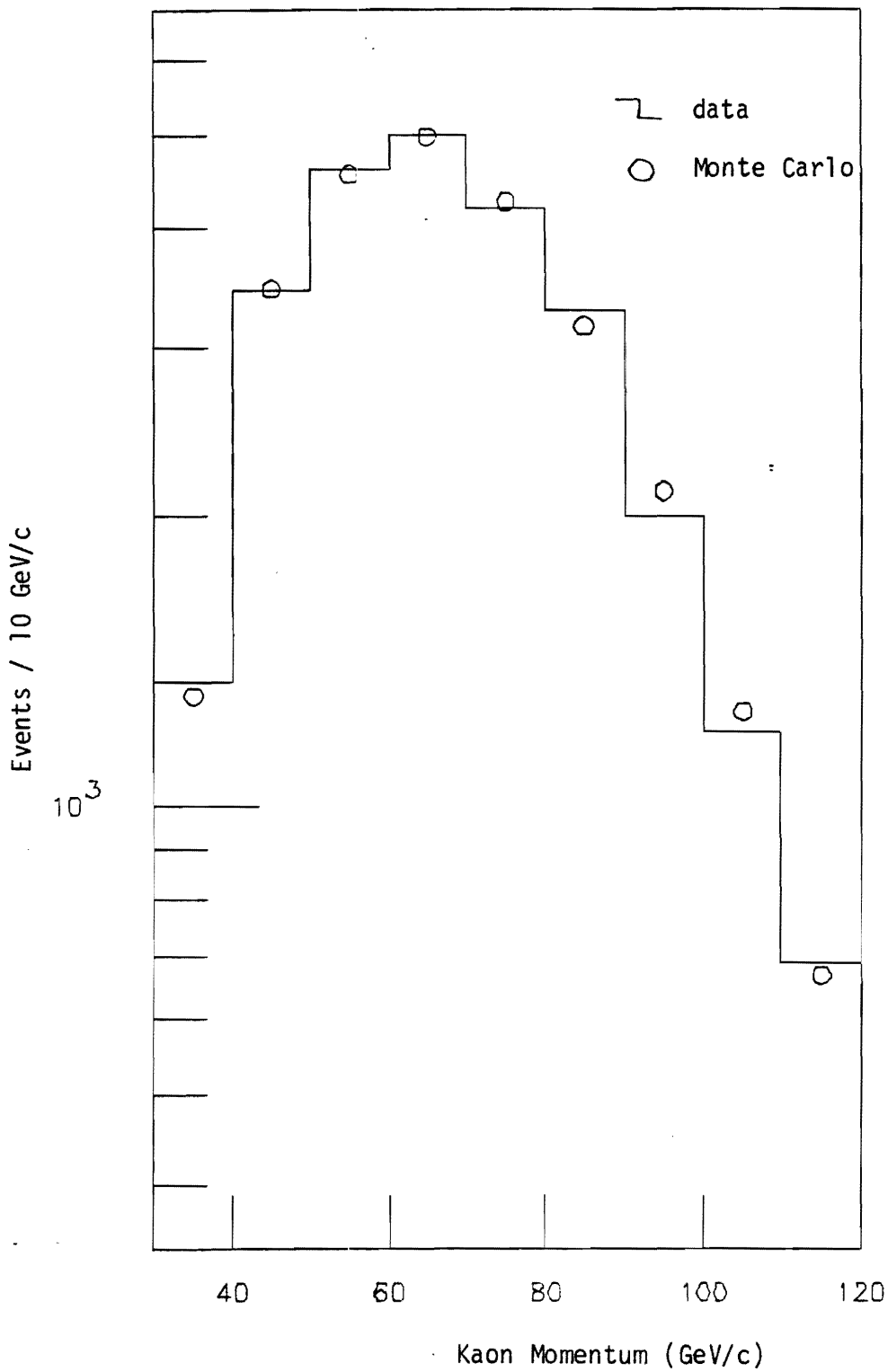
data
Monte Carlo
Events / 10 GeV/c
10^3
40
60
80
100
120
Kaon Momentum (GeV/c)

TABLE 15

ACCEPTANCES FOR $K_L, K_S \rightarrow \pi^+\pi^-$

p_K	A_L	A_S
35	.0963	.0697
45	.216	.189
55	.303	.292
65	.362	.351
75	.365	.369
85	.317	.339
95	.246	.274
115	.116	.137

REFERENCES

1. G. Lüders, Ann. Phys. 2, 1 (1957)

2. C.S. Wu, et al., Phys. Rev. 105, 1413 (1957)

3. R.L. Garwin, L.M. Lederman, and M. Weinrich, Phys. Rev. 105, 1681 (1957) J.I. Friedman and V.L. Telegdi, Phys. Rev. 105, 1681 (1957)

4. J.H. Christenson, J.W. Cronin, V. Fitch and R. Turlay, Phys. Rev. Lett. 13, 138 (1964)

5. G. Senjanovic and T. W. Stecker, Phys. Lett. 968, 285 (1980)

6. M. Gell-Mann and A. Pais, Phys. Rev. 97, 1387 (1955)

7. K. Kleinknecht, Ann. Rev. Nucl. Sci. 26, 1 (1976) This is an excellent review article; Section II contains a more complete discussion of CP-phenomenology than can be given here.

8. Ibid., p. 6

9. T.T. Wu and C.N. Yang, Phy. Rev. Lett. 13, 380 (1964)

10. E. Commins, Weak Interactions (McGraw-Hill, 1973), pp. 155-157

11. S. Aronson et al., Phys. Rev. Lett. 25, 1057 (1970) and Geweniger et al., Phys. Lett. B52, 108 (1974) are two of the Δm measurements. A complete listing is avainable from the Particle Data Group (C.C. Wohl et. al.) Rev. Mod. Phys. 56, 2, Part II.

12. J.H Christenson et al., Phys. Rev. Lett. 43, 1209 (1979)

13. F. Niebergall et al., Phys. Lett. B49, 103 (1974)

14. M.F. Losty et al., Nucl. Phys. B69, 185 (1974); also the CERN-Munich Collaboration, in the Fourth International Conference on Meson Spectroscopy, Boston, 1974.

15. M. Banner et al., Phys. Lett. 13, 569 (1964)

16. M. Holder et al., Phys. Lett. B40, 141 (1972)

17. J.H. Christenson et al., Phys. Rev. Lett. 43, 1209 (1979)

18. L. Wolfenstein, Phys. Rev. Lett., 13, 569 (1964)

19. M. Kobayashi and K. Maskawa, Prog. Theor. Phys. 49, 652 (1973)

20. F.J. Gilman and M.B. Wise, Phys. Lett. B83, 83 (1979). The original arguments were made in M.A. Shifman, A. I. Vainshtein and V. I. Zakharov, JETP Lett. 22, 55 (1975); Nucl. Phys. B120, (1977); JETP (Sov. Phys.) 45, 670 (1977)

21. The literature here is extensive. We quote three excellent papers: B. Guberina and R.D. Peccei, Nucl. Phys. B163, 289 (1980); A.J. Buras et. al., Max Planck Institute Preprint MPI-PAE/PTH 77/83, October 1983, and F. Gilman and J. Hagelin, Phys. Lett. 133B, 443 (1983). We will refer to this last paper frequently and refer to it as Gilman and Hagelin, 1983.

22. CLEO Collaboration, A. Chen et. al. ,Phys. Rev. Lett. 52, 1084 (1984)

23. Gilman and Hagelin, 1983.

24. R. N. Mohapatra and D. P. Sidhu, Phys. Rev. D17, 1876 (1978) M. Wakano, Prog. Theor. Phys., 70, 1460 (1983)

25. S. Weinberg, Phys. Rev. Lett. 37, 657 (1976) ; D. Chang, Phys. Rev. D, 25, 1318 (1982); J. Donoghue, J. Hagelin, and B. Holstein, Phys. Rev. D, 25, 195 (1982)

26. H. W. Atherton et al. , CERN Publication # 80-07 (1980)

27 Radio Corporation of America, Electronic Components Division, Harrison, N.J. 07029

28. W. Molzon, Ph. D. Thesis, University of Chicago (1979) (unpublished)

29. G.H. Sanders et al., IEEE Trans. Nucl. Sci. Ns-25, No. 1, 56 (1978)

30. D. Hedin, Ph. D. Thesis, University of Wisconsin, Madison (1980) (unpublished)

31. D.P. Coupal, Ph. D. Thesis, University of Chicago (1984) (unpublished)

32. Schott Optical Glass Company, Duryea, Pa.

33. W. B. Atwood, Ph. D. Thesis, SLAC Report RT-185. The appendix on lead glass is a useful and well-written reference.

34. W. Morrison et al., Nucl. Inst. and Meth., 143, 311 (1977)

35. Eastman-Kodak, Rochester, N.Y.

36. Dow Corning Corp., Silicone Dielectric Gel Q3-6527, Midland, Michigan 48640

37. Radio Corporation of America, Photomultiplier Manual, Electronic Components Division, Harrison, N.J. 07029

38. Amperex Electronic Corp., Hicksville Division, Long Island, N.Y. 11802

39. Conetic foil is manufactured by the Perfection Mica Company, North Thomas Drive, Bensenville, Il. 60106

40. LeCroy Research Systems, 700 South Main Street, Spring Valley, N.Y. 10977

41. Xenon Corp., 64 industrial Way, Wilmington Ma. 01887

42. Valtec Corporation, 99-T Hartwell Street, West Boylston, Ma. 01583

43. H.W.M. Norton, Ph. D. Thesis, University of Chicago (1984) (unpublished)

44. Ibid.

45. D. Carlsmith, Ph. D. Thesis, University of Chicago (1984) (unpublished)

46. J.F. Bartlett et al., IEEE Trans. Nucl Sci. Ns-26, No. 4, 4427 (1979)

47. A. Gsponer et al., Phys. Rev. Lett. 42, 13 (1979); A. Gsponer et al., Phys. Rev. Lett. 42, 9 (1979)

48. J. Roehrig et al., Phys. Rev. Lett. 38, 1116 (1977); erratum, ibid. 39 674 (1977)

49. J. Roehrig, Ph. D. Thesis, University of Chicago (1977) (unpublished)

50. Molzon, op. cit.

51. Banner et al., op. cit.

52. J. Christenson et al., Phys. Rev. Lett., 43, 1209 (1979)

53. Gilman and Hagelin, 1983. The values of τ_b are derived from : Mark II Collaboration, N.S. Lockyer et al. ,Phys. Rev. Lett., 51(1983) 1316; MAC Collaboration, E. Fernandez et al. , Phys. Rev. Lett., 51, 1022 (1983)

54. F. Gilman and J. Hagelin, private communication.

55. C. Rubbia, Dortmund Conference on High Energy Physics (1984)

56. Fermilab Proposal P731; the experiment will start data-taking around January 1985.

57. CERN Proposal CERN/SPSC/81-110, SPSC/P174 (1981). Data taking for this experiment will begin in early 1985.

58. Fermilab Proposal P621; the experiment took preliminary data as of June, 1984.